Fatigue Assessment of Brick Masonry Arch

By Strain-Life Approach

Arnab Chakraborty

Submitted in accordance with the requirements for the degree of

Doctor of Philosophy

The University of Leeds
School of Civil Engineering

July 2024

I, Arnab Chakraborty, confirm that the work submitted is my own and that appropriate credit has been given where reference has been made to the work of others.

Acknowledgements

Abstract

Masonry arch bridges are integral to any national infrastructure carrying daily passenger and freight traffic supporting the national economy, 85% of these assets are single spans less than 10m. Improved knowledge of damage and load-life understanding will create significant difference to safe management and planning of interventions to asset owners.

Popular analysis methods correctly determine the four-hinge collapse mode. All present load capacity assessments are limited to stability conditions. Overall estimates of the collapse load do not appreciate arch behaviours under long term cyclic loadings. Present fatigue assessment for masonry arches relies on probabilistic models. All these models are primarily based on tests carried out on masonry prisms. Lately researchers have started testing masonry arches in laboratories.

Two fundamental limitations of present approaches are firstly they compare compressive strength based on tests of undamaged specimen and secondly numerical models ignore deformations. Recent guideline removed material factors from test properties. Material properties do not represent present state of a very complex multiple contributors to arch capacities. These include cumulative damages due to repeated and increased traffic, environmental damages, material deterioration, contribution and stiffnesses of backfill and spandrels. Therefore, predicted load capacities are unrealistic and their application to probabilistic models lead to unreliable outcome.

The assessment of masonry arches shall confirm that the traffic loading does not reach levels that can cause further distress and reduce the life of the arch (CS 454).

This research has evolved from the principles of progressive deformations, i.e., induced damages, over life of an arch. Masonry arch is tested to failure under progressive cyclic loading. Cyclic loading causes stress reversals therefore represent actual damage. Fatigue model for commonly occurring isotropic materials is well understood. Masonry is an inhomogeneous and highly anisotropic in nature. This research has simplified damage modelling by limiting to stiffness degradation. For an arch this is calibrated by comparing direct measurements to numerical results. Arch deflections are now possible to measure under passing live loads with reasonable resolution. Finally, a parametric strain-life analogy has been presented for prediction of arch life corresponding to arch capacity and resulting deflection. Additionally, strain-life approach can predict residual life of an arch by directly measuring their

deformation under live loads. Damage modelling is proposed based on calibration of in-situ measurements and analytical model.

For obvious reasons the strain-life graph is based on limited laboratory tests carried out on multi-ring segmental arches. Proposal is validated through similar previous tests. A non-linear numerical modelling tools considering interface masonry modelling is recommended.

Large scale in-situ test on real scale single span arches will further improve reliability of this proposed damage-based understanding of strain-life relation. Critical understanding of deformation, damage and life will allow practicing engineers and asset owners to predict the residual life with confidence and credibly plan for future maintenance of these historic sustainable assets.

Table of Contents

List of Tables

List of Figures

Preface

Author has worked extensively for design and assessment of highway and railways bridges. While assessments of concrete and steel bridges are carried out with sufficient level of confidence, this is not the case for masonry arches. This is more so when arches develop severe damages due to multiple reasons. These are inherent to their geometry, support conditions, environmental factors, quality and depth of backfill beside increase loads and frequency due to traffic demands. Present assessment methods are based on available analysis tools including simpler spreadsheet methods to sophisticated finite element applications. Modelling and material properties are derived from in-situ surveys and tests carried out on existing arches. Recommended factors are then applied to derive the permissible capacity representing existing condition of the arch based on judgments of experienced assessors and bridge inspectors. Though this is an accepted practice, the author's experience particularly for assets with severe levels of deterioration led to this research. Present analysis and inspections are based on observations made under wheels-free or no live load conditions. Capacities based on stresses are calculated without any considerations for existing deteriorations. National and international guidelines do not provide any serviceability criteria for acceptance. This research has sought to provide the concept of assessments based on inspection and measurement on arches under applied loading. Proposed numerical modelling is based on stiffness degradation to capture the present condition of the arch as opposed to theoretical properties based on static tests. Finally offering methods for inspection, measurements, and prediction of safe life of an arch before planning for any major maintenance of the asset.

Author sincerely hopes this novel attempt of strain-life analogy for an arch assessment will lead the way for much awaited serviceability limit state criteria of a Masonry arch. Methodologies presented are more suited for practicing engineers.

Chapter 1
Introduction

Masonry arch bridges form an integral part of the railway infrastructure in Europe and throughout the world. They are one of the oldest type of structures in the railway bridge assets still in service. A survey carried out by Sustainable bridges under their Work Package 2 claimed that 40% of the existing rail network bridges in Europe are masonry arches (*Sustainable Bridges, 2007*). More than 60% of those bridges are over 150 years old and still carry increased volumes of traffic. Thus, it is important to develop a better understanding of their life expectancy and fatigue limits. There are approximately 70,000 masonry arch bridges on the UK road and rail networks alone. Network Rail owns approximately 40,000 bridges, comprising around 20,000 masonry arches (*RSSB T360, 2005*). Consequently, arch bridges are integral to our transport infrastructure coupled with their significant heritage value; the safe management of these structures is critical.

1.1 Background

The masonry arch, whether of stone or brick construction, is one of the oldest structural forms developed to span an opening in a building or to bridge across a natural feature, canal. highway or railway (*Garrity, 2015*). The earliest remaining examples of masonry arch construction were built of sun dried, mud bricks (or adobe) about 5,000 years ago for buildings in Lower Egypt, Iran, the Eastern Mediterranean region and Mesopotamia (*Van Beek, 1987*). It is commonly accepted that the Romans probably made the first use of the masonry arch for bridges, viaducts and aqueducts some 3,000 years later (*Smith, 1993*). Following the decline of the Roman Empire, the masonry arch continued to be used in many parts of Europe and elsewhere, throughout the Middle Ages, for a variety of buildings and bridges.

Throughout the 16th, 17th and 18th centuries, before the industrial revolution and the development of the canal and railway systems in Europe, most commercial goods were transported overland by horse and cart. Where rough terrain prevented cart access it was common to transport goods in panniers carried by trains of packhorses. Stone masonry arch packhorse bridges, some only the width of a horse and often without parapets to allow the heavily laden packhorses to cross without hindrance, were constructed across streams, rivers and other obstacles on many trade routes. Many of these survive today and are public rights of way carrying pedestrian traffic; some have been widened to accommodate modern vehicular highway traffic (*Lay 1992, McEwen 2010*).

The mid-18th to early 19th century saw improvements in fired clay brick manufacturing facilitated by the industrial revolution. The development and expansion of the inland waterway and railway transportation networks in the UK and elsewhere saw rapid growth in the construction of masonry arch bridges, viaducts and tunnel linings from fired clay bricks as well as stone (*Fox 1885-6, Ruddock 1979*).

In general. masonry arch construction continued to be used until the late 19th and early 20th centuries by which time steelwork and reinforced concrete construction had been developed into more viable structural alternatives for structures such as bridges and viaducts. This pattern was also experienced in many parts of Europe and other parts of the developed World leaving a legacy of many thousands of masonry arch bridges, culverts and viaducts supporting the canal. highway and railway networks.

1.2 Present Scenario

There are approximately 40,000 masonry arch highway bridges and 33,000 railway arches still operational in UK (*Page, 1993*). Most of these were constructed between 18th, 19th and early 20th centuries. As part of a state-of-the-art review of masonry arch bridges, initiated by the International Union of Railways (UIC or Union Internationale des Chemins de fer) in 2002, a survey of the number and types of existing bridges of the railways in 14 countries was undertaken (*UIC, 2004*). Approximately 60% of the bridge stock surveyed, some 200,000 structures, was found to consist of masonry arch bridges or culverts. Of these, approximately 85% were found to be single span structures; only 8.5% exceeded a span of 10m and 70% were between 100 and 150 years old with 12% more than 150 years old.

Under modern operating conditions, some masonry arch structures, in particular those used to support railways with heavy, high speed and high frequency traffic, have been found to suffer gradually increasing deterioration caused by the effects of repeated or cyclic loading. As a result, engineers responsible for the management, maintenance and operation of such bridges are faced with the challenge of assessing the impact of cyclic loading on the load carrying capacity to avoid premature deterioration and increased maintenance costs (*Koltshida et al., 2019*). For these structures, it is vital to determine the fatigue strength rather than the ultimate carrying capacity. In doing so, the remaining service life, with possible traffic load limitations, may be estimated (*Casamassima, 2019*).

1.3 Performance Assessment of Arch Bridge

Engineers have long recognised the need to understand and determine the fatigue performance of masonry arches, particularly in bridges. Harvey (*1991*) suggested the

use of deflection and cracking criteria when assessing the strength and performance of masonry arches, despite the difficulties associated with the prediction, detection and measurement of cracks. More recently there has been increasing recognition of the need to establish serviceability limits for masonry arch bridges to safeguard against progressive damage and ensure that they continue to perform satisfactorily (*Boothby, et al. 1998, Ronca, et al. 2004, Roberts et al. 2006, Casas 2009*).

1.3.1 Assessment and Fatigue Approach

To assess or design for the Ultimate Limit State according to The Structural Assessment of Underbridges (*NR/GN/CIV/025, 2006*) a live load factor of $\gamma_{fL} = 1.4$ and $\gamma_{f3} = 1.35$ is proposed with an additional dynamic factor of 1.8. Therefore, combined factor of safety (1.35x1.4x1.8=) 3.4.

It is also recommended that, for a single axle, the allowable axle load should be obtained using the following formula:

Allowable single axle load x γ_{fL}

= Theoretical maximum single axle failure load x F_j x F_{cM}

where γ_{fL} = 3.4 (*4.11 Part 4 BA 16/97 Amendment No 2, Nov 2001*)

When multiple-axle AW vehicles are used for more precise calculations, the check for adequacy should be carried out at the ultimate limit state (ULS). A γ_{fL} value for the most critical axle should be taken as 3.4 and for the other axles as 1.9. When the configuration of a vehicle at the time of crossing is known with some precision, as in the case of some abnormal loads, γ_{fL} for all axles may be taken as 2.

Recently assessment of masonry arches according to *CS 454 version 1.1.0* is mentioned that the traffic loading does not reach levels that can cause further distress and reduce life of arch. The assessed resistance for masonry arches is verified to exceed the assessment load effects at the ULS verification. Referring to section 7 and Appendix A of the document γ_{fL} for all axles could vary between 1.3 to 5.4 depending on condition of the arches. For arches with reasonable defects a γ_{fL} value between 1.8 and 2.4 recommended. Interestingly, the partial factor for material strength γ_m is taken as 1.0.

For the Serviceability Limit State checking, there is an interesting suggestion in UIC Code for the assessment of the load-carrying capacity of existing masonry and mass-concrete arch bridges (*UIC 776-3R, 1995*) for a linear elastic model; to determine the stress resultant in an arch of thickness *d*, the resultant compressive force at the ultimate limit state should not be at a distance greater than *d/12* from the edge of the compression zone to avoid masonry crushing and resulting hinge formation.
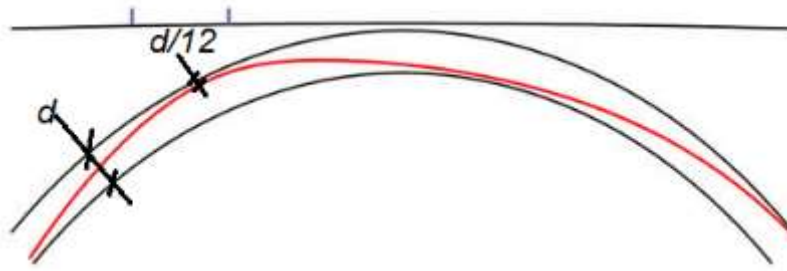
Figure - 1.1 Limiting Resultant Compressive Stress, (*UIC 778-3R, 1995)*

For railway bridges, the UIC code for the assessment of the load carrying capacity of existing masonry and mass-concrete arch bridges (*UIC 776-3R, 1995*) recommends limiting edge stress to 65% of characteristic compressive strength of masonry, f_{ck}. Furthermore, the UIC code also recommended restricting the calculated vertical deflection at the crown to 1/1000 of arch span under traffic loading.

In 1997, the then UK Highways Agency limited the accepTable in-service loads to 50% of the predicted ultimate load as a simple means of reducing the likelihood of fatigue-induced damage in their bridge assessment guidelines (*BD 21/97 1997*). This was introduced because the results of numerous large-scale and full-scale monotonic load tests on masonry arch bridges indicated that the load-deflection response remains approximately linear up to about 50% of the ultimate load (*Clark, 1994*). No attempt was made to incorporate a detailed understanding of fatigue failure mechanisms into the assessment process. In 2020, Highways England (the then successor to the UK Highways Agency) removed the 50% limit for new masonry arch bridge design (*CD 376, 2020*).

In their latest 2020 guidelines on masonry arch bridge assessment, the UIC (*IRS 70778-3:2020*) placed no limits on crack formation and opening in masonry arches as criteria for serviceability checks. Indeed, the UIC do not consider masonry arch bridges deflecting under service loads to be an issue due to their inherent rigidity. The UIC recommendations recognise, however, that a Permissible Limit State (PLS) may be useful in masonry arch bridge assessment. The occurrence of a PLS is the point at which changes will occur that measurably affect the ability of the bridge to carry its working loads for the duration of its expected life. Under the cyclic load conditions that exist with many masonry arch railway bridges, there is a high risk that the masonry can become damaged due to fatigue behaviour. Hence, the concept of a PLS particularly relevant for assessing masonry arches under cyclic loading and, therefore, represents an important step change in the assessment of masonry arch bridges. This is an integral part of the proposed SMART methodology of masonry arch bridge assessment, see 1.3.2.

1.3.2 Assessment Methods

A variety of models have been developed ranging from experimental formulas, two-dimensional models to three-dimensional finite or discrete element models. The classic approach to determining the stability of arch bridges dates to the work of Pippard (*Pippard et al.1939*). It starts from a two-hinge arch for which minimum load applied to a fixed position, that causes the arch to turn into a mechanism, i.e. four hinges. The exact positions of the last two hinges are variables to be determined. This approach was further extended by Heyman introducing thrust-lines (*Heyman, 1982*). This theory assumes that the thrust-line must become tangential to intrados or extrados in four locations at which point the structure becomes a mechanism. The parameters required for accurate estimation of the collapse load, such as compressive strength and other mechanical properties of the material are only taken into account indirectly by the inclusion of correction factors. Archie-M applies the traditional thrust line analysis combined with a zone of thrust for modelling finite crushing strength. The thrust line is found with a three-hinge system. Hence, it only provides stability conditions or coarse estimates of the collapse load and contrary to the approach presented below, these methods do not allow the precise calculation of the behaviour of arches under increasing loads.

More recent work based on the rigid-plastic approach is reported by Gilbert and Melbourn (*Gilbert et al.1994*) Hughes and Blackler (*Hughes et al.1995*) and Boothby (*Boothby, 1995*). The Rigid block theory is the basic model for the understanding of the fundamental behaviour of brick arches. Ring uses a rigid-plastic block formulation where the collapse load is found by maximizing the load factor with linear programming. A new version of the widely used RING masonry arch bridge analysis software (*Gilbert et al. 2006*) has been developed in collaboration with UIC. These methods are usually referred to as low level assessments. High-level assessments tend to be based on the use of finite element or discrete element computational models. High-level assessment is generally only necessary when a structure is found to have insufficient load capacity using a low-level assessment method, or it is necessary to analyse the effects of significant damage on the load carrying capacity (*Brencich et al. 2006*).

Audenaert (*2010*) has reported that the collapse load differences can be summarized as follows: collapse load elasto-plastic ≤ collapse load Ring ≤ collapse load Archie-M. The three models produce almost the same collapse mode.

Current guidance for highway and railway bridges assumes that masonry's 'safe' and serviceable capacity is when fd < 0.4fk (*CD 376, 2020, UIC IRS 70778-3, 2020*) where fd is the design stress and fk is the masonry strength in compression. None of the

current guides or the assessment methods refer explicitly to fatigue behaviour or any associated fatigue-induced serviceability failures.

Melbourne et al (*2007*) attempted to address this limitation within his proposed Sustainable Masonry Arch Resistance Technique (SMART). He combined existing strength assessment methods into a single methodology by considering the ultimate load capacity, the long-term behaviour and the residual life. In the technique, the stress ranges that the bridge under consideration experiences for each of the modes of failure (e.g., collapse mechanisms, ring-separation, crushing and their cumulative effects), are combined with life expectancy estimates based on S-N diagrams (also known as stress – life curves) which account for the fatigue properties of the materials.

Melbourne et al (*2007*) reported that if the range in the stress level increases from, for example, 25% to 50% of the design strength (*Sult),* and the maximum stress (*Smax)* increases to 75% of *Sult,* then the maximum number of cycles to failure reduces from approximately 10^7 to $10^{1.75}$ with the consequential reduction in residual life. This indicates that further work is needed to take account of the impact of fatigue damage on masonry arch bridge behaviour before existing guidance can be used with confidence for the design of new masonry arch bridges or the assessment of existing structures.

A series of laboratory tests on large-scale multi-ring brickwork arches under long term cyclic loading has been carried out at the University of Salford under the EU-funded Sustainable Bridges project (*Melbourne et al. 2007*). Although the four-hinge collapse mechanism is often regarded as the classical failure mode for masonry arches, all arches tested under long-term fatigue loading failed by ring separation and the fatigue limit was found to be as low as 40% of the static capacity. Moreover, a model for interactive S-N curves, where S = the maximum static stress and N is the number of load cycles, was proposed for masonry arches and masonry qualities. These curves facilitate a qualitative assessment of the residual service life under a given loading regime (see Figure - 1.2).
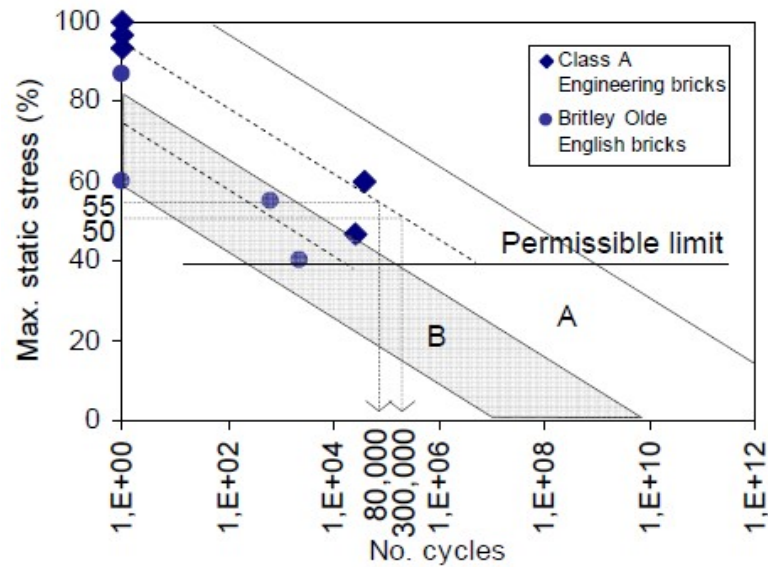
Figure - 1.2 S-N Curve for Ring Separation Failure, (*Melbourne et al. 2007*)

S-N curves have been proposed in the SMART assessment technique to provide a holistic assessment tool that can identify the bridges' service life under any operational stress level and their likely modes of failure. The S-N curves can also indicate the possible sensitivity of the bridge's life expectancy to changes in working stress levels. If, for example, the shear stresses increase from 50 to 55% of the maximum static stress, the bridge's life expectancy may reduce from 300,000 to almost 80,000 cycles) as shown in Figure - 1.2. S-N curves can also indicate the permissible limits for each failure mode and material quality below which no residual damage is likely to occur to the arch and loading can be applied for a theoretically unlimited number of cycles without requiring reinforcement or strengthening works.

S-N curves were proposed to compare the load-carrying capacity without interpreting the occurrence of damage initiation shown in Figure - 1.2. Fatigue Life is a combination of crack initiation and crack growth. The success of safe asset management depends on predicting fatigue life early enough to plan and manage the asset work bank. Damage to arches is caused by many factors. In addition to material properties of the brick, mortar additional factors are due to environmental deterioration, quality of backfill material. and stiffness contribution by the spandrel walls. The above prediction of the fatigue life overlooks these contributory factors. Cracks form in masonry arches, often at the masonry unit - mortar joint interfaces, even at very low stress levels or as a result of small movements such as abutment settlement. Under repeated loading from traffic, such cracks can propagate partially or wholly through the depth of the arch, making it very difficult to predict or estimate stresses with any accepTable level of reliability. Many researchers are continuing to work with S-N curves and many probabilistic

models have been published and reviewed. None of these works have so far tried to establish a reliable fatigue model for practical applications.

Though a stress-life approach appears to be effective for materials that perform consistently within their elastic range, it is suggested by the authors that this is inappropriate for masonry arches. All existing masonry arches have shown varying degree of deterioration due to multiple reasons. Mortar loss from brick interfaces, quality and depth of arch back fill, contributory environmental factors due to poor water managements have led to complex deterioration over the centuries. It is therefore unrealistic to calculate stresses in existing arches with any reasonable accuracy. Only reliable measurement that the asset owners can measure is the deformation of arches under passing live loads. Measured deflections can then be converted to strains using fundamental mathematical relationship, explained later in Chapter 5.

It is therefore proposed that a strain-life (ε-N) approach rather than a stress life (S-N) approach should be used for masonry arches to consider deterioration induced by fatigue loading or, indeed, any other form of damage. Given the rapid developments in the technologies used to monitor and record the condition and deformations (or strains) in masonry arch bridges (*Alexakis et al. 2020*), the strain-life approach is considered both timely and appropriate.

The primary aim of the research is to investigate the crack initiation and propagation history of masonry arches during their lifetime. Following on from the outcome apply fundamentals of fatigue theories predicting life of an arch under cyclic loading. Finally derive a strain life relationship that is simple and reliably applicable by measuring and monitoring deflections of arches under live loads. Tests have been performed as part of this research at the University of Leeds to establish the relationship between deflection and fatigue life, damage thresholds and strain-life prediction, limited to multiring segmental brick masonry arches.

1.4 Problem Statement

After reviewing the recommendations, although current masonry arch bridge assessment methods can predict the ultimate carrying capacity of the bridge with some confidence, serious concern has been identified for predicting residual life (*Melbourne et al. 2007*). The effects on masonry due to fatigue and changes in masonry properties need investigation. This is particularly significant when the line traffic regime has changed over the years. Modern day infrastructure is demanding increased number and axle loading of freight trains, resulting in increased cyclic loading. Rail Delivery Group (*2020*) is supportive of the Government's commitment to achieve net-zero carbon emissions across UK industry by 2050. While as a sector transport has become

more energy efficient, since 2016, transport has been the single-largest contributor to UK Greenhouse Gas (GHG) emissions. Even though 2050 is a generation away, infrastructure and policy decisions made now will directly affect the railway's ability to meet this target in a cost-effective way. Rail freight has an important role to play in helping the UK meet its decarbonisation targets. An average freight train moves the equivalent of 40-70 HGV loads, while only emitting 25 per cent of the equivalent carbon emissions as road transport.

Literature review, working experience and the study of industry standards UIC IRS 70778-3 (*2020*), CD 376 (*2020*) and NR/GN/CIV/025 *(2006),* and standards have led to believe that there are clear gap areas in the present methods of assessing arch bridges. Historical arch bridges have now been loaded by repeated cyclic loading for over 150 years. This will further increase with the Government's aspiration to increase rail freight to reduce carbon emission. As noted from regular inspection for assessment reports for Network Rail bridges, see Figure – 1.3, Repeated loadings over the years induce fatigue damage; this is often visible as ring separation common in railway bridges.

a) Bottom ring seperation   b) Multiple ring seperation

Figure - 1.3 Evidence of Arch Ring Separation, (*SMART, 2007*)

Prediction of the level of service load above which accumulative damage occurs is a key priority for the masonry arch bridge owners (*Wang et al., 2012*). There are still significant areas of uncertainty in high-cycle fatigue loading of brick masonry that limit the possibility to improve long term performance assessment methods and hence enable the development of a serviceability assessment for masonry arch bridges. Harvey *(1991)* advocated the use of deflection and cracking criteria despite the difficulties associated with their prediction, detection, measurement.

At present, design and assessments of masonry arches have been limited to ultimate limit state, with maximum stress limits for serviceability limit verification (*CD 376, 2020*).

However, there is no clarity on acceptable residual life and corresponding load capacity. The research described in this thesis is aligned with the PLS concept and the use of strain-life curves to provide a practical approach to embed fatigue behaviour in the assessment of masonry arch bridges under cyclic loading.

1.5 Aim

Dynamic rail loading is one of the main contributors to deterioration (*CIRIA C656*). The increases observed in the weight, length, and speed of modern trains have resulted in more onerous loading demands, which have caused damage in masonry bridge structures or foundations. Cyclic loading of damaged areas causes further deterioration, accelerating the degradation of materials due to ageing and water ingress (*UIC 2004*).

This research aims to predict residual life of existing masonry arch bridges by direct measurement of arch deformations under service live loads including damage analysis.

Scope of this work has been limited to segmental multi-ring masonry arches.

1.6 Objectives

To fulfil the aim of this research the following objectives have been identified.

- Investigate high-cycle fatigue behaviour of masonry: Review the current state of knowledge of assessment and design of railway arch bridges built of masonry or stonework;
- Understand the fundamentals of fatigue through historical works on various material regarding their fatigue responses. Propose the strain-life application for masonry based on limitations of existing practices and their opportunities;
- Plan and execute laboratory test for masonry arches subjected to cumulative damage to failure under cyclic loading, representing stress reversal. Compare progressive damages with historical work. Map parametric strain life (ε-N) behaviour of the arches during laboratory tests subjected to cyclic loading;
- Propose derivation of tangential strain from direct measurement of deformation under service (i.e., traffic) loads;
- Propose numerical models to analyse representative behaviour of masonry arch bridges failure under service load conditions, define damage properties for modelling. Commercially available software has been preferred that will help practising engineers;
- Further research recommendations: Recommend further research for carrying out strain life ε-N mapping of masonry arches.

1.7 Methodology

To fulfil the research objectives corresponding methodologies have been identified in Table – 1.1.

Table 1.1 Summary of Objectives and Corresponding Methodology

Investigate high cycle fatigue behaviour of masonry	• Undertake a literature review • Review past research works
Fundamentals of fatigue	• Literature review of classical fatigue relationship
Derive strain-life behaviour of masonry arch	• Perform laboratory tests on masonry arches subjected to cyclic loading • Validate with previous similar tests
Derive strains from measuring deformations	• Propose relationship between parametric strain and arch geometry
Numerical modelling	• Review methods of modelling masonry through literature review • Identify suitable software for this research • Simulate previous tests carried out on masonry walls and arches • Model the laboratory tested arch
Fatigue material modelling of masonry	• Using laboratory test results derive a parametric strain-life curve. • Use the curve to derive damaged properties for modelling
Further research	• Summarise limitations of the present research noted during the progress of the work

1.8 Layout of the Thesis

Chapter 1 provides a brief introduction to masonry arch bridges and the background information to the research project. It also presents the aims and objectives and provides a discussion about the proposed approach for the study.

Chapter 2 reviews published literature and are divided into six sections: an overview of the history and construction of masonry arch bridges; masonry arch mechanics using classical theory; comprehensive study of masonry in fatigue, the latest trend in masonry modelling using discrete element behaviour or bricks and mortar; this concludes the reason for author choice of ANSYS Workbench for numerical modelling. Review of the modelling techniques for masonry structures using contact elements are covered. Then confirming reasons for the preferred material modelling with linear elastic elements connected with non-linear interfaces.

The experimental works on brick-and-mortar units as well as the masonry arch specimens are presented in *Chapter 3*. It aims to provide essential information about material properties that can be used for the numerical modelling work described in later chapters. The core of this research work, deriving the parametric strain deflection relationship using arch geometry. Then proving the strain-life analogy for the arch.

In *Chapter 4*, the results of 3D finite element analysis (FEA) of the tested masonry arch have been validated. A non-linear modelling behaviour is demonstrated through load-deflection comparison.

Then in Chapter 5 the numerical models are extended to determine damaged material properties varying with the life of an arch after completion of load cycles. Proves expected post damage reduced life of an arch.

Finally, *Chapter 6* presents the main conclusions and achievements of the work, and it also provides a discussion about the recommendations for further research in this field.

1.9 Summary

Long-term fatigue damage to masonry under cyclic loading considered to be fundamental parameters to ascertain historical arch bridge safe load capacities and residual life span. Today's railway traffic has significantly increased in volume due to capacity demand, measured by equivalent million gross tonne per annum (EMGTPA). Railway traffic got further complicated due to the increase in line speed to reduce journey time. Arch bridges once constructed for much slower quasi-static nature of locomotives are now required to support the demands of higher speed and corresponding dynamic resilience understandably non-existent in the discrete structure of masonry.

This research will focus on ascertaining the fatigue effects due to high cycle fatigue nature of service (i.e. traffic) load on the arch barrel. Provide means of measuring strains from arch deformations under service loads. Propose damaged material modelling to take care of fatigue effects and predict the residual life of existing arches.

This work will comprise both physical tests to determine ε-N behaviour of masonry arches and numerical methods of modelling of masonry for fatigue.

Chapter 2
Literature Review

Glossary

ε_e	Elastic strain
ε_p	Plastic strain
ε_f'	Fatigue ductility coefficient
ε_{min}	Minimum longitudinal strain
ε_{max}	Maximum longitudinal strain
ε_N	Normal strain
γ_T	Tangential strain
$\mu\varepsilon$	Microstrain, i.e., 10^{-6}
μ	Dilatancy parameter
σ	Stress
σ'_f	Fatigue strength coefficient.
σ_a, S	Stress amplitude
τ_u, τ_d	Shear stress
τ^0_N	Normal stress
τ^0_T	Shear stress
a	Crack size
A	S_a/S_m
b	Fatigue strength exponent
c	Fatigue ductility exponent
c	Cohesion
C	Fraction of life consumed
Cr	creep corelation factor
E	Young's modulus
E_b	Young's modulus of brick
E_m	Young's modulus of mortar
E_o	Initial Young's Modulus
f_t	Tensile strength
f_b	Compressive strength of brick
f_m	Compressive strength of mortar

G	Shear Modulus
G_b	Shear modulus of brick
G_m	Shear modulus of mortar
G_{cN}	Mode I fracture energy
G_{cT}	Mode II fracture energy
I	Moment of Inertia
$\Delta K, \Delta K_{th}, \Delta K_{Ic}$	Elastic stress intensity
K	Stiffness vector
K_N	Normal stiffness
K_T	Shear/Tangential stiffness
L	Span
n_i	Number of cycles accumulated
N, N, N_c	Load cycle
N_u	Maximum Load Cycle
N_f	Number of cycles to failure
P_b	Survival probability
R	Smin/Smax
s, s_c, s_p, s_e	Relative Displacement
s_T	Tangential displacement
s_N	Normal displacement
S_a	Alternating stress
S_{min}	Minimum induced stress
S_{max}	Maximum induced stress
S_u	Compressive strength
ΔS	Stress range
t_m	Mortar thickness
t_u	Brick unit thickness
v	Poisson's ratio

2.1 History

The history of arches is long and spans from early Sumerian work in dried mud bricks to today's slender reinforced concrete arches (*ICE, 2008*). Material and practices have changed but the arch is still a good way of reaching over long spans in just one or few leaps. The shape of the arch gives mainly compressive stresses which are needed for masonry and stone constructions where tensile forces can't be handled (*Samuelsson and Wiberg, 1995*).

Although originating from Persians and Sumerians, the historical masterpieces of arch construction were erected by the Romans. The crown of them all is the 270 m long aqueduct of Pont du Gard in the south of France.

Figure - 2.1 The Aqueduct Pont du Gard. (*Nationalencyklopedin, 2010*)

The purpose of this construction was to span the river Gard with an aqueduct for a 50 km long water conduit providing water to the city Nîmes. It was constructed 63 -13 B.C. (*Nationalencyklopedin, 2010*). River Gard flows 49 meters below the aqueduct and the rise is done in three tiers, Figure - 2.1, with the top one containing the water channel. Roman arches were mostly constructed in a semi-circular shape with a span to rise relation of about 3:4. The shape of the arches has the advantage that all the voussoirs have the same shape and in Pont du Gard the arches have been constructed without using any mortar. However, the top tier contains mortar for water sealing (*Jennings, 2004*).

The next step in the development of stone arches is the segmental arch bridge. A semi-circular arch has the rise to span relation of 1:2 as shown in Figure - 2.2(a), while a

segmental can have a lower relation like 1:5, as shown in Figure - 2.2(b). Benefits of this design are larger spans which gives fewer supports and a lower roadway level for a given clearance under the bridge (*Jennings, 2004*).
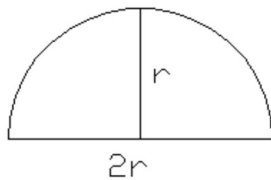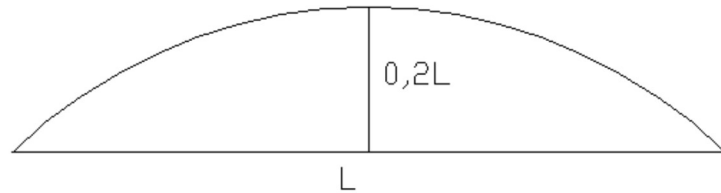
A) Semi-circular arch   c) Segmental arch

Figure - 2.2 Semi-Circular and Segmental Arch Shape.

In China, the world's first segmental arch bridge was erected in the seventh century, called the Anji Bridge, Figure - 2.3. The rise is 7 m and the span 37 m, giving a span to rise relationship of 1:5.3 approximately.

Figure - 2.3 Anji Bridge. (*Wikipedia, 2010*)

Although true arches were already known at their time the Romans were the first to realise the potential of arches for bridge construction. The development of transport infrastructure for movement of armies, trade and communications, as well as water supply to built-up areas, was vital to the spread and successful administration of the

empire. UK infrastructure maintains an impressive portfolio of masonry arch bridges and long-span viaduct.

Figure - 2.4 Royal Border Bridge, Berwick Upon Tweed. (*Network Rail Archive*)

The Royal Border Bridge, Figure – 2.4, was the last link in completing a continuous railway line running between London and Edinburgh. Designed by Robert Stephenson, the bridge was a more traditional masonry structure than its contemporaries the High Level and Britannia bridges, but it is one that has stood the test of time. Not restricted by issues of navigation, the bridge Stephenson designed was a conventional masonry structure which consisted of 28 semi-circular arches each of 61½ ft (19 m) span, arranged in a gentle curve. 13 arches spanned the river with 15 over lands to the south of the river at Tweedmouth. The bridge has a central abutment pier which enabled all 15 land arches to be completed before work started on the arches over the river. Piles for the pier foundations in the riverbed had to penetrate almost 40 ft (12 m) of dense gravel before reaching bedrock. The bridge was constructed using 8 million cubic feet (227,000 cu.m) of stone, except the inner part of the arches which required 2½ million bricks set in cement and faced with stone. The structure has a total length of 2,160 ft (656 m), a maximum height of 126 ft (38 m) above the river, while the rails are carried at a height of 120 ft (37 m). At the height of construction, the workforce numbered 2,700 men.

Although the permanent bridge had originally been scheduled for completion in July 1849, it was not ready for traffic until March 1850. The bridge was opened by Queen Victoria and Prince Albert on 29 August 1850, when she also granted her permission for it to be named the Royal Border Bridge. In 1989 electrification gantries, specially designed to reduce the visual impact on the bridge and approved by the Royal Fine Art Commission, were installed on the bridge as part of the electrification of the line between London and Edinburgh. After standing for 143 years as a major part of the East Coast Mainline, the Royal Border Bridge underwent significant maintenance for the first time in 1993 in a project in partnership with English Heritage to repair the 15 land-based arches. In 2010 to celebrate its 160th anniversary, the bridge was illuminated.

2.2 Masonry Arch Construction and Concepts

For a stone or masonry arch bridge, the foundation is critical. Large thrusts from the arch need to be transferred to non-yielding substructure keeping the arch in position. Preferably the arch foundation should, therefore, be made on solid rock, but this may not always be possible. Many techniques have been used, e.g. timber piling, faggots, Figure - 2.5. Lots of bridges have failed during the years so the stone and masonry arches we can see today are the top of the line concerning foundation (*ICE, 2008*).
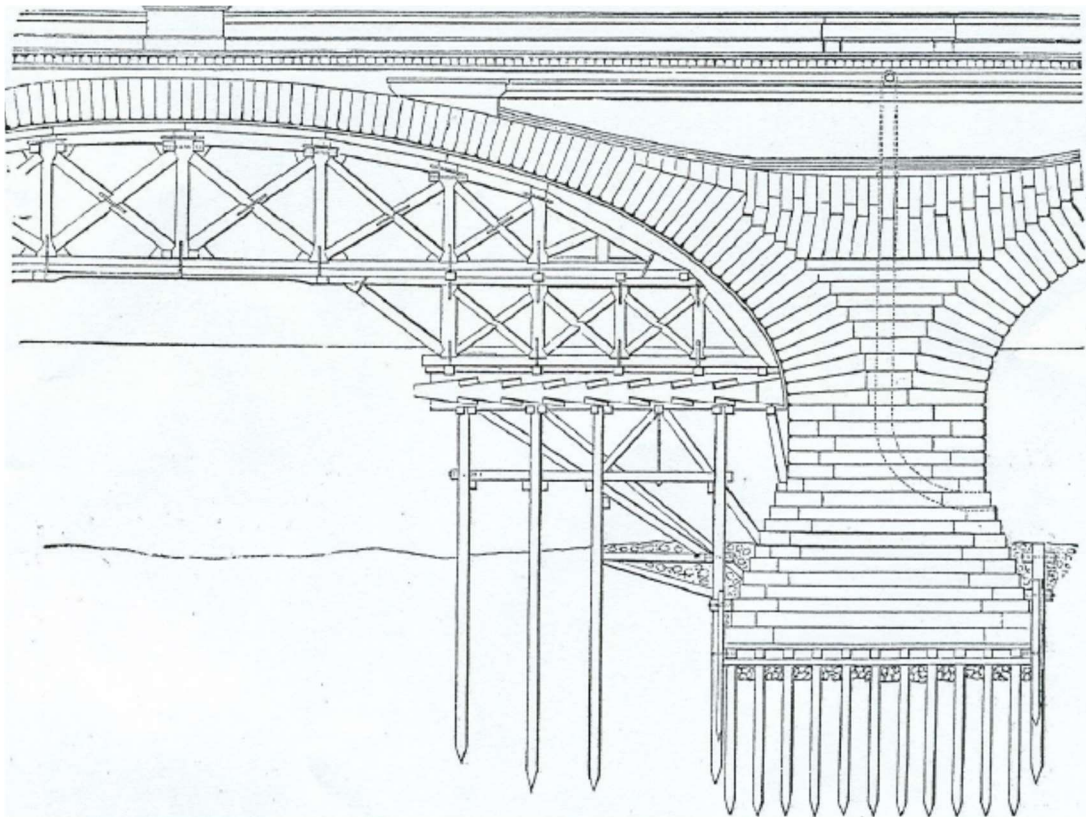
Figure - 2.5 Centre for London Bridge. (*ICE, 2008*)

The arch is erected on the foundation, called skewback or abutment. For this purpose, a falsework, or centring, made of timber is constructed that can support the arch during construction. The arch is built upon the centring.

Once the last stone, aka keystone, is inserted into the arch the falsework can be removed. During the removal. the fill must be put on the arch for stability and this need to be done in a symmetrical order for the structure to remain in equilibrium (*Heyman, 1982*).

Stones in the arch is cut into a trapezoidal shape, voussoir, and joined with mortar, type of stone and mortar varied vastly. For smaller spans the fit of the stones may not be so cautiously made, instead the stones are joined with a thicker mortar joint. The

arch can also be made from bricks joined with mortar, a construction type that is common in the UK.

2.3 Masonry Arch Mechanics

The purpose of this research work is to accurately model the masonry properties for fatigue and analyse the arch for load-carrying capacity. The mechanics of arches are presented for the basic understanding of the problem at large.

2.3.1 Funicular Polygon

"As hangs the flexible line, so but inverted will stand the rigid arch".

This is a quote by the famous scientist Robert Hooke in 1675 (*Heyman 1982*). It describes the mechanics of arches in a brief, but the sharp way. That this is true and can be shown using a simple example (*Heyman 1982*).

A weightless string is subjected to three forces, P_1, P_2, P_3 and as shown in Figure - 2.6.
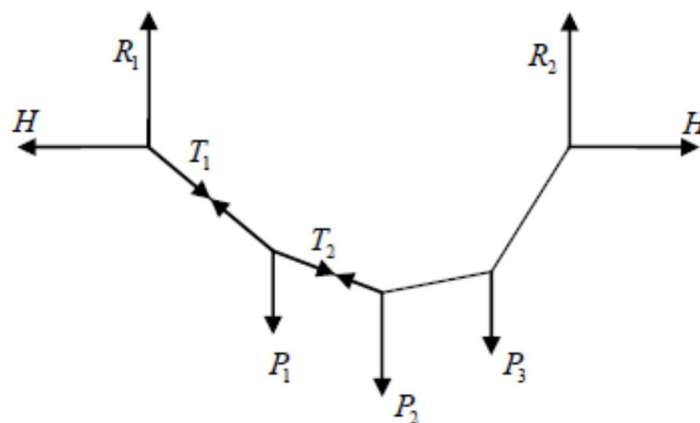
Figure - 2.6 A Weightless String Subjected to Three Forces (*Heyman 1982*).

The inclination of the two first sections of the string is found with the triangles of forces in Figure - 2.7. These also give the tension in the string. The horizontal reaction H is assumed to be known.
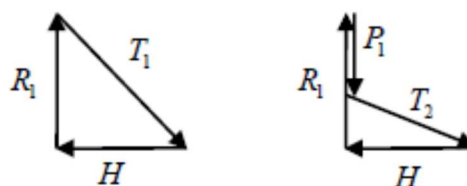
Figure - 2.7 Triangle of Forces for The String (*Heyman 1982*).

The triangles can be combined into a complete force polygon, Figure - 2.8. The reaction forces R_1 and R_2 balance the applied forces P_1, P_2 and P_3. The lines that originate from the top of the P_1 force are the inclinations for the four parts of the string.
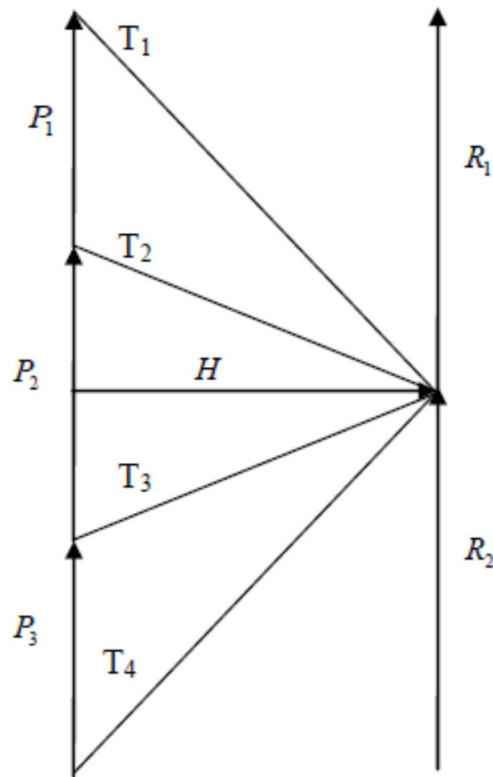
Figure - 2.8 The Complete Force Polygon (*Heyman 1982*).

To end the string – arch analogy Figure - 2.6 can be inverted into Figure - 2.9 where the funicular polygon now represents the line of thrust for an arch with the applied forces P_1 P_2 and P_3 (*Heyman, 1982*).
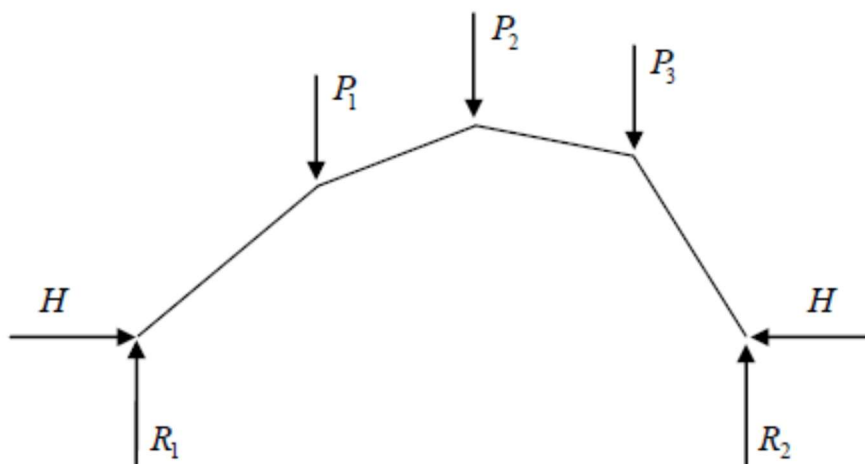
Figure - 2.9 The Inverted Funicular Polygon, i.e. The Line of Thrust for The Arch (*Heyman, 1982*).

2.3.2 Line of Thrust

If a new arch is going to be constructed, the designer would have the opportunity to calculate the best geometry for the given loading. The preferred way is to see to that no moments will occur for the so-called shape load that the arch is designed for. This means that the line of thrust will coincide with the centreline of gravity for the arch (*Cross-Rudkin et al. 2008*).
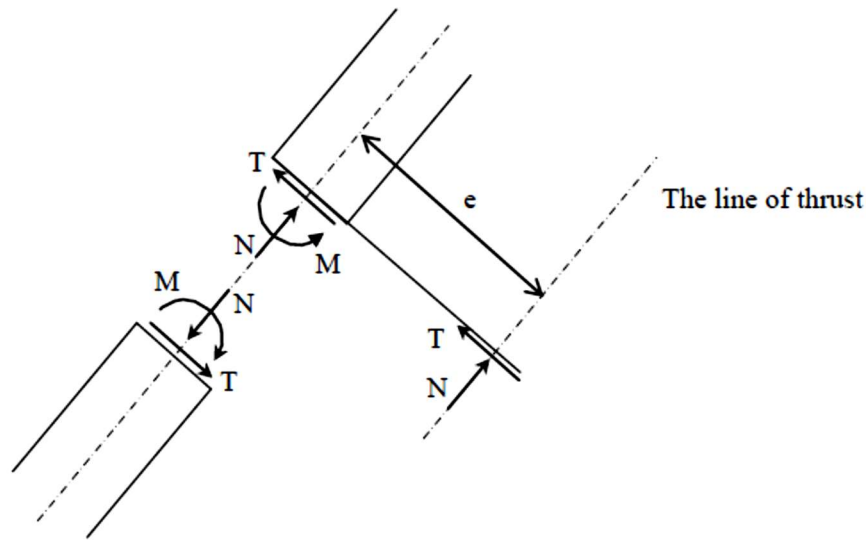
Figure - 2.10 A Cut through The Arch with Cross-sectional Forces.

Other loads than the shape load will induce a moment and a transverse force into the arch. This will be the case for masonry arches where there would have been little knowledge about today's loading situation in the design and construction phase. A cut is made to the arch and a system of forces as seen in Figure - 2.10 is introduced. Then there is a point at a distance e from the line of gravity to where all the cross-sectional forces can be moved so that the moment is zero. If the arch is cut through at several points and the distance e is calculated for each of them, the line of thrust can be drawn through these points.

Position of the line of thrust has been subject to various design and assessment criteria over the years. The earliest one is "the middle third rule".

2.3.3 Middle Third Rule

The middle third rule expresses a limit for the line of thrust to lie within the middle third of the arch thickness. It is based upon elastic theory and the assumption that no tensile stresses can be transmitted through the mortar material. This can be motivated using an example from Heyman.
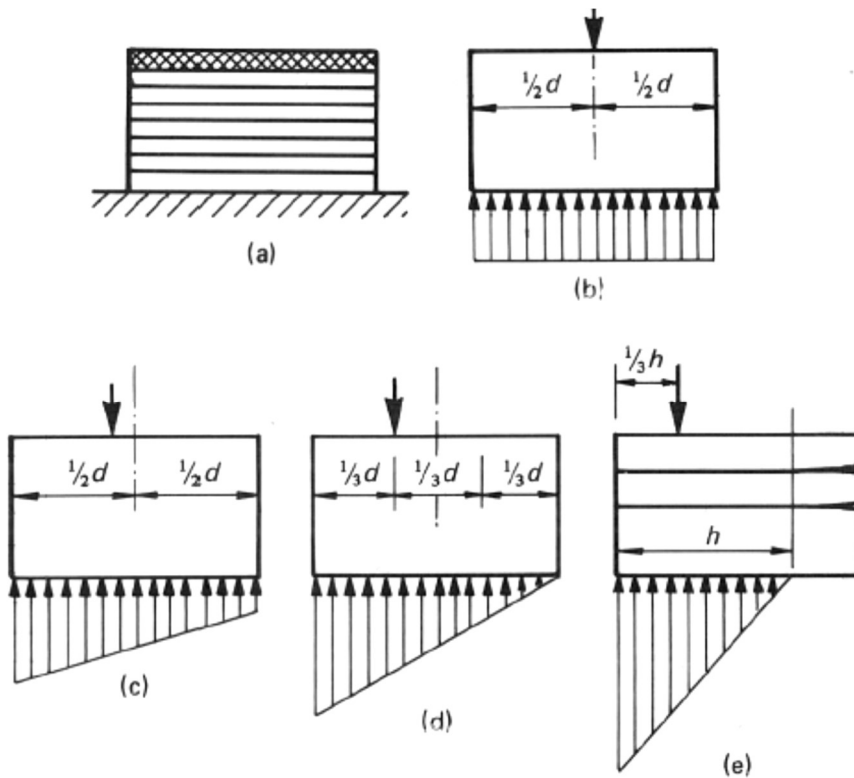
Figure - 2.11 A Pile of Stone Subjected to a Compressive Force. (*Heyman, 1982*)

Consider a pile of stones that are stacked upon a rigid foundation Figure - 2.11. If the compressive force referred to as the line of thrust for an arch, lies in the middle of the pile the stress distribution will be equal over the entire cross-section Figure - 2.11(b). For an off-centre compressive force, the stress distribution shifts to a triangular shape, Figure - 2.11(c), and when the compressive force reaches the edge of the middle third of the pile, stresses reach zero at the edge of the pile Figure - 2.11(d). Elastic theory gives that when the compressive force has gone passed the middle third the stress distribution should induce tensile force at the right part of the pile, Figure - 2.11(e), but the mortar materials inability to resist tensile force results instead cracking of the arch.

Thus, if the applied load stays within a certain 'core' of the section, stresses across the whole section will be compressive. For a rectangular section, the core has a depth of one-third of the total depth. For masonry arch barrel it is the middle third that is relevant and the 'middle third rule' has been supposed by some nineteenth (and twentieth) century engineers to be a prime requirement of design. In Figure - 2.12, an assurance of satisfactory design would be obtained if the line of thrust lies within the central thinner imaginary ring having a depth one-third of the actual arch barrel thickness.
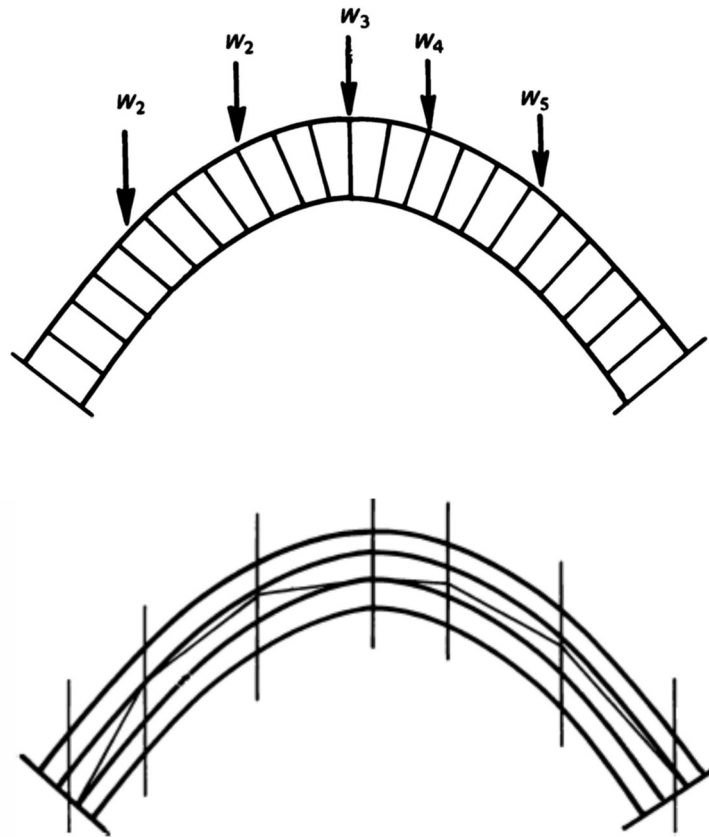
Figure - 2.12 Line of Thrust Within Arch Middle-third. (*Heyman, 1982*)

The middle third rule is very conservative and hard to reach. It requires a good design and heavy dead loads that can offset the live loads.

2.3.4 Mechanism of Collapse

It is reasonable to assume that masonry has no tensile stress. This assumption implies that no tensile forces will occur in arches. Masonry compressive stresses are considered large enough and there is no danger of crushing of material under the possible load effects.

Masonry arch (*Heyman, 1982*) is, therefore, assembly of bricks or stones arranged in a coherent structural form. The form is maintained by the compressive forces transmitted within the mass of the material. These permanent forces are generated by the self-weight of the arch and the backfill. Live loading is carried the compressive forces, considered high enough for friction to provide interlocking against slip.

The idea that tension is not permissible is significant. The thrust transmitted between the masonry is considered critical if it reaches the surface, m, permitting the "hinge" to form.

Figure - 2.13 Hinge Formation at Masonry Interface. (*Heyman, 1982*).

A three-hinge arch is satisfactory structural form, it is statically determinate and the funicular polygon for a given loading is unique. It is a fourth hinge, Figure – 2.13, that converts a statically determinate arch into a mechanism.

Therefore, the theorem of plasticity applicable to masonry is:

"If a thrust line can be found, for the complete, which is in equilibrium with external loading (including self-weight) and which lies everywhere within the masonry arch ring, then the arch is safe." (Heyman, 1982)

2.3.5 Closed form Solution

Two hinged arches are the most practical considering this is the likely condition of an arch given that most foundations accommodate little rotation (*ICE, 2008*). In the case of two-hinged arch, we have four unknown reactions, but there are only three equations of equilibrium available. Hence, the degree of statical indeterminacy is one for two hinged arches. The fourth equation is written considering deformation of the arch. The unknown redundant horizontal reaction is calculated by noting that the horizontal displacement of hinge is zero. In general. the horizontal reaction in the two hinged arch is evaluated by straightforward application of the theorem of least work, which states that the partial derivative of the strain energy of a statically indeterminate structure with respect to statically indeterminate action should be zero, i.e,$\partial U/\partial H = 0$. Hence to obtain, horizontal reaction, one must develop an expression for strain energy.

Strain energy approach closed form solution for the problem have shown that the critical deflection on arch, like 2 span beams, is proportional to EI/L^3. This relationship is considered like stiffness for arches defining load-deflection relationship.

2.4 Displacement Measurement for Arch bridges

Dynamic rail loading is one of the main contributors to deterioration (*CIRIA C565*). Demand in freight traffic led to increase in the weight and length of rolling stock. Further the speed of modern trains resulted in more onerous loading, which have caused

damage in masonry bridge structures or foundations. Cyclic loading of damaged areas causes further deterioration, accelerating the degradation of materials due to ageing and water ingress (*UIC 2004*). In UK a yearly visual assessment is carried out to keep track of degradation of bridges. A more detailed assessment is carried out every 6 years, to manually measure the size and extent of existing cracks on the structure and determine water damage and ring separation through hammer tapping. Monitoring of the structure is sometimes specified when the bridge experiences (or is expected to experience) accelerated deterioration. To investigate the bridge response, periodic displacement measurements are taken using displacement gauges (with devices such as linear variable displacement transformers, LVDT) mounted on poles and fixed on the ground. Typically, vertical crown displacement is measured with a high sampling rate and a measurement accuracy of 0.01 mm. A comprehensive two-year monitoring, with combined sensing and surveying of 19th Century Marsh Lane masonry railway viaduct at Leeds, funded by EPSRC and Innovate UK. Outcome published in their paper (*Acikgoz et al. 2018*) discusses sensing techniques and associated analysis procedures used to (a) identify the reasons for existing damage, (b) quantify their impact on the dynamic response of the structure and (c) measure degradation of the response over a period of one year.

2.4.1 Contact System - Measurement

Most relevant measures of the structural response are the dynamic displacement of the structure due to the passage of trains. The displacement measurement systems can be classified as contact and non-contact measurement systems. Contact systems involve high precision displacement transducers, such as LVDT and cables type. The main disadvantage of these systems is their dependence on a reference because they are based on the relative displacement measurement between a point of the structure and a close point that can be considered fixed. This fixed point can, in many instances, be difficult, or even impossible, to materialize as, for example, when the structure is located over a watercourse, a road or in a rugged terrain, etc.

2.4.2 Non-Contact System - Measurement

The non-contact measurement systems rely on laser technology, radar technology, GPS technology and on the processing and analysis of images obtained by video technology or digital photography (*Ribeiro et al. 2014*).

Marsh Lane viaduct, Figure - 2.14, strain and displacement monitoring was carried out using, i) Quasi-distributed sensing technique with Fibre Bragg Gratings (FBG) and ii) digital image correlation (DIC), identify the pattern pixels of each image through a correlation analysis at subpixel level. With the aid of highspeed video cameras and

high-efficiency digital image processing algorithms, the displacements of multiple measurement points can be tracked and displayed in real-time (*Pan et al. 2016*).

a) Marsh Lane Viaduct   b) Class 185 Desiro Carriage

Figure - 2.14 Marsh Lane Viaduct & Class 185-3 carriage. (*Network Rail*)

Analyses of the response to eastbound Class 185 trains [5] have revealed that changes in atmospheric temperature cause variations up to 100% in dynamic strain measurements. For every Celsius degree increase, the mean value of the peak-to-peak amplitude of the signals decreases by ~ 0.8 µε for sensors in the longitudinal direction. In the transverse direction, the effects are less significant; for every 1 °C increase the mean value of the strain variation drops by ~ 0.3 µε. This is considered a significant limitation for using FBG or in fact any strain measuring devices. Even though FBG offers better resolution compared to DIC.

Marsh Lane viaduct DIC monitoring have recorded displacement between +/- 1 mm and strain of 200 µε (0.2×10^{-3}) during regular monitoring under Class 185-3 train (*Acikgoz et al. 2018*).

Therefore, with recently improvements in technologies and analytical tools it is possible to measure masonry bridge displacements. Even though masonry bridges deflect very little in comparison to beam and slab type bridges, measuring deflection offer valuable insight to response and condition of masonry arches.

2.5 Fundamentals of Fatigue

Fatigue has been defined as the progressive, localised, and permanent structural damage that occurs when a material is subjected to cyclic or fluctuating strains at stress levels that are well below the static yield strength of the material (*Carrara et al. 2020*). A component exhibits the formation of microdefects at micro-heterogeneities, such as material imperfections, when subjected to fatigue loading. Depending on the type of material. energetic barriers prevent the evolution of microdefects when the load

level is below a fatigue threshold (*Schijve, 2003*). The fatigue life of a component has been expressed as the number of loading cycles required to initiate a fatigue crack which propagates to a critical size resulting in failure. When the fatigue process advances, the microdefects evolve into micro-cracks. These early processes are random in nature and governed by the stochastic micro-structural arrangement of the material. The micro-cracks propagate and eventually coalesce and lead to the formation of a fatigue macro-crack, whose size is sufficient to neglect the random nature of the material microstructure. This macro-crack then propagates initially in a stable manner then in an unstable manner leading to failure (*Carrara et al. 2020, Paris, 1961*). Schijve (*2003*) has collated the history of works on fatigue from crack growth to failure.

Many engineering failures are caused by fatigue. There is a little warning or no warming at all before fatigue failure, therefore the consequences are often catastrophic. The discovery of fatigue occurred in the 1800s when several investigators in Europe observed that bridge and railroad components were cracking when subjected to repeated loading.

2.5.1 Fatigue Crack Development

Bleck et al (*2009*) defined Figure - 2.15 four fatigue modes based on the fatigue life number of cyclic repetitions of loading represented in log scale (log N) and stress levels (log σ).
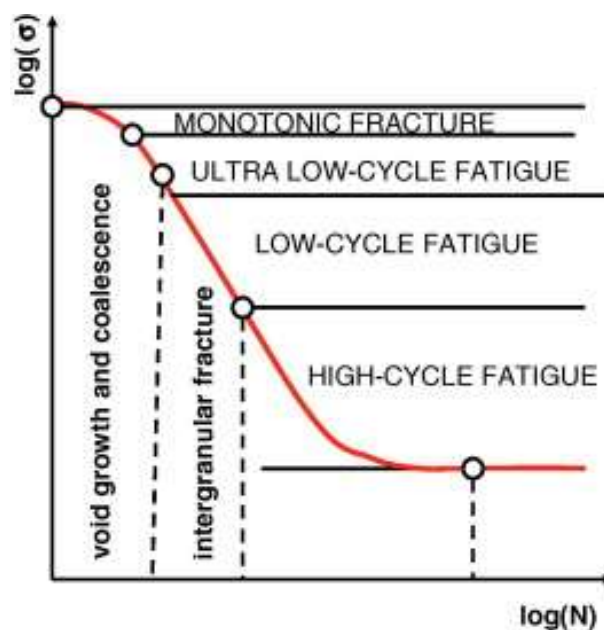
Figure - 2.15 Definition of Failure Mechanism in Dependence of Number of Cycles.
(*Bleck et al 2009*)

These are MF, Monotonic Fracture associated with uniaxial loading; ELCF, Extremely Low-Cycle Fatigue where the fatigue life is very low, typically less than 100 cycles; LCF, Low-Cycle Fatigue at less than 10,000 cycles where behaviour tends to be strain controlled and related to large strain amplitudes or high stress levels that produce both plastic and elastic components at each cycle and HCF, High-Cycle Fatigue at above 10,000 cycles where the mode of failure is associated more with low stress levels occurring in the elastic range. These were also referenced by Kim and Hwang (*2020*) in their research, Figure - 2.16, into the fatigue behaviour of low carbon steel.
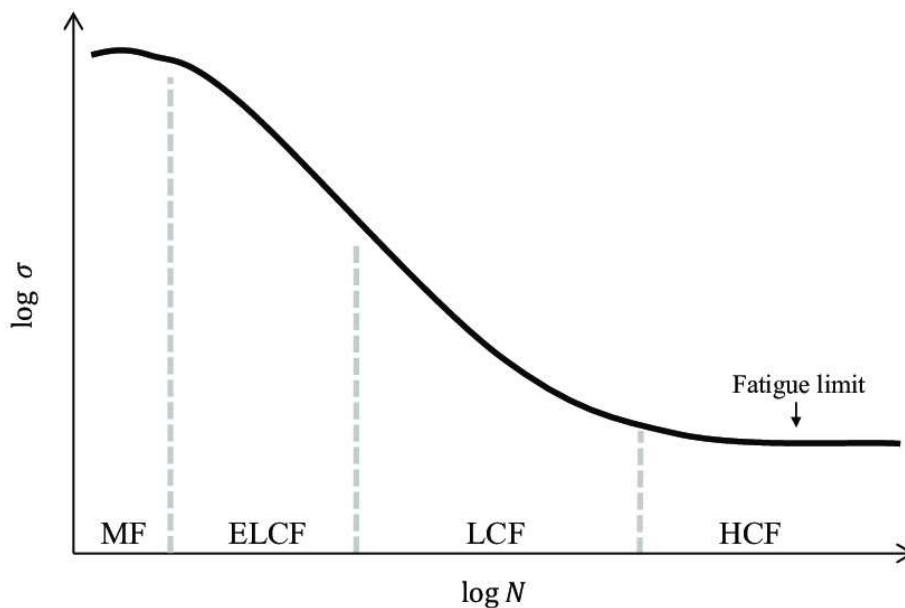
Figure - 2.16 Schematic of Classified Fatigue Modes (*Kim Y, Hwang, W., 2019*)

Fatigue life is the number of loading (stress or strain) cycles of a specified character that a specimen sustains before the failure of a specified nature occurs. For some materials, notably steel and titanium, there is a theoretical value for stress amplitude below which the material will not fail for any number of cycles, called a fatigue limit, endurance limit, or fatigue strength.

Although the mechanisms of cyclic fatigue in brittle materials are conceptually different from the well-known mechanisms of metal fatigue, some common aspects of behaviour have been found in the cyclic fatigue behaviour of both ductile and brittle materials (*Ritchie, 2002*).

According to Davidson and Hudak (*2003*), fatigue failure occurs in three stages under sustained cyclic loading, namely crack initiation (stage 1); slow, stable crack growth

(stage 2) followed by rapid fracture (stage 3). The development of fatigue cracking is illustrated in Figure - 2.17 (*Bannantine et al. 1990*).
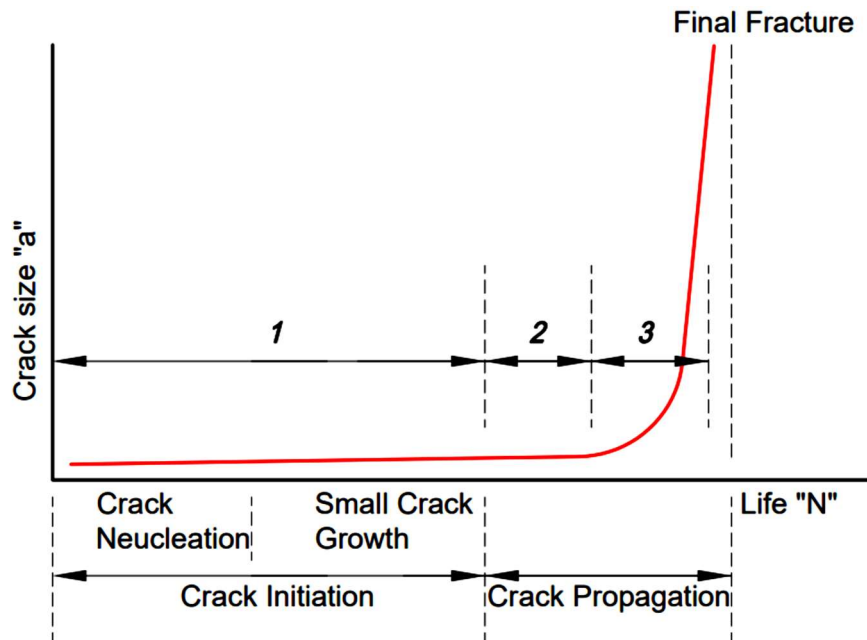
Figure - 2.17 Stages of Fatigue Cracking (*Bannantine, 1990*)

This is based on three regions of crack growth identified by Paris (*1961*). Fatigue crack initiation (stage 1), sometimes called crack nucleation, begins at micro-defect sites where localised high alternating stresses occur under external cyclic loading. Miller (*1987*) suggests that initiation sets the limit on the minimum size of a small fatigue crack, if the component does not have any existing cracks. It is a complex process that can lead to the formation of an extremely small crack (smaller than 2 µm in size) the one that initiates and grows in a stable manner, to a length of the order of 100 µm based on the works on metal fatigue.

Continued slow, stable crack growth occurs under sustained cyclic loading (stage 2). By this stage the cracks tend to align more perpendicular to the axis of the principal tensile stress. Stage 3 is strain controlled and related to large strain amplitudes or high stress levels that produce both plastic and elastic components at each cycle (*Tateishi, K., Hanji, T., 2004*) where fatigue lives are greater than >10,000 cycles. Here the initial damage created under tensile stress conditions is followed by ductility exhaustion during cyclic loading until the crack propagates to a rapid fracture. The fatigue life of a component, from the initiation of cracking through to failure is then defined as the crack initiation period plus the crack propagation period as indicated in Figure – 2.17 (*Bannantine et al. 1990*).

A study in 1992 conducted by the Scientific Advisory Board of the US Air Force targeted high cycle fatigue as the single biggest cause of turbine engine failures in military aircraft. High cycle fatigue results in rapid, essentially unpredictable failures

due to fatigue-crack propagation under ultrahigh-frequency loading. Furthermore, cracking often initiates from small defects which are associated with damage caused by a variety of drivers, including fretting and impacts by foreign objects.

The fatigue life of a component can be expressed as the number of loading cycles required to initiate a fatigue crack and to propagate the crack to a critical size. Therefore, it can be said that fatigue failure occurs in three stages – crack initiation; slow, stable crack growth; and rapid fracture.

In fracture mechanics, Anderson, Gomez, and Paris derived relationships for stage II crack growth. One way to model fatigue is with help of fracture mechanics, which is the study of crack growth shown in Figure – 2.18. The most well-known crack propagation law was suggested by Paris *et al.* (*1961, 1963*):
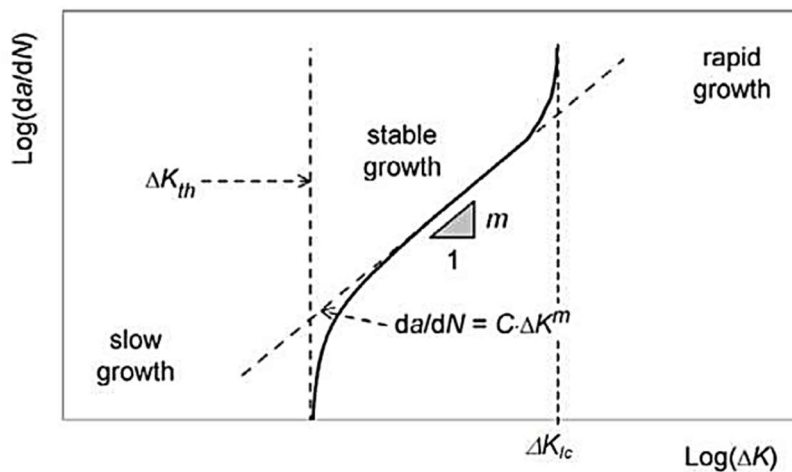
Figure - 2.18 Paris Law for Fatigue. (*Paris et al., 1961*)

$$\mathrm{d}a/\mathrm{d}N = C \cdot \Delta K^m$$

where:

- $\mathrm{d}a/\mathrm{d}N$ *is* the propagation rate of the crack length *a* [mm].
- ΔK is an elastic stress intensity factor range [N/mm$^2 \cdot \sqrt{m}$] at the crack tip; and *C* and *m* are constants.

The crack growth is slow for $\Delta K < \Delta K_{th}$ = threshold stress intensity factor range and accelerates to failure for $\Delta K > \Delta K_{lc}$ = critical stress intensity factor range for mode I.

If the diagram is rotated counter-clockwise 90° it will have a similar form as an SN-curve, refer Figure - 2.16.

2.5.2 Metal Fatigue

The early studies of fatigue are mostly empirical and based on data fitting of extensive experimental work carried out largely on carbon steels used in railways, bridges and pumps (*Suresh, 1998*). Wöhler (*1870*) studied fatigue using experimental curves relating the maximum number of cycles that a component can undergo before failure, N_u, to the (constant) applied stress amplitude σ_a (or S). These curves, named Wöhler or stress-life (S–N) curves, are still used today.

2.5.2.1 Wohler's Curve

Wöhler had already carried out experiments to obtain S-N curves on railway axles in the 19th century (*Shutz, 1996*). His approach catches some characteristic features of fatigue behaviour such as the leading role of the load amplitude, S and the presence of an upper stress amplitude related to the monotonic strength of the material and the (possible) presence of a fatigue threshold or fatigue limit, called endurance limit. For a long-time such curves were labelled as a Wöhler curve instead of the now more frequently used term S-N curve, see Figure - 2.19. It plots applied stress amplitude (S) against component life or number of cycles to failure (N). As the stress decreases from some high value, component life increases slowly at first and then quite rapidly. Fatigue is therefore very similar to brittle fractures and is characterised by the representation of its variable nature.
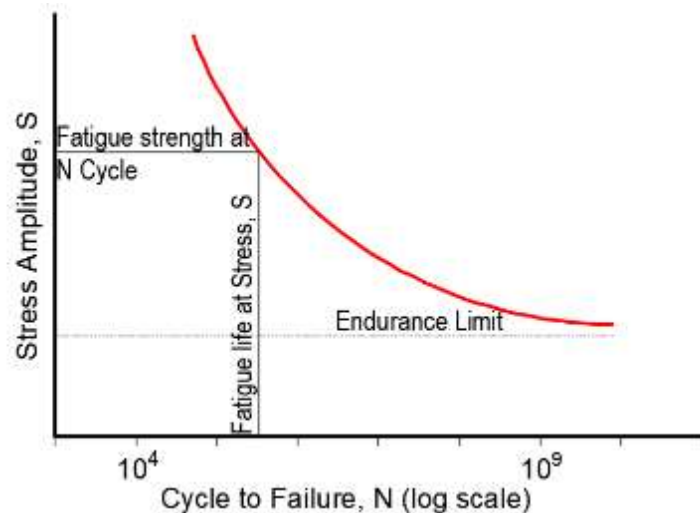
Figure - 2.19 Typical Stress Amplitude (S) vs Load Cycles to Failure (N) Curve.
(*Carraraa et al. 2020*)

Stress life concept by Wöhler has been popular and accepted for practical purposes. This is more so for metals where the relationship between stress and strains are linear at low stress levels. For materials like masonry in tension the interface between the units and mortar separates even at a very low stress level. The linear relationship no longer exists, leading to unpredictable stress-strain behaviour. Aim of this thesis and

the corresponding research is to improve the predictability of the fatigue life by strain-life method. Where strains are derived directly by measuring deflections of masonry arch under cyclic loading.

In high cycle fatigue situations, materials performance is commonly characterised by an *SN curve*, or stress-cycle curve, or fatigue curve, also known as a *Wöhler curve*. This is a graph of the magnitude of cyclic stress (*S*) against the logarithmic scale of cycles to failure (*N*).

The *SN* curve in the high-cycle region is sometimes described by the Basquin equation:

$$\sigma_a = \frac{\Delta\varepsilon_e}{2} E = \sigma_f'(2N)^b \qquad \text{(eq 2.1)}$$

where:

- σ_a is the elastic stress amplitude
- $\Delta\varepsilon_e /2$ is the amplitude of elastic strain
- E is Young's Modulus
- σ_f' is fatigue strength coefficient
- N is the number of strain cycles to failure
- b is the fatigue strength exponent, $-0.12 < b < -0.05$

SN curves are derived from tests on samples of the material to be characterised (often called coupons) where regular sinusoidal stress is applied by a testing machine which also counts the number of cycles to failure. This process is sometimes known as 'coupon testing'. Each coupon test generates a point on the plot though in some cases there is a runout where the time to failure exceeds that available for the test. Analysis of fatigue data requires techniques from statistics, especially survival analysis and linear regression.

The progression of the *SN curve* can be influenced by many factors such as corrosion, temperature, residual stresses, and the presence of notches. The Goodman-Line is a method used to estimate the influence of the mean stress on fatigue strength.

Low cycle fatigue (LCF) usually refers to situations where the stress is high enough for plastic deformation to occur, the accounting of the loading in terms of stress is less useful and the stain in the material offers a simpler and more accurate description. This type of fatigue is normally experienced by components which undergo elastic-plastic or plastic deformation. The reason why strain life is more suitable for low cycle fatigue is that the strains allow the elastic and plastic components to be distinguished from

each other, whereas the stress is way less sensitive to the plastic component in the case of high amplitude.

Low-cycle fatigue is usually characterized by the *Coffin-Manson relation* (published independently by L. F. Coffin in 1954 and S. S. Manson in 1953):

$$\frac{\Delta\epsilon_p}{2} = \epsilon_f'(2N)^c \qquad \text{(eq 2.2)}$$

where:

- $\Delta\varepsilon_p$ /2 is the plastic strain amplitude.

- $\varepsilon_f{}'$ is an empirical constant known as the *fatigue ductility coefficient*, the failure strain for a single reversal.

- $2N$ is the number of reversals to failure (*N* cycles).

- *c* is an empirical constant known as the *fatigue ductility exponent*, commonly ranging from -0.5 to -0.7 for metals in time-independent fatigue. Slopes can be considerably steeper in the presence of creep or environmental interactions.

2.5.2.2 Miner's Rule

Fatigue damage increases with applied cycles in a cumulative manner which may lead to fracture. The crack growth concepts developed in the 1950s and 1960s have enjoyed wide acceptance since cracks propagate to permanent damage. Modem technologies have provided sophisticated tools and techniques, like strain gauges, laser LVDT, Digital Image Correlation (DIC), which enable measurement of exceedingly small cracks in the order of 1 μm. Several macro fatigue crack growth models were developed in the early 1970s (*Paris, 1963, Elber, 1970*) to account for load interaction effects in the crack propagation phase (Figure - 2.16) of the cumulative fatigue damage process. More than 50 fatigue damage models have been proposed since the Palmgren damage accumulation concept and the Miner linear damage rule, LDR were introduced, reviewed and listed by Fatemi (*Fatemi, A., Yang, L.,1998*). Due to the complexity of the problem, none of these predictive models are reliable. The applicability of each model varies from case to case. Consequently, the Palmgren-Miner linear damage rule is still dominantly used in design (*Fatemi, A., Yang, L.,1998*).

As early as 1924, Pålmgren (*1924*) published the hypothesis which is now generally known as the Miner-rule or the linear cumulative damage hypothesis. According to Pålmgren applying *ni* times a cycle with a stress amplitude $S_{a,i}$ and a corresponding fatigue life N_i is equivalent to consuming a portion of *ni*/Ni of the fatigue life. Failure occurs when 100% of the fatigue life is consumed. Miner's rule is one of the most widely used and is probably the simplest cumulative damage models for failures

caused by fatigue. This is also used in all national guidelines and codes for assessing steel and concrete bridges. It is called "Miner's rule" because it was popularized by Miner (*1945*). It states that if there are k different stress levels and the average number of cycles to failure at the *ith* stress, S_i, is N_i, then the damage fraction, C, is.

$$\sum_{i=1}^{k} \frac{n_i}{N_i} = C \qquad \text{(eq 2.3a)}$$

i.e, $\quad \frac{n_i}{N_1} + \frac{n_2}{N_2} + \cdots < 1 \qquad \text{(eq 2.3b)}$

where:

n_i is the number of cycles accumulated at stress Si.

C is the fraction of life consumed by exposure to the cycles at the different stress levels. Fatigue failure occurs when C = 1.

2.5.2.3 Strain-Life Curve

The Coffine-Manson formula describes the relationship between plastic strain and fatigue life in the low-cycle high-strain fatigue regime. Basquin's equation describes high-cycle low strain behavior, as discussed above. Morrow combines elastic strain and plastic strain into a total strain relationship as follows:

$$\frac{\Delta \varepsilon_t}{2} = \frac{\Delta \epsilon_e}{2} + \frac{\Delta \epsilon_p}{2} = \frac{\sigma_f'}{E} \left(2N_f\right)^b + \epsilon_f' \left(2N_f\right)^c \qquad \text{(eq 2.4)}$$

where:

- $\Delta \varepsilon_t$ /2 is the amplitude of total strain
- $\Delta \varepsilon_e$ /2 is the amplitude of elastic strain
- $\Delta \varepsilon_p$ /2 is the amplitude of plastic strain
- E is modulus of elasticity
- N_f is the number of strain cycles to failure; $2N_f$ is the number of reversals to failure
- b is the fatigue strength exponent, commonly in the range -0.12 < b < -0.05
- c is an empirical constant known as the fatigue ductility exponent, commonly ranging from -0.5 to -0.7 for metals in time-independent fatigue. Slopes can be considerably steeper in the presence of creep or environmental interactions.

The Figure - below shows the elastic, plastic and total strain fatigue curves. The strain fatigue curves are also called *ε-N* curves as opposed to SN curves for stress fatigue curves. The elastic strain curve represents Basquin's equation; the plastic strain curve

represents Coffine-Manson's equation, and the total strain curve represents Morrow's equation. It is noticeable from the Figure - that total strain is the sum of elastic strain and plastic strain. The intersection of elastic and plastic curves is denoted as $2N_t$, which is the demarcation of material behaviours. The first half of the total strain fatigue curve on the left with higher slope represents low cycle fatigue (LCF); the second half on the right with the lower slope pertains to lower strain ranges that impart stresses in the elastic regime, which represents the high cycle fatigue (HCF).
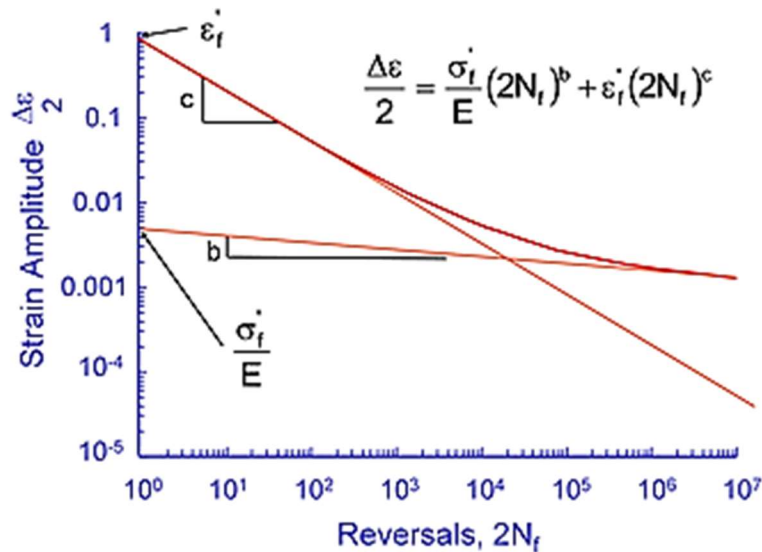
Figure - 2.20 Strain-Life (ε-N_f) Fatigue Curve.

Stress-life relationship has formed the basis of works on masonry (*Abrams et al. 1985, Clark 1994, Roberts et al. 2006*) in their works on high cycle fatigue strength on masonry prisms. Masonry arch bridges are subjected to increasing traffic loading and gradual material deterioration due to environmental impact and fatigue loading. Changes in the material properties have direct influence on the load carrying capacity and rate of deterioration of the overall structure. Changes in the deformability of a masonry arch bridge under traffic loading, observed during monitoring, can be associated with the experimentally recorded ε-N curve configuration and contribute to appropriate maintenance planning. Koltsida (*Koltsida et al. 2018*) has shown the configuration of the ε-N curve with strain changes during stage 1 and 2 and linearly at a constant rate during the second stage. An observed sudden change during long-term monitoring of a structure from linear growth of strain to a non-linear trend could mean that the structure is undergoing stage 3 and major strengthening is required or traffic needs to be diverted (*Koltsida et al. 2018*).

The strain–life method assumes that the life spent on crack nucleation and small crack growth of a notched component (like masonry mortar interface) is identical to that of a

smooth laboratory specimen under the same cyclic deformation i.e., strain-controlled material behaviour at the local crack initiation site (*Lee et al. 2011*). Early fatigue research has shown that damage is dependent on plastic deformation or strain. In the strain-life approach the plastic strain or deformation is directly measured through periodic monitoring. At extremely high cycles of load plastic strains are negligible, due to exceptionally low stresses, stress and strains are easily related (*Bannantine et al. 1990*). Most engineering structures and components are designed such that the nominal loads effects, i.e., deformations remain elastic, same applies to masonry arches. Stress concentrations or local damage often cause plastic strains to develop in the vicinity of the notches, at mortar joints. For masonry arches, cracks or separations start at the interfaces between the masonry units and the mortar joints. Crack growth is not explicitly accounted for in the strain-life method. Due to this, strain-life methods are considered "initiation" life estimates.

2.5.3 Fatigue Response of Masonry

Tomor (2013) has identified three distinct stages of fatigue deterioration in masonry based on acoustic emission levels. During Stage 1, reduction in emission was observed (0–32% of the total loading cycles for compression and 0–58% for shear). During Stage 2, emission stabilised (32–67% for compression, not evident in shear) and in Stage 3 rapid increase in emission was observed, leading to failure (67–100% for compression, 58–100% shear). One of the key aims of this research is to establish the crack deterioration history of the masonry arch subjected cyclic loading.

Casamassima (*Casamassima, D'Amato, 2019*) reviewed the relevant published fatigue models that account for deterioration effects under cyclic loads in masonry elements. He has applied some fatigue models to a case study beside also considering the deterioration of the masonry because of the cyclic loads. In this study, an updated review is provided of the following main stress-life curve models available in literatures for estimating the fatigue strength of masonry elements:

The tests carried out in Abrams et *al*. (*1985*) on masonry samples are characterised by a low frequency (0.1 Hz) and a range of high alternate loads (even up to the value of 40% of the ultimate stress) has shown that a sizable reduction in compressive strength of clay-unit masonry occurs because of repetitive forces.

Ronca et al. (*2004*) conducted a series of tests applying repeated vertical compressive loads on brick masonry prisms typically constructed of low strength grade M4 (1:1:6) mortar. All tests were conducted in accordance with BS EN998-2 (2003) to derive a fatigue model in terms of S-N curves. The brickwork prisms were tested under vertical axial compressive loading (65–80% of the ultimate compressive strength) and by

imposing a slight variation of the alternating loads with three different frequencies:1, 5, and 10 Hz. The experimental values obtained from each test together with the stress-life curves proposed have been plotted in the semi-logarithmic scale *logN* against Sa/Su in Figure – 2.21. It is important to note that fatigue strength increases as the number of cycles, N, decreases. Where Sa is the stress-induced with the alternating load (in absolute value); Su is the compressive strength of the investigated masonry.
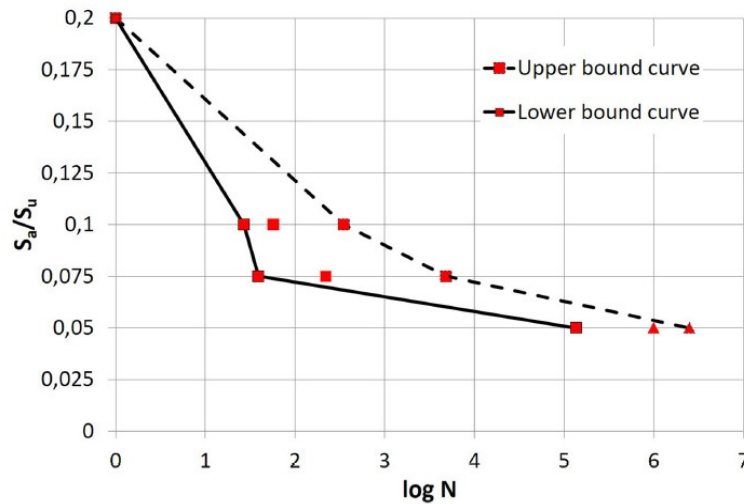
Figure - 2.21 (Ronca et al. *2004*) Fatigue Curve.

Roberts et al. (*2006*) have studied the influence of stress gradient and degree of saturation on the quasi-static and high cycle fatigue strengths of brick masonry illustrated in Figure – 2.22, intending to establish serviceability stress levels for relatively old masonry arch bridges.

Before commencing the fatigue tests, Roberts applied loads quasi-statically up to the maximum and back down to the minimum fatigue test loads. The load was then cycled sinusoidally between the minimum and maximum loads, at typically five cycles per second, until failure. He then recorded the number of load cycles to failure. Analysis of the fatigue test results was based on the reasonable physical assumption that the fatigue strength of brick masonry depends upon the induced stress range ΔS, the mean or maximum induced stress S_{max} and the quasi-static compressive strength under similar loading conditions S_u. Consequently, the test results were presented in terms of a function of the induced stresses $F(S)$ defined by:
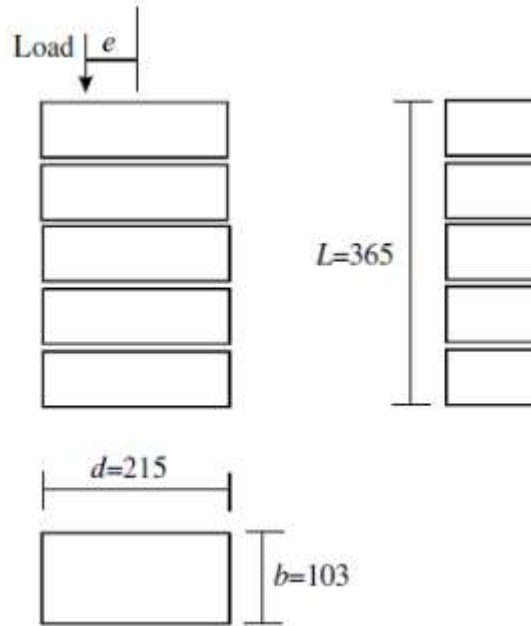
Figure - 2.22 Specimen Tested by Roberts et al. (*2006*).

$$F(S) = \frac{(\Delta S\ Smax)^{0.5}}{Su} = 0.7 - 0.05 \log N \qquad \text{(eq 2.5)}$$

Plotted against the logarithm of the number of load cycles to induce fatigue failure. This equation (2.5) defines a lower bound fatigue strength curve for dry, wet and submerged brick masonry.

A critical review of brick masonry's high-cycle fatigue behaviour (*Wang et al. 2013*) has established the high-cycle fatigue failure phenomenon in brick. Fatigue strength depends not only on the stress range but also on the mean/maximum cyclic stress and the quasi-static compressive strength of the material. The review has identified many uncertainties regarding predicting fatigue performance, mainly predicting service load above which accumulative damage will occur.

By introducing the stress ratio R = *Smin/Smax* in Equation (2.5), and substituting ΔS for the difference *Smax-Smin*, the Roberts et al. (*2006*) proposal is rewritten in the familiar form of stress-life curve *logN* against Smax/Su as follows:

$$S = \frac{Smax}{Su} = \frac{1 - 0.5 logN}{\sqrt{1-R}} \qquad \text{(eq 2.6)}$$

Casas (*2009*) post-processed the experimental results of Roberts (*2006*) and suggested a new stress life relationship for different survival probability levels under compressive loading.

$$S = \frac{Smax}{Su} = AN^{-B(1-R)} \qquad \text{(eq 2.7)}$$

the values in Table – 2.1 are obtained for the coefficients A and B for different values of the survival probability Pb.

Table 2.1 Coefficients for Different Survival Probability (Pb)

Pb	0.95	0.90	0.80	0.70	0.60	0.50
A	1.106	1.303	1.458	1.494	1.487	1.464
B	0.0998	0.110	0.109	0.102	0.094	0.087

Koltsida et al. (*2018*) tested 64 brick full-size masonry prisms according to ASTM (*2014*). Static and cyclic tests were performed with a frequency of 2 Hz. The minimum induced stress during the tests was set to 10% of the masonry compressive strength, while the maximum induced stress ranged between 55 and 80%. The limit on the number of cycles up to failure was fixed as 10^7. For a given survival probability Pb, the fatigue curve may be described as follows:

$$Pb = 10^{-0.1127(Smax.\Delta S)^{3.9252}}(logNf)^{3.8322} \quad \text{(eq 2.8)}$$

Finally, Casamassima (*Casamassima, D'Amato, 2019*) applied his studies on multiple fatigue models on brick masonry to carry out the fatigue assessment to "Cavone Bridge," which was built in Italy before the Second World War currently still open to the traffic. A case study related to the main and secondary arch of an ancient masonry arch bridge that is 140 m in length and 5.6 m wide, and it is composed of three main arches with span lengths of 22 m and three secondary arches with span lengths of 10m. The arches are supported by two piers, of which 14m are outside the riverbed. The piers have a total height from the foundation plane of about 24 m. Applying the above models the calculated residual fatigue life for the main arches have been found to be <1year. While for the secondary spans, they are found to be infinite (>10^8).

The inconsistent results from the case study of the same bridge suggest that the probabilistic models are unreliable for practical purposes. These models have been based on the laboratory test of masonry prisms in compression. On the contrary, the fatigue crack initiation and growth occurs due to alternating tensile stresses, as shown in the Figure - 2.16. Therefore, models based on compressive load testing of masonry prisms under various combinations of compressive stresses are unlikely to offer any reliable fatigue model for masonry arches. This is the driving reason for this research to directly measure fatigue performance of a full-scale arch in laboratory under cyclic loads to suggest a more credible method for predicting fatigue life.

2.5.4 Fatigue of Masonry Arches

Casas (*2011*) investigated the possibility of fatigue failure of masonry arch bridges under service loads. He has also analysed the proposal of reliability-based assessment methods at the ultimate level of the four-hinged mechanism. Casas applied the methodology to an existing bridge. The first step of any reliability-based assessment of masonry arch bridges requires the identification of the failure modes and the definition of their limit state functions. For a single square spanned bridge typically the failure mechanism involves the formation of four hinges. However, there are other failure possibilities as the formation of 3 hinges in addition to the horizontal displacement of the abutment, the crushing of the masonry, the ring separation in multi-ring arches due to their failure of the mortar between rings, punching shear failure because of failure of the radial mortar joints, foundation failure because of scour, failure of the backfill. The most reported modes of failure are the four-hinge mechanism, the ring separation in multi-ring arches and the slippage at the foundations.

The failure mode by ring separation in multi-ring arches can be also included in this category. Ring separation in multi-ring masonry arches may occur either by an increasing monotonic load (ULS) or by the repetition of a great number of cyclic loads (Fatigue Limit State). In both cases the failure is due to the rupture of the mortar between the rings due to the shear stresses. The arch may develop two failure mechanisms. For a reduced number of cycles of load, the failure is by four-hinge mechanism with a load level close to the static failure load. Whereas for a high number of cycles with lower load, failure happens due to ring separation. In this case, two failure modes are coupled. The SN diagram could be still derived, with two branches, each one modelling one failure mode as seen in Figure - 2.23. Figure - 2.23-a shows the case where for a low number of cycles of very high load, the arch fails by the four-hinge mechanism, up to a certain number of cycles of load (N*) where the critical mechanism becomes the ring separation.

In this case, depending on the compression stress level, the failure is either by the formation of the mechanism or by the ring separation. In the case of Figure - 2.23-b, there is a range of compression stresses where the failure can be both by mechanism and ring separation depending on the shear stress level induced by the load configuration in the joints of the ring.
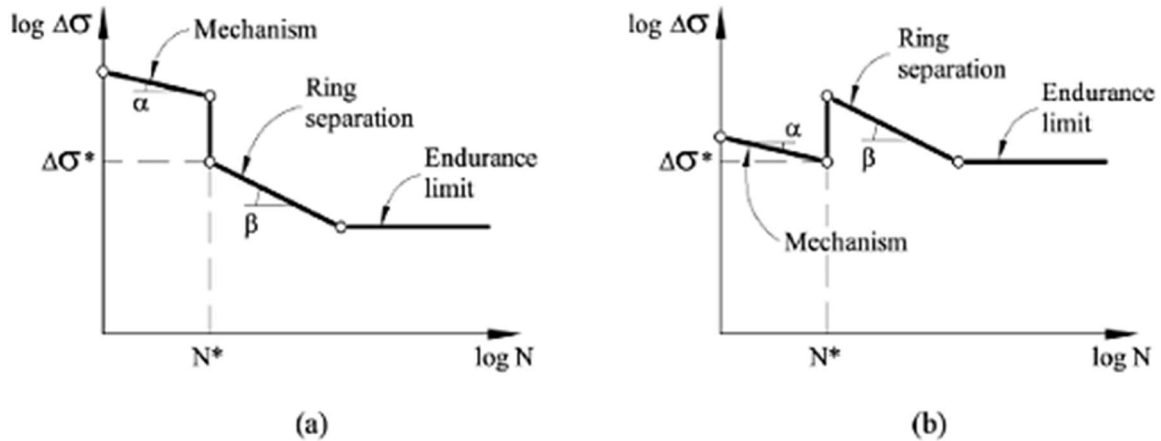
Figure - 2.23 SN Curves for The Coupled "Mechanism-ring Separation" Fatigue Behaviour. (*Casas, 2011*)

Casas have separated the fatigue failure. As he suggested that failures may occur either under the combined compression-bending action (as in the case of single ring arches) or because of the shear action in the interface unit-mortar (case of multi- ring arches). Because the two mechanisms can be of different origin, a separation is made between them and the corresponding SN curves for fatigue in each case have been proposed.

2.5.4.1 Reliability based Assessment of Masonry Arches

For compression bending, the fatigue equation (SN relation) for a survival probability of 95% for masonry in any condition (dry, wet or submerged) is:

$$S = 1.106 \, N^{-0.1034(1-R)} \qquad \text{(eq 2.9)}$$

where,

S is the ratio of the maximum loading stress to the strength, and

R is the ratio of the minimum stress to the maximum stress S_{min} / S_{max}

An endurance limit can be observed for S = 0.5

SN diagrams for masonry in shear, for multi-ring arches, the fatigue equation proposed is:

$$S = 2.69 \, N^{-0.3(1-R)} \qquad \text{(eq 2.10)}$$

An endurance limit can be observed for S = 0.4, The results from the tests show and endurance limit around 40 % of the maximum static load for 3 m span arches and good quality of brick. A similar endurance limit can be defined in the case of 5 m span arches made of weak brick.

Casas have applied the model to real arch, Figure - 2.24, and have concluded that, the assessment methodology developed can be considered as complete. However, due to

the lack of experimental data (mainly on material properties and fatigue due to shear) Casas has cautioned that the practical application to existing bridges and their results should still be looked as preliminary.
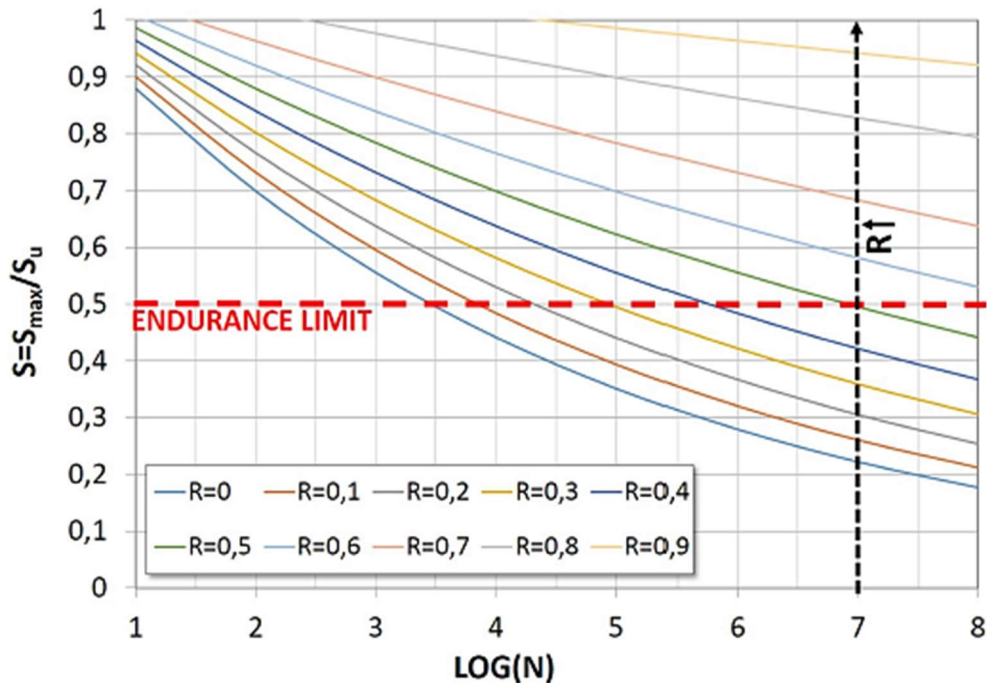
Figure - 2.24 Fatigue Curves, Referred to a 5% of Failure Probability. (*Casas, 2009*)

Tomor (*Tomor, Verstrynge, 2013*) has considered the long-term methodology for assessing masonry arch bridges and their deterioration models proposed for fatigue compressive and shear loading based on laboratory tests.

2.5.4.2 Joint Fatigue-Creep Deterioration Model

Tomor and Verstrynge (*2013*) have considered a joint fatigue-creep deterioration model for masonry with acoustic emission-based damage assessment. Their works haves been based on two independent laboratory test series, the relationship between stress level and life expectancy has been considered for fatigue and creep loading in the form of SN type models. Acoustic emission-based technique has been used to investigate the process of deterioration and characteristics of the damage accumulation process. A joint SN type deterioration model has been proposed to incorporate the static, fatigue, and creep deterioration mechanisms. Fatigue and creep are long-term, stochastic damage mechanisms with non-linear damage propagation. They are sensitive to external influences and small changes in the masonry properties, which make accurate modelling and failure prediction difficult. Fatigue and creep in masonry can be modelled by empirical formulae or by more advanced constitutive

models, e.g. based on rheological models and/or damage mechanics. Empirical models are based on regression analysis of experimental data and can predict fatigue and creep development for a specific set of data.
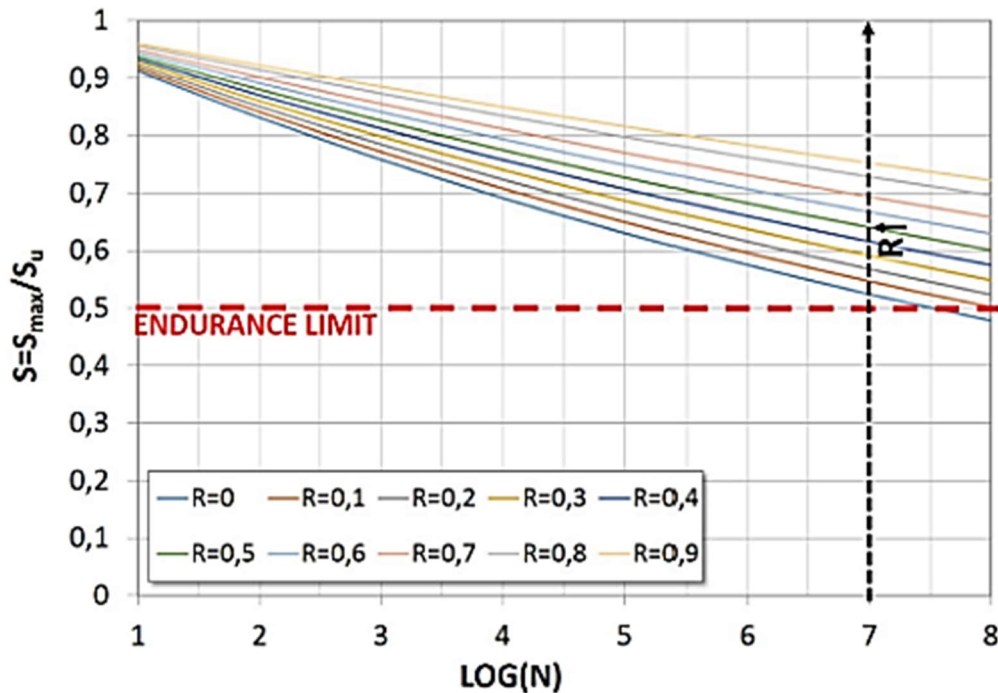
Figure - 2.25 Fatigue Curves, Referred to a 5% of Failure Probability. (*Tomor and Verstrynge, 2013*)

Based on Casas' model and fatigue-creep data in Figure – 2.25, the modified probabilistic model developed by Tomor and Verstrynge (*2013*)

For compression bending, the fatigue equation (SN relation) for a survival probability of 95% for masonry in any condition (dry, wet or submerged) is:

$$S = AN^{B(1-Cr.R)}$$
(eq 2.12)

where,

S is the ratio of the maximum loading stress to the strength

R is the ratio of the minimum stress to the maximum stress S_{min} / S_{max}

Cr is the creep corelation factor

To achieve the best correlation with the current fatigue and creep test results, the value of 0.62 has been identified for parameter Cr. The correction factor allows the interaction by taking account of the creep and fatigue phenomena adjusting the slope of the S-N curves.

While it may not be possible to identify a fatigue limit, in terms of practical application, a permissible limit state (PLS) ''at which there is a loss of structural integrity that will measurably affect the ability of the bridge to carry its working loads for the expected

life of the bridge" (*Melbourne et al., 2007*) would be of more interest. The permissible limit may be defined by the maximum possible number of cycles during the expected lifespan of a structure (e.g. number of vehicles over a bridge). If, for example, the expected life of a bridge is in the order of 300 years, under (non-realistic) continuous 24x7 duration 2 Hz loading the maximum number of cycles would add up to ca. 2×10^{10}. The related stress level for the maximum possible number of cycles would therefore indicate a permissible limit under which no fatigue deterioration is likely to take place in the structure/material.

Using the Casas' model level for compression and shear are for example 43% and 38% of the average static strength respectively. Therefore, if the fatigue stress level is below the respective 43% and 38%, no failure would occur during the lifetime of the bridge and could be classified as a safe limit. The S-N relationship is expected to vary for each failure mode and masonry type. As masonry mix and construction varies widely from bridge to bridge as well as brick to brick, as a first step typical material types should be considered (e.g. weak, medium and strong) and tested. A reliable deterioration models can be developed only after collecting sufficient test results to assist long-term life-cycle management of masonry arch bridges.

Koltsida et al. (*2018*) performed a series of experimental fatigue tests on low-strength masonry prisms under compressive cyclic load, proposing stress-life curves for different values of survival probability. A total of 64 brick masonry prisms were tested to failure under compressive fatigue loading at various maximum stress levels to investigate the fatigue life of masonry with the stress level. Tests under compressive long-term fatigue loading were conducted at 2 Hz frequency with sinusoidal load configuration. Before commencing the fatigue tests, the load was applied quasi-statically up to the mean fatigue load. The load was subsequently cycled between a minimum and a maximum stress level defined as percentages of the mean compressive strength of masonry recorded under quasi-static loading (*Medeiros, 2015*). The minimum stress levels were set to represent the dead load of the structure and were set to 10% of the compressive strength of masonry, mean strength of quasi-static tests (*Koltsida et al. 2018*). The maximum stress level represented live loading (e.g. similar to traffic on a bridge) and varied between 55% and 80% of the compressive strength of masonry.

Koltsida (*Koltsida et al., 2018*) has proposed a mathematical model to describe the fatigue life of masonry using SN-P curves, based on the model used for concrete by McCall (*McCall, 1958*). For masonry under compressive fatigue loading

$$Pb = 10^{-0.1127(S_{max}.\Delta S)^{3.9252} (\log Nf)^{3.8322}} \qquad \text{(eq 2.13)}$$

where *Pb* is the probability of survival. S_{max} is the ratio of the maximum applied stress over the quasi-static compressive strength, ΔS is the stress range and *N* is the number of cycles for fatigue failure.

The model takes the stress range and maximum stress level into account and allows the prediction of the fatigue life expectancy of masonry defined for a corresponding confidence level.
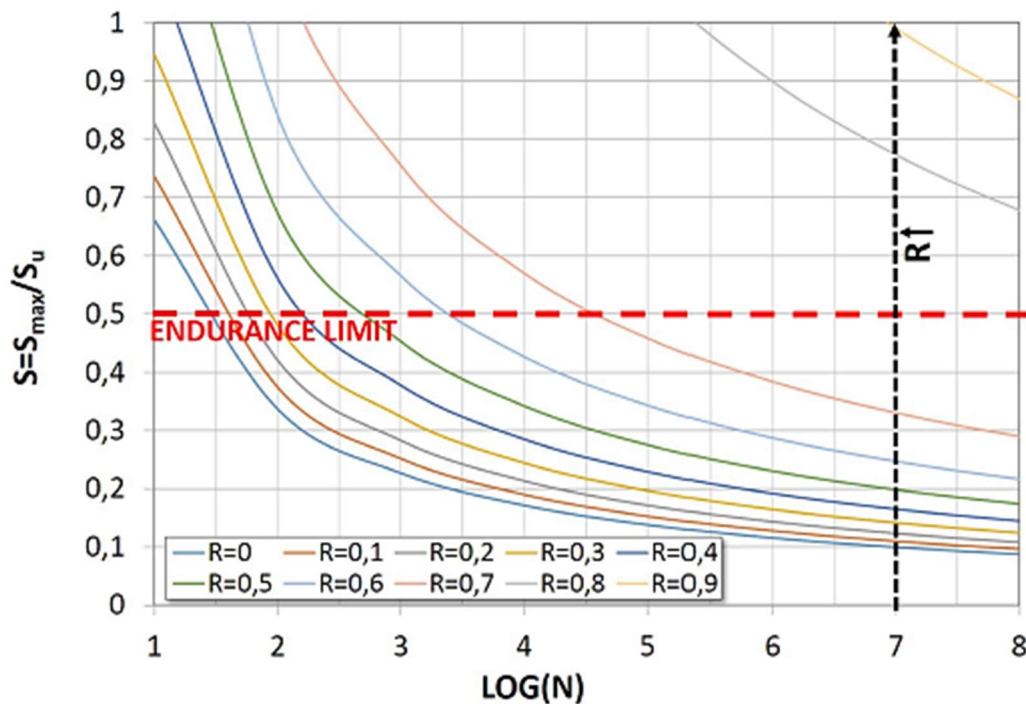
Figure - 2.26 Fatigue Curves, Referred to a 5% of Failure Probability. (*Koltsida et al. 2018*)

Casamassima (*Casamassima, D'Amato, 2019*) has reviewed recently published fatigue models that account for deterioration effects under cyclic loads in Figure - 2.23-26. He has claimed that the numerical comparisons among existing fatigue models reveal that the application of the available fatigue models is particularly problematic for ancient masonry elements, where appropriate stress-life curves are required.

2.5.5 Deterioration of Elastic Modulus

Gao et al (*2019*) have studied damage and fatigue crack growth of mechanical structures made of quasi-brittle materials subjected to repeatedly applied low-intensity loads. Their work has observed that the fatigue loading (repeated moving loads, cycles of temperature, etc.) applied to structures made of quasi-brittle materials (concrete, asphalt concrete, masonry, etc.) generates efforts that are far below the tensile strength or the fracture toughness of the material. However, they are responsible for the degradation of the material properties and fatigue crack growth, leading to the final failure state of these structures. In view of the crack initiation and propagation, the

failure modes of quasi-brittle materials subjected to fatigue loading can be described by four stages, including crack nucleation (Stage I), short crack growth (Stage II), large crack growth (Stage III), and ultimate failure (Stage IV) (Figure - 2.27). In the beginning of the lifetime, the material presents only intrinsic defects (microcracks, voids, etc.). Due to the effect of the cyclic loading, these small defects tend to grow in size and quantity which damage the material. reducing its stiffness. When the intrinsic defects become short cracks, the failure process turns into its second stage of short crack growth. With a relatively high number of cycles, these growing short cracks become large cracks, which characterize the fracture behaviour.
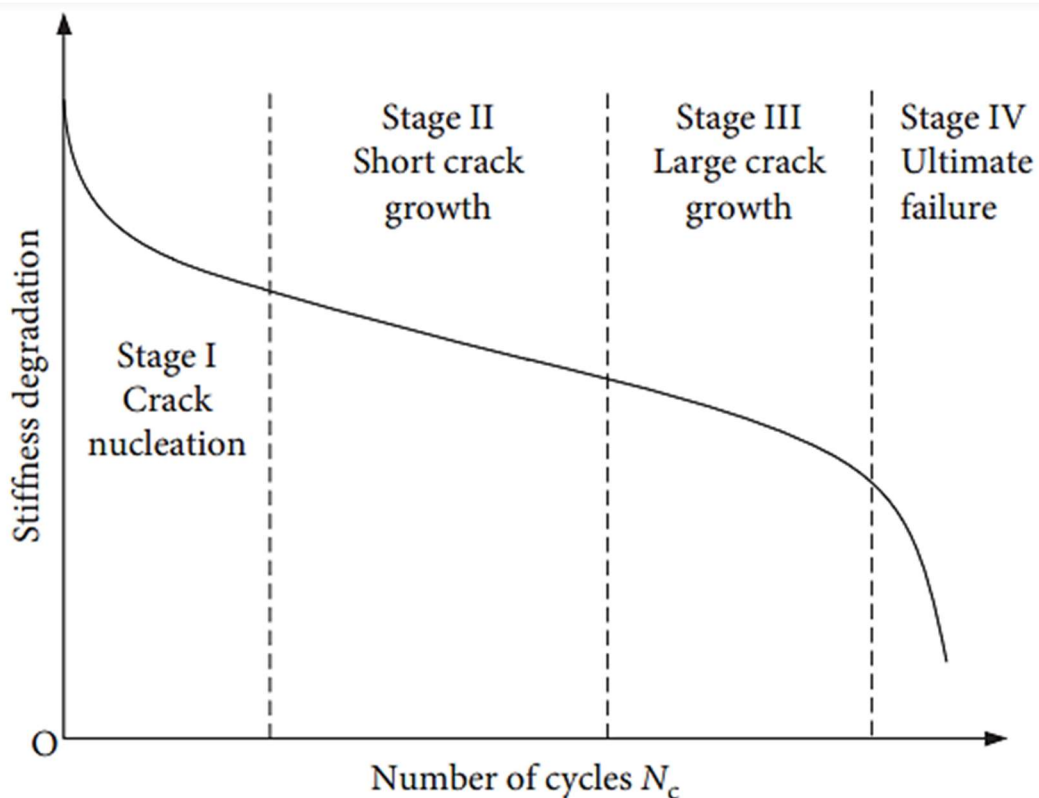
Figure - 2.27 The Four Stages of Fatigue Process (*Gao et al. 2019*)

Koltsida et al. *(2018)* investigated deterioration of the elastic modulus of masonry during compressive cyclic loading. This study has been conducted starting from similar studies regarding concrete specimens, as reported many literatures Zanuy et al. (*2011*), Vicente et al. (*2014*). Specifically, Crumley and Kennedy (*1977*) in their tests has concluded that the elastic modulus decreased by about 40% over the concrete usable life, and that a remarkable reduction of elastic modulus arose often at 75% of the fatigue life. In Holmen (*1982*) the elastic modulus of concrete cylinders consisted of three different phases: a first rapid decrease from 0 to about 10% of the number of failure cycles, a constant decrease from 10 up to 80% of the number of failure cycles, and then a sudden decrease until the specimen's fatigue failure. These reductions

resulted from increasing the number of cycles up to the failure. In addition, during the performed tests on concrete cylinders it was found that the absorbed energy at failure was the same for static and fatigue loads with different intensities.

Starting from the previous studies, a few research groups have proposed similar formulations by considering the masonry material. Among these groups, it is worth mentioning the studies conducted by Alshebani and Sinha (*2001*). In this work, the authors have concluded that deterioration of the elastic modulus began at 20% of the compressive load capacity. Moreover, the strength and stiffness deterioration depended on the number and intensity of cyclic loads, and in particular the degradation increased as the load and number of cycles increased. As mentioned above, Koltsida et al. (*2018*) have recently proposed a different formulation to describe the evolution of the stiffness degradation under cyclic loading. The tests highlighted that until 95% of the fatigue life, the variation of the elastic modulus remained constant, while beyond the 95% mark it rapidly decreased until failure.

The following function has been found as the best fit curve of the maximum induced stress, by Koltsida et al. (*2018*)

$$\frac{E}{E_0} = 1 - (3.0181S_{max}^3 - 5.6894S_{max}^2 + 3.5118S_{max} - 0.6175)\left(\frac{N}{N_f}\right)$$

(eq 2.14)

2.5.7 Strain Evaluation of Masonry under Cyclic Loading

Past test on long-term fatigue in compression have been performed on low-strength brick masonry prisms under laboratory conditions at different maximum stress levels. Based on their experimental results Koltsida et al (*2019*) have suggested that fatigue life is divided into three distinct stages. They have further developed an analytical expression for the prediction of the development of strain during the fatigue life of masonry. These curves could be used to evaluate the remaining service life, plan maintenance works minimising life-cycle costs and prevent premature failures.

Carpinteri et al. (*2014*), have performed a series of quasi-static and cyclic tests on masonry specimens and walls. A typical ε - N curve was obtained for masonry under fatigue based on which three stages of fatigue were detected.

Stage I during which the deformations increase rapidly for the first 10% of the fatigue life,

Stage II where the deformations increase at a constant rate, 10–80% of the total number of loading cycles and

Stage III which is characterised by rapid increase up to failure.

The authors Carpinteri et al. (*2014*) have proposed an equation to relate the rate of variation of the vertical deformation during Stage II, $d\varepsilon_v/dn$, and the number of cycles at fatigue failure N_f.

$$N_f = a \left(\frac{d\varepsilon_v}{dn}\right)^b \qquad\qquad \text{(eq 2.15)}$$

The parameters a and b, which are material constants, can be evaluated by applying a number of loading cycles up to the point that the deformations start growing at a constant rate.

Koltsida et al. (*2019*) have tested brick masonry prisms under compressive cyclic loading at different maximum stress levels until failure. The tests were conducted at 2 Hz frequency (i.e., 2 cycles per second) to represent the flow of traffic at 40–50 km/h speed over the bridge adopting a sinusoidal load configuration. Before commencing the fatigue tests, load was applied quasi-statically up to the mean fatigue load. Subsequently, the load was alternated between a minimum and a maximum stress level defined as percentages of the mean compressive strength of masonry. The minimum stress level aiming to represent the dead load of the structure was set equal to 10% of the compressive strength for all the tests. The maximum stress level represents the live loading e.g. due to traffic over a masonry arch bridge and varied between 80 and 55% of the compressive strength of masonry. The evolution of the maximum and minimum longitudinal strains (ε_{min}, ε_{max}) with the loading cycles was recorded for each prism. The ε - N curve exhibits an S shape (Figure - 2.28) based on which, following three distinct stages have been identified. In Figure - 2.28,

N = number of cycles, during loadings.

N_f = number of cycles at fatigue failure.

Stage I: strain grows at a high rate in the first 10% of the total life of the specimen due to initiation of micro-cracks.

Stage II: this stage is the dominant and is characterised by gradual increase of strain at a constant rate. This stage occupies approximately 80–85% of the total loading cycles during which the micro-cracks have grown steadily.

Stage III: rapid increase of strain due to coalition of micro-cracks into macro-cracks, leading to ultimate fracture of the specimen have been observed in the last 5–10% of the ε - N curve.

Three different equations have been proposed to reproduce the behaviour of masonry during the respective three stages of fatigue. Validity of these equations needed further works.
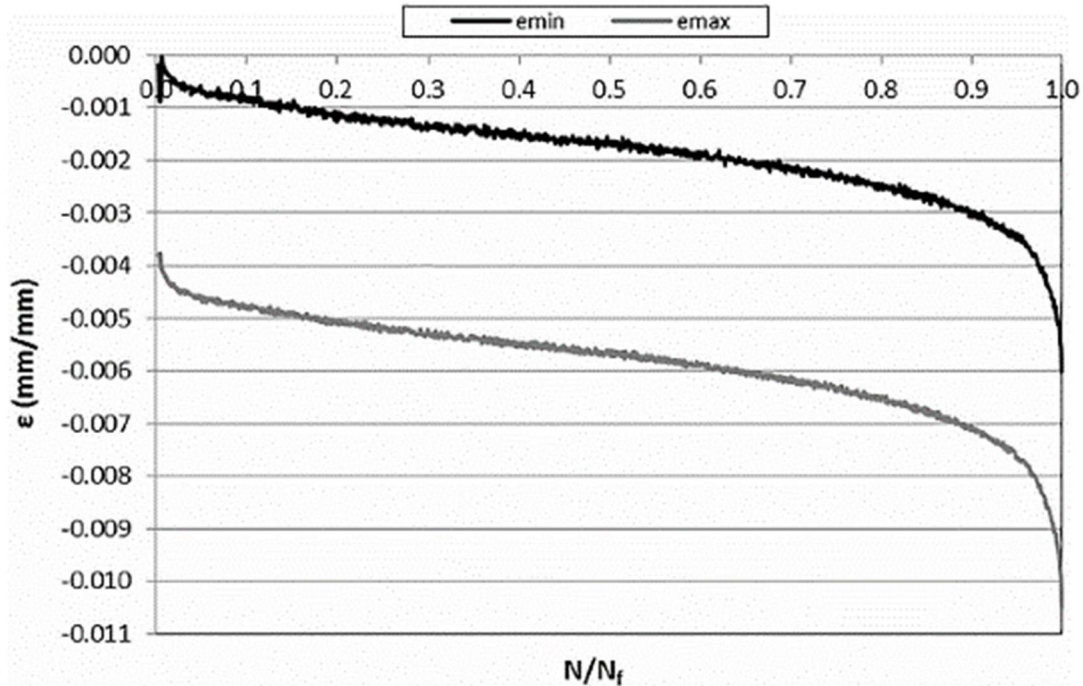
Figure - 2.28 Typical Maximum and Minimum Strain Evolution Curves. (*Koltsida et al. 2019*)

Tests and observations have successfully identified the progressive damage in brick masonry. This is remarkably interesting as the changes to the rate of growth of deformation during long term monitoring of masonry arch bridges under traffic can be associated with different stages of fatigue. The proposed prediction model for the law of evolution for the total longitudinal strain with the number of cycles is a good prediction and can be adopted to evaluate the remaining service life. Based on these predictions, the maintenance works could be planned to minimise life-cycle costs and prevent premature failures and replacement costs.

2.5.8 Authors Contribution

While deterioration due to long-term loading (fatigue) for masonry has been overlooked previously, this has lately become a serious concern and an area of research by many, with increasing traffic demands, bridges are likely to suffer increasing problems and require increasing repair and maintenance activities (*Koltsida et al. 2019, Cassamasima, D'Amato, 2019*). The weight of railway locomotives has increased from 10 tons (1825) to over 120 tons (2010) in the UK with speeds from 8 km/h (1825) to 300 km/h (2010) (*Hayward, 2011*). To avoid unintentional damage and premature failure, the long-term fatigue deterioration phenomenon needs to be understood (*Tomor, 2013*) and safe long-term loading (stress) limits identified. Guidelines for masonry arch bridge assessments (*BA 21/97, now withdrawn*) suggested 50% of the Ultimate Limit State (ULS) as the critical stress limit to avoid long-term fatigue damage.

Tests on multi-ring masonry arches have indicated the fatigue limit to be well below 40% of ULS (*Melbourne et al. 2004*).

Therefore, information on deterioration rates is needed to identify if current traffic loading is causing permanent deterioration and reduces the bridge's life expectancy. If so, by how much? Previous fatigue models of masonry were based on cyclic load tests on masonry prisms under compressive load cycles. Tests never captured the true behaviours of the masonry arch under a combination of bending moment and axial loads resulting alternating compressive and tensile stresses. Masonry arches have little, or no tensile (bond) strength compared to satisfactory compressive strengths. Alternating loads result in failure of bond strengths and corresponding development and initiation of cracks at the mortar-units interfaces (*Sacco, 2010*). Majority of the studies have been restricted to determining the relation between the applied stress and the fatigue life and developing S-N (stress–number of cycles) curves. Experimental data on the strain evolution during the fatigue life of masonry are limited and no mathematical model has been developed to relate the total longitudinal strain with the loading cycles (*Koltsidas et al. 2019*).

Soli-backfilled masonry arches are tested (*Nelson, L. A. and Swift, G 2020*) in laboratory under cyclic and quasistatic loading to investigate the residual strength and safe working loads subjected to range of loading scenarios (*Augusthus et al 2018*). Interesting observation made in this work is that the residual strength of the damaged or distorted arches vary significantly compared to virgin arches. This is relevant for the current state of the masonry arch bridge. Evidence presented in this paper suggests that under some circumstances, a damaged masonry arch may still satisfy the ULS requirements, but not the serviceability requirements since deformations can be quite large. The permissible limit state is considered PLS (*Melbourne et al. 2007*) might be a more appropriate measure of longer-term performance and capacity, although further experimental evidence is required to allow more confidence in applying the PLS.

Purpose of this study is to establish fatigue model for masonry arches through testing of full-scales arches subjected to alternating cyclic loading in laboratory conditions. This is the only credible way to study the crack growths principle from initiation to failure, as shown in the Figure - 2.17. Then apply fundamentals of fatigue principles using accumulated damage as suggested by Miner's in equation (2.2) to generate the Stress-life Wohler's curve as shown in the Figure - 2.17. Finally derive a strain-life relationship by combining life history information from the Wohler's curve against the tangential strains.

Previous studies have confirmed the existence of a high-cycle fatigue failure phenomenon in brick masonry. Fatigue strength has been shown to depend not only on the stress range but also on the mean/maximum cyclic stress and the quasi-static

compressive strength of the material. An increase in the degree of saturation reduces the fatigue strength of brick masonry.

Accuracy in predicting the fatigue life of existing masonry arches based on the previous equations are dependent on the knowledge and understanding of existing material parameters. S_{max}/S_u and ΔS rely on the ultimate compressive strength of the masonry in service. For the existing bridges masonry compressive strength varies significantly. Therefore, fatigue life predicted by the stress-life, SN curve, the approach will be dependent on the unknown strength parameters. Furthermore, non-linearity due to deterioration over the years create unknown stress concentration along the arch barrel.

The most important outcome of this literature review has been the latest studies of Koltsida et al. (*2019*). The proposed prediction model for the law of evolution for the total longitudinal strain with the number of cycles has been considered an important prediction and a better model to evaluate the remaining service life. This research is aimed at mapping the Strain-life (ε-N) curve for a segmental masonry arch and subsequently modelling to predict the residual life. Strain-life approach will overcome following uncertainties:

- Unpredictable material strength;
- Pre-existing damages;
- Unknown stiffness contributions form spandrel wall;
- Quality of backfill.

Deflection of masonry arches under live loading can be measured reasonably well for all existing bridges. Measuring deflection along the arch barrel will help with deriving existing strains. Calculated strains will then be compared with mapped strains-life to predict the residual life.

Hence this approach will offer an alternative and robust tool towards SMART assessment of masonry arches.

2.6 Computational Modelling of Masonry

Masonry imposes a great challenge to structural engineers for numerical modelling and predicting their behaviour. This is mainly due to their composite nature of construction. Bricks or stones of finite sizes are arranged in patterns and laid in mortar. By their construction and responses under the loading, masonry is undoubtedly a heterogeneous medium. According to many authors, there are different possibilities to solve the problem of modelling masonry. These alternatives depend on how detailed modelling is envisaged. Based on this if the model can describe accurately different types of failure. Usually, the alternatives are classified as: detailed micro model simplified micro-model and macro-model.

Lourenco (*1996*) has suggested computational strategies for modelling masonry.
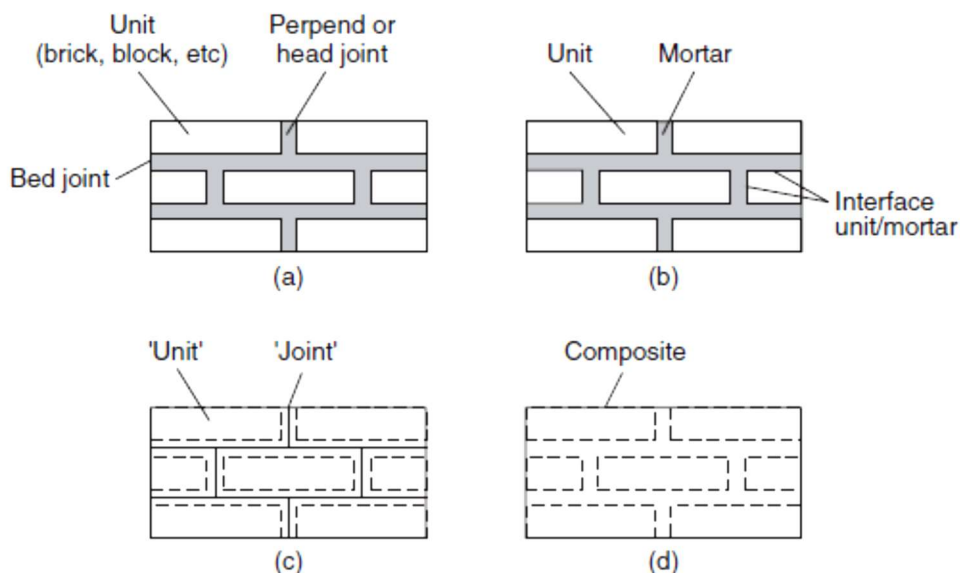
Figure - 2.29 Computational Modelling of Masonry. (*Lourenco, 1996*)

(a) Masonry Sample (b) Detailed Micro-Modelling, (c) Simplified Micro-Modelling, (d) Macro-Modelling

The first alternative in describing a masonry model is the "detailed micro model" (Figure - 2.29 b). This type of modelling considers the bricks and mortar as continuum elements with corresponding failure criteria. The interface between bricks and mortar is modelled by special elements that represent the discontinuities. In this case, the geometry of the wall is completely reproduced. Because of the level of detail of this model, it is supposed that it can represent most failure mechanisms in masonry.

In the second alternative, the "simplified micro-model" (Figure - 2.29 c), the bricks are kept as in the "detailed micro model", but the mortar joints and interface elements are combined to represent a contact area. This means that the general geometry is maintained, but the individual elements that represent joints and interface are not able

to describe the Poisson's effect of mortar over bricks. Because of this last example, some types of failure mechanisms cannot be reproduced in this type of model.

The last alternative is the "macro-model" (Figure - 2.29 d). In this case, the masonry panel (or a part of it) is considered as a homogeneous element. Because of its characteristics, this type of model should be able to reproduce the general structural behaviours of a masonry panel, but it is not able to reproduce all the types of failure mechanisms.

In his doctoral research Lourenço (*1996*) has proposed two models to describe the nonlinear behaviour of masonry. One of these models is a micro model and the other one is a macro model. Amongst the aims of this contribution was to compare the applicability of the two different types of strategies. The micro model is defined through joints which concentrate the inelastic behaviour of the masonry. The plasticity model of the joints can reproduce three different types of failure mechanisms: tension cut-off, Coulomb friction model and compression (considering an elliptical cap) and combined shear-compression failure. As a drawback, this type of models requires a huge amount of computational time and memory and, because of that, it is recommended for the study of small structures and structural details.

Considering the reasons given in the previous paragraph, Lourenço proposed a second model, specially oriented for the use with large structures. This model is defined by considering an orthotropic continuum model for a masonry which considers a Rankine type yield criterion for tensile failure (cracking) and a Hill-type yield criterion for compressive failure (crushing). This model requires many input parameters related to tension and compression tests in different directions and fracture energy (also in tension and compression).

According to previous works (*Page, 1978; Lourenço, 1996*), mortar and bond between bricks and mortar are responsible for significant nonlinear behaviour of masonry. Following this argument, the most effort in the construction of the model has been put on the definition of the type of elements to represent mortar and contact between brick and mortar.

Campbell (*2012*) in his works had proposed a "Simplified micro-model". The bricks were represented by solid finite elements blocks and mortar and bond between bricks and mortar, in this case, were represented by nonlinear springs and contact elements. These elements were combined to describe the mechanical and structural behaviour of a typical joint. Campbell's model was completely implemented in ANSYS (*2009*), which is a software package oriented to solve complex problems in many fields of civil engineering.

2.6.1 Campbell's Model

The unique approach of this model is the representation of horizontal and vertical joints. A group of nonlinear springs and a contact element were used in combination to describe the mechanical and structural behaviour of a typical joint. Two nonlinear spring elements, Figure – 2.30, connected in parallel, combined with one contact element in series with the spring elements were used.
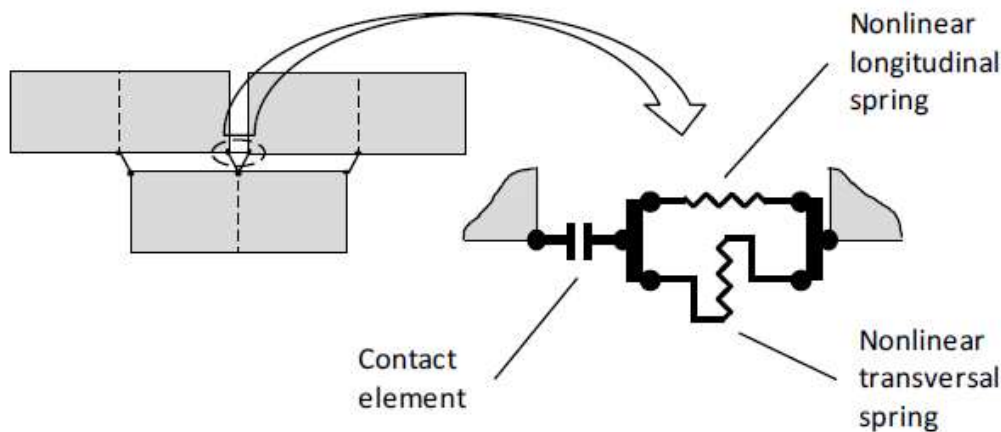
Figure - 2.30 Campbells' Model for A Joint Between Bricks and Mortar.

The properties of the two springs represent the axial and transversal behaviour of mortar. The mechanical properties of the springs are determined considering the tributary area of the brick over the node. The contact elements represent the bond between brick and mortar and its properties, which are also associated with mortar, but it also considers the friction and the adherence limit between these two elements. Campbells' model has been discussed in further detail in following numerical modelling section of this thesis.

2.6.2 Chaimoon-Attard's Model

In their work, Chaimoon and Attard (*2007*) have also used simplified micro-modelling approach. The mortar joint, which is the plane of weakness, is represented through interface nodes of zero thickness. The formulation devised by Attard and Tin-Loi (*Attard 2006*) for the numerical simulation of fracture in concrete was extended to model shear compression failure in masonry. The advantages of this formulation are that, as with the discrete crack models, there is no length scale required. The formulation also allows the tracking of interacting and/or branching cracks without re-meshing. The formulation of Attard was based on a linear complementarity formulation as in Bolzon et al. (*1996*) and uses a mathematical programming algorithm to obtain solutions to a non-holonomic rate form within a quasi-prescribed displacement approach. The inelastic failure surface of a structure is an assembled piecewise-linear

failure surface. Chaimoon and Attard (*2007*) used this approach for the analysis of unreinforced masonry shear walls. Compressive failure was not considered. The Bolzon's proposal was limited because of the existence of unacceptably high compressive stresses at the wall toe. The purpose of Chaimoon and Attard's study aimed to enhance the formulation by including compressive failure to capture the behaviour of shear walls under shear and compression considering possible fracture in the mortar joints and brick units. The masonry unit has been subdivided using triangular finite element units. A finite element discretisation of a simple wall modelled using five bricks, Figure – 2.31, stacked one on top of each other. The wall is subjected to uniaxial compression. Each masonry unit has been subdivided into 16 basic triangular segments.
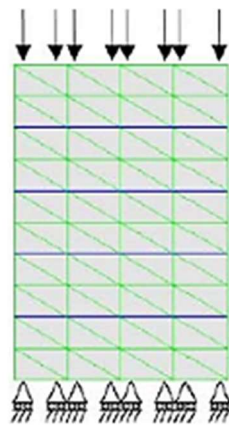
Figure - 2.31 Chaimoon's Model for Studying Compression Failure.

The inelastic failure surface for the mortar interfaces was modelled using a Mohr–Coulomb failure surface with a tension cut-off and a linear compression cap while the inelastic failure surface for the brick interfaces was modelled using a Mohr–Coulomb failure surface with a tension cut-off.

2.7 Discrete Element Modelling (DEM)

Continuous Finite Element Modelling (FEM) has the advantage of being a simple tool while having the disadvantages that only collapse load and collapse mechanism can be obtained and loading history can hardly be included. A discontinuous medium is distinguished from a continuous one by the existence of contacts or interfaces between the discrete bodies that make up the system. Discrete (or discontinuous) modelling techniques are commonly referred to as the discrete element method (DEM). Primarily considered as an assembly of separate blocks or particles (*Cundall, 1971*; *Cundall, Hart, 1992*).

Plastic theory (*The Masonry Arch – Heyman J, 1982*) applicable to masonry arches lead to the understanding of principles of masonry behaviours applicable to arch bridges. Masonry, in general. is a composite material formed by units and joints (*Lourenco, 2013*) with or without mortar and different bond arrangements. It is, therefore, best represented as "discontinuum" separately considering the mechanical behaviour of the units and the interaction between them, thus regarding the joints as surfaces between them. The aim of this approach is modelling the non-linear behaviour, including joint sliding and total separation which may involve large relative displacements between the units resulting in changes to structural geometry and connectivity. Masonry structures are represented by discrete element models as assemblies of blocks or particles, an idealization of their discontinuous nature that governs the mechanical behaviour. This 'discontinuum' approach, an alternative to modelling masonry as a homogenized continuum, is particularly suited for detailed models used in fundamental research and the interpretation of experiments (*Lemos, 2007*). Fundamentally masonry is represented as an assembly of component blocks or particles in mechanical interaction. This block discrete element (DE) models are composed of sets of polygonal or polyhedral bodies. Therefore, the starting point is a discontinuous system as against finite element (FE) method. Following features set the DE method apart from the FE method:

I. Interaction between the blocks is represented by a set of point contacts or edge-to-edge contacts. With no attempt to obtain continuous stress distribution throughout the contact surface,

II. DE models allow full separation between the blocks and the analysis continues up to a large displacement.

Principles of Discrete Element Methods (DEM):

1. Collision detection determines pairs of colliding bodies.
2. Contact forces computed based on the constitutive relation (spring-damper model)
3. Requires small time-steps.
4. Newton's Second Law used to compute accelerations.
5. Numerical integration used to compute velocity, the position of all bodies.

The mathematical formulation of problems of discontinua involves the interaction law between particles and balance principles. Analytical solutions of these equations are rarely available, and approximate numerical solutions are sought instead. The most advanced and most often used numerical methods are Discontinuous Deformation Analysis (DDA) and Discrete Element Methods (DEM). These methods are designed to handle contact situations for irregular particles.
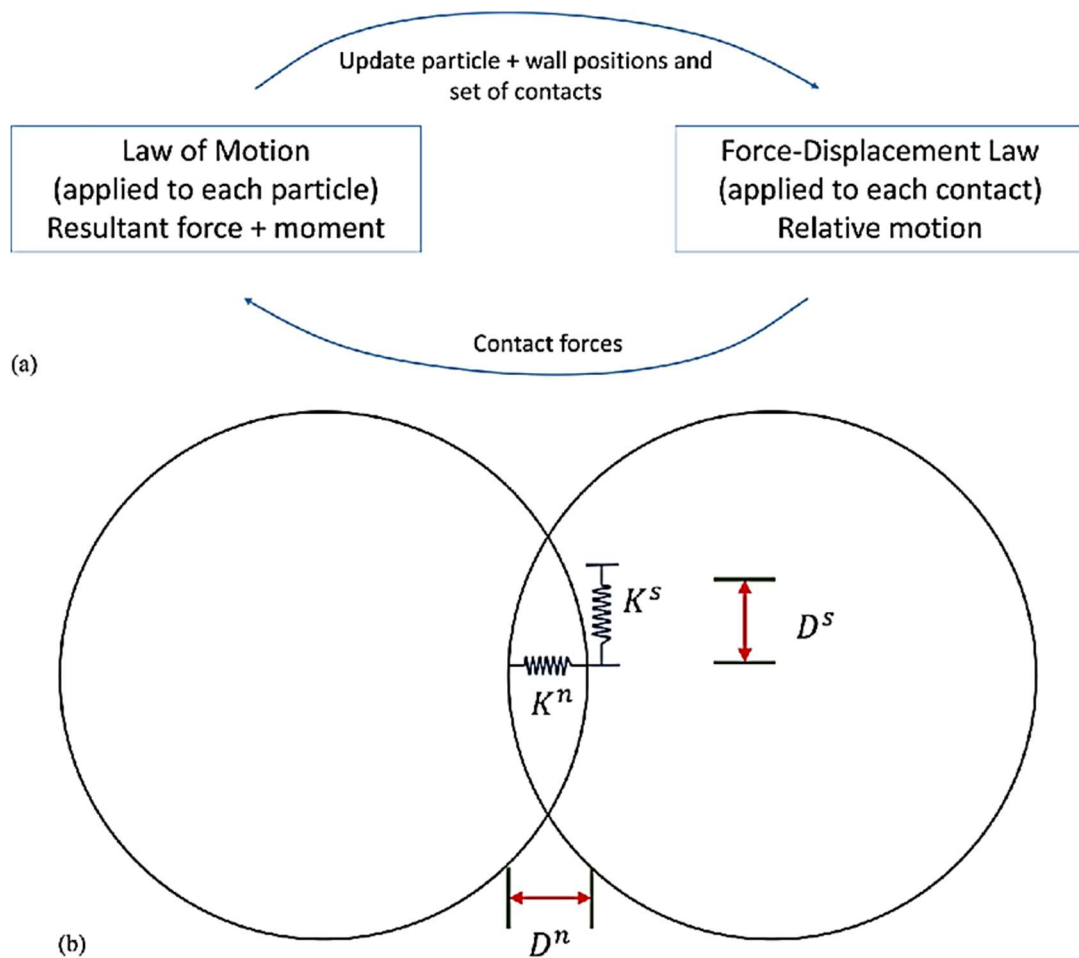
Figure - 2.32 DEM Calculation Flow Chart, Normal and Shear Contact Model. (*Yifei et el, 2017*)

The force-displacement law explains the relative displacement between two entities at a contact and the contact force that acts on the entities. The DEM calculation flowchart is shown in Figure – 2.32. For both ball–ball and ball–wall contacts, this contact force arises from contact that occurs at a point.

2.7.1 Critical Review of FDEM over DEM

The primary feature of masonry is its composite nature, formed by discrete units (stones or bricks) separated by joints, which may be dry or mortared, and possibly by infilling materials. There are two fundamental approaches to model such a complex material: equivalent continuum and discontinuum idealizations, which are also designated as macro- and micro-modelling (e.g., *Lourenco, 2002*).

Limit analysis methods are based on assumptions made on: (1) Masonry structures do not have a tensile strength, (2) masonry structures have an infinite strength in compression, and (3) sliding cannot occur between joints. Heyman (*1982*) was among

the first to use these assumptions in the stone arch stability analysis. Traditional limit analysis methods made use of a static approach that was based on the use of graphic statics during the graphic interpretation of thrust lines of stone arches. If the thrust line was located inside the outline of an arch, the arch would be considered statically stable. Limit analysis methods are appropriate to determine failure mechanisms for structures subjected to an assumed load. Their imperfection is the impossibility to analyse the dynamic response of a structure over time. To analyse the dynamic response of simple structures such as standing pillars, dynamic analytic methods are appropriate but, with an increase in the number of structural elements, these methods become inappropriate because of many analytic equations.

When it comes to calculation, the simplest way of modelling masonry structures using the finite-element method is the discretisation of structures using the skeletal system and linear finite elements. The material and geometric nonlinearity and Mohr-Coulomb criterion of failure in shear, are included in the model. In recent times, many studies have been aimed at modelling masonry structures using macro elements, which contributed to the reduction in the number of degrees of freedom and duration of calculation. Macro-modelling has been intensively used to analyse the seismic response of complex structures like arch bridges (*Roca et al. 2010, Radnić, et al 2012)*. A drawback of most macro models is the fact that they are not able to simulate discontinuity that appears between blocks or parts of a masonry structure. These discontinuities that are already determined, like in case of old stone structures, or that can appear later in form of cracks, can lead to various problems such as the sliding or rotation of certain parts of a structure, separation of blocks, etc. Since masonry structures, due to their very small ultimate tensile strengths, demonstrate an explicit nonlinear behaviour already at very small loads, the use of linear analysis in the modelling of masonry structures is considered unacceptable, as it can lead to wrong results and inappropriate conclusions.

2.7.1.1 Features of Discrete Element (DE) Modelling

The various DE methods differ in several ways (*Lemos, 2007*). There are, however, some features that set them apart from FE modelling:

1. DE models allow the assumption that blocks are rigid, and the system deformability is concentrated in the joints. Today, however, many DE models include deformable block formulations;

2. In most DE models, the interaction between blocks is represented by sets of point contacts, or sets of edge-to-edge contacts, with no attempt to obtain a continuous stress distribution throughout the contact surface. In general. a deformable block may be discretized independently from its neighbours;

3. DE models are designed to allow full separation between blocks, and most of them permit the analysis to continue into the large displacement regime. The main codes perform contact detection and update tasks automatically;

4. DE models tend to employ time-stepping algorithms, either in a real-time scale or as a numerical device to solve quasi-static problems.

- The main advantages are:

  The formulation for large displacements, including contact update, and an independent mesh for each block, in case of deformable blocks.

- The main disadvantages are:-

  The large number of contact points required for an accurate representation of interface stresses and time-consuming analysis, especially for 3D problems.

Based on the adopted solution algorithm, DEM implementations are broadly divided into explicit and implicit methods. The term distinct element method refers to a particular class of DEMs that use an explicit time-domain integration scheme to solve the equations of motion for rigid or deformable discrete bodies with deformable contacts (*Cundall and Strack, 1979*). The most notable implementations of this group are arguably represented by the universal distinct element code (UDEC) (*Itasca Consulting Group Inc., 2013*) and the particle flow code (PFC) (*Itasca Consulting Group Inc., 2012*). On the other hand, the best-known implicit DEM is the discontinuous deformation analysis (DDA) method (*Shi and Goodman, 1988*). Although DEMs were originally developed to model jointed structures and granular materials, their application was subsequently extended to the case of systems where the mechanical behaviour is controlled by discontinuities that emerge as a natural outcome of the deformation process, such as fracturing of brittle materials. Specifically, the introduction of bonding between discrete elements allowed capturing the formation of new fractures and, thus, extended the application of DEMs to also simulate the transition from continuum to discontinuum.

As observed by Bicanic (*2003*), the original boundary between continuum and discontinuum techniques has become less clear as several continuum techniques can deal with emergent discontinuities associated with the brittle fracture process. The hybrid approach is known as the combined finite discrete element method (FDEM) (*Munjiza et al., 1995; Munjiza, 2004*) effectively starts from a continuum representation of the domain by finite elements and allows a progressive transition from a continuum to a discontinuum with the insertion of new discontinuities.

2.7.1.2 The Universal Distinct Element Code (UDEC)

In UDEC the computational domain is discretised into blocks using a finite number of intersecting discontinuities. Each block is internally subdivided using a finite difference, or a finite volume, scheme for the calculation of stress, strain and displacement. The mechanical interaction between blocks is characterised by compliant contacts using a finite stiffness together with a tensile strength criterion in the normal direction, and a tangential stiffness together with a shear strength criterion (e.g. Coulomb-type friction) in the tangential direction to the discontinuity surface. Like PFC, static problems are treated using a dynamic relaxation technique by introducing viscous damping to achieve steady-state solutions.

When using the classic formulation of UDEC, rock failure is captured either in terms of plastic yielding (e.g. Mohr-Coulomb criterion with tension cut-off) of the rock matrix or displacements (i.e. sliding, opening) of the pre-existing discontinuities. That is, new discontinuities cannot be driven within the continuum portion of the model and therefore discrete fracturing through intact rock cannot be simulated. However, Lorig and Cundall (*1989*) showed that this shortcoming can be overcome by introducing a polygonal block pattern, to the UDEC capability.

Figure - 2.33 UDEC Modelling of Fracture Propagation in Rock.

(a) Normal and shear stiffnesses between blocks. (b) Constitutive behaviour in shear and tension (i = s, n). (*Kazerani et al 2010*)

In Figure - 2.33, a physical discontinuity is created when the stress level at the interface between block exceeds a threshold value either in tension or in shear. Although new fractures are so propagated, this technique is not based on a linear elastic fracture mechanics (LEFM) approach. That is, unlike classic LEFM models, fracture toughness

and stress intensity factors are not considered. Furthermore, material softening in the FPZ, typically captured using cohesive-crack models, is disregarded.

2.7.1.3   Finite-Discrete Element Method (FDEM)

In the hybrid continuum-discontinuum technique known as the combined FDEM, the simulation starts with a continuous representation of the solid domain of interest. As the simulation progresses, typically through explicit integration of the equations of motion, new discontinuities can form upon satisfying some fracture criterion, thus leading to the formation of new discrete bodies. In general. the approach blends FEM techniques with DEM concepts (*Barla and Beer, 2012*). The latter algorithms include techniques for detecting new contacts and for dealing with the interaction between discrete bodies, while the former techniques are used for the computation of internal forces and the evaluation of a failure criterion and the creation of new cracks.

Smoljanovic *et al.* (*2015*) have shown a new numerical model in the finite element and a new material model in the contact element which simulate the connection between block and mortar. The material model in finite element considers the orthotropic and cyclic behaviour, the possibility of failure and softening in pressure. The numerical results showed that the presented model can capture the main features that characterize the behaviour of masonry shear walls under monotonic increasing and cyclic loading.

2.7.1.4   Comparison of DEM and FDEM

This review summarises the use of both DEMs (either particle- or grain-based) and combined FDEM codes and their use to investigate the failure behaviour of brick masonry under a variety of loading conditions. The introduction of bonds between discrete elements has extended the application of the DEM, which was originally developed to simulate the behaviour of solids whereby pre-existing discontinuities have spacing comparable to the scale of interest of the problem under analysis (e.g. blocky rock masses, granular media), to capture the growth of new fractures. The main domain of application of DE models to masonry has been in the study of structures that fail predominantly by mechanisms. The capabilities of simulation of complete block separation and large movements, with substantial changes in the contact structure, are important features of these models. The development of deformable block formulations has brought DE models close to discontinuum FE models with joint elements.

Hybrid formulations combining features of both methods are in use today. The available numerical model based on the hybrid FDEM is extended to capture the main features related to the behaviour of masonry structures. The improvement relates to a new numerical model in the finite element and a new material model in the contact element which simulates the connection between block and mortar. The material

model in finite element considers the orthotropic and cyclic behaviour, the possibility of failure and softening in pressure. The numerical model of the contact element considers the possibility of failure and softening behaviour in tension and shear, increasing of fracture energy in shear due to increasing pre-compression stress, decreasing friction coefficient due to increasing shear displacement as well as cyclic behaviour in the interface element.

Owen et al. (*1998*) illustrated the capabilities of discrete/finite element numerical techniques for predictive modelling of situations involving masonry units, back-fill and geotechnical foundation material. The problem is treated as a combined finite/discrete element problem with the masonry blocks being represented by deformable discrete elements in frictional contact, the fill material by spherical discrete elements and the foundation medium beneath the central pier modelled as a Mohr-Coulomb material. A further development which is currently in progress involves an extension of the procedure to fully three-dimensional problems. A disadvantage of this approach is numerous discrete elements required to model the masonry arch bridge.

Following Table - 2.2 lists down comparisons between DEM and FDEM discussed as above.

Table 2.2 Comparison Between DEM and FDEM

DEM	FDEM
The discrete element method DEM has been used in fracture mechanics studies of heterogeneous media. One of the current limitations of particle/discrete methods for fracture analysis is related with the high number of particles/elements that are necessary for the discretization, which limits the use of particle systems in larger structures.	To apply the particle method to the analysis of larger structures, a Hybrid method is proposed which uses the DEM in the discretization of the fracture zone, and uses for the surrounding areas a discretization based on the finite element method FEM. Works of Smoljanovic et al. (*2015*) has shown FEM/DEM method and the available experimental results show high accuracy in predicting the behaviour of block-mortar connection and masonry prisms under monotonic and cyclic loads. This is particularly encouraging in predicting the fatigue life of masonry arches subjected to cyclic loading due to passage of locomotives.
The initial DEM which was based on rigid blocks Several improvements have been adopted which have introduced FEM technology in the DEM formulation. Now allows also the blocks to deform by discretizing each block with an internal FEM mesh.	In FDEM the simulation starts with a continuous representation of the solid domain of interest. As the simulation progresses, typically through explicit integration of the equations of motion, new discontinuities can form upon satisfying some fracture criterion, thus leading to the formation of new discrete bodies. In general. the approach blends FEM techniques with DEM concepts (*Barla and Beer, 2012*)

In discrete models, joints are thus viewed as the surfaces where contact between blocks takes place, governed by appropriate constitutive laws. Therefore, the starting point of a DE model is a discontinuous system.	In contrast with the FE method, evolved from the representation of a continuum.

2.7.2 Combined Finite Discrete Element Method

Combined finite discrete method (FDEM) merges the finite element tool and techniques with discrete element algorithms (*Munjiza, 2004*), like a discrete element based transient dynamics, contact detection and contact interaction solution with the added feature to capture deformability. Resulting in a large number of deformable bodies interacting with each other and in the process can break, fracture or fragment. A typical FDEM element system will involve a large number of interacting solids, in these instance masonry units as discrete elements. One key issue to note in the development of FDEM is how the contact is treated i.e., the enforcement of constraint that no point in space occupied by more than one body at the same time. The two aspects to contact in the FDEM method:

- Contact detection;
- Contact interaction.

Contact detection aims to identify only discrete elements that are close to each other eliminating the need to couple the elements that are far from each other therefore reducing CPU time.

After detecting the couples of discrete elements, a contact interaction algorithm is employed to evaluate the contact forces between discrete elements in contact.

The performance of the presented numerical model by Smoljanovic et al (*2015*) was investigated on two masonry walls. The numerical results showed that the FDEM model has been able to capture the main features that characterize the behaviour of masonry shear walls under monotonic increasing and cyclic loading.

The advantage of the FDEM model is its ability to simulate the behaviour of the masonry structure through the entire failure mechanism from the continuum to the discontinuum which has been recognized as vital in modelling the collapse of masonry

structures due to hazardous loading conditions such as intensive seismic excitation, explosions, and missile impact.

2.7.2.1 Combined Smeared and Single Crack

Fracture and fragmentation of masonry are realised by the combined smeared and single crack model (*Munjiza et al., 1999*). This is based on a stress-strain curve for material in tension, those are divided into two sections.

Non-linear behaviour of masonry under tension (*Pluijm, 1997*) suggests that the behaviour of units and mortar joints under tension, Figure – 2.34, is similar to that of concrete.
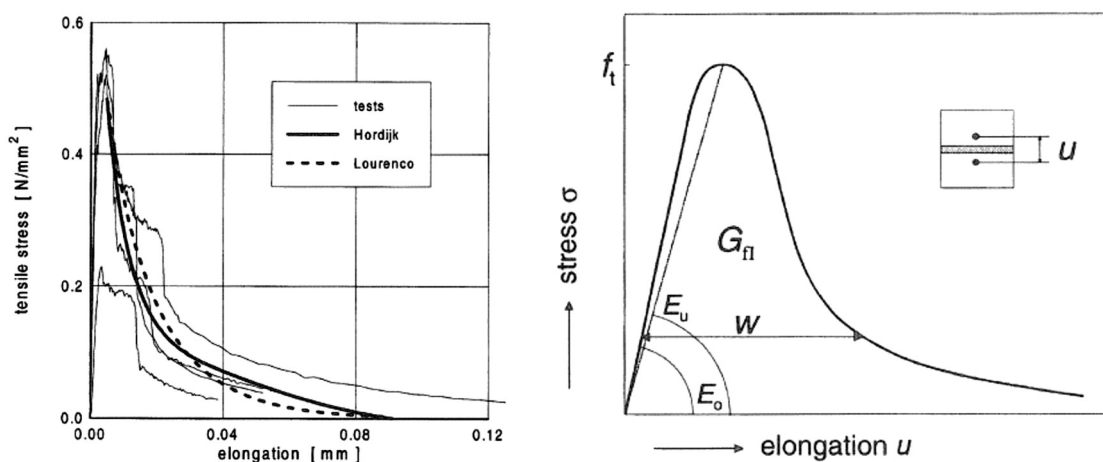
Figure - 2.34 Test Results and Schematic Diagram of Deformation Controlled Tensile Test. (*Pluijm, 1997*)

Masonry, in general. is considered as an assembly of extended within the FDEM context. Elements relate to zero thickness interface (i.e., mortar) elements. Dimensions of each brick units are extended to the axis of mortar joints. Each unit is discretised (meshed) with its own constant strain triangular finite element mesh.

Cracks are reasonably assumed to coincide with the finite element edges those are defined by the simplified micro-modelling of masonry, Figure - 2.29(c). This idealisation of predefined cracking also coincides Heyman's hinge formation and therefore relates to Plastic theory of the masonry arch.

Within the framework of the FEM/DEM method the masonry structure is considered as an assemblage of extended unit elements connected with zero thickness interface elements Figure – 2.35 which simulate the behaviour of the mortar joints and unit-mortar interface.
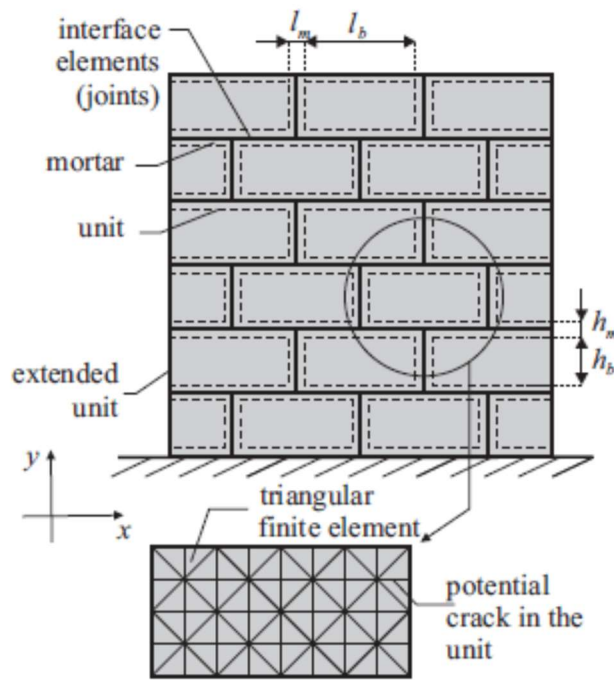
Figure - 2.35 Discretisation of Masonry Structure. (*Smoljanovic, et al. 2015*)

Separation of the element edges develops bonding stress, which is a function of separation, δ. No physical separation occurs before the tensile strength is reached, i.e., $\delta = \delta_t = 0$. In the modelling, this phenomenon is included by the penalty function method (*Munjiza et al. 1999*) - i.e. normal springs, Figure - 2.36.

Normal springs   Shear (Tangential) springs
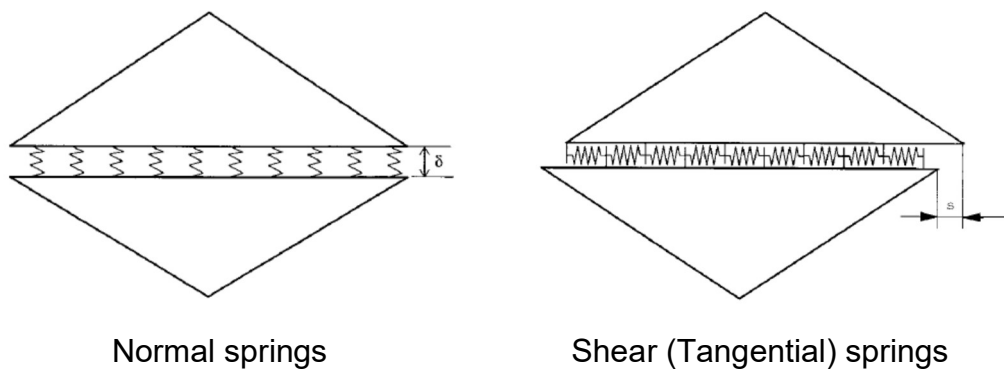
Figure - 2.36 Normal and Tangential Springs

2.7.2.2 ELFEN

The continuum formulation of ELFEN is based on the explicit finite element method. Material softening (or hardening) is captured using a non-associative Mohr-Coulomb elastoplastic model with shear strength parameters, including cohesion, friction angle and dilation, defined as a function of the effective plastic strain. The localization of strain is obtained by regularizing the standard description of the continuum with the

incorporation of fracture mechanics principles in the equations governing the evolution of state variables (*Owen and Feng, 2001; Klerck et al., 2004*). Material softening associated with fracturing is captured under the main assumption that quasi-brittle failure is extensional in nature. As thoroughly described by Klerck (*2000*), extensional failure is modelled directly and indirectly for the cases of tensile stress and compressive stress fields, respectively. Under direct tension, several constitutive models can be used such as the rotating crack and the Rankine tensile smeared crack. With these models, material strain softening is fully governed by the tensile strength and the specific fracture energy parameters. Under compressive stress fields, a Mohr-Coulomb yield criterion is combined with a fully anisotropic tensile smeared crack model. With this approach, known as the compressive fracture model, the extensional inelastic strain associated with the dilation response is explicitly coupled with the tensile strength in the dilation direction. That is, increments of extensional strain are associated with tensile strength degradation in the perpendicular direction. Upon localization of damage into crack bands and complete dissipation of the fracture energy, a discrete fracture is realized. Hence, the transition from continuous to discontinuous behaviour involves transferring a virtual smeared crack into a physical discontinuity in the finite element mesh (*Owen and Feng, 2001*). The mesh topology update is based on a nodal fracture scheme with all new fractures developing in tension (i.e. Mode I) in the direction orthogonal to the principal stress direction where the tensile strength becomes zero. This procedure is numerically accomplished by first creating a non-local failure map for the whole domain based on the weighted nodal averages of a failure factor, defined as the ratio of the inelastic fracturing strain to the critical fracturing strain. Secondly, a failure direction is determined for each nodal point where the failure factor is greater than one based on the weighted average of the maximum failure strain directions of all elements connected to the node. Finally, a discrete crack is inserted through the failure plane.
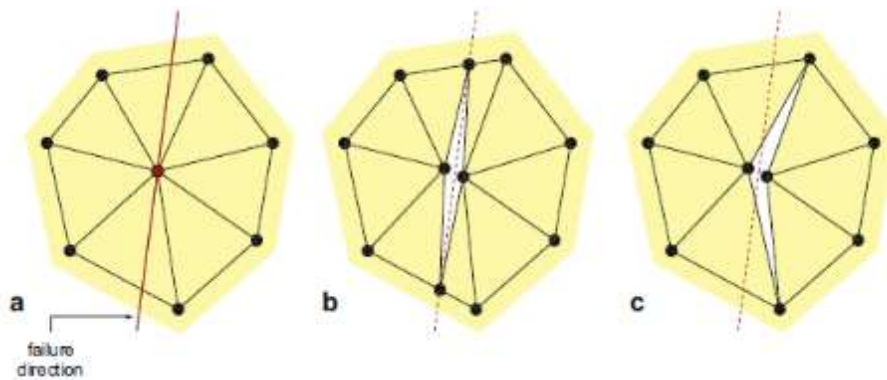
Figure - 2.37 Nodal Fracture Scheme of ELFEN. (*Klerck, 2000*)

As depicted in Figure - 2.37 (a) Initial state before fracturing, (b) intra-element crack insertion, and (c) inter-element crack insertion. Figure - redrawn after Klerck (2000).

The insertion of a new crack can be accomplished using two different algorithms (*Klerck et al., 2004*). The intra-element insertion drives a new fracture along the crack propagation direction by directly splitting the finite elements. In this case, a local adaptive re-meshing may be necessary to achieve an acceptable element topology and avoid highly skewed sliver elements that could decrease the numerical stability threshold of the integration time step. Conversely, with the inter-element insertion, the discrete crack is snapped to the existing element edge most favourably oriented to the failure plane. Following the crack insertion, the damage variables in the adjacent finite elements are set to zero and the contact along the two newly created surfaces is treated using a contact interaction algorithm (e.g. penalty or Lagrangian multiplier method).

2.7.2.3 ANSYS Workbench

The work of Wang (*Wang et al 2014*) has shown the numerical model with contact elements enables good prediction of tests carried out on triplet specimen. In his work on Numerical modelling of masonry arch bridges: investigation of spandrel wall failure (*Wang et al. 2014*) he has used ANSYS commercial software for modelling masonry. The work has reviewed the development of a non-linear interface element for three-dimensional mesoscale analysis of brick-masonry structures (*Macorini and Izzuddin 2011*). However, the required parameters for this model, especially the non-linear properties for the interface are difficult to determine. The consideration of both geometry and material nonlinearity during analysis requires high computational resources, which has limited the application of the model. Wang's work has considered micro modelling of triplets using Drucker Prager material behaviour at the mortar interface and concrete material models. In the concrete model, the cracking is modelled by the modification of the stiffness matrix and material properties when the maximum tensile stress was reached. The cracking occurred in the model is considered as a `smeared band', rather than discrete cracks. Wang then further considered micro-modelling with an interface by using ANSYS 'contact elements" and "cohesive zone material' (CZM) modelling. Finally, Wang has concluded that the FEM with interface 'contact' elements successfully predicts the failure pattern in masonry walls, along with reasonable predictions of load/deformation behaviour. More discussion on ANSYS contact modelling is continued in the following chapter.

2.8 Masonry Arch Modelling

Masonry imposes a great challenge to structural engineers for numerical modelling and predicting their behaviour. This is mainly due to their composite nature of construction. Bricks or stones of finite sizes are arranged in patterns and laid in mortar. Masonry is undoubtedly a heterogeneous medium due to their construction and

responses under the loading. Lourenco (*Lourenco, 2013*) has suggested computational strategies for modelling masonry*.*

There are two modelling approaches which are widely used. These are micro modelling and macro modelling (also refer chapter 2.5, Figure - 2.29). The micro modelling approach simulates the actual texture of masonry structures, as the units and mortar joints are considered separately and characterized with respective properties. The macro modelling defines an equivalent continuum to represent the global behaviour of masonry. Micro modelling has been used for the detail analysis of small structures where the stress and displacement states are of primary interests. This approach requires more data from small-scale laboratory tests and a relatively fine mesh is frequently used in the finite element model, especially if non-linear properties are involved in the problem. The macro-modelling has been preferred for the global analysis of a structure with sufficient size, where the interaction between brick-and-mortar joints is not important. A coarser mesh configuration is chosen, and the necessary material properties are obtained from tests on masonry prisms with sufficient size under homogeneous applied stress conditions.

The brick/stone and mortar units are modelled individually using continuum elements. The brick/mortar interfaces for both the bed and head joints are also taken into consideration. It is possible to treat the brick-and-mortar units as either elastic or inelastic materials and even the interface could be assigned as having inelastic behaviour. In principle, all possible failure mechanisms can be reproduced using this approach. Main disadvantages of this detailed level of modelling include a high computational time and resource requirement. This is due to finer mesh configuration used for the model to capture the behaviour of different components, especially when inelastic materials are involved. Micro modelling approach also requires detailed material properties and constitutive laws for the brick (stone) units and mortar joints. Still, it is difficult to model the junctions between the head joints and the bed joints. The dominant failure patterns of masonry arches are delamination at the brick/mortar joint interface. For the detailed modelling approach, there are two possible ways to achieve this: one is to create a contact between the bed and head joint using interface elements, where there will be three types of interfaces in the masonry system. These are the interface between a brick unit, bed joint, and the interface between a brick unit and head joint, the interface between the bed and head joint. It has been found *(Campbell, 2012, Wang et al. 2014)* that the identification of the contacts at different interfaces is difficult and modelling process become very time consuming. Alternatively, the mortar joint can be considered as a continuum, and introduce fracture mechanics principle at the intersection between mortar joint to allow cracking and fracture to occur. This means specific material properties, like fracture energies and

constitutive laws need to be developed. Given the complexity and dependency on material properties and high demand for resources, the micro modelling approach has been limited to small structural elements where the states of stress and displacement are of great interest.

In simplified micro modelling, the masonry sample is considered to consist of only the unit and joint. The units are expanded to keep the geometry unchanged and represented by continuum elements while the behaviour of the mortar joints and two unit-mortar interfaces are represented by a modified `joint'. Masonry is considered as a set of elastic (extended) blocks bonded by potential fracture / slip lines at the joints. Compared with the detailed modelling approach, only one interface is required for the mortar joint as a result increases the computation efficiency as considerably fewer elements are involved in the analysis. A significant disadvantage of this approach is the loss of accuracy under some conditions as the Poisson's effect of mortar is not included (*Lourenco et al., 1995*).

Interaction between the units and mortars can be ignored for large scale structures to determine their global structural behaviour. The macro-modelling approach treats masonry as a homogeneous anisotropic composite without any distinction between individual brick units and joints. A complete macro-model can be representative if they represent an orthotropic material with different tensile and compressive strengths along the material axes as well as different inelastic behaviour for each material axis (*Lourenco et al.1995*).

2.9 Interface Modelling

Lourenco (*1996*) has developed an interface model based on the simplified modelling strategy. He has used the interface elements as potential crack, slip or crushing planes. He has defined this model by a convex composite yield criterion which consists of a tension cut-off for tensile failure. The Coulomb friction model for shear failure and an elliptical cap mode for compressive failure has been considered, shown in Figure - 2.38.
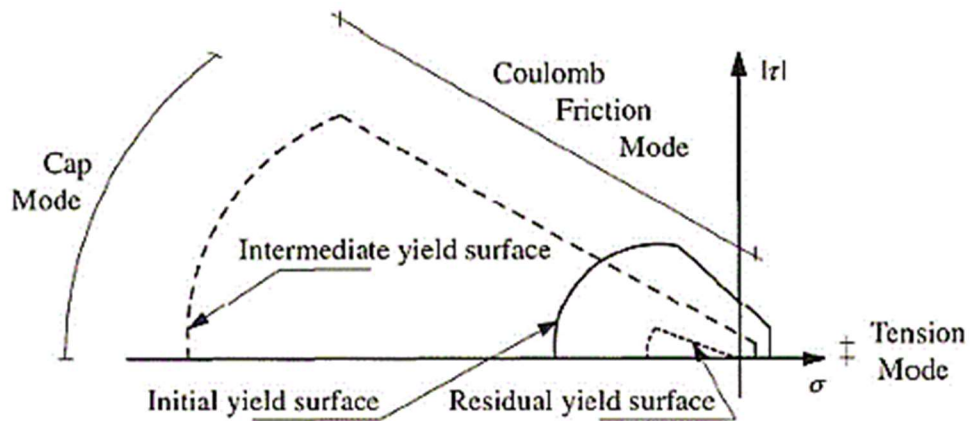
Figure - 2.38 Proposed Cap Model for Interfaces. (*Lourenco, 1996*)

The brick units have been discretised with continuum elements and the joints have been discretised with interface elements, shown in Figure - 2.39. Further interface elements have been introduced in the middle of each brick unit to simulate the possible cracking that could occur in the units.
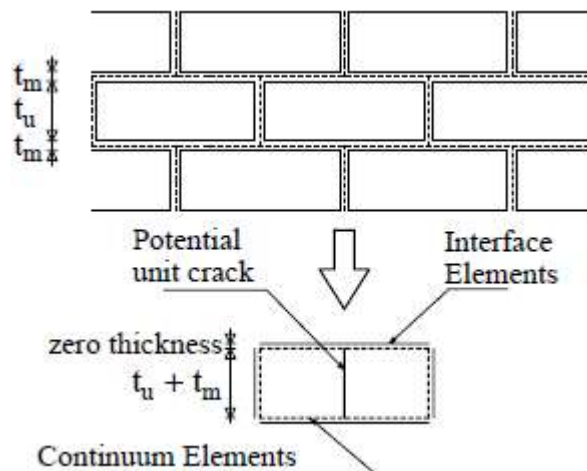
Figure - 2.39 Suggested Modelling Strategy. (*Lourenco, 1996*)

The proposed model has been validated with experimental tests on shear walls and a deep beam. The model has shown to reproduce the complete path of the structures up to and beyond peak until total degradation of strength. Parametric studies have identified the crucial roles of the dilatation angle, compressive capacity and cracking of the units, and the mesh density of the interface model.

Macorini and Izzuddin (*2011*) have written a paper to describe their work on the development of a non-linear interface element for three-dimensional mesoscale analysis of brick-masonry structures. They have also adopted a simplified micro modelling approach in their work. Three-dimensional continuum solid elements have

been used to model the blocks. the mortar and brick-mortar interfaces have been modelled by means of a two- dimensional non-linear interface element. Though it is possible to model small scale shear walls by this method, however it is difficult to reasonably determine the required parameters for this model, especially the non-linear properties. The consideration of both geometry and material nonlinearity during analysis require high computational resources, which has further limited the application of the model to small scale shear walls.

An interface cohesive model combining damage and friction has been proposed by Sacco and Toti (*2010*), modelling the mechanical behaviour of masonry elements regarded as heterogeneous systems, made of mortar and bricks joined by means of interfaces.

The interface model has been developed based on the mechanical model proposed by Alfano and Sacco (*2006*) and by Alfano et al. (*2006*). A micromechanical damaging process, Figure - 2.40(a), has been analysed with reference to typical interface zone between brick and mortar. Three different states have been recognized at the brick-mortar interface, Figure - 2.40(a). At the interface point *A*, the mortar-brick connection is intact or considered undamaged, at the interface point *B*, partial decohesion between the two contact surfaces of the different materials occurred, at the interface point *C*, the decohesion phenomenon is complete.

Sacco has introduced a concept of representative elementary volume (REV) of the interface. REV is characterized by the height *h*, Figure 2.40(b), obtained as the sum of the thicknesses of the mortar and brick involved in the degradation phenomenon at interface, the length *b*, determined as the characteristic distance between the microcracks, and the width *w*, which depends on the size of the mortar-brick. The decohesion phenomenon of the two materials has been believed to occur with a physical degradation of thin layers in the adherents, where microcracks and micro voids arise. The thickness of the layers involved in the damage process of the adherent materials can be considered as a mechanical property of the mortar and brick. Thus, the height *h* of the REV depends on the specific materials in adhesion; the two layers involved in the damage process are often characterized by different thicknesses. Typically, a mortar layer of 1–3 mm and a brick layer of 0.5–2 mm can be considered implicated in the interface degradation. Considering the REV of interface at the point *A*, the contact surfaces do not present any detachment. The REV of interface associated to point *B* contains partial decohesion due to the presence of microcracks, so that the representative area can be split in two parts: an undamaged part and a damaged one. In the REV corresponding to point *C* the coalescence of microcracks results a total decohesion.
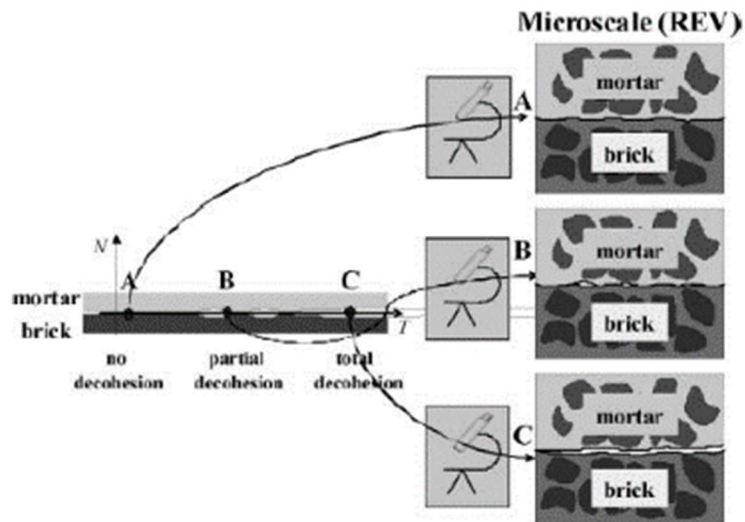
a) Micromechanical states of brick-mortar interface.
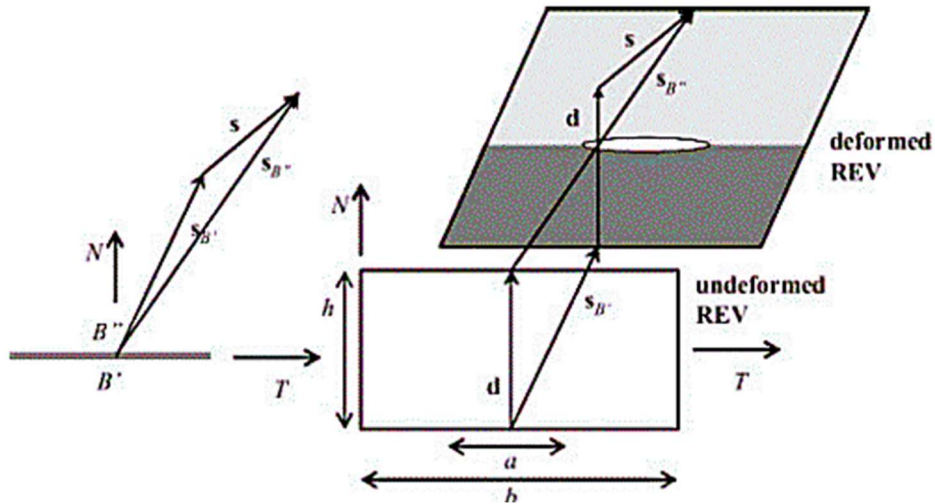
b) Kinematics of representative elementary volume.
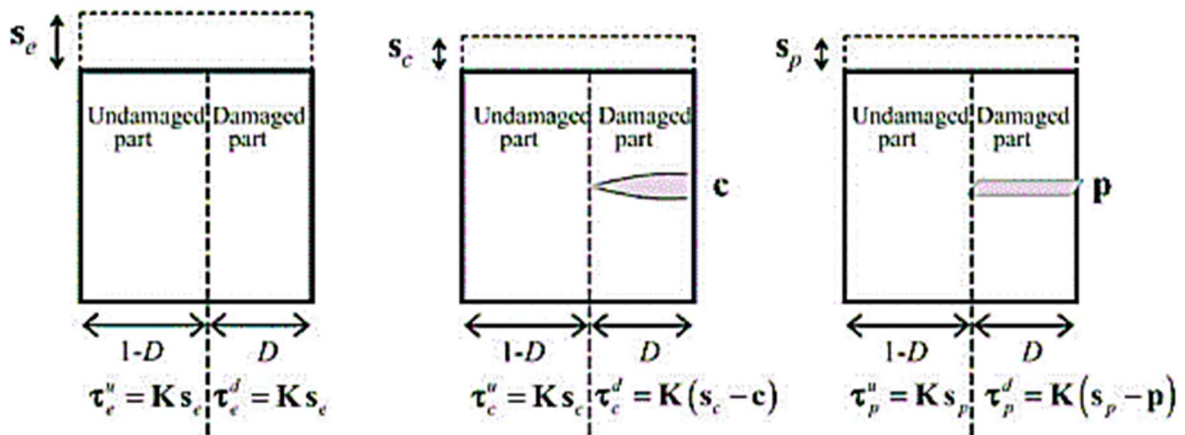
c) Micromechanical states of responses for the half of REV.

Figure - 2.40 Micromechanical Damage and Kinematics. (*Alfano and Sacco, 2006*)

Summarizing, the total area A at the brick-mortar material discontinuity in the REV, obtained as $A = b.\,w$, this area is made up of two components an undamaged part $A_u = (b{-}a).\,w$ and a completely damaged part $A_d = a.w$, such as $A = A_u + A_d$. Following standard arguments of continuous damage mechanics, the damage parameter D has been introduced as the ratio between the damaged part and the whole area:

$$D = \frac{A_d}{A} = \frac{a}{b}$$

That gives; $A_d = D.A$ and $A_u = (1\text{-}D).\,A$

Denoting with the subscripts N and T the component in the normal and tangential direction to the interface Figure - 2.40(b), respectively, the relative displacement can be written as

$$s = \{s_N + s_T\}$$

the relative displacement s contributes only the average strain components in the REV $\varepsilon_N = s_N/h$ and $\gamma_{NT} = s_T/h$.

In Figure - 2.40 (c), where only a half of the REV is reported, the overall behaviour of the REV can be obtained as the superposition of three states: the first state considers the REV subjected to a relative displacement s_e, assuming the relative displacement of the crack mouths equal to zero; in the second state, a relative displacement c at the crack mouth, able to account for the crack opening, leading to the overall relative displacement s_c; in the third state, the REV is subjected to a relative displacement p at the crack mouths, due to the frictional sliding, which induces an overall relative displacement s_p. In such a way, the overall relative displacement s is obtained as:

$$s = s_e + s_c + s_p$$

With reference to the three states illustrated in Figure - 2.40(a), the average stress vectors in the undamaged and damaged parts of the REV have been obtained as

$$\tau^u = \tau_e^u + \tau_c^u + \tau_p^u = K\,s_e + K\,s_c + K\,s_p = K\,s$$
$$\tau^d = \tau_e^d + \tau_c^d + \tau_p^d = K\,s_e + K\,(s_c - c) + K\,(s_p - p)$$
$$= K\,[s - (c + p)]$$

$$K = \begin{bmatrix} K_N & 0 \\ 0 & K_T \end{bmatrix}$$

respectively, where the inelastic displacement vector $c + p$ accounts for the uniaxial nature of the contact and for the friction phenomenon, while K is a diagonal matrix, which collects the stiffness values in the normal end tangential directions to interface.

The parameters K_N and K_T have a mechanical meaning, representing the normal and tangential overall stiffnesses of the REV, i.e. of the thin layer involved in the brick-mortar interaction.

The overall interface stress vector on the REV has been represented by τ and it is obtained by combining the two stresses τ^d and τ^u.

$$\tau = (1 - D)\tau^u + D\tau^d$$

$$= (1 - D)Ks + DK[s - (c + p)]$$

$$= K[s - D(c + p)]$$

the damage parameter D, a model which accounts for the coupling of mode I of mode II of fracture has been considered. G_{cN} and G_{cT} are the specific fracture energies, Figure 2.41, in mode I and mode II, respectively.
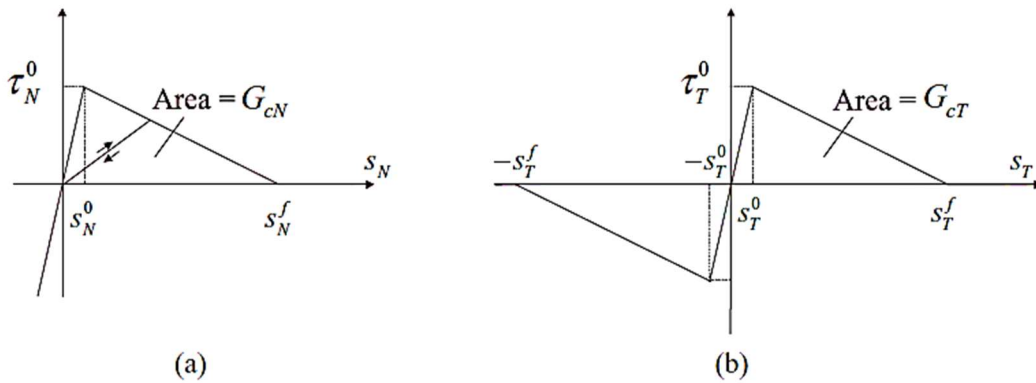
Figure - 2.41 Normal (a) and Tangential (b) Stress-displacement Relationship (*Alfano and Sacco, 2006*)

Sacco has considered the following interface properties, Table 2.3, in his numerical studies.

Table 2.3 Interface Properties (*Sacco and Toti, 2010*)

τ_N^0	G_{cN}	K_N	τ_T^0	G_{cT}	K_T	μ
(N/mm^2)	(N/mm)	(N/mm^3)	(N/mm^2)	(N/mm)	(N/mm^3)	
0.3	0.3	1500	3	0.3	750	0.5

2.10 Non-Linear Behaviour of Masonry Arch

Milani and Lourenco (*2012*) have numerically analysed the static non-linear behaviour of masonry bridges by means of a 3D FE numerical code. They have carried out the three-dimensional behaviour of the structures subjected to eccentric loads, the actual

3D geometry of the bridges, particularly important for skew arches, and the strengthening effect induced by the backfill.

It is known that the masonry material behaviour is elastic, plastic and nonlinear. The limit analysis remains the most common approach for estimating the load carrying capacity of the structure. The limit analysis (*Pippard, 1948*) starts from a two-hinge arch. Aim is to determine the minimum load applied to a fixed position, that results to a mechanism constituted by four hinges. The exact positions of the two plastic hinges are the variables determined by the analysis. Pippard's approach has been further extended by Heyman (*1982*) introducing thrust-lines. The procedure has been considered quite easy to understand and handled without complex computational assistance. The thrust line concept fits well with experimental data for simple arches without backfill and under specific loading conditions.

Later works (*Gilbert, Melbourn 1994; Hughes and Blacker 1997; Boothby 1995*) have been based on limit analysis on rigid block discretisation of the arches within finite element. Cavicchi and Gambarotta (*2005*, *2006*) have presented a powerful tool for 2D bridges by using plane-strain rigid-plastic elements and interfaces to investigate the load distribution through backfill.

The code developed by Milani and Lourenco (*2012*) discretise the 3D domain by means of rigid eight-node elements interconnected by non-linear interfaces. The arch has been modelled by means of a macroscopic approach but respecting in the front view the actual disposition of the blocks, to have a more precise evaluation of the position of the plastic hinges forming the failure mechanism. To solve the non-linear structural analysis problem, a Sequential Quadratic Programming procedure with a discretization by means of eight-node rigid elements and non-linear interfaces, Figure - 2.42, like that proposed in Cecchi (*Cecchi et al.2008*) and Milani (*Milani, Tralli, 2011*) was adopted.
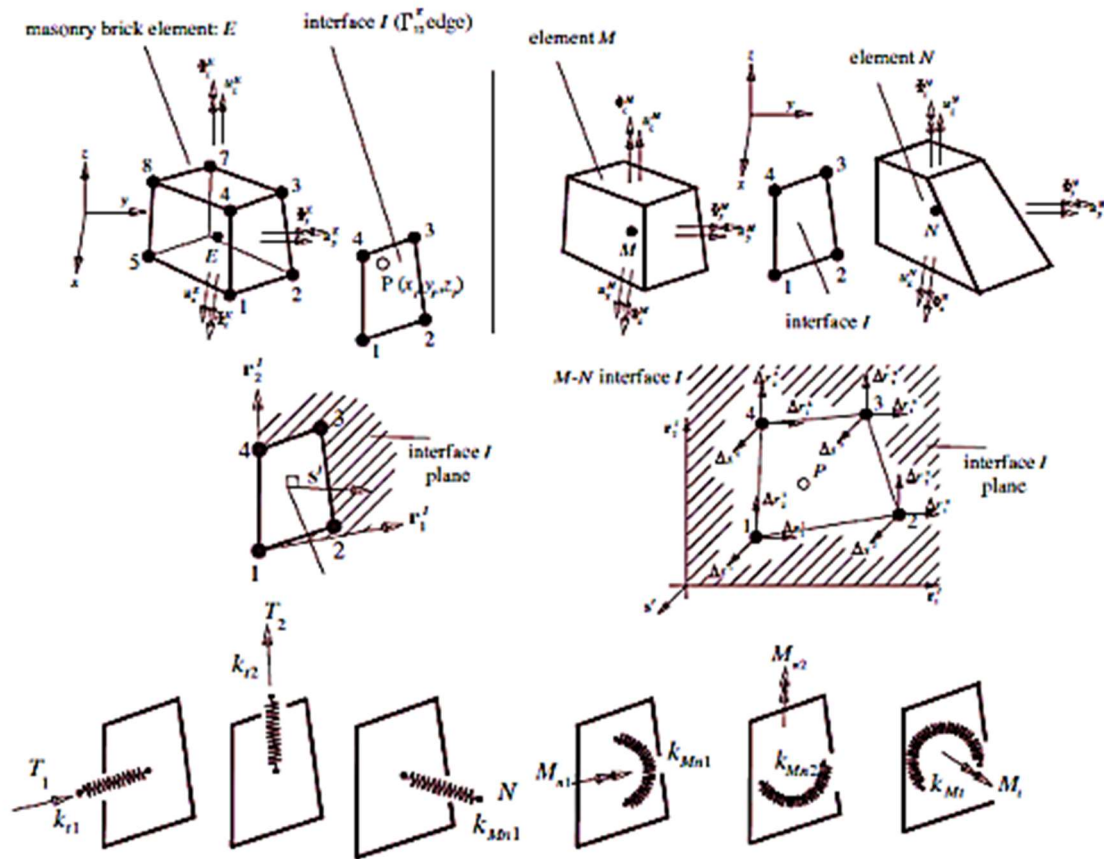
Figure - 2.42 Rigid 8-node Elements and Kinematics of Interfaces Between Contiguous Elements. (*Cecchi et al.2008*)

Following approaches noted.

1. Joints have been reduced to interfaces and exhibit an elastoplastic behaviour with softening, Figure - 2.42. The Representative Element of Volume (REV) has been discretized by means of non-linear interfaces (joints) and elastic three-node triangles (bricks). An estimation of the in-plane homogenized behaviour to be used at a structural level has been obtained suitably solving an incremental boundary value problem on the REV. The choice of a REV which geometrically correctly represents the actual disposition of the blocks (also along the thickness) is crucial for the numerical analyses reported hereafter. It is possible to map the superficial geometry of the structure under consideration with very high accuracy by means of photogrammetric surveys, making use of the modern digital technology. It is also possible to interface data acquired by means of laser scanner surveys to the structural code. However, for old masonry structures, the actual disposition of the blocks along the thickness remains unknown. Anyway, for the cases under consideration, sections and planar views of the structures are directly available. In absence of such data, the matter persists, and experimental tests should be

performed to have an estimation of the actual disposition of the blocks along the thickness.

2. At the structural level bridges have been discretized by means of parallelepiped rigid elements and quadrilateral elasto-plastic with softening interfaces where all deformation occurs, refer Figure - 2.42.

3. Each interface has been interconnected with adjoining elements by means of three non-linear displacement and three non-linear rotational springs.

4. The non-linear uniaxial behaviour of the displacement springs has been derived directly using the constitutive behaviour, Figure - 2.43, for the backfill and the mortar joints belonging to the arch, when it is chosen to adopt a heterogeneous approach to model the arch. Bending and torsional behaviours have been derived from displacement springs by means of a specific integration procedure.
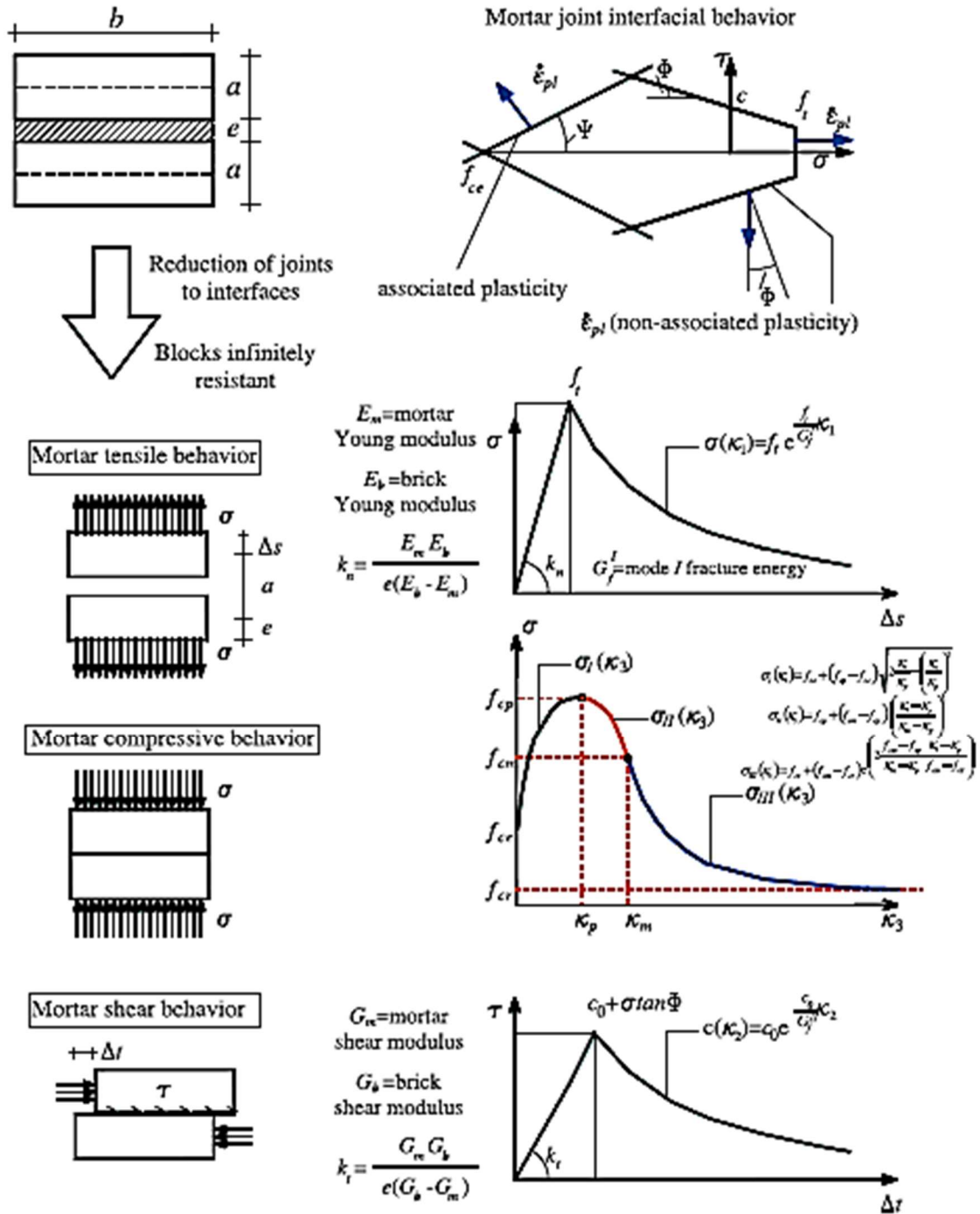
Figure - 2.43 Mortar Joints Non-Linear Behaviour. (*Cecchi et al.2008*)

2.10.1 Discretisation with Rigid Element and Non-Linear Interfaces

The discretisation has been carried out through 3D rigid infinitely resistant eight-node elements interacting by quadrilateral nonlinear interfaces exhibiting softening. Any shape of the parallelepipeds can be managed, ideally trapezoidal hexahedra can be used, i.e. also distorted meshes may be handled in the code, as commonly done in commercial software.

Within these assumptions, all deformation (linear and non-linear part) has been concentrated exclusively at interfaces (modelled assuming an isotropic frictional material. as for the backfill, or by means of a homogenized orthotropic material as in case of spandrels), thus requiring a small number of optimization variables for analysis.

In their work, Milani and Lourenco (*2012*) have modelled masonry arches behaviour in the nonlinear range, the semi-circular arch, geometry shown in Figure - 2.44a. This has been earlier analysed by Orduna (*2005*) by means of both a limit analysis approach with non-associated plasticity and by means of standard commercial FEM. The arch constructed by 30 large stone blocks of dimensions 30x 10 cm^2 and dry joints. The dry joint interfaces have been modelled with a small but non-zero tensile strength, which well approximates a material unable to withstand tensile stresses, eventually exhibiting a friction behaviour. The geometrical dimensions of the arch been shown in the Figure - 2.44a. The arch under consideration has a span S equal to 5 m, a rise R equal to 2.5 m, is 30 cm thick and 1 m wide. Assuming that the arch is subjected to a permanent load *p* not dependent on the load multiplier equal to 35 kN/m^3, a concentrated point load k increased up to failure is applied at quarter span.
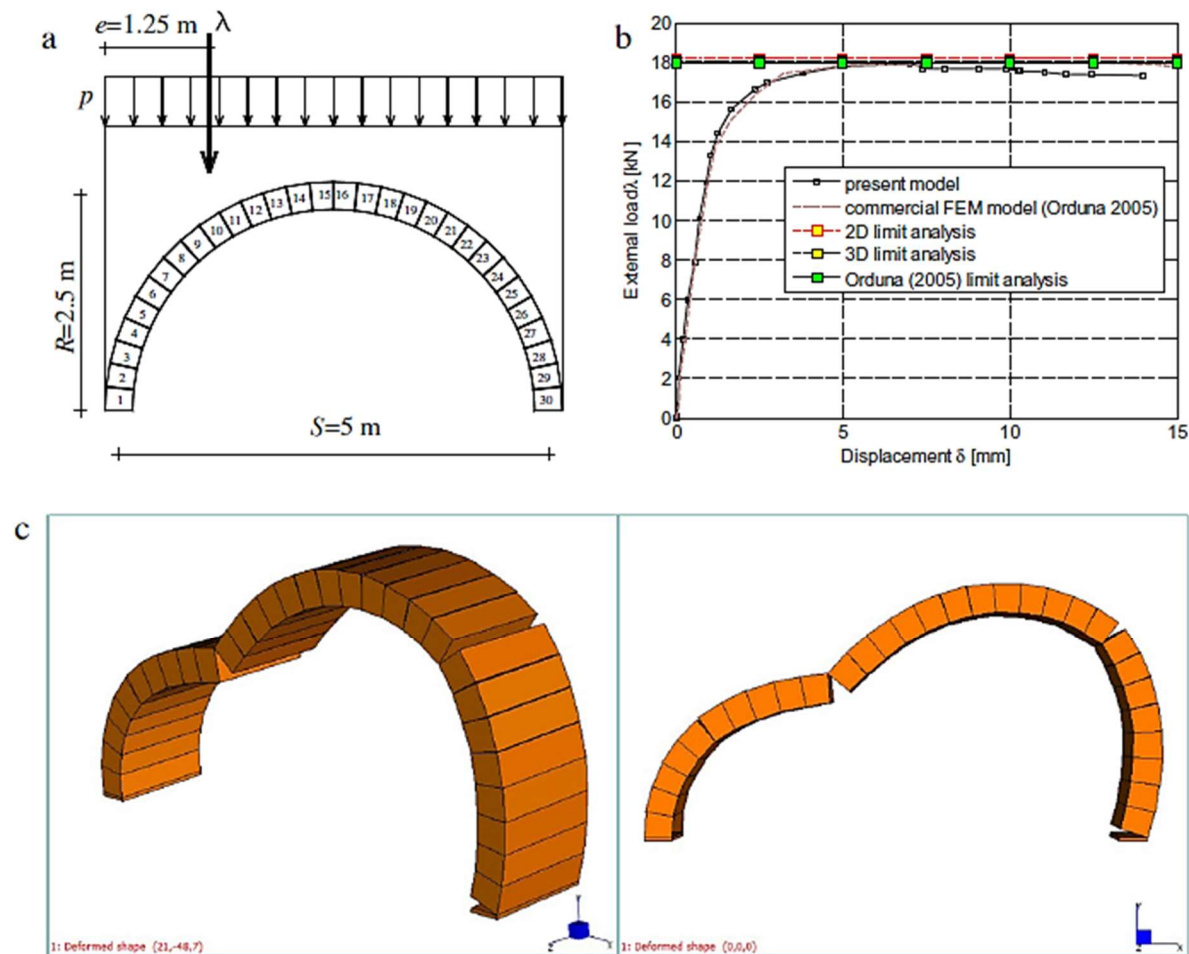
Figure - 2.44 Semi-circular Arch Analysis. (*Orduna, 2005*)

The arch has been modelled by a heterogeneous approach with rigid and infinitely resistant blocks meshed with parallelepiped interface elements. Mechanical properties assumed in the numerical simulations for dry joints are following: K_N = 2400 N/mm^3 (normal stiffness of the mortar interface), K_T= 1000 N/mm^3 (tangential stiffness of the interface), tanϕ = 0.75 (tangent of the friction angle for mortar), infinite blocks compressive strength.

They have further continued their work to verify the skew arch experimentally tested by Melbourne and Hodgson (*1994*), and a five-ring existing railway arch bridge, located in the south Italy. For the first bridge, a vertical eccentric load has been applied up to collapse and the behaviour of the bridge has been evaluated by means of the non-linear FE model proposed.

Milani and Lourenco (*2012*) provided compressive list of mechanical properties, in agreement with experimental data provided by Melbourne et al (Wang and Melbourne, 1996, Melbourne and Hodgson, 1996), for masonry and backfill, those are summarized in Table 2.4.

The Milani and Lourenco (*2012*) software offered suitable analysis of massive existing masonry arch bridges, because specifically conceived for handling such kind of structures. By carrying out the preliminary homogenization procedure before structural analyses, a more precise characterization of the masonry material has been possible at a structural level, with independent modelling of tension and compression behaviour and possibility to account for masonry orthotropy in presence of different textures.

Table 2.4 Bolton Institute Bridges. Mechanical Properties of Masonry and Backfill Milani and Lourenco (*2012*)

Masonry interfaces				
E	18,000		[MPa]	Young modulus
G	E/2		[MPa]	Shear modulus
c	1.0 f_t		[MPa]	Cohesion
f_t	0.30		[MPa]	Tensile strength
f_{ce}	$1/3 f_{cp}$	–	[MPa]	Compressive hardening/softening behavior
f_{cp}	28		[MPa]	
f_{cm}	$1/2 f_{cp}$	–	[MPa]	
f_{cr}	$1/7 f_{cp}$	–	[MPa]	
κ_p	0.09	–	[–]	
κ_m	0.49	–	[–]	
Φ	37	45	[°]	Friction angle
Y	45	–	[°]	Angle of the linearized compressive cap
G_f^I	0.010	10	[N/mm]	Mode I fracture energy
G_f^{II}	0.0050	10	[N/mm]	Mode II fracture energy
Backfill				
E	3200		[MPa]	Young modulus
G	E/2		[MPa]	Shear modulus
c	1.0 f_t		[MPa]	Cohesion
f_t	0.05		[MPa]	Tensile strength
f_{ce}	$1/3 f_{cp}$	–	[MPa]	Compressive hardening/softening behavior
f_{cp}	2.6	–	[MPa]	
f_{cm}	$1/2 f_{cp}$	–	[MPa]	
f_{cr}	$1/7 f_{cp}$	–	[MPa]	
κ_p	0.09	–	[–]	
κ_m	0.49	–	[–]	
Φ	37	45	[°]	Friction angle
Y	45	–	[°]	Angle of the linearized compressive cap
G_f^I	0.010	10	[N/mm]	Mode I fracture energy
G_f^{II}	0.0050	10	[N/mm]	Mode II fracture energy

2.10.2 Discretisation with Linear Elastic Element and Non-Linear Interfaces

Sacco (*Sacco, Toti, 2010*) have applied finite element modelling with a linear or nonlinear material model for the brick units, mortar joints and the developed interface elements for the contact zones. A micromechanical approach has been assumed for modelling the masonry arch. In fact, the clay bricks and the mortar joints have been modelled by four nodes quadrilateral elements, and the mortar-brick interface and the brick-arch support interface by the developed four node interface elements.
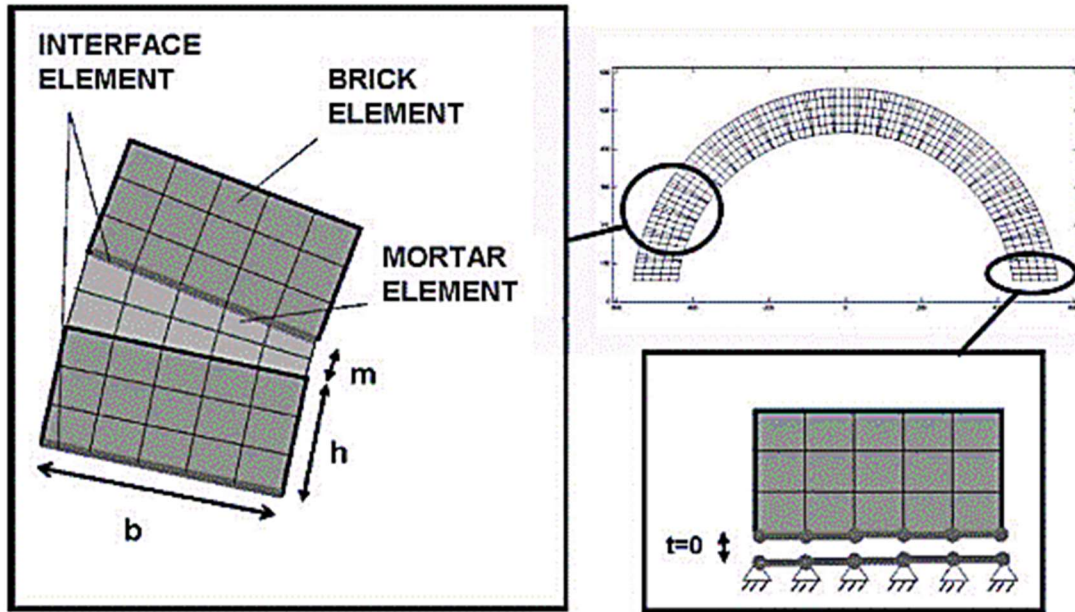
Figure - 2.45 Finite Element Mesh and Constraints. (*Cancelliere et al. 2010*)

Experimental evidence has shown that the decohesion phenomenon between a mortar joint and two adjacent bricks has been activated mainly on only one of the two interfaces. For this reason and to simplify the finite element model of the arch, only one nonlinear interface has been considered for each mortar bed. Figure - 2.45 & 2.47 illustrates the geometric model of the arch, and Figure - 2.46 shows the four-hinge formation during the test. The opening of the joints has demonstrated single sided decohesion. Hence Sacco (*Sacco, Toti, 2010*) has applied the interface elements on only one of the two surfaces joining the mortar with the bricks, while a perfect mortar-brick adhesion has been assumed for the other surface.
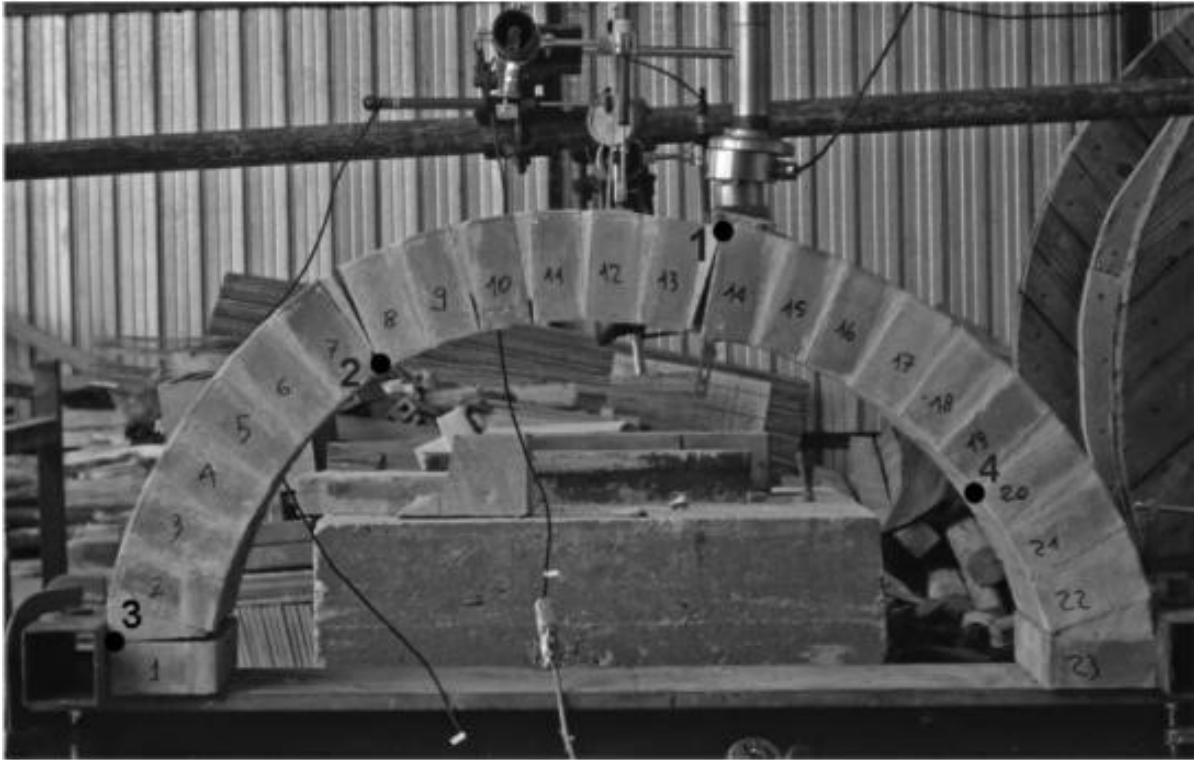
Figure - 2.46 Collapse Mechanism Developed by The Unreinforced Arch and Position of The Four Hinges. (*Cancelliere et al. 2010*)
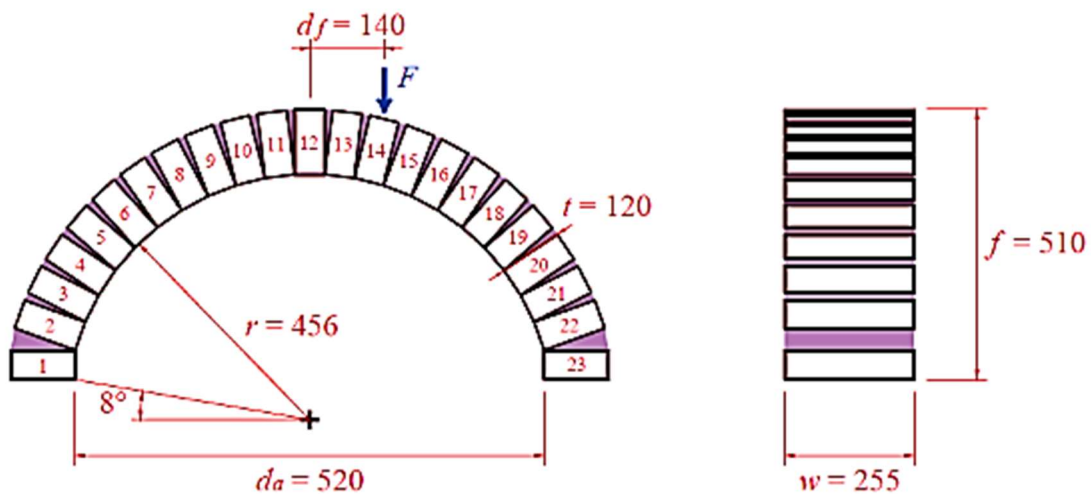
Figure - 2.47 Geometry of The Arch. (*Addessi et al. 2017*)

Sacco has compared his numerical analysis with the experimental results, obtained from a previous experimental test carried out by Cancelliere et al. (*2010*). The geometrical dimensions of the semi-circular arch have been shown in Figure - 2.46. The experimental test of the unreinforced masonry arch showed that the first hinge formed on the extrados between the mortar number 13 and the clay brick number 14,

the second hinge formed on the intrados between the mortar number 7 and the clay brick number 8, the third hinge formed between the extrados between the mortar number 1 and the clay brick number 1, and the fourth hinge formed on the intrados between the mortar number 19 and the clay brick number 19 (Figure - 2.46).

Sacco (*Sacco, Toti, 2010*) has modelled the arch using quadrilateral elements for the mortar and bricks and four-node interface elements for the mortar brick interface. A plane stress two-dimensional analyses has been performed. The mechanical properties see Table - 2.5 of the brick and mortar have been taken from test conducted by Cancelliere et al. (*2010*).

Table 2.5 Material Parameters for The Bricks and Mortar of The Circular Arch.

Brick	Mortar
E_b = 16000 (N/mm^2)	E_m = 1500 (N/mm^2)
v_b = 0.20	v_m = 0.20
f_b = 31.1 (N/mm^2)	f_m = 8.8 (N/mm^2)
	G_{cl} = 0.0003 (N/mm^2)
	μ = 0.50

Sacco (*Sacco, Toti, 2010*) has noted that the linear elastic model can be adopted to simulate the masonry behaviour of the unreinforced arch. This is because the collapse mechanism for unreinforced arch has been observed mainly governed by the unilateral behaviour of the mortar-brick interface, while no material failure due to compressive stresses has been noted during the experimental tests. The mechanical properties considered for the interface elements have been tabulated in the Table 2.3.

The normal and shear stiffnesses have been determined homogenizing the composite material obtained considering two thin layers of brick and mortar:

$$K_N = \frac{E_b E_m}{h_b h_m \left(\frac{E_b}{h_b} + \frac{E_m}{h_m} \right)}$$

and

$$K_T = \frac{G_b G_m}{h_b h_m \left(\frac{G_b}{h_b} + \frac{G_m}{h_m} \right)}$$

where E_b, G_b and E_m, G_m are the normal and shear moduli of the brick and mortar, respectively.

Sacco (*Sacco, Toti, 2010*) has performed his analysis for range of interface parameters to verify the interface response and the behaviour of the arch. He has confirmed that the variation of the overall response of the arch as a function of the contact stiffnesses are insignificant, whereas the deformation of the structure depends mainly on the elasticity of the masonry. This work has shown particularly good response between the numerical prediction with the experimental data.

2.11 Fatigue Modelling of Masonry Arch

Tomor (*2013*) has demonstrated the practical application of SN curves, examples for stress levels and associated life expectancy, Table 2.6, based on the Casas model (*2011*).

Table 2.6 Examples of Approximate Life Expectancy Based on The Model by Casas (10% minimum stress).

Compression			Shear		
Stress	Life Expectancy		Stress	Life Expectancy	
%	Cycles	Ratio	%	Cycles	Ratio
45	8×10^9	$35^{\#}$	45	1×10^8	$18^{\#}$
50	2×10^8	1	50	7×10^6	1
55	1×10^7	1/20	55	6×10^5	1/12

- Author has noted discrepancies in the multipliers. Should read as 40 and 14 respectively.

Under compression, the life expectancy for 50% average stress level is around 2×10^8 cycles. If the stress level is reduced 5% (from 50% to 45%), the life expectancy increases 35 times (from 2×10^8 to 8×10^9). If the stress level is increased 5% (from 50% to 55%), the life expectancy reduces to around 1/20 (from 2×10^8 to 1×10^7). Similarly, under shear if the stress level is reduced from 50% to 45%, the life expectancy increases 18 times (from 7×10^6 to 1×10^8) and if the stress level is increased from 50% to 55%, the life expectancy reduces to around 1/12 (from 7×10^6 to 6×10^5).

The SMART method has proposed a methodology for estimating the life expectancy for masonry arch bridges. The corresponding life expectancy at a stress level has been estimated, from a known SN curve. The permissible limit state has been used as a safe limit below which no deterioration would occur for the expected lifetime of the structure, 120 years. Considering a constant 24/7 loading at 2 Hz, the maximum number of vehicles/ axles over the bridge would be up to ca. 2×10^{10}. The associated stress using Casas (*2010*) model for compression and shear has been calculated to be 43% and 38% of the average static strength respectively. Therefore, it has been

considered that if the fatigue stress level is below the respective 43% and 38%, no failure would occur during the lifetime of the bridge and could be classified as a safe limit.

Laterza et al. (*2016*) have shown that apart from the ultimate carrying capacity, the cyclic service loads also induce non-acceptable damages to masonry elements reducing the service life of the bridge. He has applied the methods published in literatures for assessing the masonry fatigue strength to an old Italian multi-span masonry arch road bridge, still in service. The Cavone Bridge, Figure – 2.48, located in the South of Italy has total length of about 140 m and a width of 5,6 m, with a series of brick masonry arches. The bridge has four secondary arches of 10 m span length with a barrel thickness of 0,7 m, and three main arches of 22,0 m span length with 1,15 m of barrel thickness.

In their analysis Laterza et al. (*2016*) has considered the *Fatigue Load Model 3* in accordance with Eurocode1 (*EC1-2, 2003*) for assessing the fatigue life. Each axle of load fatigue model is equal to 120 kN. Has been suggested appropriate for typical heavy traffic on European main roads or motorways.

Figure - 2.49 shows the loads acting on each voussoir: the selfweight P_M, the weights of the overhanging backfill P_F, and load P_Q due to the traffic. W_{axle} is the load of each axle, B is the bridge width, and L is the length of the spreading area. The numerical model of arches has considered the horizontal passive pressure, lumped at each joint of the arch by means of the force $P_a = k_p , P_F, \tan\alpha$, where k_p is the passive fill pressure coefficient set equal to 0,5 and α is the angle formed between the P_a direction and the arch straight line as described in Figure - 2.49. The stress range $\Delta\sigma_i$ due to the *Fatigue Load Model 3* has been evaluated starting from the permanent load condition (self-weight of all elements) by considering the most unfavourable position of the moving load in terms of compressive stresses.

In the absence of any fatigue assessment for Masonry to this date, Laterza et al. (*2016*) has followed the EC3-1-9 (*2003*) procedures. According to EC3, the stress range $\Delta\sigma_i$ resulting from the transit of the fatigue load model along the arch has been amplified by γ_{Ff} equal to 1.35, while the fatigue strength has been divided by γ_{Mf} equal to 1.0, for obtaining from the factored stress-life curve. Considering two different compressive strength based on the knowledge level (KL) The assumed mean value of masonry compressive strength for KL1 and KL3 2.4 and 3.2 N/mm^2 has been considered, respectively, see Table - 2.7. The strengths have also been reduced by confidence factors 1.35 for KL1, and 1 in the case of KL3.
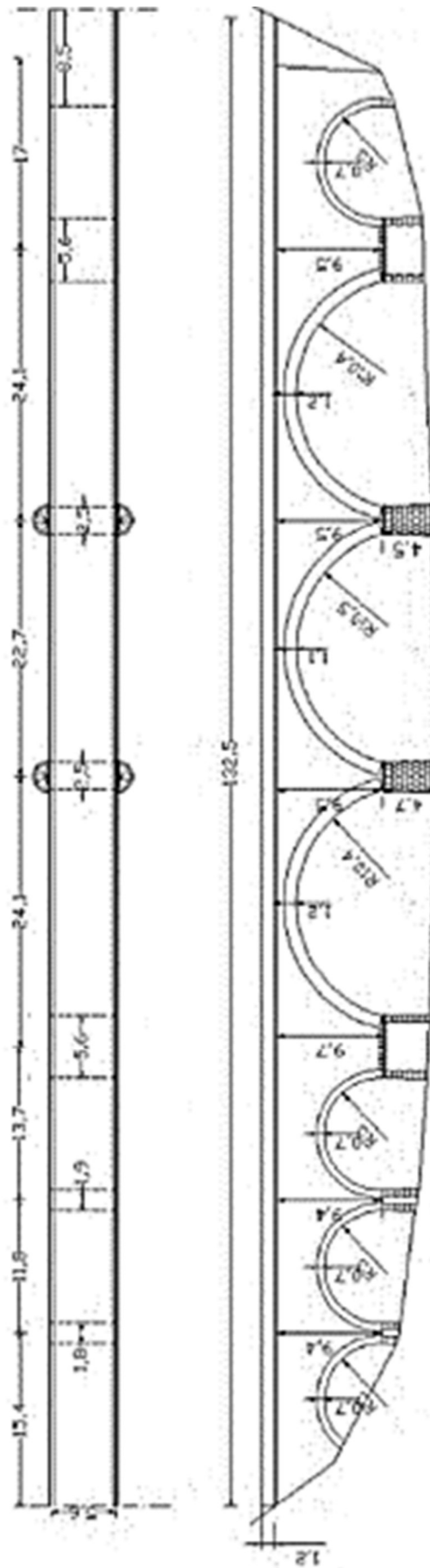
Figure - 2.48 Cavone Bridge Geometry. (*Laterza et al. 2016*)
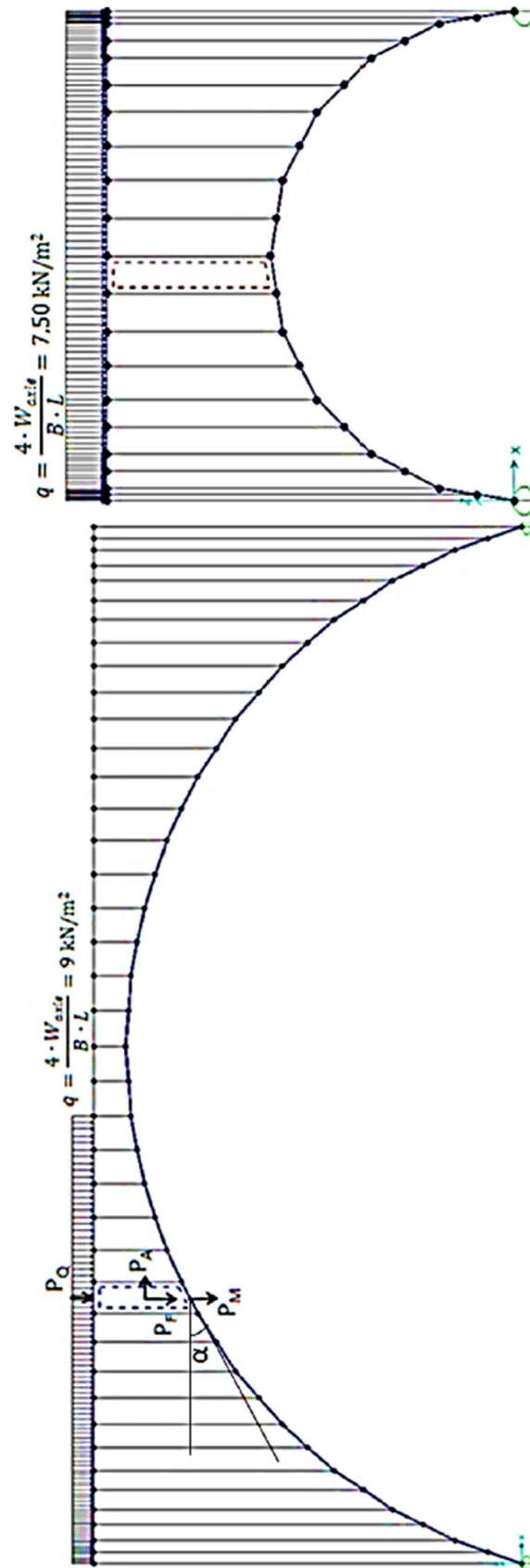
Figure - 2.49 Cavone Bridge Load Diagram. (*Laterza et al. 2016*)

Table 2.7 Stresses Calculated for The Main and the Secondary Arches.

	Main Arch		Secondary Arch	
Induced Stress	KL1=2.4/1.35	KL3=3.2	KL1=2.4/1.35	KL3=3.2
S_u (N/mm^2)	1.778	3.200	1.778	3.200
S_{max} (N/mm^2)	1.405	1.405	0.878	0.878
S_{min} (N/mm^2)	1.220	1.220	0.766	0.766
$R = S_{min}/S_{max}$	0.868	0.868	0.872	0.872
$S = S_{max}/S_u$	0.790	0.439	0.494	0.275

Using the fatigue curves proposed by Roberts et al. (*2006*), Casas (*2009*) and Ronca et al. (*2004*) and the respectively factored curves, Figure 2.50, for the main and secondary arch, Laterza et al. (*2016*) has concluded that in case of the secondary arch the S_{max}/S_u ratios on the most stressed sections is always less than the value 0.5 has been indicated as endurance limit. In this case the residual life under cyclic loading can be assumed infinite since the number of load cycles N related to the fatigue failure are greater than 10^9, and consequently, the residual service life results greater than 2000 years (the assumed number N_{obs} of heavy vehicles passing on the bridge is 0.5 x 10^6). For the main arch in the case of KL1, an exceptionally low residual life has been obtained by all three fatigue models.
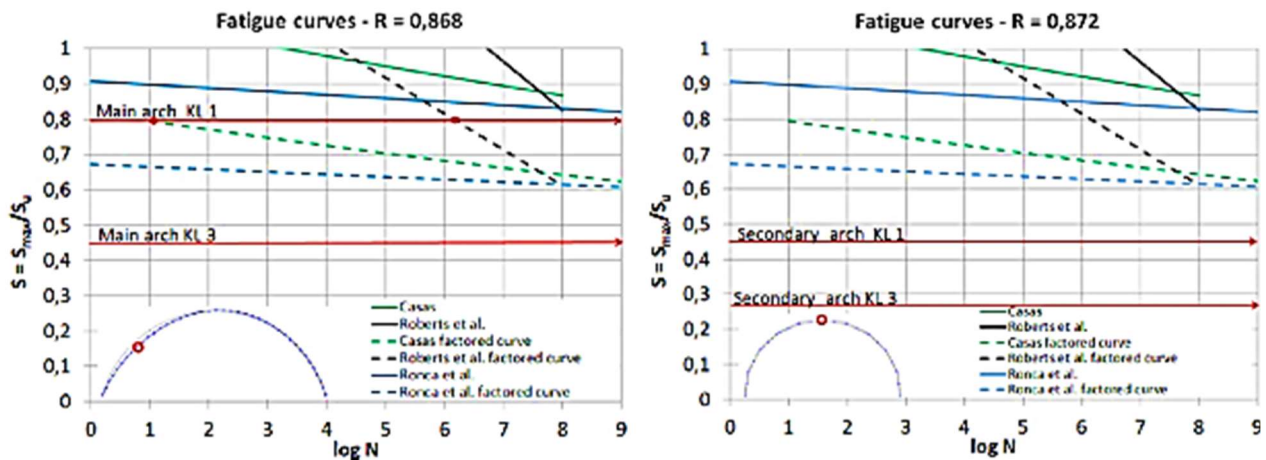
Figure - 2.50 Cavone Bridge Stress-life. (*Laterza et al. 2016*)

2.12 ANSYS Workbench Fatigue Domain

Fatigue has been defined by the weakness in materials caused by repeated variations of stress leading to the initiation and subsequent growth of a crack, or growth from a pre-existing defect until it reaches a critical size. Arches have been originally designed by their static failure stress due to largely monotonic or quasi static increasing loading. Fatigue cracks are caused by cyclic loading, the loading may not change. Material or part can fail even if the stresses are not high enough compared to ultimate stress.

A simple representation of constant amplitude cyclic loading is illustrated by means of sine-curve in Figure – 2.51 (*Al Hancq 2006*). Definitions of different cyclic loading terms are explained in Table - 2.8.
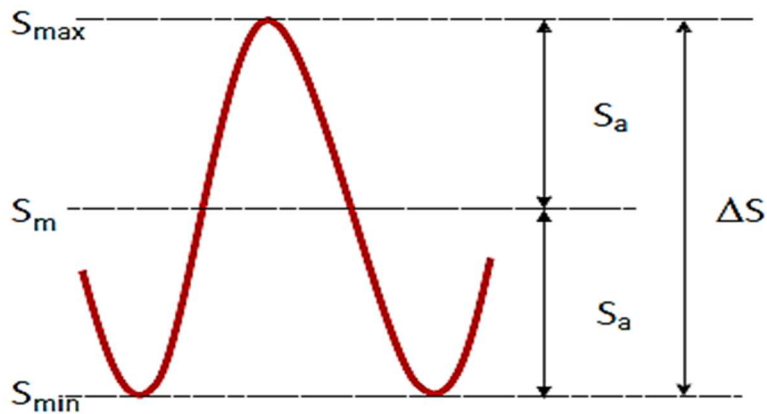
Figure - 2.51 Cyclic Loading Terms.

Where,
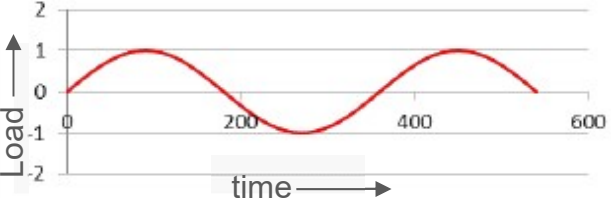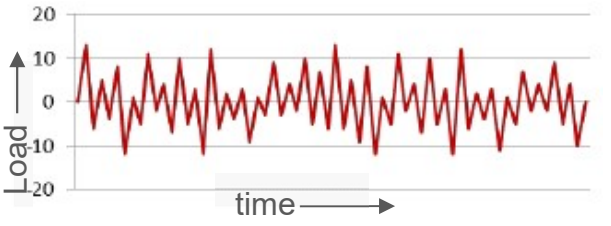
S_{max} = maximum stress
S_{min} = minimum stress
S_m = mean stress
S_a = alternating stress
ΔS = stress range
Stress ration R = S_{max}/S_{min}
Amplitude ration A = S_a/S_m

For some common types of loading,

Fully reversed, R = -1, A = infinity
Zero to Maximum, R = 0, A = 1

Fatigue cycles are defined by the change of stress or strain.

Table 2.8 Cyclic Load Definitions

Proportional loading	- Load direction is always in the same plane. i.e., tension/compression, principal surface stress axes do not change with time.
Non-proportional loading	- Load direction changes with time. i.e., complex combination of different types and magnitude of load acting at the same time, principal surface stress axes do change with time.
Constant amplitude	- Magnitude of individual load is constant with time
Variable amplitude	- Magnitude of individual load varies with time
For this thesis Rain-flow Cycle counting is not considered	

Within the ANSYS fatigue module, the first decision that needs to be made in performing a fatigue analysis is which type of fatigue analysis to perform – Stress Life or Strain Life. Stress Life is based on empirical S-N curves and then modified by a variety of factors (*Roberts et al. 2006*), (*Casas 2009*) and (*Ronca et al. 2004*). Stain Life is based upon the Strain Life relation equation where the Strain Life Parameters are values for a particular material that best fit the equation to measured results. The Strain Life Relation requires a total of 6 parameters to define the strain-life material properties: four strain-life parameter properties and the two cyclic stress-strain parameters.

The first assumption is that the unknown ε-N curve, Figure – 2.52 is reasonably represented by a straight line in logarithmic scale this straight-line elastic behaviour can be transformed to Basquin's equation:

$$\Delta\varepsilon/2 = (\sigma'_f\,/E)\,(2N_f)^{\,b} \qquad\qquad (eq.2.11.1)$$

where N_f is the number of cycles to failure, σ'_f is the ultimate stress of the material. and b is the straight-line slope. Cyclic tests for steel and aluminium are typically continued to 3×10^6 cycles to determine the slope parameter b. This assumption simplifies the process since the number of parameters to be determined is now reduced to just two: σ'_f and b. The ultimate stress of the material. σ'_f, may be obtained from a series of static tests. Several specimens are statically loaded up to failure to determine a meaningful ultimate stress average σ_f. For existing in-situ arches ultimate strength and Young's modulus can be determined by performing laboratory tests on core samples obtained from site investigation.
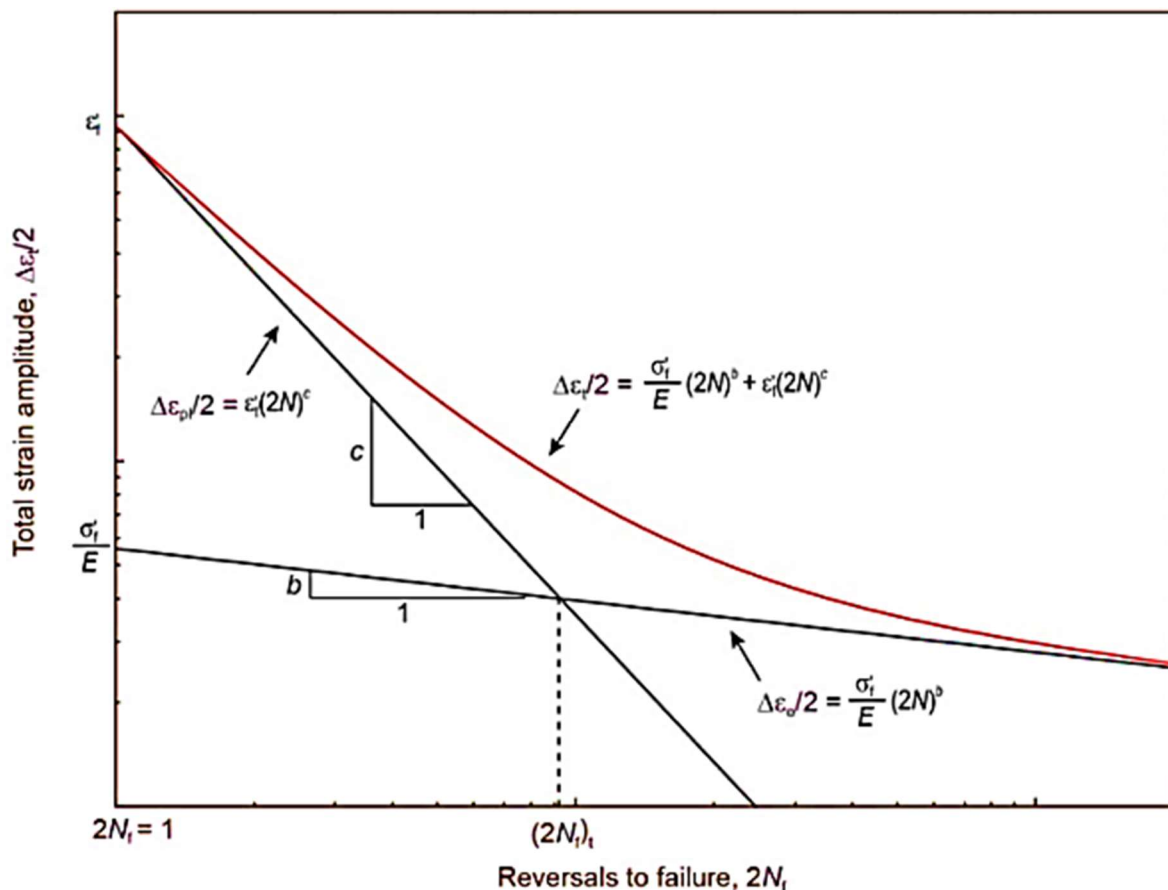
Figure - 2.52 Fatigue Failure as a Function of Strain Amplitude.

The Manson-Coffin-Morrow is a mathematical model relating total strain and cycles to failure. The total strain amplitude (red) is equal to the sum of elastic strain (slope 1:b) and the plastic strain (slope 1:c) terms. Plastic strain behaviour dominates at low cycle

counts with high amplitude strain cycles. Elastic strain dominates at high cycle counts with low amplitude strain cycles.

The relation between plastic strain and life is (Manson-Coffin relationship):

$$\Delta\varepsilon_p/2 = \varepsilon'_f \, (2N_f)^c \qquad\qquad\qquad (eq.2.11.2)$$

Therefore:

$$\frac{\Delta\varepsilon}{2} = \varepsilon_a = \frac{\Delta\varepsilon_e}{2} + \frac{\Delta\varepsilon_p}{2} = \frac{\sigma'_f}{E}\left(2N_f\right)^b + \varepsilon'_f\left(2N_f\right)^c$$

Where:
$\Delta\varepsilon/2 = \varepsilon_a$	= total strain amplitude,
$\Delta\varepsilon_e/2$	= elastic strain amplitude = $\Delta\sigma/2E = \sigma_a/E$, see Figure --2.51
$\Delta\varepsilon_p/2$	= $\Delta\varepsilon/2 - \Delta\varepsilon_e/2$ = plastic strain amplitude, see Figure --2.51
ε_f'	= fatigue ductility coefficient
c	= fatigue ductility exponent
σ_f'	= fatigue strength coefficient
b	= fatigue strength exponent
E	= modulus of elasticity
$\Delta\sigma/2 = \sigma_a$	= stress amplitude

2.12.1 Mean Stress Corrections for Strain Life

For Strain Life, the ANSYS Fatigue Module has a variety of mean stress correction methods including no mean stress effects, Morrow and Smith-Watson-Topper (*Al Hancq, 2006*).
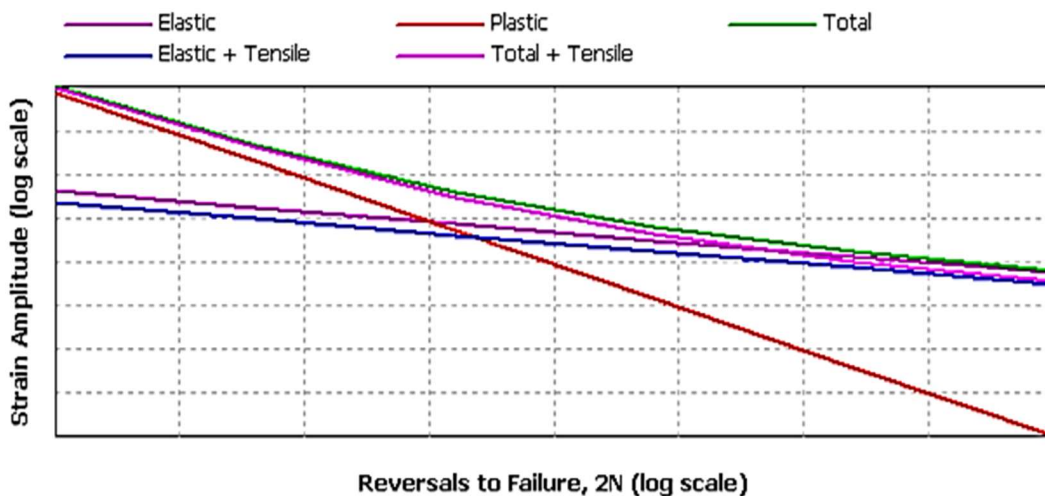
Figure - 2.53 Strain Life Accounting for Morrow Mean Stress Correction (*Al Hancq 2006*).

In Morrow's method, Figure - 2.53, the elastic term in the strain-life equation is modified by the mean stress. This modification is consistent with observations that the mean stress effects are significant at low values of plastic strain, where elastic strain dominates, and that mean stress has little effect at shorter life, where plastic strains dominate. Unfortunately, it incorrectly predicts that the ratio of elastic to plastic strain is dependent on mean stress, which is not true.
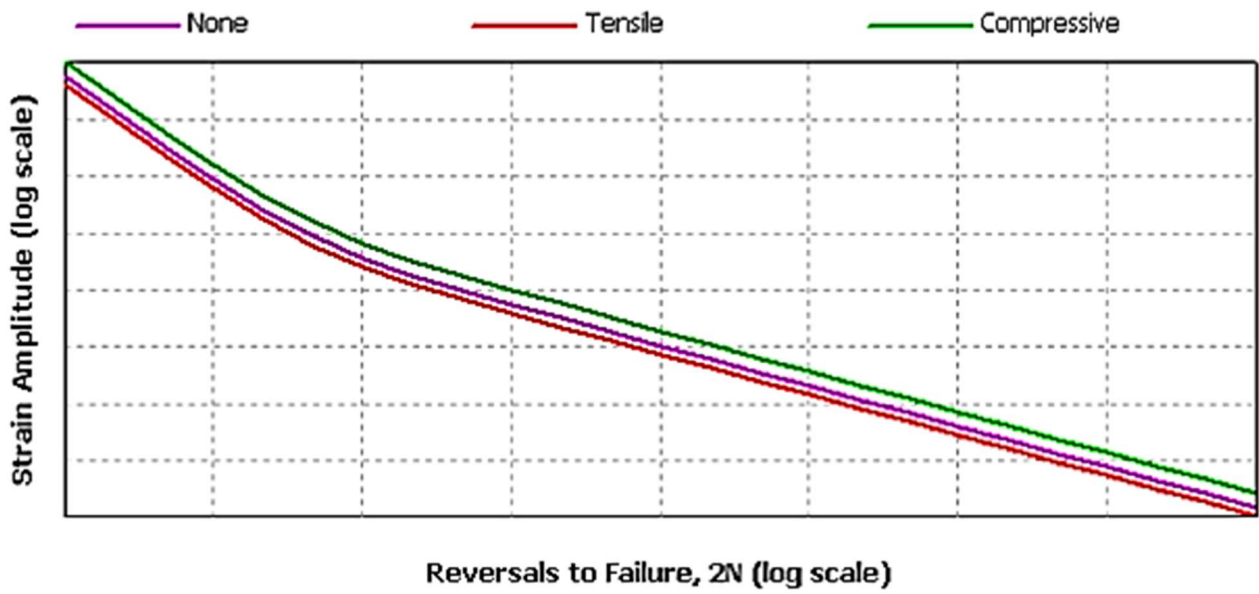
Figure - 2.54 Strain Life Accounting for Smith, Watson and Topper Mean Stress Correction (*Al Hancq 2006).*

Smith, Watson and Topper *(Al Hancq, 2006)* have suggested a different equation, Figure – 2.54, to account for the presence of mean stresses. It has the limitation that it is undefined for negative maximum stresses. The physical interpretation of this is that no fatigue damage occurs unless tension is present at some point during the loading.

2.12.2 Multiaxial Stress Correction Factors

Experimental test data is mostly uniaxial whereas FE results are usually multiaxial. At some point, stress must be converted from a multiaxial stress state to a uniaxial one. Von-Mises, max shear, maximum principal stress, or any of the component stresses can be used to compare against the experimental uniaxial stress value. A "signed" Von-Mises stress may be chosen where the Von-Mises stress takes the sign of the largest absolute principal stress. This is useful to identify any compressive mean stresses since several of the mean stress theories treat positive and negative mean stresses differently.

2.13 Summary

More recently, FDEM, by combining fracture mechanics with FEM and DEM, has emerged as an appealing alternative numerical tool for Brick masonry applications where an explicit consideration of fracture and fragmentation processes is of paramount importance under cyclic and dynamic nature of loading.

The comparison between the numerical results obtained by the FDEM method and the available experimental results shows high accuracy in predicting the behaviour of block-mortar connection and masonry prisms under monotonic and cyclic loads (*Smoljanović et al., 2015*). The performance of the numerical model investigated two masonry walls. The numerical results show that the presented model can capture the main features that characterize the behaviour of masonry shear walls under monotonic increasing and cyclic loading. The advantage of the presented model is its ability to simulate the behaviour of the masonry structure through the entire failure mechanism from the continuum to the discontinuum.

Simplified micro modelling has been adopted for this study. In this approach, each joint, consisting of mortar and the two unit-mortar interfaces has been lumped into an "average" interface while the units are expanded in order to keep the geometry unchanged. Masonry is thus considered as a set of elastic blocks bonded by potential fracture/slip lines at the joints. Accuracy is lost since Poisson's effect of the mortar is not included. This problem is compensated by FDEM modelling where each Masonry elements are considered deformable instead of rigid (as in DEM approach).

Based on the above literature, past works and availability of software to employ for the proposed work which is relevant to the use of the outcomes of this project by practising designers, this thesis has adopted ANSYS Contact Element based approach for the numerical modelling.

For this research FDEM approach using ANSYS is preferred due to:

1. Brick masonry arch requires a high number of individual particles modelling for bricks and infill. FDEM approach will simplify modelling without compromising the discrete element (DE) advantages.

2. The numerical model of an interface element considers failure and softening in tension and shear, increasing of fracture energy in shear due to increasing pre-compression stress, decreasing friction coefficient due to increasing shear displacement as well as the cyclic behaviour in an interface element.

3. The ability of the FDEM model to capture the main features related to tensile and shear behaviour of joints under cyclic loading (*Smoljanović et al., 2015*) is the principal criteria for selection and considered appropriate application for studying

the fatigue behaviour of brick masonry arch bridges. ANSYS Fatigue modelling feature will allow designers to predict the residual life of brick masonry arches.

4. Considering both discretisation approach using rigid and elastic elements, the elastic approach has been chosen for this research work. Overall deformation of the arch has been shown to be dependent on the elastic modulus of the element (*Sacco*, *2010*). To measure and model the strain-life behaviour accurately, it has become imperative to adopt the discretisation using elastic element.

2.13.1 Authors Critical Review

It has been observed that for the analysed arch the residual life significantly changes by improving the knowledge level. The analyses show that the models provide very conservative results as in the case of main arches where the residual service life is less than one year. This is due, most likely to the fact that the considered stress-life curves (Roca et al. Roberts, Casas et al.) have been established with few experimental data and has been obtained with masonry specimens with different compressive strengths. Laterza et al. (*2016*) has also made a good observation, that the load frequencies applied in the laboratory tests are higher than the ones indicated in EC1 (*EC1-2, 2003*) for roads and motorways, in the case study it is 0.015 sec.

Therefore, to establish a more credible strain-life curve the author has chosen a single mortar (1:2:9) and brick (75 N/mm^2) combination for the laboratory tests. The tests are conducted at 0.5 Hz frequency (i.e. 1 cycle per 2 seconds) to avoid any impact damages.

2.13.2 Preferred discretisation approach

Considering both discretisation approaches using rigid and elastic elements, the elastic approach (*Sacco, Toti, 2010*) has been chosen for this research work. Overall deformation of the arch has been shown to be dependent on the elastic modulus of the element. To measure and model the strain-life behaviour accurately, it has become imperative to adopt the discretisation using elastic element. This method models the interaction between brick-mortar contact surfaces as interface, which considers the combined effect of the damage and the friction in decohesion process.

Chapter 3
Material Testing of Masonry Constituents and Arch

Glossary

δq	Strain at quarter point
e	Axial strain
ε_θ	Tangential strain
$\varepsilon_{e'}$	Elastic strain
$\varepsilon_{p'}$	Plastic strain
εp	Parametric strain
ϕ	Friction angle
γ_{FL}	Live load factor
γ_{f3}	Factor for inaccurate assessment of loading
$\mu\varepsilon$	Microstrain, i.e., 10^{-6}
σ_1	Major principal stress
σ_3	Minor principal stress
τ, τ_u, τ_d	Shear stress
A	Area
Ao	Initial cross-sectional area
Cu	Shear strength
Do	Initial diameter
E	Young's modulus
E_b	Young's modulus of brick
E_m	Young's modulus of mortar
f	Flexural strength
f_t	Tensile strength
f_b	Compressive strength of mortar
f_k	Characteristic value
F_m	Compressive strength of brick
$f_{m'}$	Mean value
n_i	Number of cycles accumulated
N, N, N_c	Load cycle
N_u	Maximum Load Cycle

N_f	Number of cycles to failure
P	Force
Ps	Section property parameter
r, Rq, Rc	Radius, Radius at quarter point, Radius at crown respectively
R	Smin/Smax
s_f	Standard deviation
S_a	Stress range
S_u	Compressive strength
S_{min}	Minimum induced stress
S_{max}	Maximum induced stress
S_u	Compressive strength
ΔS	Stress range
t_m	Mortar thickness
t_u	Brick unit thickness
u	Radial displacement
v	Poisson's ratio

3.1 Introduction

In their critical review of research on high cycle fatigue behaviour of brick masonry, Wang (*Wang et el, 2013*) have identified the lack of investigation on the high cycle fatigue behaviour. Even today there are uncertainties of the research published by Roberts (*Roberts et al. 2006*) to Koltsida (*Koltsida et al. 2018*). The few available experimental data on the fatigue behaviour of masonry under high-cycle loading have been primarily under compression. Further there has been very little information available of the fatigue behaviour of masonry under shear. In his work, Clark (*1994*) has suggested that the fatigue limit of dry brick masonry is approximately 50% of its quasi-static compressive strength. Therefore, by limiting the magnitude of cyclic loading to 50% of the crushing strength of the masonry, a practically infinite number of load cycles could be carried by brick masonry. Even recently the complete works carried out by Koltsida (*Koltsida et al. 2018*) a total of 64 brick masonry prisms have been tested to failure under compressive fatigue loading at various maximum stress levels to investigate the fatigue life of masonry in relation to the stress level. Stack-bond brick masonry prisms were built from full-size bricks and mortar joints according to ASTM standards (*2014*). The total dimensions of the prisms were 210 × 100 × 357 mm (five handmade solid bricks and four 8 mm mortar joints). The tests were performed using a 250 kN capacity servo-controlled hydraulic actuator to apply static or long-term fatigue loading. The detailed experimental work process and results have been presented in Koltsida (*Koltsida et al. 2018*).

The previous works have tried to the predict the fatigue life expectancy of masonry for any desired confidence level based on compressive stress experiments. The works have also recognised that the rate of deterioration and remaining service life is essential to optimise assessment and inspection techniques and minimise the cost of maintenance for masonry arch management. S-N-P curves seemed a useful tool to help evaluate the remaining service life of masonry arch bridges at different confidence levels, based on material properties and traffic load levels.

On the contrary as explained in the Chapter 2.4, The fatigue life of a component is expressed as the number of loading cycles required to initiate a fatigue crack and to propagate the crack to a critical size. Therefore, the S-N-P curves based on the compressive stress tests on the masonry prisms fail to predict the crack initiation. The thrust line (*Heyman, 1982*) concept provides the ultimate capacity of the arch. Masonry compressive stresses are considered large enough and there is no danger of crushing of material under the possible load effects. Experimental evidence has shown that the decohesion phenomenon between a mortar joint and two adjacent bricks activated mainly on only one of the two interfaces leads to crack initiation, Sacco (*Sacco and Toti, 2010*).

Aim of the laboratory tests are primarily different to previous works, where focus was on the compressive strength and testing of masonry prism. But these tests have been aimed to study the fatigue failure over three stages from the crack initiation and their progressive growth leading to rapid fracture. To establish the high cycle fatigue (HCF>10,000 cycles) under alternating stresses, arches have been tested under cyclic loading.

3.2 Material Testing

Elementary properties of the bricks, mortar and prisms have been determined by the following tests.

3.2.1 Bricks

Class B solid engineering bricks manufactured by Wienerberger in accordance with the European Standard Specification for clay masonry units BS EN 771-1 have been procured for this work with following properties in Table – 3.1.

Table 3.1 Brick Properties

Size (LxBxD)	212 x 100 x 62	mm
Compressive strength (supplier)	75	N/mm^2
Compressive strength[#] (laboratory)	107	N/mm^2
Modulus of Elasticity[#] (laboratory)	31762	N/mm^2
Water absorption	7%	
Gross density	2310	kg/m^3
Bond strength (General Mortar)	0.15	N/mm^2

\# - EPSRC test results (*Liu et al. 2023*)

3.2.2 Mortar

Mortar plays an important role in the bonding of bricks in masonry. The strength of the bond mainly depends on the properties of mortar. The mortar mixes used to manufacture the brick masonry test specimens have been considered representative of the mixes used in the construction of old brick masonry arches. Mortar mix of 1:2:9 (cement: lime: sand) mixed by volume with water/cement ratio of 0.45, similar to Type IV (BS 5628: 1992) and their classifications have been considered. The Portland cement and hydrated lime have been obtained from a local supplier, freshly bagged to

avoid deterioration due to hydration in the laboratory. A commercially available natural sand has been used.

The specimens have been tested at the same time with the arch loading to ensure same maturity in strength.

Determination of Flexural and Compressive Strength of Hardened Mortar: BS EN 1015-11

The flexural strength of a hardened mortar has been determined by three-point loading of a prism specimen. Prism mould compartments are 160 x 40 x 40 mm (each mould assembly produces three prism specimens), prior to use they are lubricated with a thin layer of mineral oil. The mould is filled in two layers each layer being compacted in shaker Table.
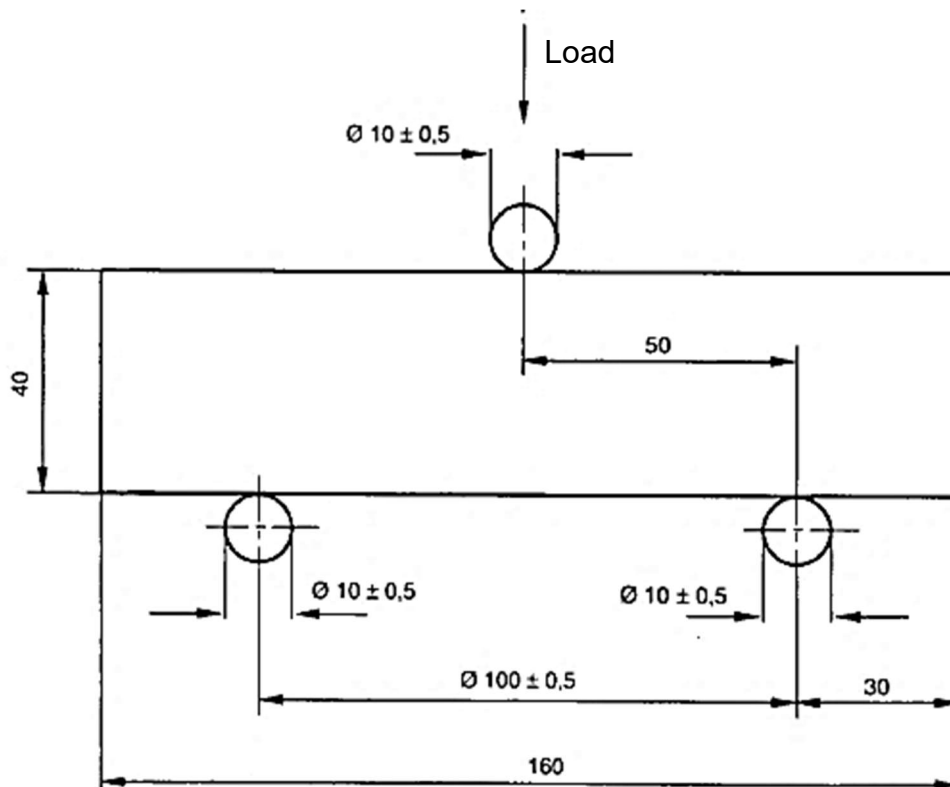
Note: All dimensions in 'mm'

Figure - 3.1 Flexural Tensile Test, Geometry. (*BS EN 1015-11*)

The testing machine is required to have two supporting rollers and a third roller (the loading roller, located above the test specimen and midway between the supporting rollers). The prism is placed so that one of its faces, which has been cast against the steel mould, is in contact with the supporting rollers, see Figure – 3.2 for actual test set-up. The load is applied to the test specimens at a rate that produces failure in a time of thirty to ninety seconds. The flexural strength (f) is calculated from the equation:

$$f = 1.5 \frac{F.l}{b.d^2} \qquad \text{(eq 3.1)}$$

Where b and d are the internal dimensions of the prism mould, l is the distance between the supporting rollers, i.e, 100 mm. The result is recorded to the nearest 0.05 N/mm^2 and the average of the set of results reported to the nearest 0.1 N/mm^2. Results are tabulated in Table – 3.2 and plotted in in Figure – 3.3.
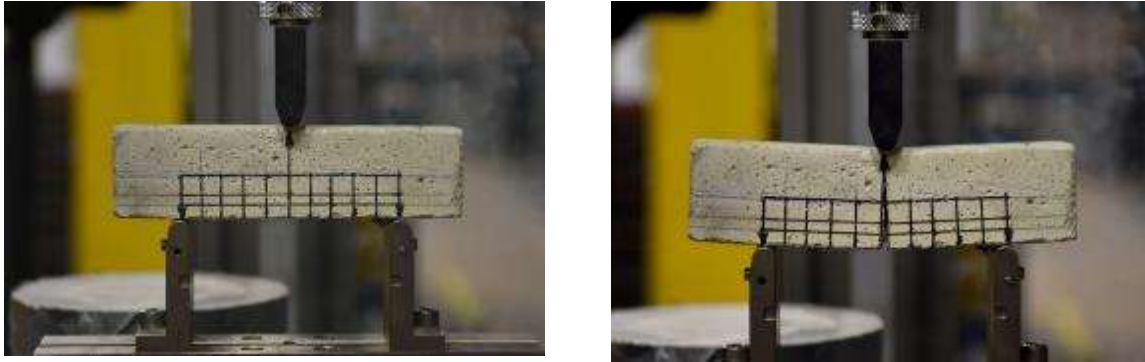
Figure - 3.2 Flexural Test, Before and After.
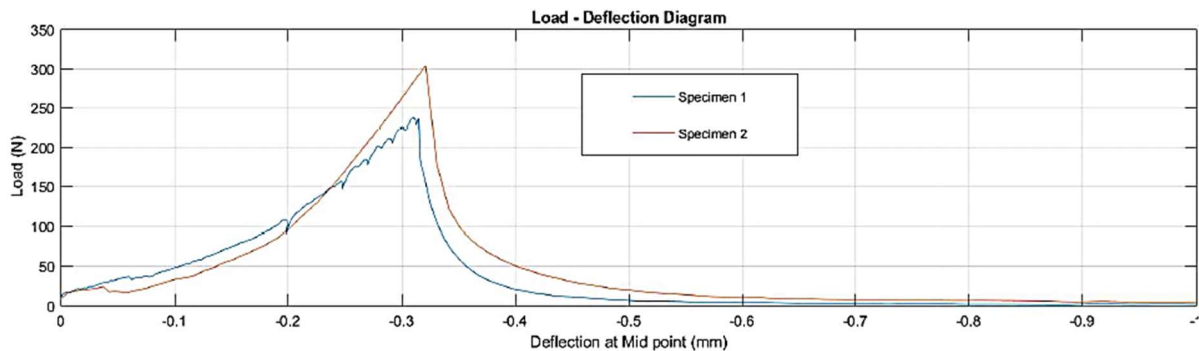
Figure - 3.3 Flexural Tensile Test, Load Deflection Curve.

Table 3.2 Mortar Flexure Test Results

Date of Testing	Specimen No	Weight of Specimen	Density	Maximum Load	deflection (mm)	Flexural Tensile strength
		(kg)	(kg/m³)	(N)		(N/mm²)
08/11/2019	I	0.46	1797	235.884	0.315	0.553
08/11/2019	II	0.45	1758	303.445	0.321	0.711
08/11/2019	III	0.45	1758	301.235	0.322	0.706
					Mean Value	**0.66**

The compressive strength is determined on the 50 x 50 x 50 mm cubes by using a compression jig in a testing machine, care being taken that the load is applied to a face

cast against the steel face of the mould. The load is applied to the test specimens at a rate that produces failure in a time period of thirty to ninety seconds. The compressive strength is similarly recorded to the nearest 0.05 N/mm^2 and the mean result reported to the nearest 0.1 N/mm^2. Mortar test results are plotted in Figure – 3.4and results are interpreted and calculated in Table – 3.3.
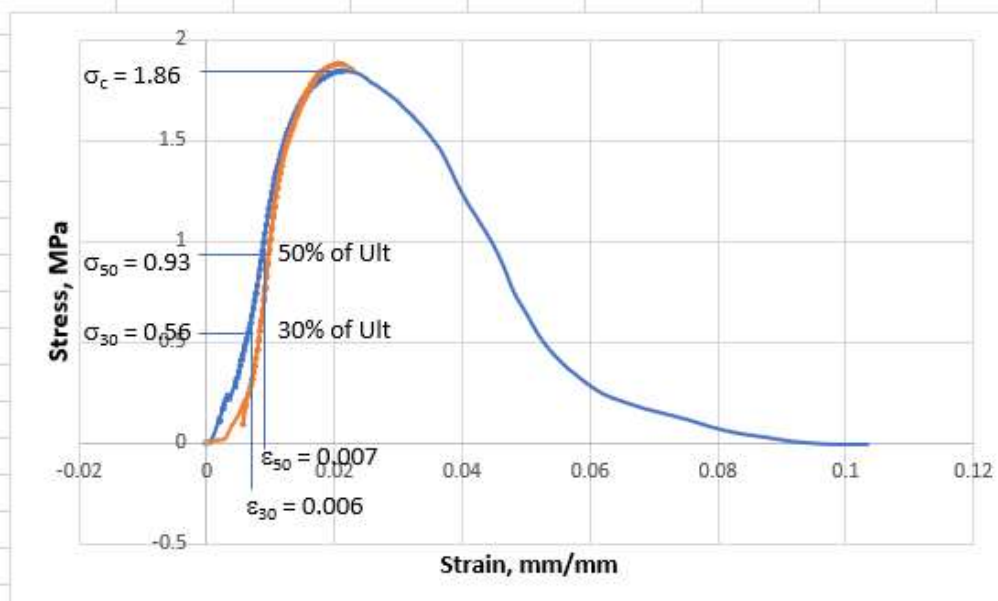
Figure - 3.4 Mortar Compressive Test, Stress-strain Curve.

(MPa = N/mm^2)

Table 3.3 Mortar Cube Test Results

Date of Testing	Cube No	Weight of Cube	Density	Maximum Load	Compressive strength
		(kg)	(kg/m^3)	(N)	(N/mm^2)
08/11/2019	I	0.24	1920	4608	1.843
08/11/2019	II	0.24	1920	4756	1.902
08/11/2019	III	0.24	1920	4596	1.838
					1.861

Date of Testing	Cube No	$\Delta\sigma$		$\Delta\varepsilon$		E
		50%	30%	50%	30%	(N/mm^2)
08/11/2019	I	0.922	0.553	0.0086	0.0065	175.7
08/11/2019	II	0.951	0.571	0.0098	0.0084	271.4
08/11/2019	III	0.919	0.551	0.0068	0.0055	283.1
	Mean values					**243.4**

Determination of Shear Strength of Hardened Mortar: BS 1377-7

The shear strength parameters of the mortar have been determined similar to the methods of test for determining shear strength parameters of soils in terms of total stresses. Shear strength is determined either by measuring the shearing force causing failure (direct shear tests), or by derivation from the measured compressive strength (unconfined or triaxial compression tests).

Determination of shear strength by direct shear (small shear box apparatus)

In the direct shear test a square prism of mortar is laterally restrained and sheared along a mechanically induced horizontal plane while subjected to a pressure applied normal to that plane. The shearing resistance offered by the mortar as one portion is made to slide on the other is measured at regular intervals of displacement. Failure occurs when the shearing resistance reaches the maximum value which the mortar can sustain. Test carried out on a set of three similar specimens, specimens of 60 mm square and 20 mm high, of the same mortar under different normal pressures, the relationship between measured shear stress at failure and normal applied stress is obtained. Test data enable the shear strength parameters c and ϕ to be derived.

From each set of data obtained during the shear test calculate the horizontal shear force, P (in N), applied to the specimen. Calculate the shear stress on the surface of shear, τ (in N/mm²), for each set of readings from the equation, Refer to Table -3.4 for calculated values..

$$\tau = \frac{P}{A} \qquad \text{(eq 3.2)}$$

where, A is the initial plan area of the specimen (in mm²).

Table 3.4 Mortar Direct Shear Test Results

Date of Testing	Cube No	L	B	D	Weight of Cube	Density	Maximum Load	Shear strength
					(kg)	(kg/m³)	(kN)	(N/mm²)
08/11/2019	I	60	60	20	3.76	1920	0.767	0.213
08/11/2019	II	60	60	20	3.76	1920	0.760	0.211
Mean value								**0.212**

Determination of the undrained shear strength in triaxial compression without measurement of pore pressure (definitive method)

The undrained strength of a specimen of mortar is determined (similar to cohesive soil) when it is subjected to a constant confining pressure and to strain-controlled axial loading, when no change in total moisture content is allowed. Tests are usually carried

out on a set of similar specimens, subjected to different confining pressures. The test is carried out in the triaxial apparatus on specimens in the form of right cylinders of height approximately equal to twice the diameter. Specimen diameter is 38 mm.

In the test the specimen is confined in an impervious membrane between impervious end caps in a triaxial cell which can be pressurized by water. The axial load is increased by applying a constant rate of strain until the specimen fails, normally within a period of 5 min to 15 min.

From each set of readings calculate the axial force, P (N), applied to the specimen by multiplying the difference between that reading and the initial reading of the gauge on the force-measuring device (divisions or digits) by its calibration factor (in N/division or N/digit).

Calculate the cross-sectional area, A (mm^2), of the specimen, on the assumption that it deforms as a right cylinder, from the equation:

$$A = \frac{A_0}{1-e} \qquad \text{(eq 3.3)}$$

Where, A_0 is the initial cross-sectional area of the specimen (in mm^2) calculated from the initial diameter D_0;

And e, is the axial strain $\Delta L/L_0$

Calculate the principal stress difference, i.e. the deviator stress, $(\sigma_1 - \sigma_3)$ (in N/mm^2), for sufficient sets of readings to enable the maximum value to be derived from the equation.

$$\sigma_1 - \sigma_3 = \frac{P}{A} \qquad \text{(eq 3.4)}$$

Shear strength, $Cu = 0.5\,(\sigma_1 - \sigma_3)$

Application of correction factors are in accordance with BS 1377-7.

Mohr-Coulomb parameters from Figure – 3.5 are tabulated in Table - 3.5 for both the specimen.
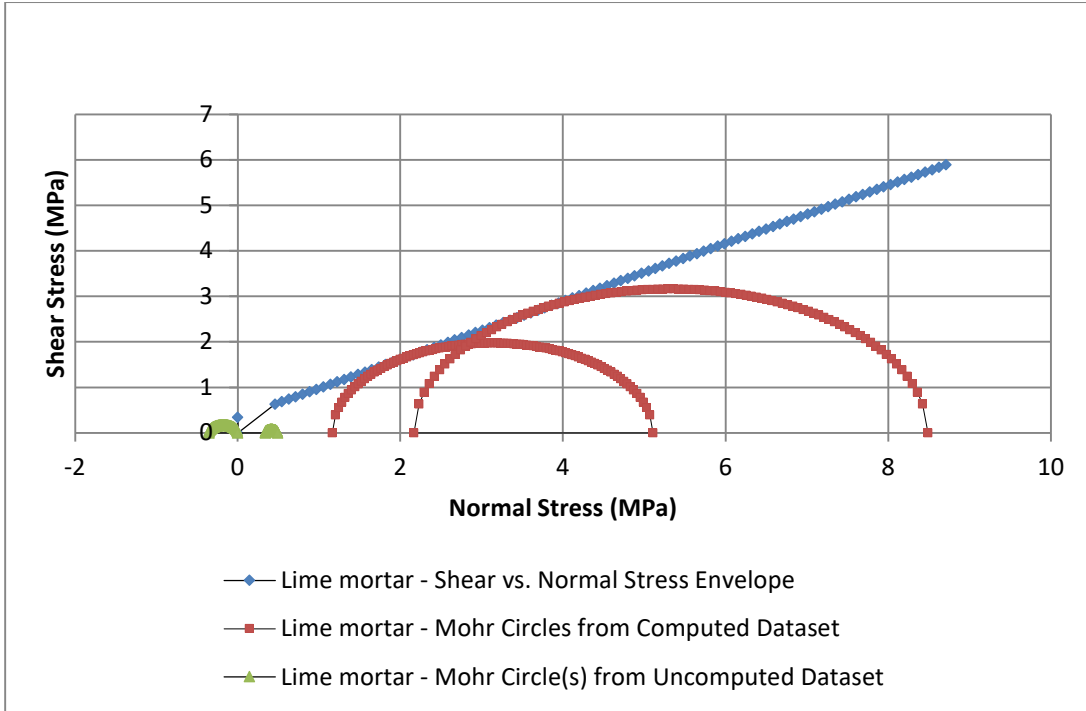
Figure - 3.5 Mortar Shear Strength, Mohr-Coulomb.

(Note: MPa = N/mm^2)

Table 3.5 Mortar Mohr-Coulomb Parameters

Shear strengths parameters	Sample I	Sample II	Mean	Units
Cohesion	0.333	0.341	**0.337**	N/mm^2
Friction angle	30.8	32.5	**31.7**	degrees

3.2.3 Prism

The behaviour of unreinforced brick masonry is evaluated by applying compression load on the brick prisms. Triplet brick prism or three stack bond prisms as shown in Figure - 3.6 are prepared for the mortar ratio 1:2:9. Compression load is applied at a rate of 500 N/s on the triplet brick prisms till failure. The thickness of the mortar layer is maintained as 12 mm. Test data of the prism are summarised in Table - 3.6.
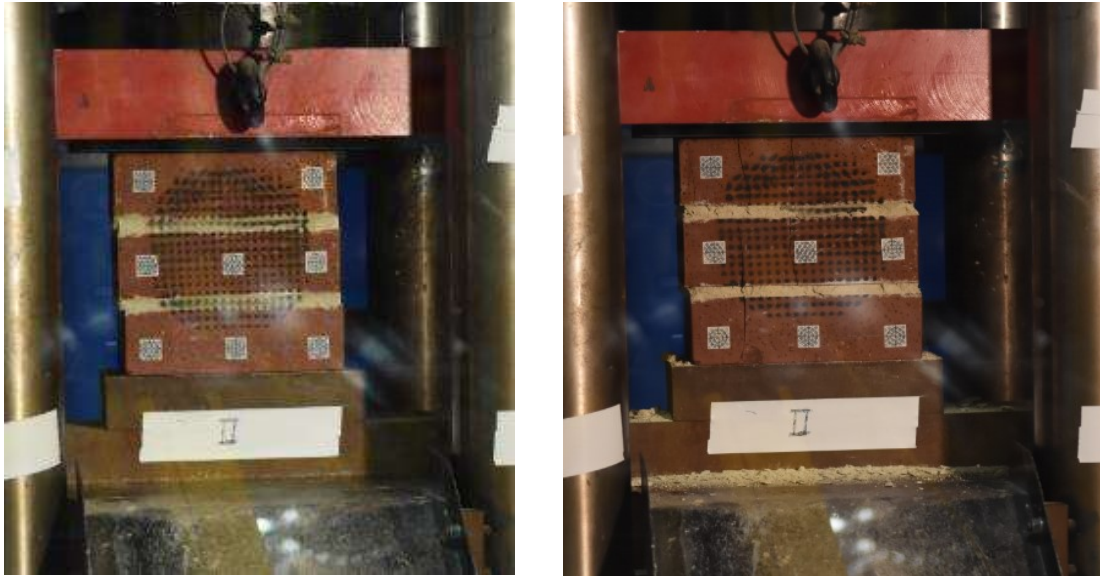
Prism Before test   Prism After Test

Figure - 3.6 Prism - Compressive Strength Test.

Table 3.6 Prism Compressive Strength Test Results

Date of Testing	Prism No	L	B	Overall H	Weight of Prism	Density	Maximum Load	Compressive strength
		mm	mm	mm	(kg)	(kg/m³)	(kN)	(N/mm²)
01/11/2019	I	212	62	211	10.53	2354.02	522.8	24.66
01/11/2019	II	212	62	210	10.47	2351.75	477.4	22.52
08/11/2019	III	212	62	212	10.59	2356.27	426.0	20.09
Mean Values						**2354.0**		**22.4**

3.2.4 Masonry Properties

The characteristic values of material parameters have been derived from the limited number of tests by IRS-70778 (*2020*) guidelines. This is done by applying corrective factors to the mean values of the parameters. The mechanical parameters of masonry have been assumed to follow a Gaussian (normal) distribution law, which allows characteristic values (95% confidence level) to be deduced from the mean value and from the standard deviation as given in the equation:

$$f_k = f_{m'} - K.S_f = (1-k\mu) \, f_{m'} = K.f_{m''} \qquad \text{(eq 3.5)}$$

where;

f_k is the characteristic value

$f_{m'}$ is the mean value of the measured data.

s_f is the standard deviation of the measured data.

$m = s_f/f_{m'}$ is the coefficient of variation of the distribution

k and K = $(1-K\mu)$ are parameters considering the number of measurements

for the number of specimen 3-6, $\mu = 0.3$ (30%) and confidence level of 95%, the values of k and K are

N	3	6	8	10	12	16	20	25	≥ 30
k	2,33	2,19	2,14	2,10	2,07	2,03	2,00	1,97	1,94
K	0,30	0,34	0,36	0,37	0,38	0,39	0,40	0,41	0,42

Considering mean strength of the prisms = 22.4 N/mm^2, the characteristic strength can be derived from the above values,

$$f_k = 0.3 \times f_{m'} = 0.3 \times 22.4 = \textbf{6.7 N/mm}^2$$

in accordance with EC6 (*1995*), the characteristic strength of the bonded masonry,

$$f_k = 0.5 \, f_b^{\,0.7} \, f_m^{0.3}$$

$$= 0.5 \times (107)^{0.7} \times (1.86)^{0.3}$$

$$= \textbf{15.8 N/mm}^2$$

f_b, f_m = *are mean compressive strength of the bricks and mortar respectively.*

       = *107 N/mm^2 (Table 3.1) and 1.86 N/mm^2(Table 3.3)*
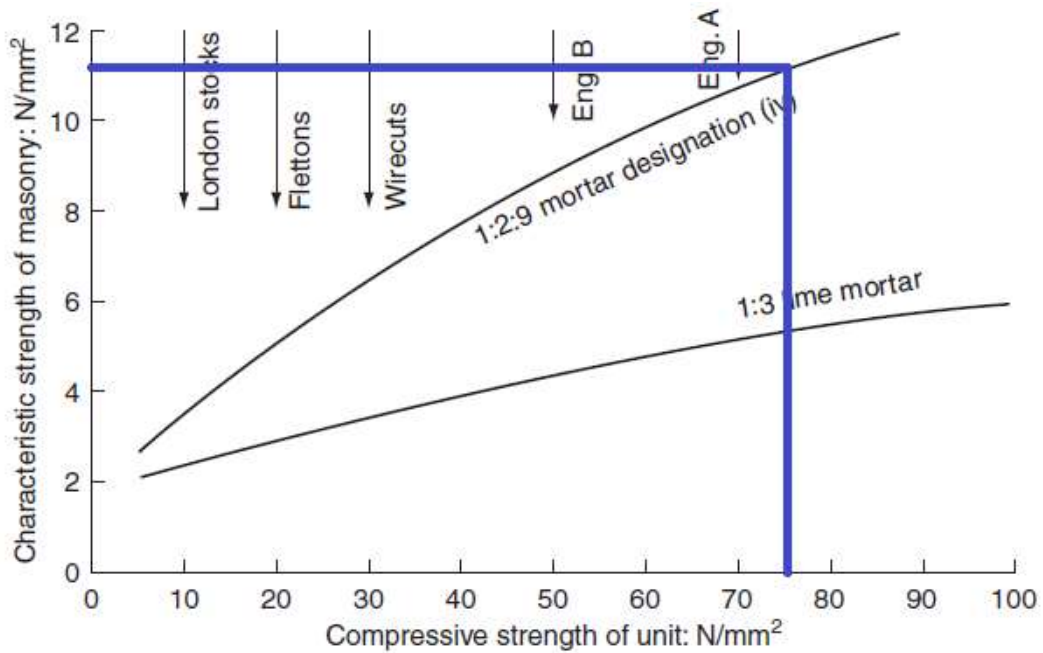
Figure - 3.7 Characteristic Strength of Brickwork. (*Page, 1993*)

The maximum compressive strength should be determined from laboratory tests if possible. In the absence of any actual strength tests data, conservative estimates may be made using available data; Figure - 3.7 and gives examples of characteristic strengths.

The short-term secant modulus of elasticity E in the UK National Annex4 to EC6 Part 1-1, is the same as that recommended in the Code, being 1000 fk. IStructE (*2005*).

Therefore, the *E* value lies between

IRS 70778 *(2020)*
        = 1000 x 6.7 = 6700 N/mm^2

EC6 (*2006*)
        = 1000 x 15.8 = 15800 N/mm^2

Page (*1983*)
        = 1000 x 11.7 = 11700 N/mm^2

Due to significant variation in secant modulus between three approaches, it has been decided to verify the actual values after loading the arch under 2x11 kN then model updating with the reasonable secant modulus of elasticity value.

3.3 Arch Test

A series of large-scale tests have been carried out at the University of Salford on multi-ring masonry arches to assess their endurance limit and cyclic load capacity Melbourne (*2007*). While the classical mode of failure of arches under static loading has been the four-hinge mechanism, all arches within the test series under cyclic loading have shown ring separation over the middle section of the arch. Cyclic loading therefore influences the mode of failure. This work has shown that.

- Ring separation for multi-ring arches can occur at a considerably lower load level than that associated with a four -hinge mechanism failure;

- Cyclic load capacity and endurance limit of multi-ring arches can be around 60% lower than the static load capacity and can modify the mode of failure;

- A model for an Interactive S-N curve to allow assessment of residual life and fatigue performance for general arch bridge assessment has been proposed;

- Shear capacity of mortar-brick joints seems to be exponentially related to the extent of mortar bond under static loading however it appears to be independent of mortar bond under cyclic loading;

- Shear capacity of small and large-scale samples have demonstrated the significance of the size of the test sample and the necessary consideration of the extent and quality of the mortar bond;

- ANSYS can conveniently be used for modelling arches as a continuum for a mechanism type failure under static loading; however, methodology lacks suitability for modelling multi-ring arches where there is the possibility of ring separation.

Above work also recognises that currently there is not enough data available for calibrating and modelling arches under cyclic loading.

There are mentions of deflections in this work during failure, but little have been inferred out of this data. Arch deflection has been significant during their failure. Measuring deflections to define strains and load cycle at failure, Stain-Line (ε-N) curve, Figure - 2.14, will potentially offer reliable fatigue curve for masonry and this can be adopted in practice by assessment engineers across the globe. Advantages of the strain-life approach are such that arch failure is predicted by deformation. When developed, this curve can be directly applied to in-situ service arches by measuring strains and deflections under services loadings then predicting residual life under expected cyclic loading. Therefore, contributory effects in a real structure e.g., backfill, track-structure interaction, stiffening due to spandrel wall will solely focus on measuring strains and deflections instead. Finally, a single variable, i.e., arch strains are monitored to assess and predict the life of an arch.

This thesis presents a new simplified approach that could be used to obtain a useful ε-N curve. The method assumes that the unknown ε-N curve possibly be represented by a parabolic line in log-log scale, Figure - 2.14. This assumption alone simplifies the process significantly since the number of parameters to be determined is now reduced to just two. Large scatter, along with prolonged testing times, make fatigue characterization a tedious process. The method assumes that the unknown ε-N curve beyond 1×10^6 cycles may be represented by a straight line in logarithmic scale. This assumption allows the test duration to practical 10-12 weeks.

3.3.1 Test Set-up

Test set-up is shown in Figure – 3.8 also. Image of actual set-up is presented in Figure – 3.10. Instrumentation set-up is shown in Figure – 3.9 and actual images of the instrumentation is presented in Figures – 3.11 to 3.13. Two specimen arches are tested for load applied at 1/3 points of the arch and continued in alternating cycles.

After completing the brick laying arches are cured for 28 days for allowing mortars to gain strength before removing the centring.

Figure - 3.8 Arch Test Set-up.

Following removal of cantering, the arch is subjected to static loads of 2x11 kN at 1/3 point to represent the permanent backfill (300 mm). This load is maintained constant for the whole duration of the test. Load is applied at two stages per ram and

corresponding deflections are measured. This is to confirm actual Secant modulus of the arch, to be used during analysis.
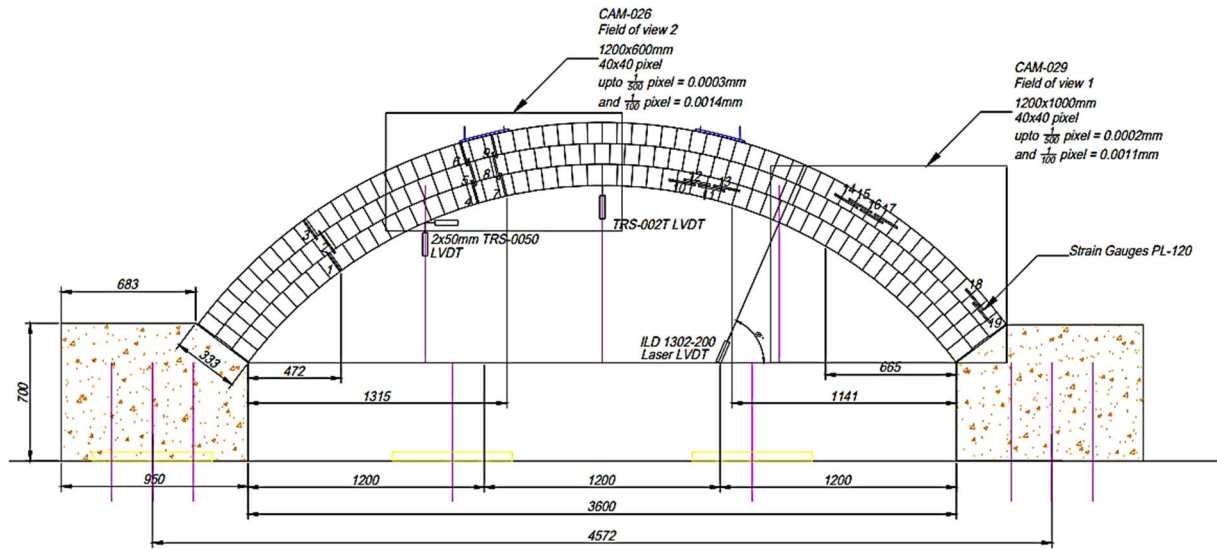
a) ARCH 01.
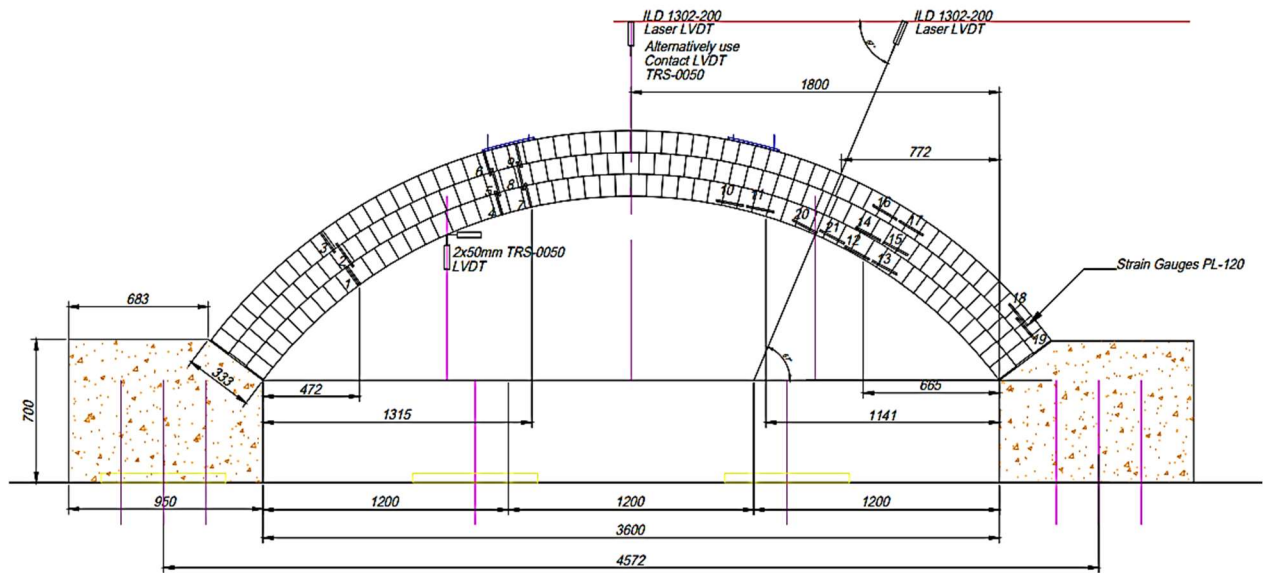
b) ARCH 02.

Figure - 3.9 Instrumentation Set-up.

Loading has been applied at 0.5 Hz to achieve following cycles with elapsed time.

			Load cycle	
0.5	Hz	=	2	/Seconds
		=	30	/Minutes
		=	1.80E+03	/Hour
		=	4.32E+04	/Day
		=	1.30E+06	/Month

The tests are conducted at 0.5 Hz frequency (i.e. 1 cycle per 2 seconds) to represent the flow of traffic at 5 km/h speed over a bridge to avoid additional impact damage. Applied load has been programmed to a sinusoidal load configuration, refer to Figure – 3.14. Before commencing the fatigue tests, load is applied quasi-statically up to the mean fatigue load. Subsequently, the load has been alternated between a minimum and a maximum stress level.

Figure - 3.10 Test Set-up.

Figure - 3.11 Strain Gauges.

Figure - 3.12 LVDT Positions.

Figure - 3.13 Data Logger.

3.3.2 Arch 1 – Constant Load Cycle

Additional load of 10 kN at each 1/3 point is applied in stages to represent the wheel loads. Unlike the permanent load this load is applied in alternative cycle at 1/3 points, resulting complete stress reversal. See Table - 3.7 for Arch 1 loading protocol.

Table 3.7 Arch 1 Loading Protocol

Test Schedule					25/11/2019	10:00:00	
No of Cycles		Time (Sec)	Day	Time Lapsed		Clock Time	Log Scale
1	2.0E+00	2	Day 1	00:00:02		10:00:02	0.3
10x10^0	1.0E+01	20		00:00:20		10:00:00	1
10x10^1	1.0E+02	200		00:03:20		10:03:20	2
10x10^2	1.0E+03	2000		00:33:20		10:33:20	3
10x10^3	1.0E+04	20000	Day 1	05:00:00	**25/11/19**	15:00:00	4
10x10^4	1.0E+05	200000	Day 3	02:00:00	**28/11/19**	12:00:00	5
40x10^4	4.0E+05	800000	Day 10	22:40:00	**05/12/19**	08:40:00	5.6
70x10^4	7.0E+05	1400000	Day 17	22:40:00	**12/12/19**	08:40:00	5.8
90x10^4	9.0E+05	1800000	Day 21	15:06:40	**16/12/19**	01:06:40	6.0
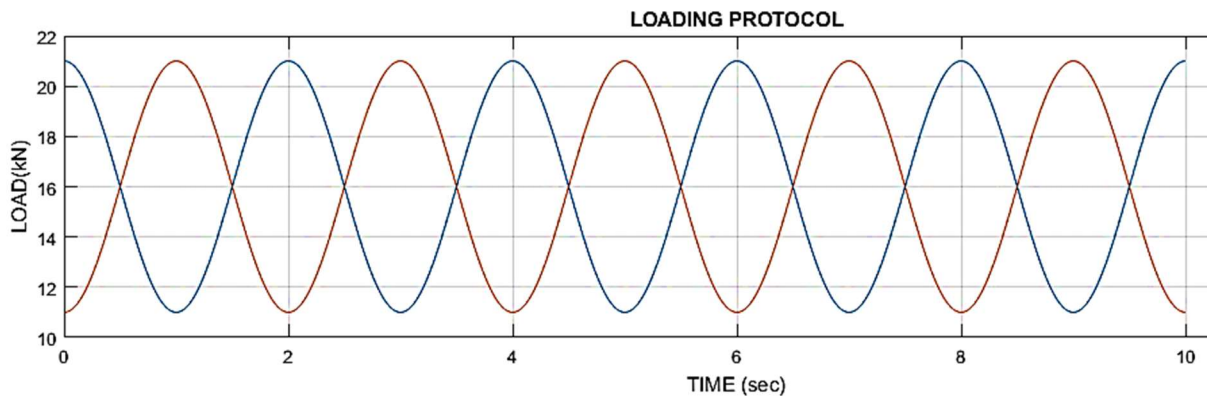
Figure - 3.14 Cyclic Loading Protocol. (frequency = 0.5 Hz)

3.3.3 Arch 2 – Increasing Load Cycle

Additional load of 15 kN at each 1/3 point is applied in stages to represent the wheel loads. Unlike the permanent load this load is applied in alternative cycle at 1/3 points, resulting complete stress reversal. This loading is continued for 10^5 cycles, then increased in steps to failure. See Table 3.8 below for Arch 2 stages of loading.

Table 3.8 Arch 2 Loading Protocol

No of Cycles		Time (Sec)	Day	Time Lapsed		Clock Time	Log Scale
Test Schedule					**04/11/2020**	**10:00:00**	
Cyclic Load = 15kN							
1	2.0E+00	2	Day 1	00:00:02		10:00:02	0.3
10x10^0	1.0E+01	20		00:00:20		10:00:00	1
10x10^1	1.0E+02	200		00:03:20		10:03:20	2
10x10^2	1.0E+03	2000		00:33:20		10:33:20	3
10x10^3	1.0E+04	20000	Day 1	05:00:00	04/11/20	15:00:00	4
10x10^4	1.0E+05	200000	Day 3	02:00:00	06/11/20	12:00:00	5
Cyclic Load = 20kN							
1	2.0E+00	2	Day 6	00:00:02	09/11/20	10:00:02	
10x10^4	1.0E+05	200000	Day 8	02:00:00	11/11/20	12:00:00	5.3
Cyclic Load = 25kN							
1	2.0E+00	2	Day 9	00:00:02	12/11/20	10:00:02	
10x10^4	1.0E+05	200000	Day 11	02:00:00	14/11/20	12:00:00	5.47
Cyclic Load = 30kN							
1	2.0E+00	2	Day 13	00:00:02	16/11/20	10:00:02	
10x10^4	1.0E+05	200000	Day 16	02:00:00	19/11/20	12:00:00	5.6
Cyclic Load = 35kN							
1	2.0E+00	2	Day 16	00:00:02	19/11/20	10:00:02	
10x10^4	1.0E+05	200000	Day 18	02:00:00	21/11/20	12:00:00	5.69
Cyclic Load = 40kN							
1	2.0E+00	2	Day 20	00:00:02	23/11/20	10:00:02	
10x10^4	1.0E+05	200000	Day 22	02:00:00	26/11/20	12:00:00	5.78

No of Cycles		Time (Sec)	Day	Time Lapsed		Clock Time	Log Scale
Test Schedule - Failure					**26/11/2020**	**10:00:00**	
Cyclic Load = 50kN							
1	2.0E+00	2	Day 22	00:00:02	26/11/20	10:00:02	
10x10^3	1.0E+04	20000	Day 22	05:00:00	26/11/20	15:00:00	5.79
Cyclic Load = 60kN							
10x10^0	1.0E+01	20	Day 22	00:00:20	**26/11/20**	15:30:00	5.79

3.4 Discussion on Results

Deflections at the quarter points and the crown were recorded at periodic intervals for the duration of cyclic loading. Results, recorded in Appendix A. Following completion of both the tests the results have been summerised and deflection at arch crown and quarter points have been plotted for both the arches in Figure - 3.15.

3.4.1 Deflection-Load Cycle

Arch 01 was tested under low-stress cyclic loads. During the tests, no visible damage was observed. The dial gauge reading observed during the load cycles indicated elastic behaviour of the arch for the 10^6 cycles.

The Arch 01 survived without any noticeable defects for 10^6 cycles at 10 kN alternate loading, which is 16% of the maximum fatigue loading (considering that Arch 02 failed at 60 kN when subjected to cumulative damage cyclic loading).
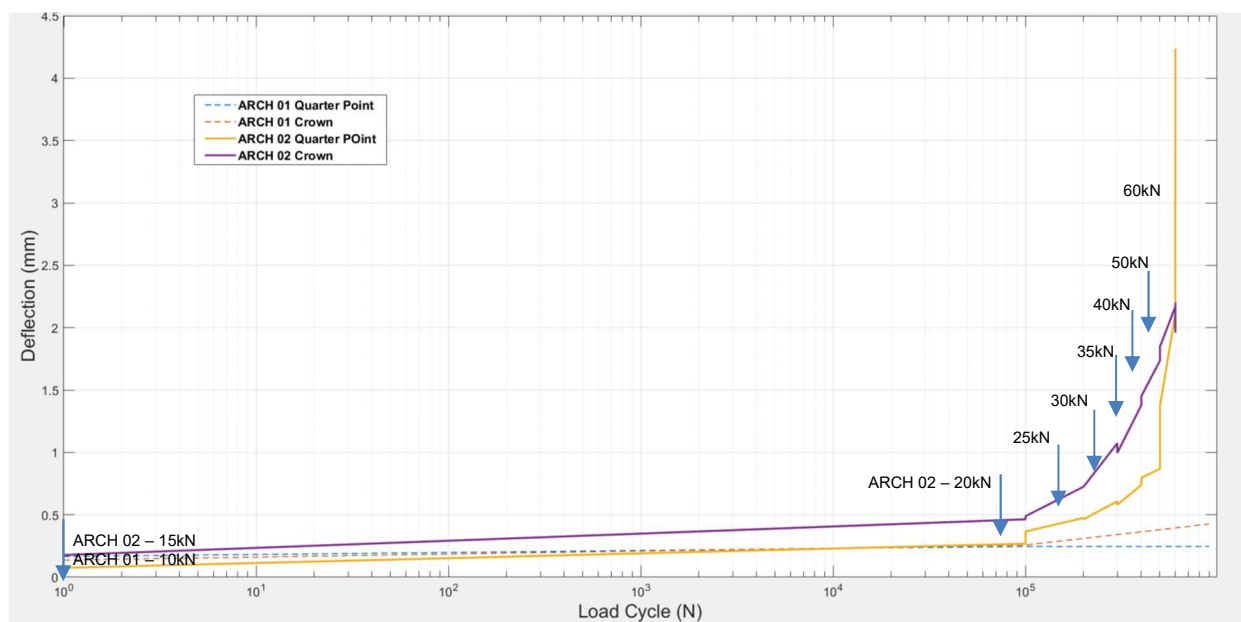
Figure - 3.15 Deflection – Load Cycles, Arch 1 and Arch 2 Plotted Together.

Arch 02 was tested to multiple stages of increased cyclic loading repeated every 10^5 cycles. As the loads were increased, the deflections tend to increase rapidly and enter the inelastic range. First visible signs of cracks noted in the laboratory at the alternate load of 25 kN, this is considered 50% of the fatigue failure load of 50 kN. Beyond this point, further increase in loads caused rapid growth in deflection, finally leading to sudden brittle type collapse of the Arch 02.

Comparing Figure - 3.15 with the stages of cracking, refer Figure - 2.16 (*Bannantine et al. 1990, Tateishi and Hanji, 2004*) work here, it is observed that the stage 1 crack

initiation had started after 10^4 cycles for both the arches. The crack propagation, stage 2 crack growth process continued up to 10^5 cycles for Arch 01 subjected to 10 kN alternating load, 20% of the maximum failure load in fatigue. Stage 2 crack propagation has also been found to have started immediately after 3×10^4 cycles for Arch 02 loaded at 15 kN, i.e.,30% of failure load. Therefore, arches reach the crack propagation phase even at a considerably low level of cyclic loading.

Interestingly (*Nelson et al. 2018*) work at University of Salford on full scale arch test recorded significant deflection fluctuation at quarter point during cyclic loading even at 10% of failure load. Work only focussed on loads without further investigation into deflections.

3.4.2 Crack Mapping

During tests continuous monitoring of visible arch deteriorations have been recorded. Following sketches in Figure – 3.16 show development of radial cracks and ring separations observed for the Arch 02 at different stages of loadings.
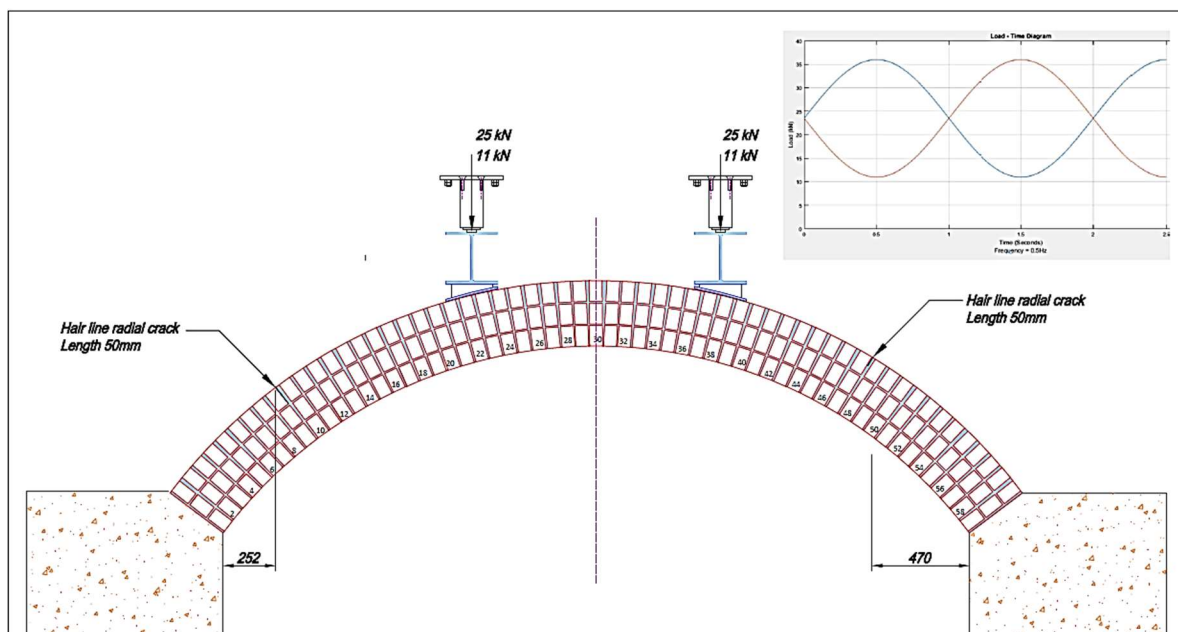
a) Radial cracks at extrados, Loading 25 kN cyc.
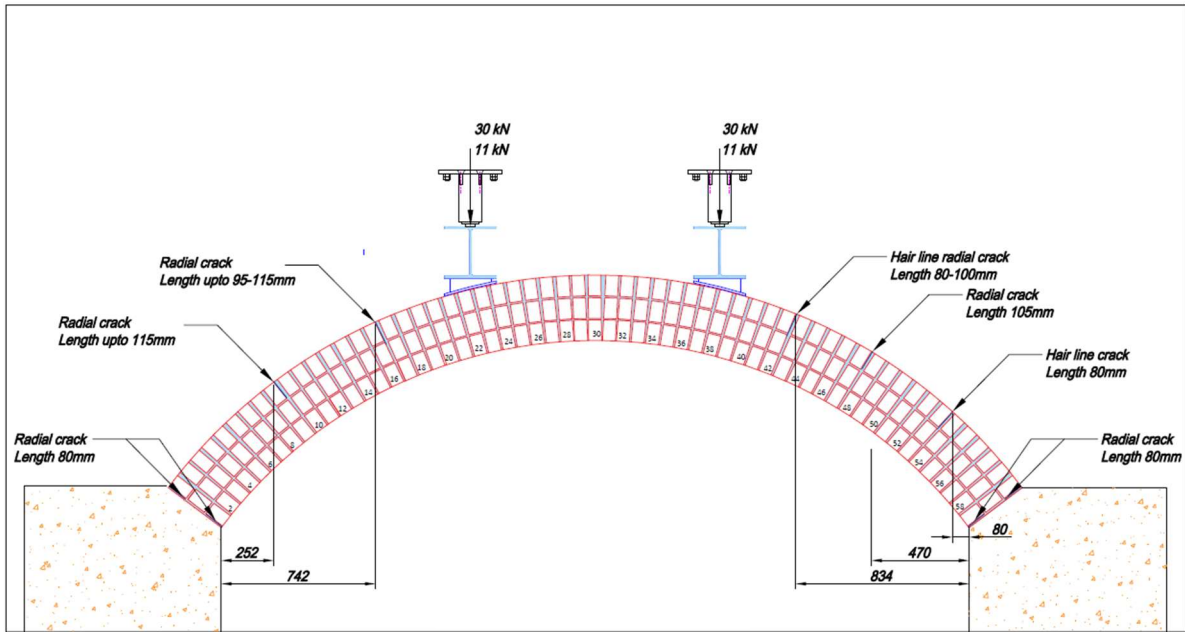
b) Radial cracks extended at extrados,
c) New cracks appeared at extrados,
d) Cracks at support intrados. Load 30 kN cyc.
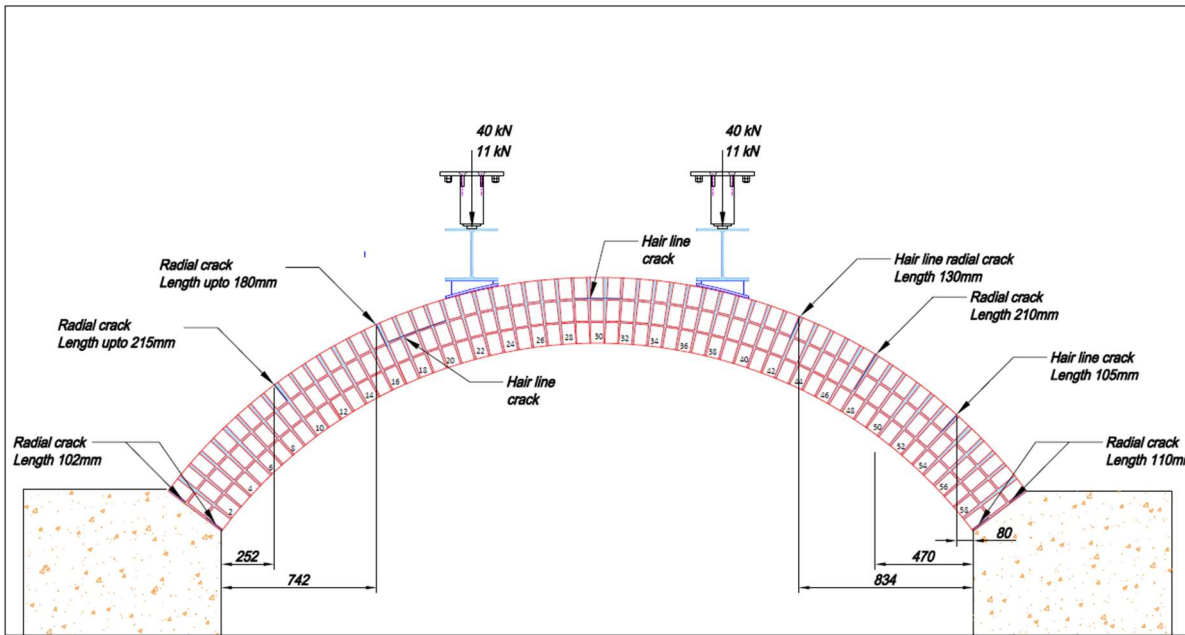
e) Hair line Ring separating cracks appearing Load 40 kN cyc
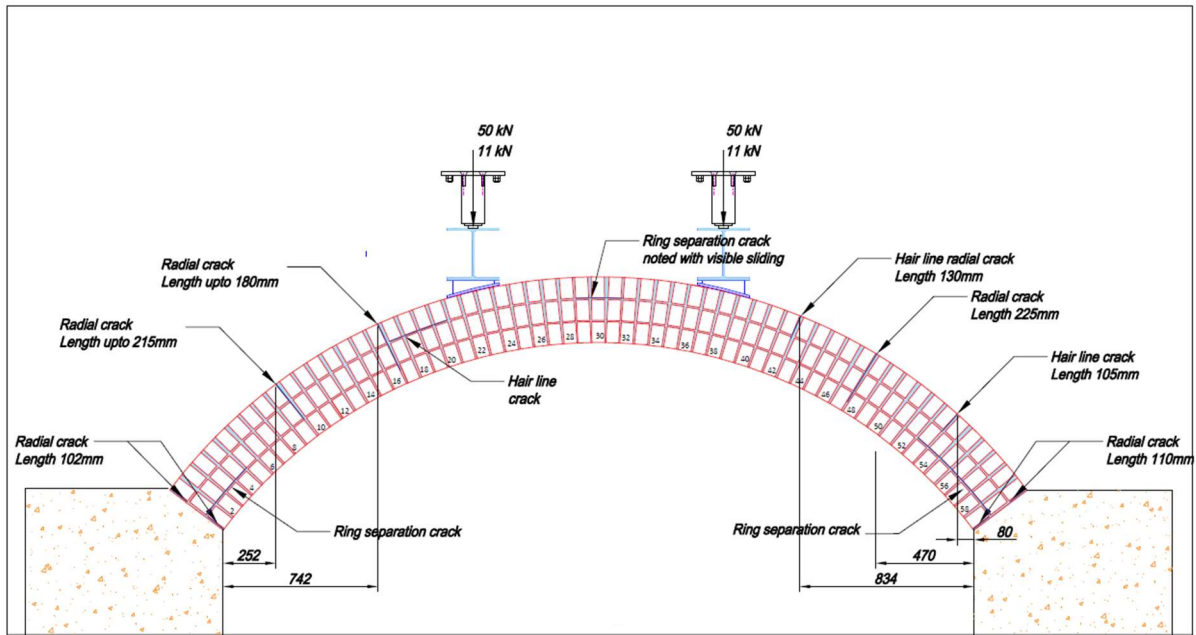
f) Extended radial cracks

g) Ring separations extended Load 50 kN cyc

Figure - 3.16 Visible Cracks Recorded During Cyclic Load Tests on Arch 02.

Contrary to common understanding cyclic loading on arches result significant cracking initiate from extrados. For arches covered with backfill it is not possible to inspect these cracks.

3.4.3 Modulus of Elasticity-Load Cycle

For the Arch 01 it has been observed that deformations continue to increase with repeated load cycles. This phenomenon clearly suggests that arch stiffness continue to deteriorate over their life span even under constant amplitude alternating loads. Stiffness degradation and damage modelling has been discussed in **chapter 5**.

3.4.4 Stress-Life

The Figure - 3.15 is further encouraging, since the arch damages follow conventional crack pattern followed historically during fatigue studies on various materials, it is reasonable to apply the Wöhler curve, Figure - 2.18.   The test results from the series of arches tested at Salford University, discussed in the section 2, were never analysed to establish the classical stress-life S-N diagram. Even today, this is considered one of the most helpful methods characterised by an S-N curve, the Wöhler curve, Figure - 2.18. One primary aim of this research is to establish a S-N curve for its use in the later deduction for strain-life parameters. The Arch 02 was purposefully tested for

cumulative damage to destruction. The Arch 02 was tested under increased loading applied for 10^5 cycles at each stage up to failure. The Miner's rule, equations 2.3a 2.3b, have been applied in the following derivation in Table - 3.9, to predict corresponding life at every loading stages.

Table 3.9 Load, Stress and Life Cycle Summary for Arch 2

Load (kN)	Smax (N/mm²)	Smin (N/mm²)	Sm (N/mm²)	Sa (N/mm²)	A=Sa/Sm	N (Test)	Ni Figure - 4.17	ni/Ni
15	0.268	-0.218	0.025	0.243	9.7	100000	1.480E+07	0.01
20	0.357	-0.290	0.034	0.324	9.7	100000	4.141E+06	0.02
25	0.446	-0.363	0.042	0.405	9.7	100000	1.622E+06	0.06
30	0.536	-0.436	0.050	0.486	9.7	100000	7.206E+05	0.14
35	0.625	-0.508	0.059	0.567	9.7	100000	3.640E+05	0.27
40	0.714	-0.581	0.067	0.648	9.7	100000	2.077E+05	0.48
50	0.893	-0.726	0.084	0.810	9.7	1000	7.712E+04	0.01
60	1.071	-0.871	0.100	0.971	9.7	10	3.511E+04	0.00
							Damage Σ	1.00

For further validation, the Miner's rule has been extended to the Salford University 5m span Arch ' O' as well (*Melbourne et al. 2007*), these results were also plotted in Figure - 3.17. Both tests have shown a good correlation. Refer to Figure - 2.50 for the terms and Appendix A for the calculated stresses.

Figure - 3.17 clearly identifies the critical component of the stresses that lead to fatigue failure. Alternating stresses result in cracking or separation the mortar bonds at the masonry-mortar interfaces. For the Arch 02 visible cracks appeared at 25 kN, this is equivalent to alternating stress of 0.405 N/mm². The following relationship has been derived between the alternating stress against the life of the arches for this purpose.

$$S_a = (1 + A)N^{-B} \qquad \text{(eq 3.6)}$$

Constant B varies between 0.2 – 0.22 for the arches.
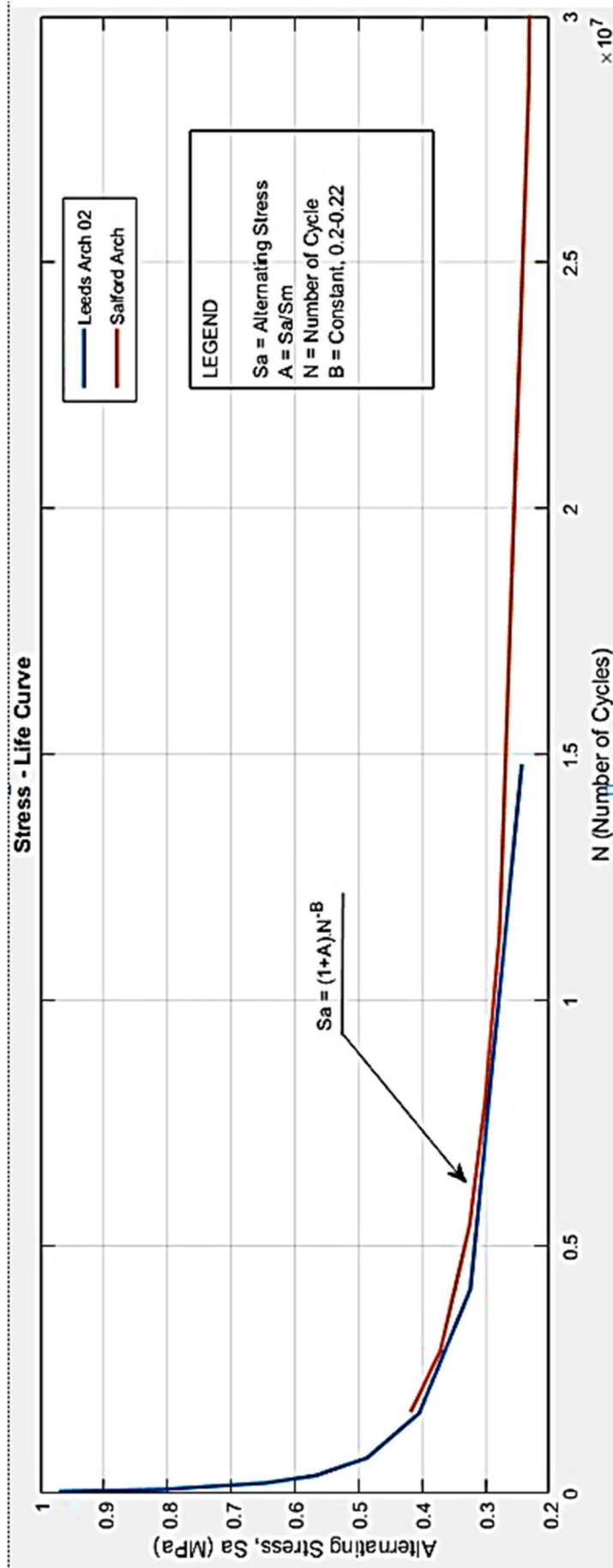
Figure - 3.17 Stress – Life, S-N Curve for Test Arches.

3.4.5 Summary

a) Observations made from Deflection-load cycle behaviour, Figure - 3.15:

Key aim of the designers and the asset owners should remain in limiting the loading that would prolong the Stage 2 beyond million cycles and avoid the rapid fracture Stage 3 for the survival of the arches. Test on Arch 01 shows that by limiting the allowable load the crack propagation period can be considerably prolonged.

The visible cracks, Figure - 3.16, appeared under cyclic loading at 25 kN, this is 50% of the fatigue failure load of 50 kN. This is about 30% of the static capacity, considering the analytical static capacity of the arch is 80 kN, refer 5.2.2. For bridges supporting passenger loads visible signs of radial cracking/separation under live loads are the best indicators for planning for immediate repair. Therefore, all assets are recommended to be monitored under live loads for any visible instantaneous defects. There cracks are agile and close after withdrawal of the loads. Inspecting arches under wheels free (no live load) conditions fail to predict the true condition.

b) Observations made from Equation 3.6:

For analytical purposes it is necessary to check the magnitude of alternating stresses that an arch is expected to experience. This suggests that analytical criteria for fatigue life shall be limited by maximum allowable alternating stress under live loads. Presently there are no guidance or practices where the serviceability criteria are defined by the allowable stress.

Knowing the intended service life of an arch the Equation 3.6 can be used to determine the maximum allowable alternating stress under live load. This relationship defines the serviceability criteria for the masonry arch.

3.5 Strain-life interpretation

Arches deteriorate over the years due to multiple reasons including increased load effects, environmental conditions, transverse load distribution and stiffness contribution from the spandrel walls. Typically, longitudinal and transverse cracks are commonly noticed in arches during their inspections by the asset owners. The stress life relationship discussed in equation 3.6 and probabilistic models developed by previous researchers (*Ronca et al. 2004, Roberts et al. 2006, Casas, 2009, Koltsida et al. 2018*) are a good prediction however it is extremely complicated to model the defects in arches for the accurate prediction of stresses.

3.5.1 Tangential Strain

Only parameter that can be reliably measured for the arches in service today is their deformation under live loads. Therefore, a strain -life approach is considered credible

to predict the residual life of existing arches for all practical applications. A numerical approach has been proposed in the following section to derive the strain-life relationship followed by the methodology for calculating tangential strains from the measured deformations.

As illustrated in Figure – 3.18, consider an element at radius *r* and defined by an angle increment *dθ* and a radial increment *dr*. Consider that there is only a radial displacement *u* given by line aa'. Point c is displaced radially by *(u + du)* given by line cc'. The original length of the line ab is *rdθ* and line a'b' is length *(r - u) dθ*.
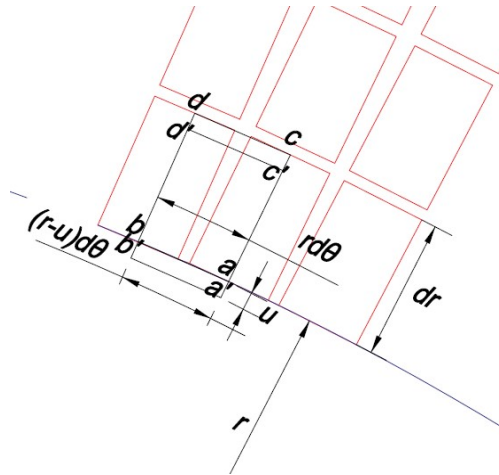
Figure - 3.18 Tangential Strain Calculation for Arch.

The tangential strain is thus:

$$\varepsilon_\theta = \frac{rd\theta - (r-u)d\theta}{rd\theta} = \frac{u}{r} \qquad \text{(eq 3.7a)}$$

3.5.2 Why Parametric Strain

Tangential strain derived in equation 3.7 measured directly with strain gauges if the arch is within their elastic range. If strain gauges are installed across brick-mortar joints, they often fail to log further data following development of wider cracks or after joint opening. Alternatively, this strain can be derived by measuring radial deflection at arch intrados divided by radius of curvature at the same point.

Irrespective of method of measurements, for the purpose of this research, going forward in following sections in this research document the tangential strain is termed as "Parametric Stain", ε_p.

$$\varepsilon_p = \frac{u}{r} = \frac{\delta_q}{R_q} \qquad \text{(eq 3.7b)}$$

i.e., parametric stain measured at intrados quarter point is $\dfrac{\delta_q}{R_q}$

3.5.3 Arch Deformation

The arch displacements at the quarter points and the crown have been recorded during the laboratory tests using the LVDTs. For the crown TRS-0050 contact, LVDT was used, and for the quarter points, two separate systems were used. ILD 1302-200 Laser was directed radially at the extrados, while 2x TRS 0050 contact LVDTs were used for the intrados. See Figure - 3.19 for the LVDT positions.
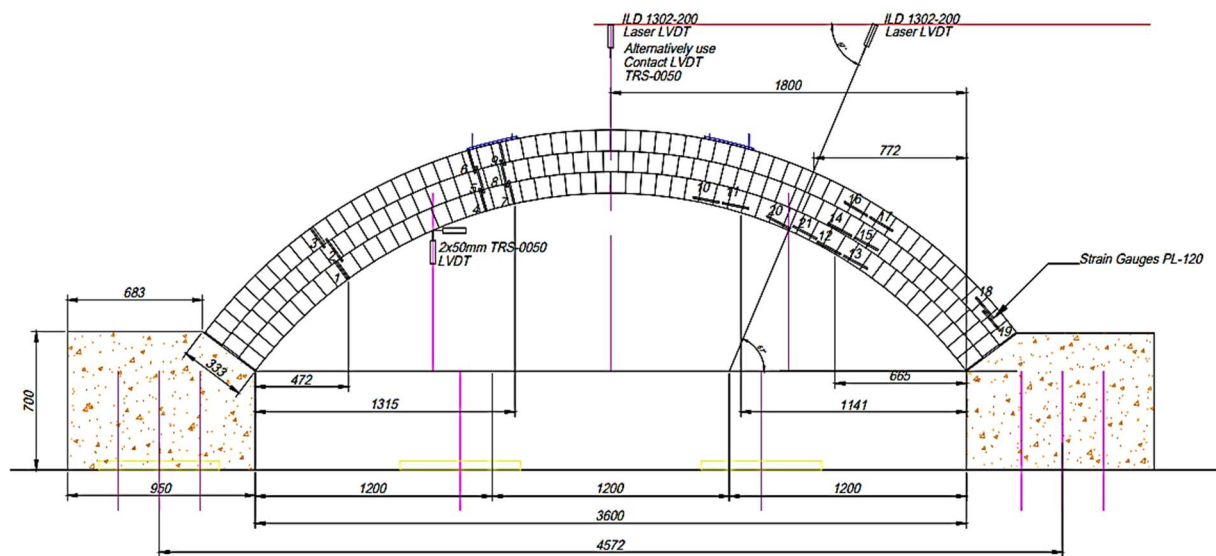
Figure - 3.19 LVDT Positions for Arch 2.

The Table 3.10 summarises both arch deflections measured at the start and end of the load cycles. Values from Table - 3.10 has been plotted in Figure - 3.20. This Figure clearly suggest that a constant amplitude cyclic loading applied on arch continues to increase deflections. Therefore, arches continue to deflect under applied cyclic loading over their ages. This is particularly important and form the basis of this research work.

The first hinge formation has been visually recorded at the left-hand quarter point at the variable load of 25 kN. This is noted in Table by reduction in deflection as the arch has moved towards the laser LVDT, therefore reducing the deformation reading. Second hinge formation at the right-hand extrados have occurred at the variable load of 40 kN. The arch has shown significant downward moment therefore rapidly increasing the deformation noted at the LVDT.

Table 3.10 Arch 01 & 02 Arch Deflections

Arch	Load (kN)		Load	Cumulative	Deflections (mm)		
	Cell 1	Cell 2	Cycle	Cycles	Crown	Intrados	extrados
ARCH 01	11.0	11.0	0	0	0.0827	0.0494	0.0552
	11.0	21.0	1	1	0.1372	0.1660	
	11.0	21.0	900000	900000	0.4259	0.2463	
	21.0	11.0	1	1			0.1530
	21.0	11.0	900000	900000			0.4241

Arch	Load (kN)		Load	Cumulative	Deflections (mm)		
	Cell 1	Cell 2	Cycle	Cycles	Crown	Intrados	extrados
ARCH 02	11.0	11.0	0	0	0.0888	0.0522	0.0451
	11.0	25.0	1	1	0.1776	0.0749	
	11.0	25.0	100000	100000	0.4639	0.2684	
	25.0	11.0	1	1			0.1145
	25.0	11.0	100000	100000			0.1583
	11.0	11.0	0	100000	0.3805	0.1126	0.0079
	11.0	31.0	1	100001	0.4892	0.3663	
	11.0	31.0	100000	200000	0.7245	0.4752	
	31.0	11.0	1	100001			0.1689
	31.0	11.0	100000	200000			0.5741
	11.0	11.0	0	200000	0.5012	0.1866	0.4214
	11.0	36.0	1	200001	0.7236	0.4639	
	11.0	36.0	100000	300000	1.0739	0.6080	
	36.0	11.0	1	200001			0.5775
1st Hinge	**36.0**	**11.0**	**100000**	**300000**			**0.1977**
	11.0	11.0	0	300000	0.7654	0.3279	0.3561
	11.0	41.0	1	300001	0.9961	0.5809	
	11.0	41.0	100000	400000	1.3788	0.7388	
	41.0	11.0	1	300001			0.6495
	41.0	11.0	100000	400000			0.2890
	11.0	11.0	0	400000	1.2484	0.4340	-0.1190
	11.0	46.0	1	400001	1.4502	0.7966	
	11.0	46.0	100000	500000	1.7366	0.8689	
	46.0	11.0	1	400001			0.8980
	46.0	11.0	100000	500000			0.6611
	11.0	11.0	0	500000	1.5382	0.5008	0.1327
	11.0	51.0	1	500001	1.8484	1.3726	
	11.0	51.0	100000	600000	2.1657	2.1051	
	51.0	11.0	1	500001			0.7782
	51.0	11.0	100000	600000			0.6348
	11.0	11.0	0	600000	1.8934	1.8512	-0.2293

Table 3.10 continued

Arch	Load (kN)		Load	Cumulative	Deflections (mm)		
	Cell 1	Cell 2	Cycle	Cycles	Crown	Intrados	extrados
ARCH 02	11.0	61.0	1	600001	2.0050	2.5112	
	11.0	61.0	1000	601001	2.2006	3.5532	
	61.0	11.0	1	600001			1.0897
	61.0	11.0	1000	601001			1.1559
	11.0	11.0	0	601001	1.9589	3.4741	0.2322
	11.0	71.0	10	601011	2.1320	4.2374	
	71.0	11.0	10	601011			1.4102
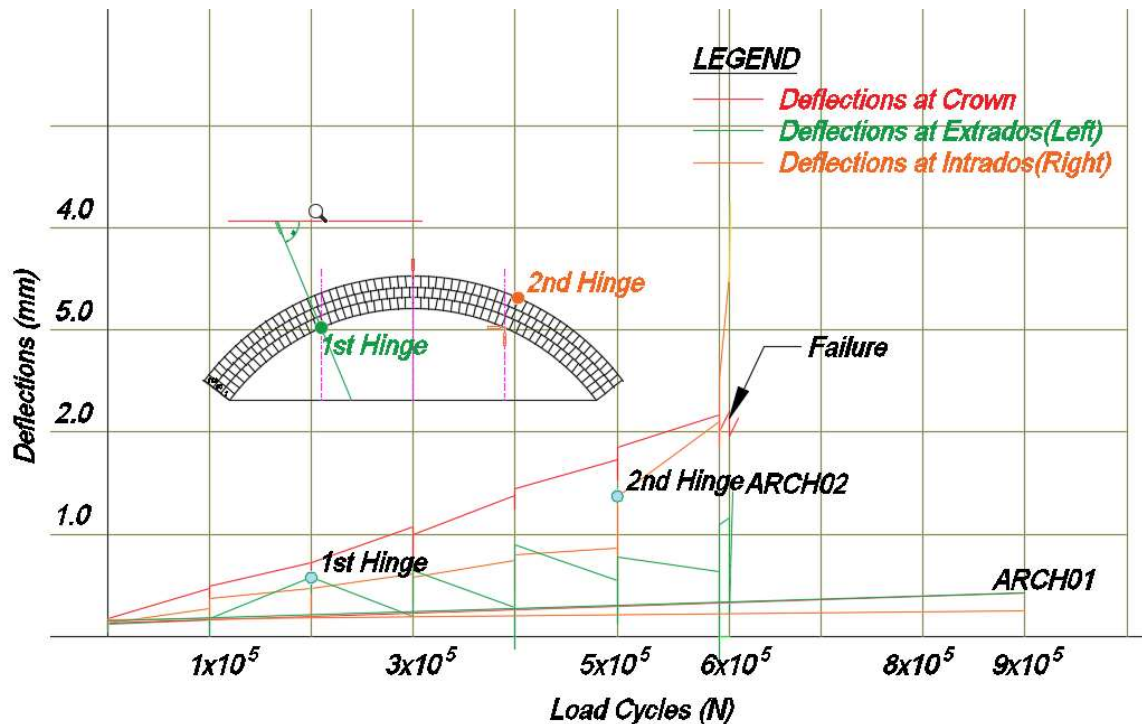
Figure - 3.20 Deflections – Load Cycles Plot for ARCH01 and ARCH02.

3.6 Supplementary experimental data

Unfortunately, first arch was demolished prematurely to prioritise other research projects. Immediately after construction of the second arch unforeseen pandemic delayed the project. Second arch has been successfully tested following cumulative load increments. To overcome the limitation of number of tests this research work has referred to similar arch tests carried out University of Salford under Sustainable bridges development programme between 2003-2007.

A series of laboratory tests were carried out at the University of Salford on large-scale multi-ring brickwork arches under long term cyclic loading. Objectives of the test series were to investigate the behaviour, possible modes of failure, capacity and permissible limit state of multi-ring masonry arches under long-term fatigue loading. Based on the test results, a model for interactive SN curves has been proposed for masonry arches and masonry qualities that allow qualitative assessment of the residual service life under a given loading regime.

The arches were constructed on reinforced concrete abutments bolted into the reinforced strong floor. Two types of 215 x 102.5 x 65 mm bricks were used for construction: strong class A engineering bricks to represent high quality brickwork and weak Britley Olde English bricks to represent aged brickwork which is commonly found in the railway network. For all tests 1:2:9 (cement: lime: sand) mortar was used.

In order to represent the weight of the typical backfill on arches, dead loads were applied at the ¼ and ¾ points of the arches either by steel weights or by hydraulic jacks, Figure - 3.21. Live load was applied at the ¼ point for static tests by 1 kN increments and at the ¼ and ¾ points for cyclic tests. Cyclic loading was applied at 2 Hz frequency to represent the flow of traffic at ca. 25-30 miles/hours speed over the bridge. Cyclic loading was applied for 10^6 cycles at each load level, starting from a relatively small load. If after 10^6 cycles no damage or deterioration was observed, the load was increased by 2 kN, and the process repeated until failure occurred.
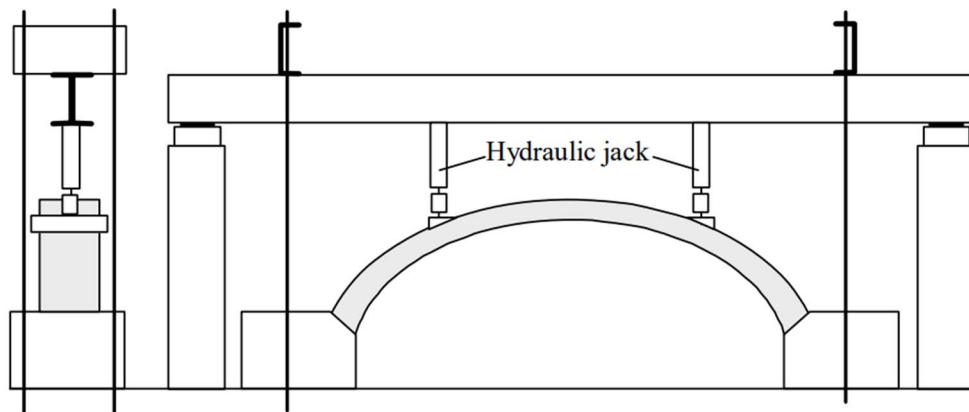
Figure - 3.21 Salford University Arch – Loading Frame. (*Sustainable Bridges, 2007*).

Horizontal and vertical deflection was measured at the ¼ and ¾ span using LDVTs, Figure – 3.22. Refer to Table – 3.11 for details of test arches.
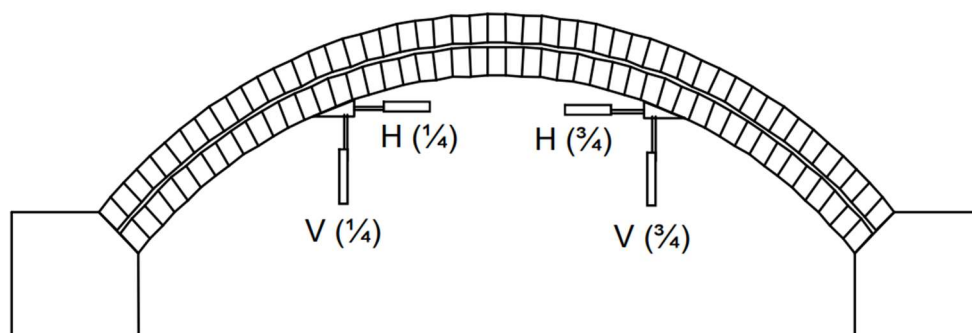
Figure - 3.22 Salford University Arch – Deflection Gauge Positions. (*Sustainable Bridges, 2007*)

Table 3.11 Salford Arches - Dimensions

	3 m Arch	5 m Arch
Span (mm)	3000	5000
Rise (mm)	750	1250
Ring Thickness (mm)	215	330
Arch width (mm)	445	675
Number of rings	2	3
Dead Load (kN)	2 x 10	2 x 22.5
Span: rise	4:1	
Shape	Semi-circular	

University of Salford arch construction material. loading arrangement and test procedure in-principle are similar to the arches tested at University of Leeds for this thesis work and considered suitable for validation.

3.6.1 Salford – Static test ARCH G (3 m span)

Arch G was loaded gradually to failure. The arch became unstable after opening of the 4th hinge near the ¾ span and failed by four-hinge mechanism under 28 kN. Deflections, measured at ¼ and ¾ span show slight change in curvature around 15 kN. The first significant change in deflection, Figure - 3.23, is shown around 27 kN, shortly before opening of the 4th hinge and four-hinge mechanism failure. It is possible for the 1st and 2nd hinges to have opened around 15 kN although they only became visible under higher loads around 22 kN.
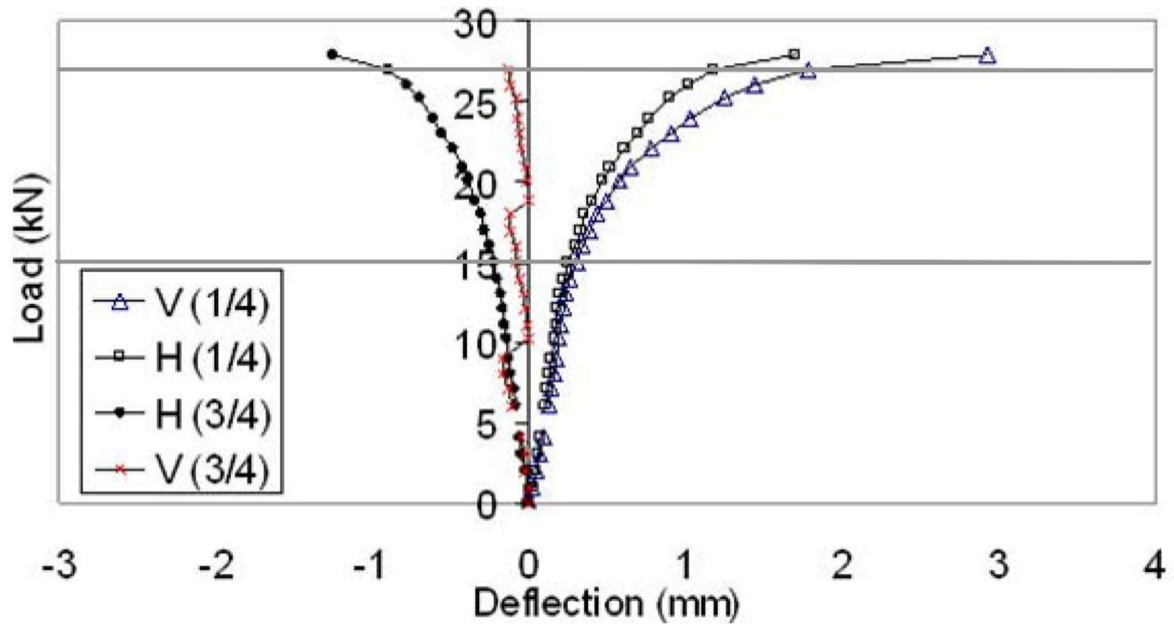
Figure - 3.23 Salford Arch G – Load- deflection. (*Sustainable Bridges, 2007*)

3.6.2 Salford – Cyclic test ARCH O (5 m span)

Following application of deal loads at ¼ and ¾ spans, cyclic loading was applied for 10^6 cycles at a series of load levels starting from a relatively small (6 kN) load. No damage was observed under 6, 8, 10, 12, 13 kN loading series. Under 14 kN the existing radial cracks at the ¼ and ¾ spans extended slightly however no further damage occurred for the rest of 10^6 cycles. See Table – 3.12 below for loadings detail. The arch finally failed under the 18 kN loading series with ring separation in the middle section of the arch after 340,000 cycles.

Considering the similarities between Salford and Leeds arches, **Dr Adrienn Tomor** kindly agreed to share the test outputs for validation of this thesis. Typical load-deflection output is shown in Figure - 3.24.

Following section investigate the effect of variable loading and its effect on the arch.

Table 3.12 Salford Arch O – Loading and Crack History.

Live Load (kN) (% static capacity)*	Crack location			Type
	Intrados	Middle	Extrados	
0	22/23	23/24		Radial crack
	55/56			Radial crack
6 (20%)				
8 (27%)				
10 (33%)				
12 (40%)				
13 (43%)				
14 (47%) 500,000 cyc.		24-25 36-43 56-57	25-26 57-44 57-59	Longitudinal crack
16 (53%)				
18 (60%) 340,000 cyc.		36-43	37-44	Ring separation

*% of the 30 kN static capacity of the 5m strong brick arch M
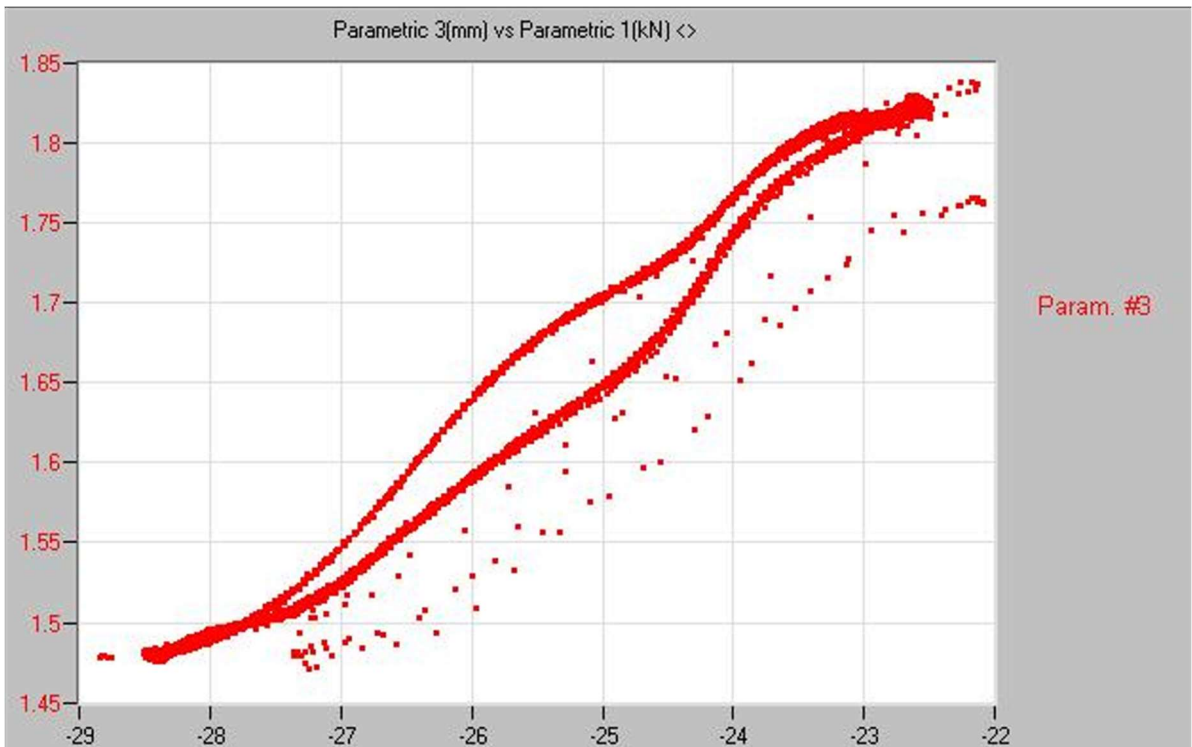
(a) Deflection at V(1/4), refer Figure 3.21
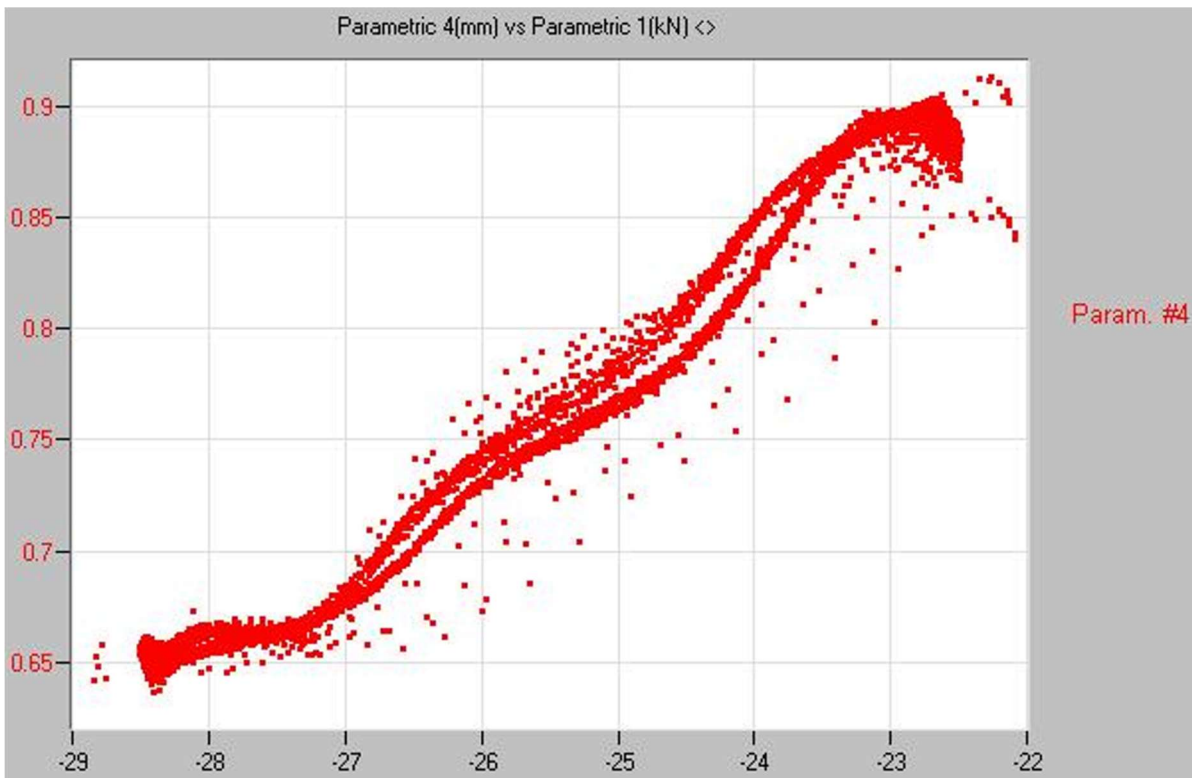
(b) Deflection at H(1/4), refer Figure 3.21
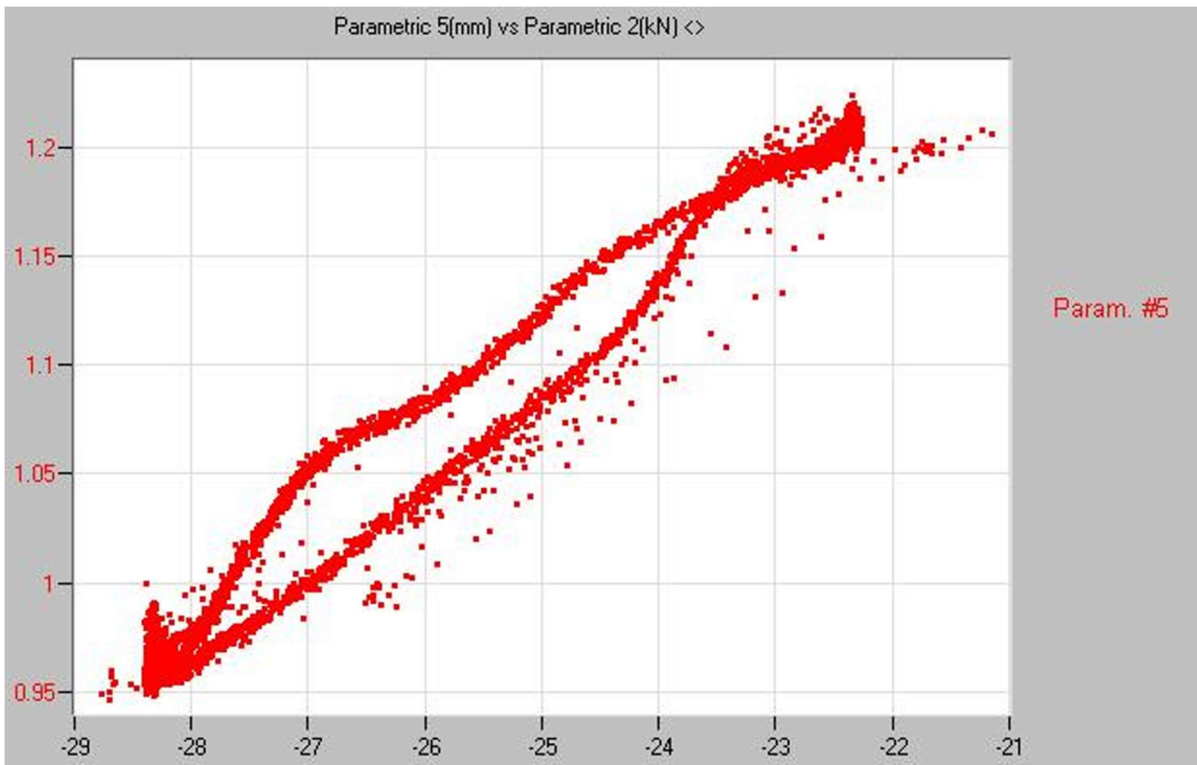
(c) Deflection at H(3/4), refer Figure 3.21
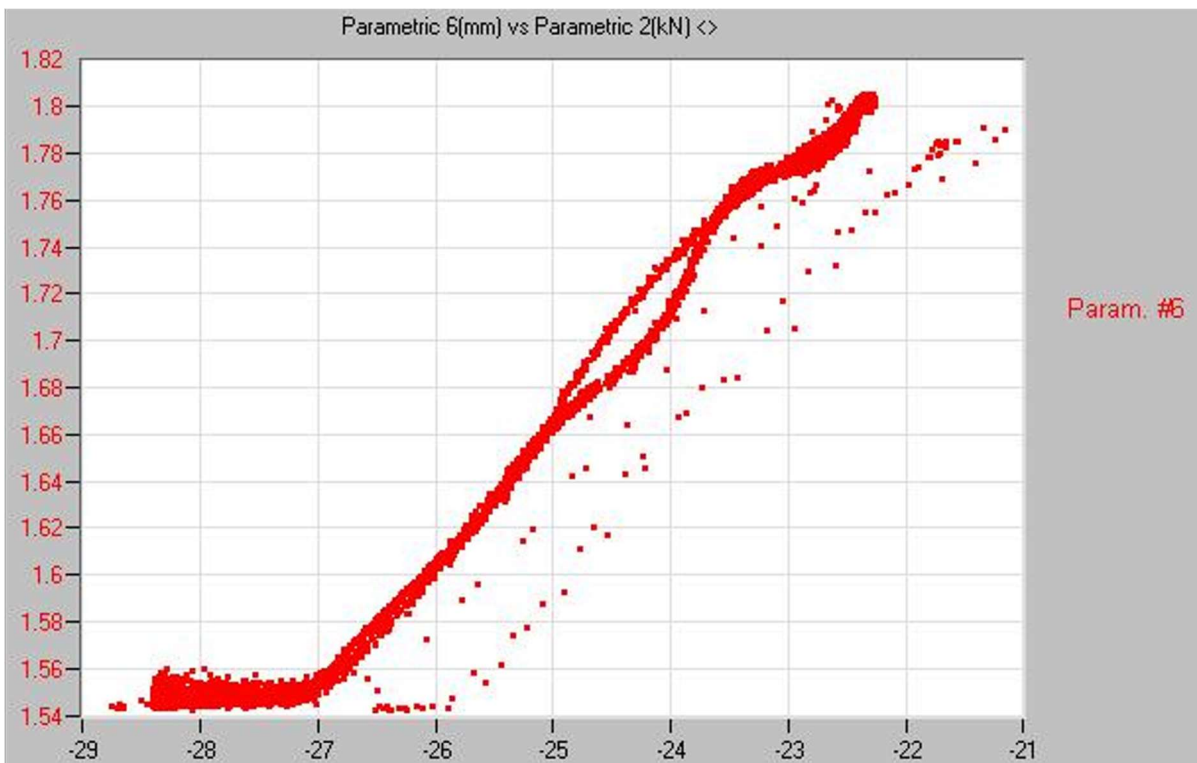
(d) Deflection at V(3/4), refer Figure 3.21

Figure - 3.24 Salford Arch O – Load- deflection Plot at 6 kN Live Load

(Courtsey: Dr Adrien Tomor)

3.7 Strain-Life (ε-N) Curve

The deformations prior to first hinge formations are considered largely linear (elastic). Therefore, corresponding strains calculated using the equation 3.7 are also considered linear (elastic) strains. Further deformations under increased loadings following the formation of the first hinge are considered non-linear (plastic). For the Arch 01 the deformation is considered elastic due to lower stress intensity and no signs of cracking were observed after 9×10^5 cycles.

Both arches are tested with constant load 11 kN maintained at two load points for the entire duration of the tests to represent favourable effect of backfill. Then variable alternating cyclic loads are applied in stages to represent live loads scenarios that arches undergo in real life.

Table - 3.13, further extended to separate the variable loads deflections at every stage of loading.

Calculated strains and corresponding life (Figure - 3.16) have been tabulated in the following Table - 3.13. For quarter points only the intrados measures have been considered in the following Table. This is because in real arches we are only able to measure the intrados deformations under live loads.

Plotting Table - 3.13 for the crown deformation in Figure - 3.25, following observations can be made. If the measured parametric strain at the crown under live load is less than < 300x 0.1με, i.e, 30×10^{-6} then the arch is expected to endure fatigue damage. This is equivalent to **Rc/33,000**, *Rc* is the radius of curvature at crown intrados.
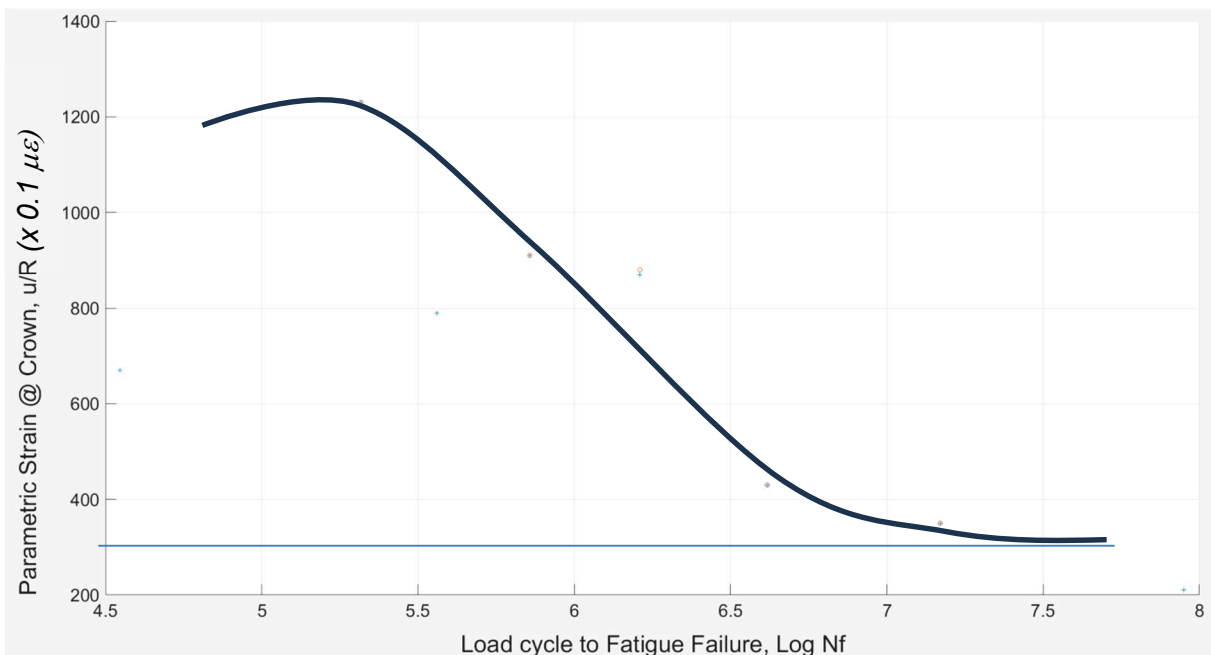
Figure - 3.25 Strain-Life Measured at The Arch Crown.

Table 3.13 Arch 01 & 02 Live Load Parametric Strain, εp

(calculations based on Equation 3.7)

				Displacements (mm)			
Load	N	Ni	ni/Ni	Extrados (radius r = 2570mm)		Intrados (r= 2250)	
(kN)	(Test)	(Figure - 4.17)		Crown (Table 3.10)		Qtr Point (Table 3.10)	
				δq (avg)	$\varepsilon p = \delta q/Rq$	δq (avg)	$\varepsilon p = \delta q/Rq$
Linear deformation (before first hinge)							
ARCH 01							
10	900000	8.928E+07	0.010	0.056	2.17E-05	0.116	5.15E-05
ARCH 02							
15	100000	1.480E+07	0.007	0.092	3.57E-05	0.068	3.00E-05
20	100000	4.141E+06	0.024	0.111	4.32E-05	0.250	1.11E-04
Non-Linear deformations (following first hinge)							
25	100000	1.622E+06	0.062	0.226	8.79E-05	0.272	1.21E-04
30	100000	7.206E+05	0.139	0.235	9.13E-05	0.288	1.28E-04
35	100000	3.640E+05	0.275	0.205	7.96E-05	0.982	4.36E-04
40	100000	2.077E+05	0.481	0.316	1.23E-04	0.867	3.85E-04
50	1000	7.712E+04	0.013	0.307	1.20E-04	1.686	7.49E-04
60	10	3.511E+04	0.00	0.173	6.74E-05	1.157	5.14E-04

Damage Σ   1.00

Table 3.14 Salford Arch O Live Load Parametric Strain

(calculations based on Equation 3.7)

Load	N	Ni	ni/Ni	Displacements (mm)		
				Intrados (r= 3125)		
(kN)	(Test)	(Figure - 4.17)		Qtr Point		
				δq (avg)	$\varepsilon p = \delta q/Rq$	Ps.$\delta q/Rq$
Elastic Strains (before first hinge)						
6	1.00E+06	3.26E+08	0.000	0.430	1.38E-04	5.78E-05
8	1.00E+06	8.30E+07	0.001	0.570	1.82E-04	7.66E-05
10	1.00E+06	2.86E+07	0.005	0.724	2.32E-04	9.73E-05
Plastic strains (following first hinge)						
12	1.00E+06	1.13E+07	0.019			
13	1.00E+06	7.95E+06	0.039	0.962	3.08E-04	1.29E-04
14	1.00E+06	5.45E+06	0.082	1.186	3.80E-04	1.59E-04
16	1.00E+06	2.89E+06	0.348			
18	340000	1.65E+05	0.506	2.555	8.18E-04	3.43E-04
		Damage Σ	1.000			

Table 3.13 Leeds Arch 02 and Table 3.14 Salford Arch O Parametric Strain-life values at quarter points at intrados are plotted in Figure - 3.26. Note Salford arch is 5 m span with different ring thickness. Therefore, a parametric correction is applied as.

[*2170 Ps*]

Where *Ps* = 1.9×10^{-4}, **Refer section 5.4.1 for detail**.

Multiplier = $2170 \times 1.9 \times 10^{-4} = 0.42$.

The Figure - further interpreted similar to elastic and plastic strain life curve called ε-N curve (2.4.2.3). MATLAB curve fitting is used to derive following relationships.

Linear load displacement behaviour, similar to Basquin's high cycle low strain (elastic) phenomenon.

$$\varepsilon_{e\prime} = bN + c_e \qquad \text{(eq 3.8)}$$

where constants, $b = -2.1 \times 10^5$

$c_e = 0.00025$

Non- Linear load displacement behaviour, similar to Coffin-Mandon low cycle high strain (plastic) fatigue regime.

$$\varepsilon_{p\prime} = cN + c_p \qquad \text{(eq 3.9)}$$

Where constants, $c = -4.711 \times 10^4$

$c_e = 0.00299$
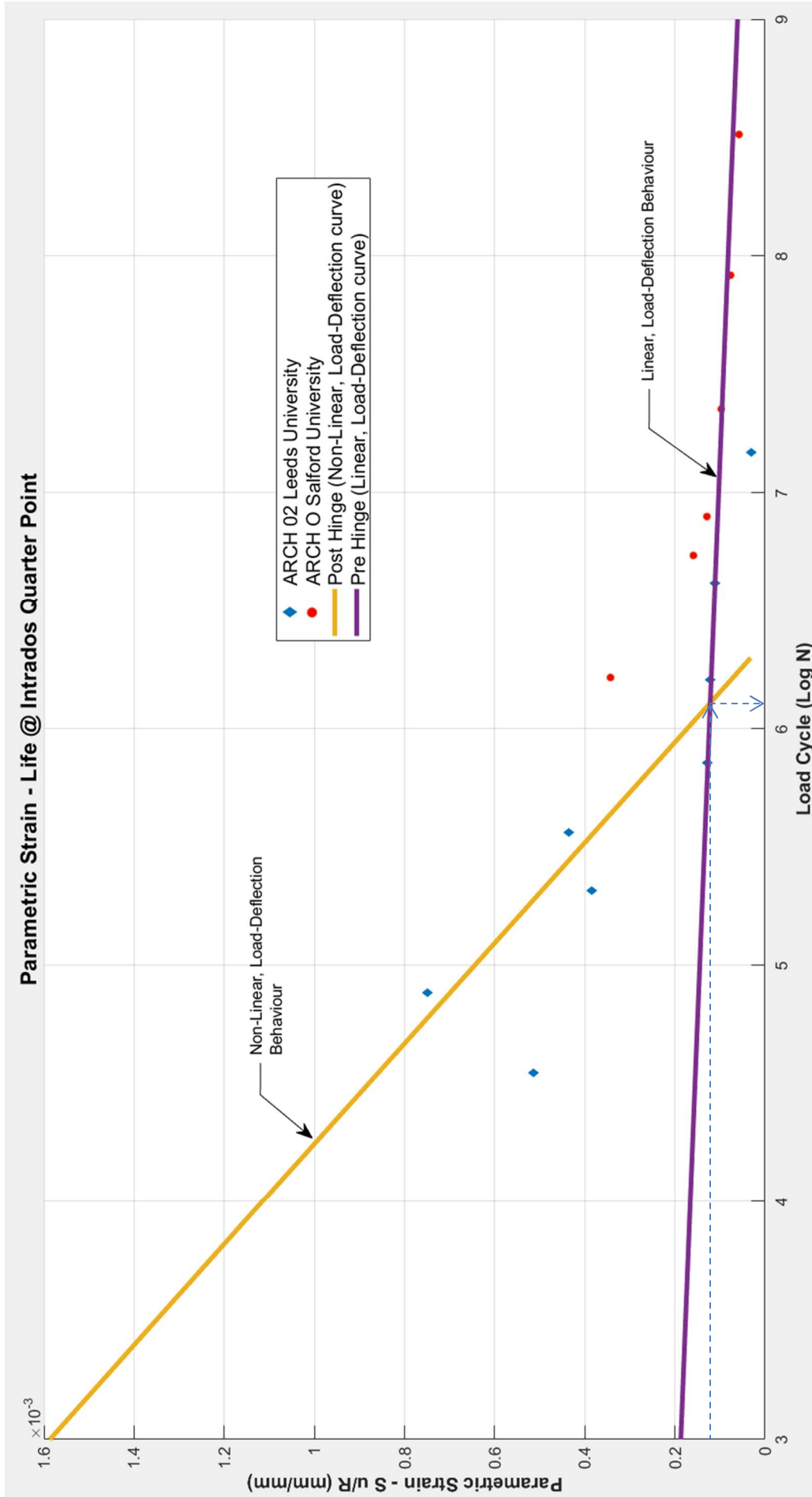
Figure - 3.26 Strain Life Curve for Arch at Intrados Quarter Point.

3.8 Summary

Finally, Figure - 3.26 and the equations 3.8 and 3.9 reasonably predicts the residual life of arches. Validation of Salford Arch O over the Leeds Arch 02 has shown excellent correlation between deflection and residual life of arch for pre-hinge linear load-deflection stage. Both these arches this is about this is between 30-35% of the load capacity.

Limiting design capacity according to The Structural Assessment of Underbridges (*NR/GN/CIV/025, 2006*) a live load factor of γ_{fL} = 1.4 and γ_{f3} = 1.35 is proposed with an additional dynamic factor of 1.8, this is [100/ (1.8x1.35x1.4) =] 30%. Critical point to note here, these factors are applied to virgin material properties and do not consider progressive damages.

Therefore, it is reasonable to consider for all practical acceptable load limits, arch load-deflection behaviour remains linear. When measures parametric strain is less than 100-150 $\mu\varepsilon$, aches are expected to survive more than $2x10^6$ cycles, see dotted line-arrows in Figure - 3.26. any factor of safety therefore needs to be based on present state of material properties determined through tests and calibration rather than assumptions.

In-situ measurements of the arch deformations are not only reliable, also have the additional advantage that the contributory effects of masonry defects, contributions from the backfill, spandrels and any transverse distribution of loadings are all captured. Therefore, this approach of parametric strain-life prediction will offer the real value to all practising engineers and the asset owners in assessing the residual life of arches as demonstrated in the previous sections.

Chapter 4
Numerical Model

Glossary

β	Drucker-Prager parameter
βy	Isotropic Masonry property parameter
δ	Displacement
$\varepsilon_R, \varepsilon_u,$	Tolerances
$\in$	Isotropic Masonry property parameter
η	Artificial damping
λ	Langrange multipler
$\mu\varepsilon$	Microstrain, i.e., 10^{-6}
μ	Friction coefficient
ϕ	Friction angle
σ	Stress
σ_c	Compressive Stress
σ_t	Tensile Stress
σ'_f	Fatigue strength coefficient.
σ_a, S	Stress amplitude
σ_1	Major principal stress
σ_3	Minor principal stress
σ_y	Drucker-Prager stress parameter
$\tau, \tau_u, \tau_d, \tau_t$	Shear stress
τ^0_N	Normal stress
τ^0_T	Shear stress
c, c_u	Cohesion
Cp	Contact normal stress
Cs	Contact friction stress
d_n, d_m	Debonding parameter
E	Young's modulus
E_b	Young's modulus of brick
E_m	Young's modulus of mortar

E_o	Initial Young's Modulus
F^a, F^{nr}	Applied loads
F_n	Normal force
F_t	Tangential force
G	Shear Modulus
G_b	Shear modulus of brick
G_m	Shear modulus of mortar
G_{cN}, G_{cn}	Mode I fracture energy
G_{cT}, G_{ct}	Mode II fracture energy
G_n	Normal fracture energy
G_t, G_s	Tangential fracture energy
h_m	Mortar thickness
h_b	Brick unit thickness
ΔK, ΔK_{th}, ΔK_{Ic}	Elastic stress intensity
K	Stiffness vector
K_i^T	Jacobian matrix
K_N, FKN, K_t, k_t	Normal stiffness
K_T, FKT, K_n, k_n	Shear/Tangential stiffness
ΔL	Gauge length
P, p	Contact pressure
Pe	Penetration between contact and target surface
$\{R\}$	*Residual vector*
t	Thickness
U, U_t	Displacement
ΔU_i	Increment vector
v	Poisson's ratio
x_n	Penetration into target face

4.1 Introduction

Discretisation using Sacco (*Sacco, Toti, 2010*) model described in 2.9.2 adopted for this research. ANSYS Workbench cohesive zone modelling (CZM) using contact elements is implemented. This section demonstrates numerical modelling of Masonry arches. Following sections describe the ANSYS features used in the modelling before analysing the Sacco (*Sacco, Toti, 2010*) model, Figure - 2.44. Further the model is validated against University of Salford Arch G under static loading.

4.2 Modelling Contact in ANSYS Workbench

Simplified micro modelling is adopted for this study. In this approach, each joint, consisting of mortar and the two unit-mortar interfaces, is lumped into an "average" interface while the units are expanded to keep the geometry unchanged. Masonry is thus considered as a set of elastic blocks bonded by potential fracture/slip lines at the joints. Poisson's effect of the mortar is ignored. This problem is compensated by FDEM modelling where each masonry elements are considered deformable instead of rigid (as in DEM approach).

The numerical modelling work has been performed by using a commercial finite element analysis package, ANSYS Workbench. This is so as the approach developed shall be readily available to the practising Engineers to apply in future for real Masonry Arch assessment. The work solely focused on the application of models to the problem of masonry arch bridges rather than the development of constitutive materials. Works of Wang (*Wang et al. 2014*) have already considered various approaches for numerical modelling within ANSYS and have proposed a better simulation in terms of load-displacement relationships.

"Contact" modelling refers to constituent surfaces interacting with each other and a changing status non-linearity. In physical sense, the contact surfaces do not interpenetrate. Surfaces transfer compressive, i.e. normal. and tangential. i.e. shear forces. Usually, they do not transfer tensile normal forces. One part of the surface is called "contact" side, and the other part is called "target" side. When one side is designated as the contact and the other side as the target, this is called "asymmetric" contact. If both sides are made to be contact and target this is called "symmetric" contact. For the contact algorithm, the Augmented Lagrange (Default) formulation is considered suitable for most problems. Pure Penalty can be used if contacts are occurring only on Edge or Corner. For the Augmented Lagrangian method and penalty method, normal and tangential contact stiffness are required. The amount of penetration between contact and target surfaces depends on the normal stiffness, illustrated in Figure – 4.1. The amount of slip/sticking contact depends on the tangential

stiffness. Higher stiffness values decrease the amount of penetration/slip but can lead to ill-conditioning of the global stiffness matrix and to convergence difficulties. Lower stiffness values result in certain amount of penetration/slip and produce inaccurate solution.
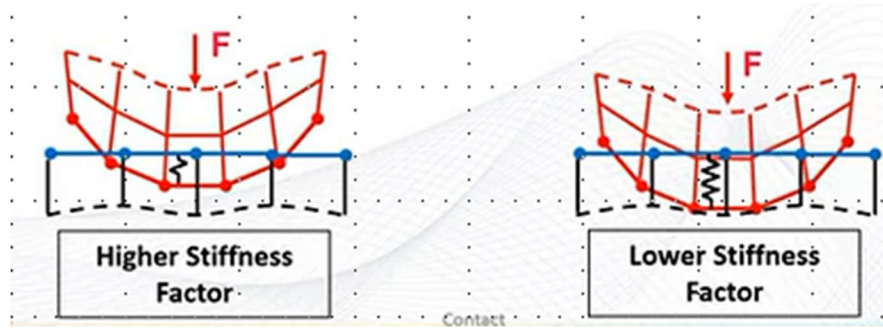
Figure - 4.1 Effect of Stiffness Factor.

Out of five contact options provided by ANSYS, this work will utilise "friction" contact option to model the interface. The friction interface is based on the Coulomb friction model, two contacting surfaces can carry shear stresses up to a certain magnitude across their interface before they start sliding relative to each other. This is known as "sticking". The equivalent shear stress, τ, at which the sliding on the surface begins as a fraction of the contact pressure, p, is expressed by the following equation:

$$\tau = \mu p + c \qquad \text{(eq 4.1)}$$

μ, is the friction coefficient and c, is the cohesion sliding resistance. Once the shear stress is exceeded, the two surfaces slide relative to each other.

The behaviour of these elements is controlled by many parameters with different features. Among the most important ones are the normal contact stiffness *FKN*, friction coefficient μ, penetration between contact and target surface *Pe* and tangential contact stiffness *FKT*. The stress state along the contact area is primarily determined by these factors which have the following relationships:

$$C_s = C_p \mu \qquad \text{(eq 4.2)}$$

And

$$C_p = P_e\, FKN \qquad \text{(eq 4.3)}$$

where *Cs* is the contact friction stress and *Cp* is the contact normal stress. The contact normal and tangential stiffness can be input as a factor or a constant. The contact normal stiffness is initially determined by the programme based on the material properties, element size, and the total number of degrees of freedom in the model. The

tangential contact stiffness is defined as a function of μ and the normal stiffness *FKN*. The amount of penetration between contact and target surfaces is mainly determined by the normal stiffness. The *FKN* and *Pe* are important parameters for finite element solution of sliding condition. Care should be taken for choosing these values especially when there is a lack of reliable date for material properties. For the detailed numerical implementation in the programme can be referred to the ANSYS contact technology guide (*ANSYS, 2009a*).

In their work on micromechanical computational strategy in modelling of the masonry structures Sacco (*Sacco and Toti, 2010*), has proposed the values of the mechanical properties adopted of the interface elements. The normal and shear stiffnesses have been determined homogenizing the composite material obtained considering two thin layers of brick and mortar:

$$FKN = \frac{E_b E_m}{h_b h_m \left(E_b/h_b + E_m/h_m \right)} \qquad \text{(eq 4.4)}$$

$$FKT = \frac{G_b G_m}{h_b h_m \left(G_b/h_b + G_m/h_m \right)} \qquad \text{(eq 4.5)}$$

where E_b, G_b and E_m, G_m are the normal and shear moduli of the brick and mortar, respectively. The brick-and-mortar thicknesses are h_b and h_m respectively. Typically, a mortar layer of 1–3 mm and a brick layer of 0.5–2 mm can be considered implicated in the interface degradation.

In their work on numerical (*Ravi et al., 2014*) modelling of masonry a numerical homogenisation of elastic brick masonry has been proposed. The composite brick prism model requires the young's modulus of isotropic masonry, which was suggested by (*Kuczma and Wybranowska, 2005*) as given in equation:

$$E = E_b \frac{1.25\in + 1}{1.25\in + \beta y} \qquad \text{(eq 4.6)}$$

where, E_b and E are the modulus of elasticity of brick and homogenised brick masonry, respectively.

$$\beta y = \frac{Youngs\ Modulus\ of\ Brick, Eb}{Youngs\ modulus\ of\ Mortar, Em} \qquad \text{(eq 4.7)}$$

$$\in = \frac{Heigh\ \ of\ brick, hb}{Thickness\ of\ Mortar, hm} \qquad \text{(eq 4.8)}$$

4.3 Cohesive Zone Modelling (CZM)

CZM have been extensively used for non-linear incremental analysis of interface debonding in few literatures Alfano (2001). Unlike other methods that are solely based

on fracture mechanics, CZM do not require the presence of an initial crack, can be more easily coupled with material and geometric non-linearities, and allow for efficient implementations in a finite element setting via interface elements. The fracture process, isolated from surrounding continuum constitutive material. is remarkably simple: traction versus separation. It is easy to implement the CZM in the finite element method using interface elements or contact elements. The CZM has been successfully used in solving the complicated fracture problems such as mixed mode fracture Bosch (*Bosch and Schereurs*, 2006), fatigue fracture Llu (*Llu et al.2010*) and dynamic fracture Miller (*Miller et al. 1999*).

The choice of a constitutive law for the cohesive zone is the most delicate aspect of this approach to fracture mechanics. Due to the small scale of the cohesive zone in most materials, it is experimentally quite difficult to determine the precise nature of the constitutive behaviour in the cohesive zone. Thus, it has become common to postulate a cohesive zone model based on the fracture characteristic of the material. for example, ductile or brittle modes. In the literature, several cohesive zone constitutive models can be found. Typical cohesive zone laws include linear decreasing form Hilerborg (*Hilerborg et al. 1976*) cubic and exponential form Needleman (*1990*), constant form Yuan (*Yuan et al. 1996*), bilinear form Geubelle (*Geubelle, Baylor,1998*), trilinear form Tvergaard (*Tvergaard, Hutchinson, 1992*) and polynomial form Chaboche (*Chaboche et al.1997*).

The debonding analysis in ANSYS, simulates the separation of bonded contact. It can be used to simulate interface delamination where the interface is modelled using bonded contact with the Augmented Lagrangian method or pure penalty method. A cohesive zone material must be used to define the traction separation behaviour of the interface. This analysis can be done with contact element Types like CONTA171, CONTA172, CONTA173, CONTA175, CONTA176 and CONTA177. The cohesive zone model consists of a constitutive relation between the *Tension* T acting on the interface of material. see Figure - 4.2, and the corresponding interfacial *Opening* δ. The definitions of traction and separation depend on the element and the material model.
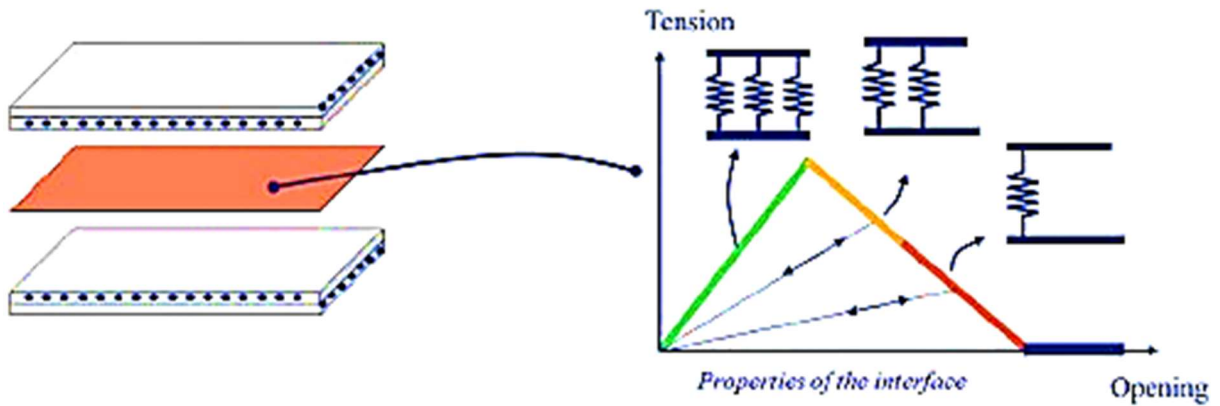
Figure - 4.2 Cohesive Zone Relation. (*ANSYS, R18.2 Theory*)

The debonding can be modelled in ANSYS in two ways:

4.3.1 Interface Element

For interface elements, the interfacial separation is defined as the displacement jump δ, i.e., the difference of the displacement of the adjacent interface surface,

$$\delta = U^{top} - U^{bottom}.$$

The interface elements are available for 2D and 3D models according to the nodes, like

- INTER202 – 2D - 4NODE COHESIVE
- INTER203 – 2D – 6NODE COHESIVE
- INTER204 – 3D – 16NODE COHESIVE, Figure – 4.3,
- INTER205 – 3D – 8NODE COHESIVE

These elements can be modelled with structural loads along with nodal or element temperature loads.
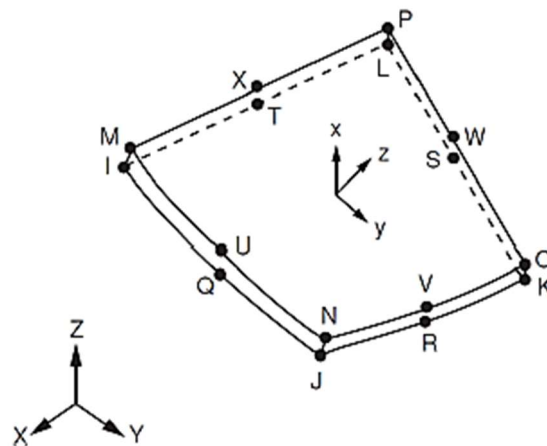
Figure - 4.3 INTER204 – 3D -16 Node Interface Element. (*ANSYS, R18.2 Theory*)

4.3.2 Contact Element

Analysis of delamination with contact elements is quite simple, can be used directly with the existing model with including few parameters. Debonding with contact elements has the following advantages over delamination with interface elements,

- Parts forming the interface can be meshed independently,
- Existing models with contact definitions can be easily modified for debonding,
- Standard contact and debonding can be simulated with the same contact definitions,
- Debonding can be used for various applications, for example, delamination, spot weld failure and stitch failure.

This method of delamination, using contact elements is used in this research. Debonding can be defined in all models that included surface-surface (CONTA171–174), node-surface (CONTA175), line-line (CONTA176) and line-surface (CONTA177). To enable debonding in a contact pair, the following contact options must be enabled for the contact element.

- Augmented Lagrangian Method or Pure Penalty Method (Keyopt (2) = 0 or 1)
- Bonded Contact (Keyopt (12) = 2,3,4,5 or 6)

Also, for the material model according to material data, the CZM with bilinear behaviour should be configure -d to enable delamination. There are two bilinear material models available.

- Bilinear material behaviour with traction and separation distance (TB, CZM command with TBOPT=CBDD)
- Bilinear material behaviour with tractions and critical fraction energies (TB, CZM command with TBDATA=CBDE)

4.3.3 Debonding Modes

In this thesis, the interface layer between two material/elements is very thin hence considered as negligible illustrated in Figure – 4.4.
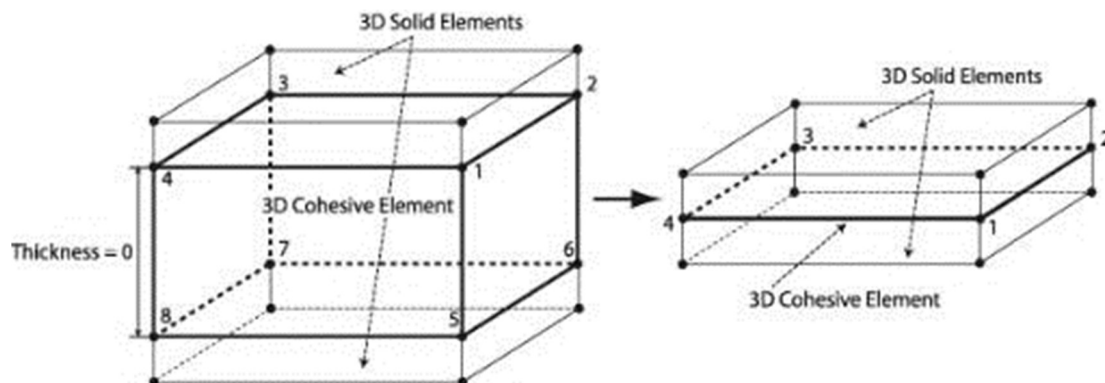
Figure - 4.4 Interface Element. (*ANSYS, R18.2 Theory*)

4.3.3.1 Mode I Debonding

Mode I debonding defines a mode of separation of the interface surfaces where the separation normal to the interface dominates the slip tangent to the interface. Refer to Figure – 4.5, the graph between the normal contact stress and contact gap behaviour shows a linear elastic loading (OA) and a linear softening (AC). The maximum normal contact stress is achieved at a point A. Debonding begins at maximum stress, point A, and is completed at point C while the normal contact stress reduces to zero. The area under the curve (OAC) is the energy released due to debonding. This energy is known as the critical fracture energy. The slope of the line OA determines the contact gap at the maximum normal contact stress, and this helps in determining the reduction in contact distance by normal contact stress. This shape of curve characterizes the fracture as brittle or ductile. After initiation of debonding, it is assumed to be cumulative. Any further loading and unloading occurs in a linear elastic manner along line OB.
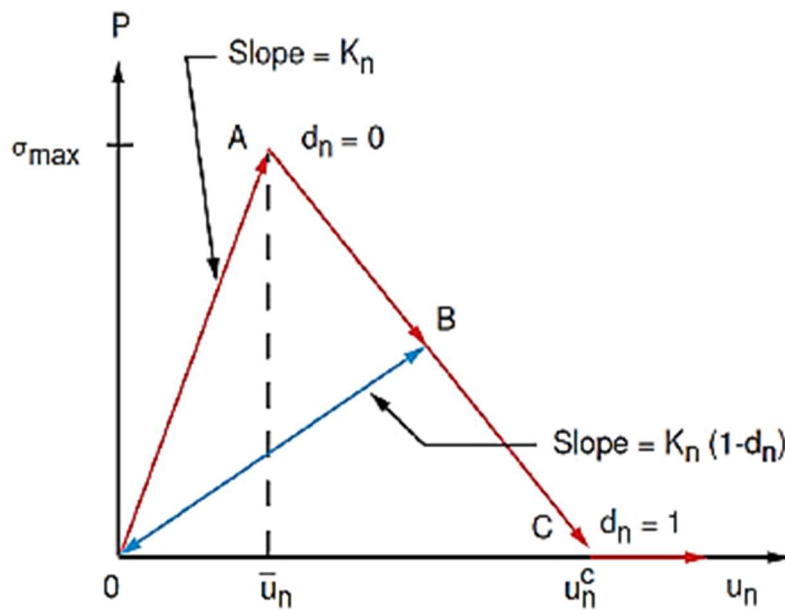
Figure - 4.5 Material Model – Bilinear Behaviour (*ANSYS, R18.2 Theory*)

The equation for the curve OAC can be written as

$$P = K_n U_n \left(1 - d_n\right) \qquad \text{(eq 4.9)}$$

where

  P- Normal contact stress (In tension),

  K_n- normal contact stiffness,

  U_n- contact gap,

  $\overline{U_n}$ contact gap at the maximum normal contact stress,

Un^c - contact gap at the completion of debonding,

dn- debonding parameter.

The debonding parameter for mode I debonding is expressed as

$$d_n = \left(\frac{U_n - \bar{U}_n}{U_n}\right)\left(\frac{U_n^c}{U_n^c - \bar{U}_n}\right)$$

(eq 4.10)

Therefore, the normal critical fracture energy is calculated with the below expression.

$$G_{cn} = 1/2\sigma_{max}U_n^c$$

(eq 4.11)

Where σmax- maximum normal contact stress.

For mode I, the tangential contact stress and tangential slip behaviour follows the normal contact stress and contact gap behaviour, which is expressed as

$$\tau_t = K_t U_t(1 - d_n)$$

(eq 4.12)

Where τt- tangential contact stress, Kt-tangential contact stiffness, Ut-tangential slip distance.

4.3.3.2 Mode II Debonding

Mode II debonding defines a mode of separation of the interface surfaces where tangential slip dominates the separation normal to the interface. The expression for the tangential contact stress and tangential slip distance behaviour is.

$$\tau_t = K_t U_t(1 - d_t)$$

(eq 4.13)

The debonding parameter for mode II is given as

$$d_t = \left(\frac{U_t - \bar{U}_t}{U_t}\right)\left(\frac{U_t^c}{U_t^c - \bar{U}_t}\right)$$

(eq 4.14)

In 3D stress state an isotropic behaviour is assumed and the debonding parameter is computed using an equivalent tangential slip distance.

$$U_t = \sqrt{U_1^2 + U_2^2}$$

(eq 4.15)

Where U_1 and U_2 – slip distance in the two principal directions in the tangent plane. They have individual tangential components. The tangential critical fracture energy is expressed as

$$G_{ct} = 1/2\tau_{max}U_t^c$$

<div align="right">(eq 4.16)</div>

Where τ_{max}- maximum tangential contact stress

The normal contact stress and contact gap behaviour follows the tangential contact stress and tangential slip behaviour:

$$P = K_n U_n (1 - d_t)$$

<div align="right">(eq 4.17)</div>

4.3.3.3 Mixed Mode Debonding

In mixed mode debonding the interface separation depends on both normal and tangential components. The equation for the normal and the tangential contact stresses are expresses as.

$$P = K_n U_n (1 - d_m)$$

<div align="right">(eq. 6.18)</div>

And

$$\tau_t = K_t U_t (1 - d_m)$$

<div align="right">(eq. 6.19)</div>

The debonding parameter is calculated as follows.

$$d_m = \left(\frac{\Delta_m - 1}{\Delta_m}\right)\chi$$

<div align="right">(eq. 6.20)</div>

where

$$\Delta_m = \sqrt{\Delta_n^2 - \Delta_t^2}$$

$$\chi = \left(\frac{U_n^c}{U_n^c - \overline{U_n}}\right) = \left(\frac{U_t^c}{U_t^c - \overline{U_t}}\right)$$

<div align="right">(eq. 6.21)</div>

The constraint on χ that the ratio of the contact gap distances be the same as the ratio of tangential slip distances is enforced automatically by appropriately scaling the contact stiffness values. For mixed mode debonding both normal and tangential contact stresses contribute to the total fracture energy and debonding is completed before the critical fracture energy values are reached for the components. Therefore, a power law-based energy criterion is used to define the completion of debonding.

$$\left(\frac{G_n}{G_{cn}}\right) + \left(\frac{G_t}{G_{ct}}\right) = 1$$

<div align="right">(eq. 6.22)</div>

where

$$G_n = \int P dU_n$$

$$G_t = \int \tau_t d U_t$$

Are, respectively the normal and tangential fracture energies.

4.3.4 Material Model – Bilinear Behaviour

This is a linear elastic material behaviour with linear softening characterized by maximum traction and critical fracture energies. To define this material in ANSYS, Table - 4.1 lists corresponding material constants.

Table 4.1 Bilinear Material Behaviour with Tractions and Critical Fracture Energies

CONSTANT	SYMBOL	DESCRIPTION
C1	σmax	Maximum normal contact stress
C2	G_{cn}	Contact gap at the completion of debonding
C3	τmax	Maximum equivalent tangential contact stress
C4	G_{ct}	Tangential slip at the completion of debonding
C5	η	Artificial damping coefficient

Artificial Damping - Debonding is generally accompanied by convergence difficulties in the Newton-Raphson solution. Artificial damping can be used to stabilize the numerical solution. It is activated by specifying the damping coefficient η. The damping coefficient has units of time and should be smaller than the minimum time step size so that the maximum traction and maximum separation values are not exceeded in debonding calculations.

Pinball Radius and Mesh Density - Mesh Density is an important parameter to detect the stress concentrations and stress distribution. Inflation at the contact face can help the solver to converge faster. When using a fine mesh for underlying elements of bonded surfaces, the pinball radius must be increased for that contact elements to ensure that it is greater than the maximum separation value in normal direction. If it is smaller, debonding calculation will be bypassed.

4.3.5 Solver – Newton-Raphson Method

The Newton-Raphson method is one of the most useful and best-known algorithms that relies on the continuity of the function. The finite element discretization process yields a set of simultaneous equations.

$$[K]\{U\} = \{F^a\}$$

where, $[K]$ – coefficient matrix, $\{U\}$ – vector of unknown degrees of freedom values, $\{F^a\}$ – vector of applied loads. If the coefficient matrix $[K]$ is itself a function of the unknown DOF values, then it becomes a nonlinear equation. The Newton-Raphson method is an iterative process of solving the nonlinear equations and can be written as

$$[K_i^T]\{\Delta U_i\} = \{F^a\} - \{F_i^{nr}\}$$

$$\{U_{i+1}\} = \{U_i\} + \{\Delta U_i\}$$

where $[K_i^T]$ – Jacobian Matrix (tangent matrix), i -subscript representing current iteration, $\{F_i^{nr}\}$ – vector of restoring loads corresponding to the element internal loads.
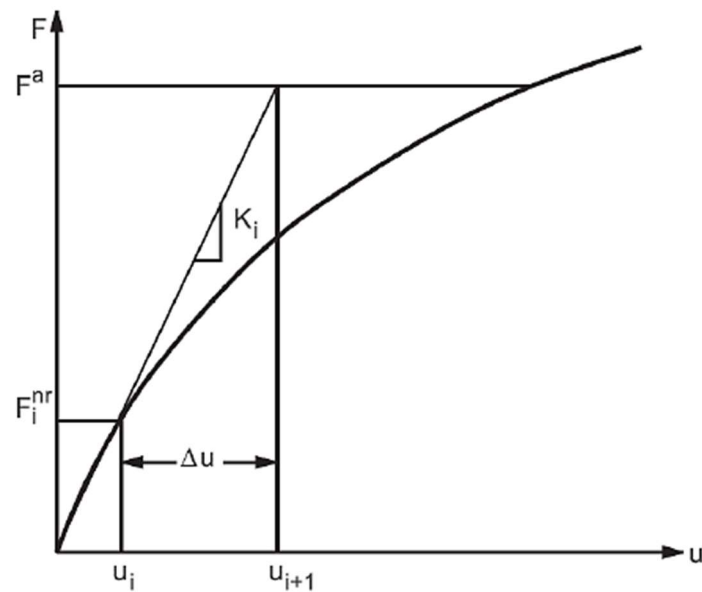
Figure - 4.6 Newton-Raphson Solution – One Iteration. (*ANSYS, R18.2 Theory*)

Both $[K_i^T]$ and $\{F_i^{nr}\}$ are based on the values given by $\{U_i\}$. The difference between the applied load and restoring internal loads is the residual or out of balance load vector. i.e., the amount the system is out of equilibrium. A single solution iteration is shown in Figure – 4.6.

The general algorithm is as follows:

- Assume $\{U_0\}$ usually the converged solution from the previous time step. On the first-time step, it is zero.

- Compute the updated tangent matrix $[K_i^T]$ and restoring load $\{F_i^{nr}\}$ from configuration $\{U_i\}$.
- Calculate $\{\Delta U_i\}$
- Add $\{\Delta U_i\}$ to $\{U_i\}$ to obtain the next approximation $\{U_{i+1}\}$
- Repeat until convergence criteria is obtained.

When the stiffness matrix is updated every iteration, the process is termed as full Newton-Raphson procedure. Stiffness matrix could be update less frequently using modified Newton-Raphson procedure.

Convergence - The iteration process continues until convergence criteria is achieved. The maximum number of allowed equilibrium iterations are performed to obtain convergence. Convergence is assumed when,

$$\|\{R\}\| < \varepsilon_R \, R_{ref}$$

$$\|\{DU_i\}\| < \varepsilon_U \, U_{ref}$$

Where $\{R\}$ is residual vector, $\{R\} = \{F^a\} - \{F^{nr}\}$

This is the right-hand side of the Newton-Raphson equation. $\{\Delta U_i\}$ is the DOF increment vector, ε_U and ε_R are tolerances and R_{ref} and U_{ref} are reference values. $\| \ \|$ is a vector norm, that is a scalar measure of the magnitude of the vector.

The convergence is obtained when size of the residual is less than a tolerance times a reference and/or when the size of the DOF increment is less than a tolerance times a reference value. The default is to use out-of-balance convergence checking only. The default tolerances are 0.001 for both.

4.4 Contact Algorithm

ANSYS offers various kinds of contact formulations. It defines the behaviour of contact and target bodies and prevents/minimizes penetration. To define delamination, it is suitable to use the below algorithms.

4.4.1 Augmented Lagrange Method

This method reduces the possibility of ill conditioning of the sub problems that are generated by introducing explicit Lagrange multiplier at each step into the function. It also tends to yield less ill conditioned sub problem and iterates to stay strictly in the feasible region. In structural mechanics, the function is potential energy Πp that variables are degree of freedom $\{D\}$, and the prescribed relations are multipoint constraints. The unknowns become $\{D\}$ and the Lagrange multipliers. To impose constraints by Lagrange multipliers, the constraint equation is multiplied by a row

vector containing as many Lagrange multipliers as there are constraint equations. This is expressed as.

$$F_n = k_n x_n + \lambda \qquad \text{(eq 4.23)}$$

Because of the contact pressure λ, Augmented Lagrange formulation is less sensitive to normal stiffness. Larger the value of the Lagrange multiplier, larger the dividend to relax the constraint or the larger the penalty to tighten the constraint. The advantage is that the original stiffness is not altered when constraints are applied. Therefore, constraints can be changed without having to refactor the original stiffness. This property is helpful in problems where different load cases involve different constraints, or in a contact problem where constraints increase in number as the load level increases.

4.4.2 Pure Penalty Method

The objective of the algorithm is to obtain an optimum point of the objective function and satisfying the constraints. Penalty function is designed to quantify this balance and control the algorithm. A sub step will be accepted only if it leads to a sufficient reduction in the penalty function. Whenever a contacting point penetrated normally by an amount, x_n into a target face, it will be pushed back by a normal force, F_n. This is expressed as

$$F_n = k_n x_n \qquad \text{(eq 4.24)}$$

Where k_n is called the Normal Stiffness of the contact region. A normal stiffness has no real physical meaning; it is just a numerical parameter of the penalty algorithm. Solution convergence behaviour is usually sensitive to this parameter. A larger k_n usually gives a more accurate solution but may arise convergence issues. Reducing k_n usually helps convergence but results an increasing penetration.

If tangential sliding, is prohibited, a similar treatment can be implemented. Whenever a contacting point slides tangentially by an amount, it will be pushed back by a tangential force.

$$F_t = k_t x_t \qquad \text{(eq 4.25)}$$

The simulation settings must be defined carefully to obtain desired results. The above said parameters are of high importance in achieving convergence of the defined finite element simulation. Contact formulation algorithm is significant because the delamination behaviour depends on this parameter. Solver can be set program defined if the user is not sure of the method, while the software will automatically solve using Newton-Raphson method. Since there will be fracture in the material the convergence of the problem will be quite slow.

4.5 Model Validation

4.5.1 ANSYS CZM Validation

In this section a single course brick masonry arch has been validated. The numerical results are compared with the experimental work of Cancelliere (*Cancelliere et al. 2010*). Geometrical data for the tested arch are shown in the Figure - 2.46. internal radius r = 456 mm, width w = 255 mm, thickness t = 120 mm, height f = 510 mm, abutment angle = 8º and internal distance between the abutments, da = 900 mm. The arch was built in the experimental laboratory using 23 standard clay bricks and 22 mixed mortars and the conventional numeration of bricks is clearly shown in Figure - 2.46. In the first part of the experimental tests, the arch in addition to its weight was subjected to a point load of 650 N was applied with an eccentricity df = 140 mm with respect to the keystone; in particular, the load was applied on the 14th brick by the action of a hydraulic jack. The arch was restrained at the springs by very rigid steel elements, to avoid horizontal sliding and to generate an undesired failure mechanism. The experimental test of the unreinforced masonry arch showed that the first hinge appeared on the extrados between the mortar number 13 and the clay brick number 14, followed by the second hinge formed on the intrados between the mortar number 7 and the clay brick number 8, the third hinge formed between the extrados between the mortar number 1 and the clay brick number 1, and the fourth hinge formed on the intrados between the mortar number 19 and the clay brick number 19 (Figure - 2.45). The mechanical properties of the brick and the mortars considered are mentioned in the Table 2.5. The interface properties considered are listed in Table 2.3.

The normal and shear stiffnesses are determined homogenizing the composite material obtained considering two thin layers of brick and mortar using equations 4.4 and 4.5 respectively. The brick-and-mortar thickness are set h_b = 0.5 mm and h_m = 1 mm, respectively. The Figure - 4.7 demonstrates the validity of the ANSYS analysis and output in comparison to a tested arch.
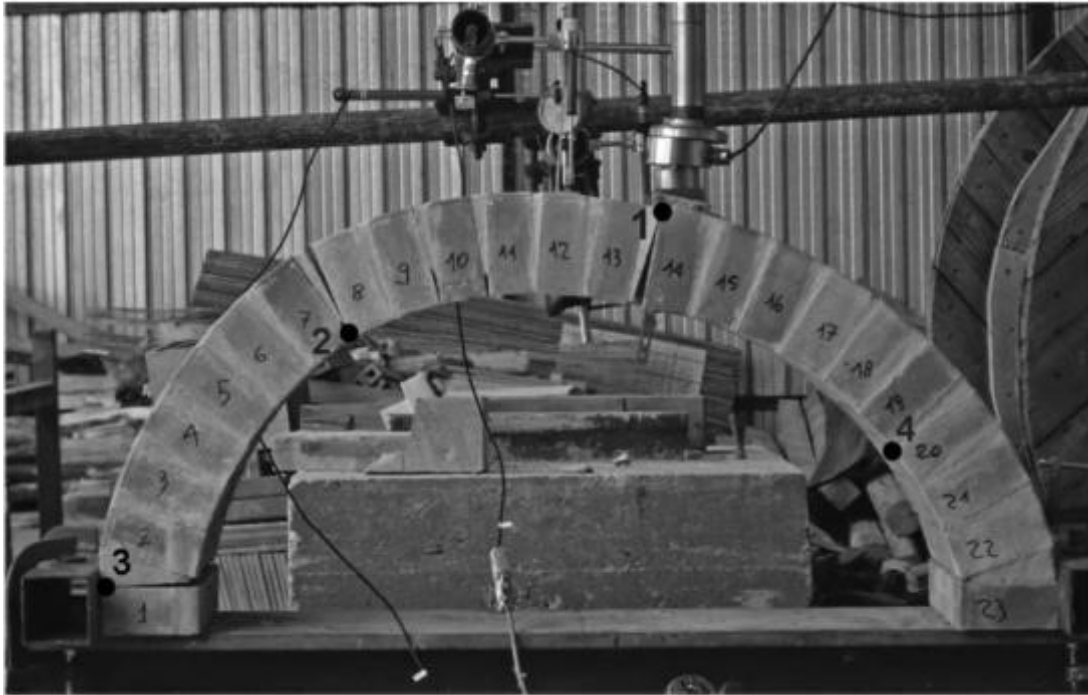
a) Laboratory Image of The Loaded Arch (*Alfano and Sacco 2010*)
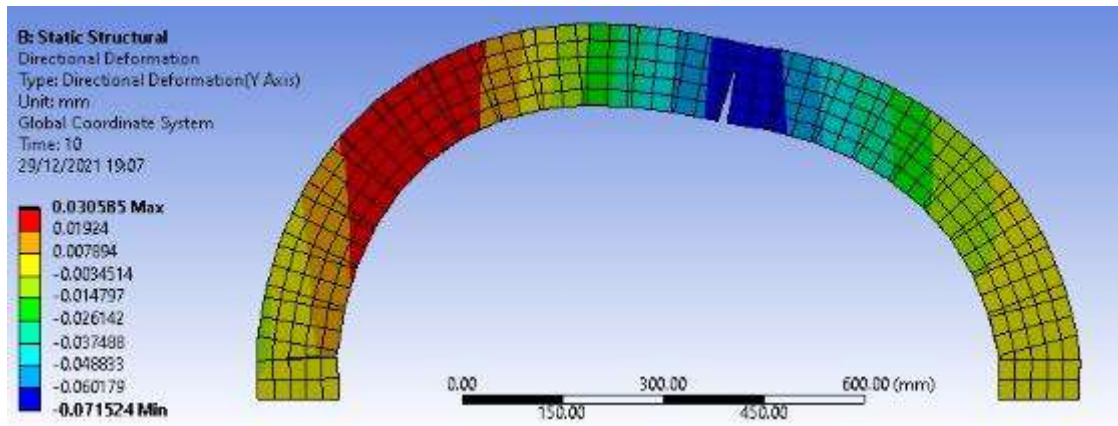
b) ANSYS – CZM modelling result.

Figure - 4.7 Model Validation Using CZM in ANSYS

4.5.2 Test Arch Validation (Non-linear)

In this section the Salford University Arch G is validated. Aim of this validation is to demonstrate that behaviours of masonry arches are non-linear. Cohesive zone modelling, Figure – 4.8, discussed in previous section extended to tested arches with material properties determined at laboratory. Masonry prism and interface properties are ascertained and confirmed by convergence comparison of deformations measured during the laboratory tests.
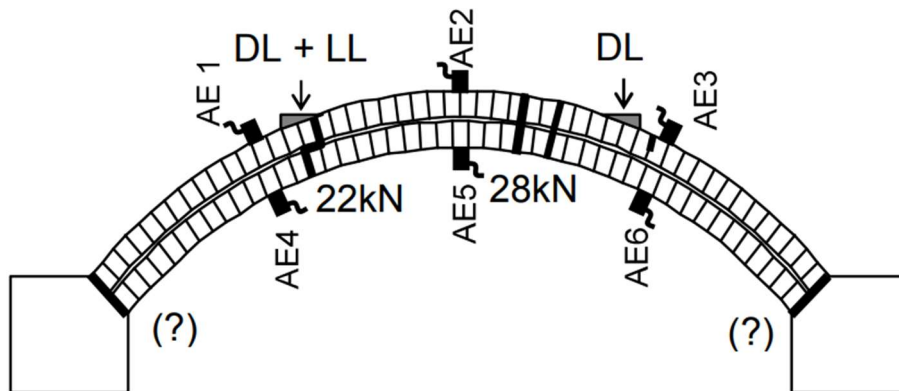
a) Salford Arch G Schematic
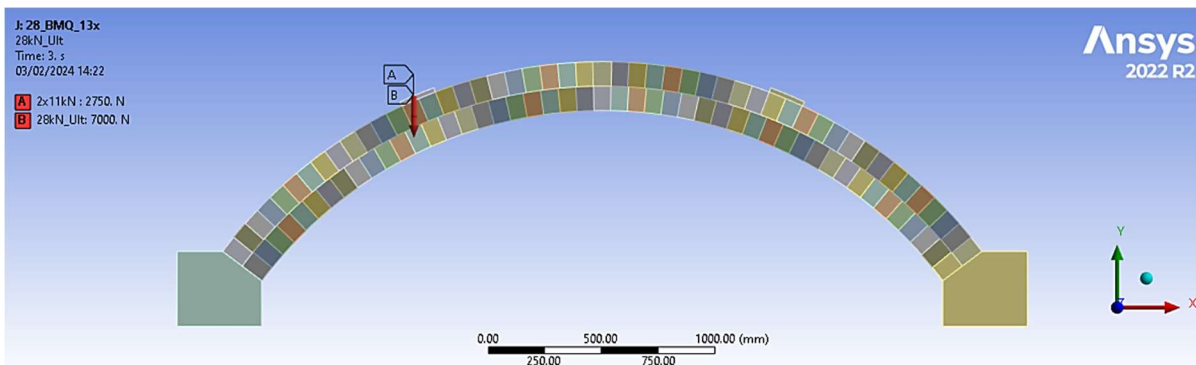
b) ANSYS – Model

Figure - 4.8 ANSYS Geometry and Model for Arch G.

The "simplified micro model" is considered, which combines bricks and mortar as continuum elements with prism properties. The interface between bricks and mortar is modelled by "interface" elements that represent the discontinuities. Representation of three modelling are illustrated in Figure – 4.9

(a) Detailed Micro-Model   (b) Simplified Micro-Model   (c) Macro-Model
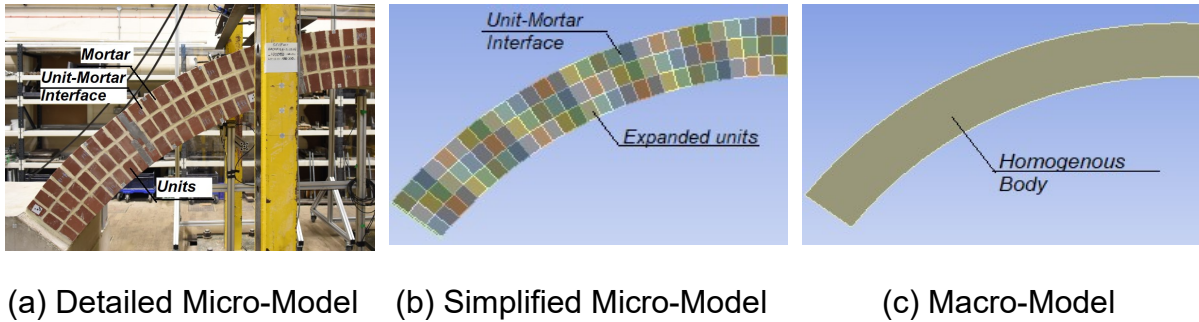
Figure - 4.9 Masonry Modelling Approaches.

This validation has been approached in two stages. In stage one (Stage I) masonry properties have been validated. Then interface properties are ascertained in stage two (Stage II).

4.5.2.1 Stage I - Masonry Prism

Masonry prism has been modelled with Drucker-Prager plasticity shown in Figure – 4.10 in terms of principle stresses. This is a rate-independent plasticity model available for frictional materials such as soil and concrete developed from the Mohr-Coulomb law (*Chaimoon and Attard, 2007*, *Mynarz and Mynarzova, 2018*). Following constants could be used as the input values: the cohesion value.
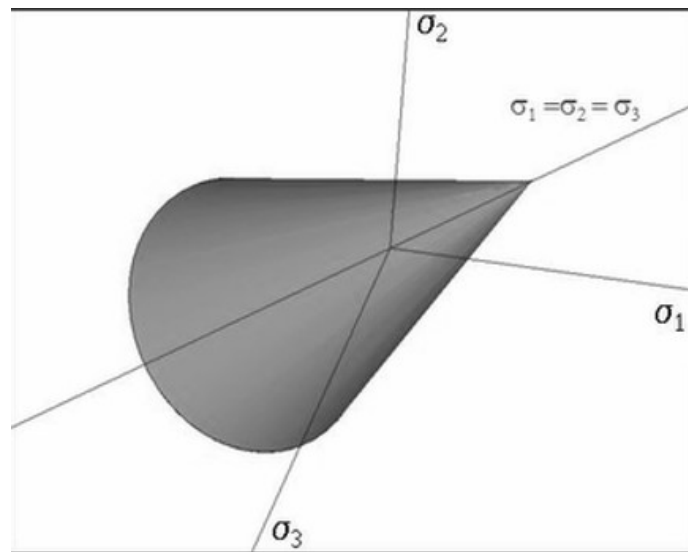
Figure - 4.10 Drucker Prager Yield Surface in the Principal Stress Pane. (*Mynarz and Mynarzova, 2018*)

$$c_u = \frac{\sigma_y \sqrt{3}(3-sin\varphi)}{6.cos\varphi}$$ (eq 4.26)

and the angle of internal friction

$$\varphi = sin^{-1}\left(\frac{3\sqrt{3}\beta.}{2+\sqrt{3}\beta}\right)$$ (eq 4.27)

For known compressive (σ_c) and tensile (σ_t) stresses of material. required constants can be calculated following the material parameter β and σ_y

$$\beta = \frac{\sigma_c-\sigma_t}{\sqrt{3}(\sigma_c+\sigma_t)}$$ (eq 4.28)

$$\sigma_y = \frac{2.\sigma_c\sigma_t}{\sqrt{3}(\sigma_c+\sigma_t)}$$ (eq 4.29)

4.5.2.2 Stage I - Secant Modulus

Following two approaches have been considered for comparison.

IRS 70778 *(2020)*

Uniaxial compressive strength, σ_c = 6.7 N/mm² (refer equation 3.5)

Uniaxial tensile strength, σ_t = 0.3 N/mm² (see Figure - 4.11)

Bi-axial compressive strength = 1.2x σ_c = 8.04 N/mm²

Secant modulus have been derived using the IRS 70778 *(2020)* to start the analysis.
        = 1000 x 6.7 = **6700** N/mm²

Page (*1983*)

Uniaxial compressive strength, σ_c = 11.7 N/mm² (Figure - 3.7)

Uniaxial tensile strength, σ_t = 0.3 N/mm²

Bi-axial compressive strength = 1.2x σ_c = 14.04 N/mm²

        = 1000 x 11.7 = 11700 N/mm²

As seen above recommended guidance vary significantly. For confirmation, secant modulus is confirmed by comparing crown deformations measured during the test. Once the load is stabilised, measurements are noted.

Properties derived using the UIC recommendations for the inspection, assessment, and maintenance of masonry arch bridges (*2020*) provide better results in comparison

to the recommendations of by Page (*1993*). The EC6 formulas derived for building masonries are not considered for application to masonry arches.

Uniaxial tensile strength of the masonry prism is found to influence arch results. Prism cracking become pronounced over interface separation. Arch failures always initiate from masonry mortar interface. Lower values of tensile strength shown single separation. Higher tensile strength made the arch stiffer and failed similar like the loads punching though the arch. Arch behaved as expected and satisfactorily converged with uniaxial tensile strength, σ_t = 0.3 N/mm^2.
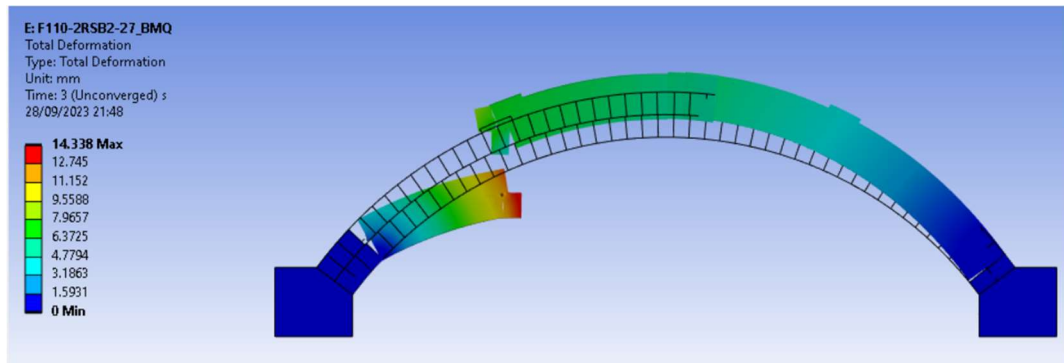
a) uniaxial tensile strength, σ_t = 0.4 N/mm^2.
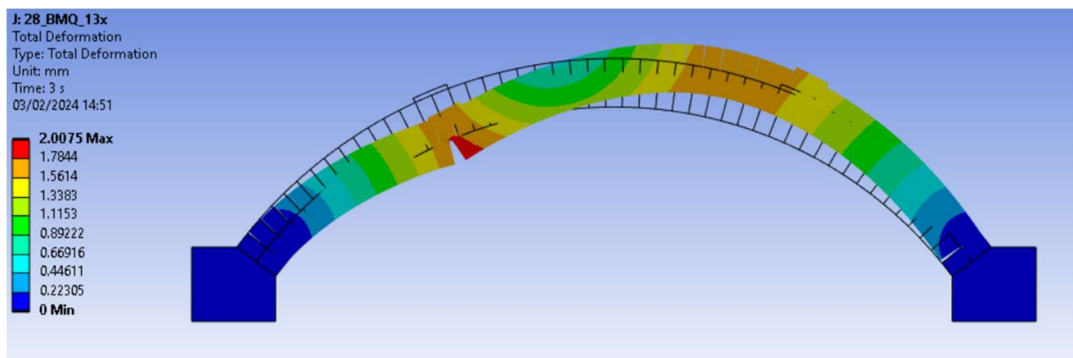
b) uniaxial tensile strength, σ_t = 0.3 N/mm^2.
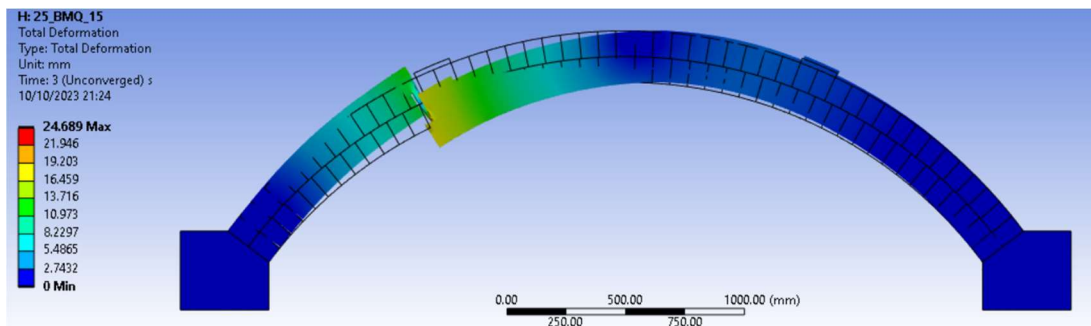
c) uniaxial tensile strength, σ_t = 0.2 N/mm^2.

Figure - 4.11 Masonry Prism Ultimate Tensile Strength.

4.5.2.3 Stage II - Interface properties

During this thesis research University of Leeds secured further work funded by the EPSRC project 'Exploiting the resilience of masonry arch bridge infrastructure: a 3D multi-level modelling framework' (ref. EP/T001348/1). Same brick and mortar units have been tested in detail and later published (*Liu et al. 2023*). These tests results are used for the modelling purposes.

Masonry has little resistance to horizontal loads acting parallel to the bed joint. This is seen in previous section and discussions that most masonry walls develop cracks at the unit-to-mortar interfaces due to the lower tensile strength of discontinuities. The tensile strength and shear behaviour of unit-to-mortar interfaces are influenced by a variety of factors, including the surface texture and water absorption of units, the mortar composition, temperature, and humidity condition. For numerical analysis, bond properties between bricks and mortar can significantly affect the out-of-plane behaviour of masonry. Direct tensile tests and triplet shear tests performed in the study to comprehensively assess the bond properties of unit-to-mortar interfaces (*Bowen, 2023*) discussed below for relevant properties.

Results from the cross-couplet and full couplet specimens have shown a high degree of variance from 0.043 N/mm^2 to 0.342 N/mm^2, with an average value of **0.166** N/mm^2 and a CV of 54.3%. The significant scatter in the data was due to various factors, including the inherent variations in material properties, inconsistent quality of the workmanship of the bricklayer, differences in surface texture and the suction behaviour of bricks etc. The dispersed results obtained under laboratory conditions also emphasised the heterogeneity of real masonry arch bridges.

Masonry triplet shear tests were carried out on thirteen specimens under different levels of pre-compression (i.e., 0.1, 0.2, 0.6, and 1.0 N/mm^2), following the requirements outlined in (*BS EN 1052-3*). All masonry triplets were constructed with type A dry bricks bonded with 10 mm thick mortar joints. Joint thickness is same as the main arch construction. Corresponding to normal strength of 0.1 N/mm^2 peak shear strength of **0.292** is recorded. The shear box strength in Table - 3.4 resulted 0.212 N/mm^2.

The peak shear strength and the linear regression analysis results suggested that the friction angle and cohesion of the unit-to-mortar interface were equal to 36.3º and 0.29 N/mm^2, respectively. While the values of residual friction angle and residual cohesion were equal to 31.0º and 0.12 N/mm^2, respectively. Interestingly these values compare reasonably well with the Table -3.5 Mohr-coulomb properties determined by tri-axial compression test.

Following Table – 4.2 summarise masonry-mortar Interface properties taken from EPSRC reference (*Liu et al. 2023*).

Table 4.2 Interface Properties

τ_N^0 (N/mm^2)	G_N (N/mm)	τ_S^0 (N/mm^2)	G_S (N/mm)
0.166	0.01-0.04[1]	0.3	0.05-0.125[1]

[1] - Non-linear behaviour of masonry under tension, (*Pluijm, 1991*), (*Chaimoon and Attard, 2007*) tabulated wide range of values. This validation is performed with combination of G_N and G_S.

Masonry have been modelled using SOLID186 elements and interfaces have been modelled using the CONTA174 elements, shown in Figure – 4.12 for illustration. The contact stiffness has been retained as programme controlled to start with. Main objective of this analysis is to validate the stiffness and interface properties for the initial loadings.
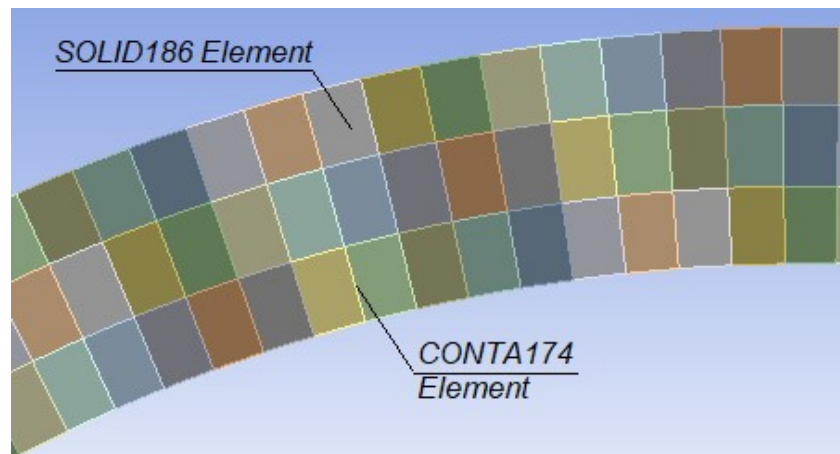
Figure - 4.12 ANSYS Model with SOLID186 and CONTA174 Elements.

4.5.2.4 Numerical Model Validation

Stage I analysis have only considered the secant modulus and uniaxial tensile strength of the masonry. To verify the interface response, series of analysis have been performed. Mode I fracture energy and guided tensile strength of the unit mortar interface influenced the convergence. In addition, mesh size also improved convergence.

Mode I tensile strength of 0.15 N/mm^2 (Figure - 4.13, model reference 25_BMQ_14) and fracture energy of 30 N/m (i.e., 0.030 N/mm) shown best convergence but only up to 25 kN, about 90% of the failure load (28 kN) measured during text.
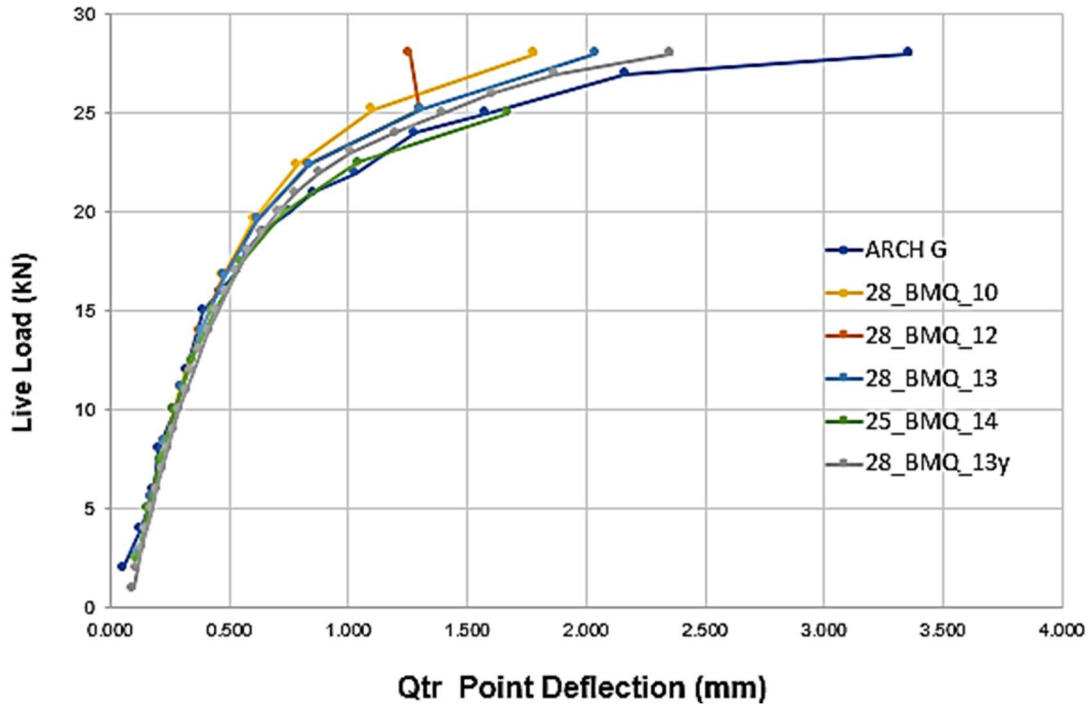
Figure - 4.13 Numerical Load-deflection Plot Compared with Test Results of Arch G.

To improve load-deflection convergence the fracture energy is increased to 40N/m (i.e., 0.04 N/mm) in model 28_BMQ_10, Figure - 4.13. Model converged due to reduced deflection. Model behaved very similar up to 15-16 kN, around 55% of failure load, of load for all analysis, then increased fracture energy affected the behaviour.

Further analysis with reduced fracture energy to 30 N/m (i.e., 0.03N/mm) improved but increased tensile strength to 0.166 N/mm^2 deflection but diverged at 25 kN. This problem is improved through finer mesh size, from 20 mm to 15 mm. Mesh sizing of 1/5th of minimum brick size improved convergence and hence recommended. Improved mesh size analysis in model 28_BMQ_12, Figure - 4.13 is considered reasonable convergence between the numerical model and laboratory tested arch.

Further convergence is achieved, 28_BMQ_13y, after calibrating normal stiffness to suit laboratory tests. The brick-and-mortar thickness are set h$_b$ = 0.5 mm and h$_m$ = 1 mm, respectively.

Following properties are therefore confirmed,

Mesh size: 1/5th of Brick units.

Secant Modulus: 6700 N/mm^2

Contact Normal Stiffness: 242 N/mm^2/mm.

Mode I; tensile strength = 0.166 N/mm^2, Fracture energy = 0.03 N/mm

Mode II: shear strength = 0.3 N/mm^2, Fracture energy = 0.06 N/mm

4.6 Failure Mode Validation through Crack Width

Numerical model from previous section is now extended to calculate crack width for the arch. Interface modelling offers the advantage of calculating crack widths even at low loads. Only visible cracks are noticeable to bridge inspectors and assessors. Micro cracks remain unnoticed therefore opportunity for early warnings is missed out, see Figure - 4.14.
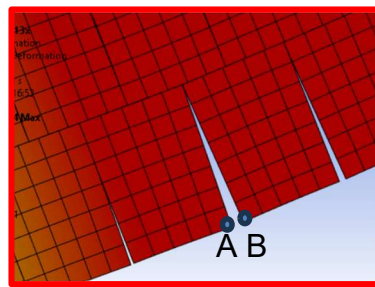
a) Cracks visible in scaled view.
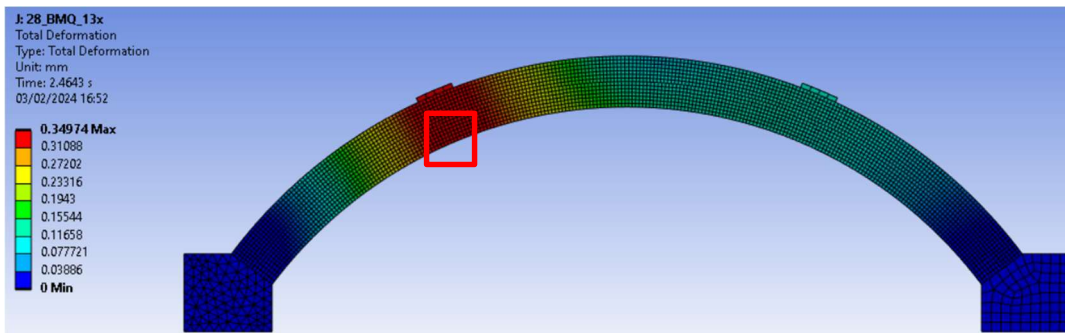
b) Micro cracks not visible in true scale.

Figure - 4.14 Crack widths Measure From Model.

It is possible to measure crack width from the model by extracting coordinates of units before and after analysis. The distance between coordinates at A, B, Figure - 4.14 a) is the measure of crack width under the load. Figure - 4.15 plots the calculated crack widths at the intrados crack widths for the Arch G. Discussion on damaged crack widths

and its relevance to residual life of arch is detailed in next chapter through crack width and life curve.
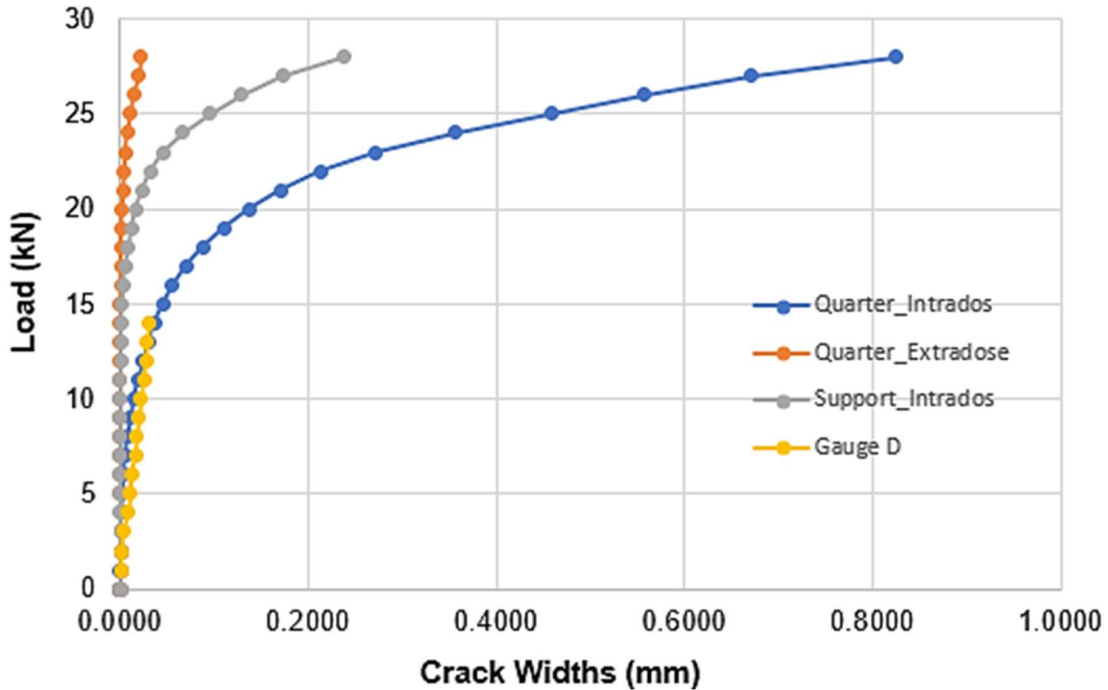
Figure - 4.15 Numerical Load-Crack Widths Plot (validation with Gauge D).

Beside measuring horizontal and vertical deflections at ¼ and ¾ span using LDVT, additional strain gauges were installed. Vibrating wire gauges (GAUGE TYPE T/S/R. 139 mm gauge length) used to monitor surface strains. Strain gauges have a range of 0.5-3000 microstrains and were attached to masonry surface with epoxy resin adhesive. During test, clear change of strain was noticed from 14 kN load indicating radial hinge opening crack width progression correlate with the strains measured by gauge B, Figure - 4.16 b). Openings were visually observed from 22 kN when crack width as per above Figure - 4.15 reached 0.2 mm.
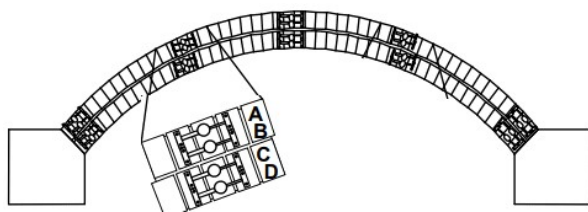
a) Strain-gauge locations   b) Load-strain plot
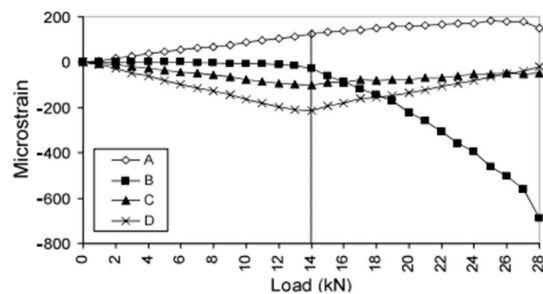
Figure - 4.16 Arch G Load-strain. (*Sustainable Bridges, 2007*)

Notably gauge D strain reaches 200$\mu\varepsilon$ change in strain is noted. Salford University test also recorded acoustic emission and first significant emission was recorded at 14 kN. Gauge D strains are converted to ΔL by multiplying with the gauge length of 139 mm and plotted in Figure - 4.15 for verification. After 14 kN the gauge reversed, indicating that masonry has undergone changes. This is a limitation of using strain gauges for brick arches. Therefore, this thesis relied on measuring deflection and converting it to a parametric strain, see section 3.5 for more details.

4.7 Discussion on Numerical Modelling

UIC recommendations for the inspection, assessment, and maintenance of masonry arch bridges (2020) offer better guidance on material properties and should be preferred over other similar references. All previous works on masonry tests, properties and modelling were based on compressive strength of prisms. For arches tensile strength and mode I fracture energies are found to have critical influence on their behaviour. Therefore, future assessment of masonry arches needs to include tensile strength tests of in-situ specimen. UIC guidance need to extend and include fracture energy determinations and recommended properties for analysis.

As guidance mesh sizing of 1/5th of bricks minimum dimension is found suitable for convergence of numerical models.

Masonry arches are satisfactorily modelled in ANSYS Workbench platform using CZM interface elements. Load-deflection and crack width follow expected arch behaviour under applied loading. Discretisation using Drucker Prager plasticity for masonry prism and cohesive zone representation of interface elements results in non-linear representation of arch. Load-deflection plot in Figure - 4.13 clearly validates non-linear response.

Furthermore, interface modelling approach allows crack width calculation even at very low loads. Therefore, it is possible to predict micro cracks in masonry arches. Importance of crack width calculations in discussed further in next chapter.

Once masonry interface starts separation, strains become unresponsive, refer gauges C, D Figure - 4.16 b). Therefore, tangential strain analogy, section 3.5, from direct deflection is derived for this thesis.

Chapter 5
Proposed Fatigue Damage Model for Arch

Glossary

εp	Parametric strain
γ_{FL}	Live load factor
γ_{f3}	Factor for inaccurate assessment of loading
$\mu\varepsilon$	Microstrain, i.e., 10^{-6}
B	Width of arch
C_{min}	Abnormal load factor
δ	Deflection
df	Load eccentricity
dt	Ring thickness
δ_q	Numerically calculated deflection at quarter point
$\delta_q\, S$	Measures in-situ deflection at quarter point
D	Damage variable
E	Young's modulus
E_o	Initial Young's modulus
f_d	Design capacity
f_k	Characteristic value
F_b	Arch brick bond factor
I	Moment of Inertia
K_{N0}	Initial normal stiffness
K_N, FKN, K_t, k_t	Normal stiffness
K_T, FKT, K_n, k_n	Shear/Tangential stiffness
L	Arch span
n_i	Number of cycles accumulated
N, N, N_c	Load cycle
N_u	Maximum Load Cycle
N_f	Number of cycles to failure
P_{LL}	Applied live load
Ps	Section property parameter
r, Rq, Rc	Radius, Radius at quarter point, Radius at crown respectively

5.1 Introduction

Repeated loading, even at low intensities, weakens quasi-brittle materials like masonry constituted of bricks and mortars. Prolonged and repetitive application of varying loads is responsible for degradation of the material properties, see Section 2.4.5 for literature review. Cyclic loading causes growth of small imperfections, always present between brick-and-mortar joints, leading to separation of their interfaces. Overall damaging parent geometrical as well as material properties of the arch and therefore reducing stiffness. Fatigue failure process is characterised by four stages of crack growth, refer Figure - 2.26. The continued deformation of Arch 01 under constant amplitude cyclic loading even at its low intensities, i.e., stresses, have established underlying decreasing stiffness due to cyclic loading. The damage model proposed in the following section therefore based on the stiffness degradation.

5.2 Limitations of Limit State Based Analyses

Current guidance for highway and railway bridges assumes that masonry's 'safe' and serviceable capacity is when $f_d < 0.4f_k$ (*CD 376, 2020*, *UIC IRS 70778-3, 2020*) where f_d is the design stress and f_k is the masonry strength in compression. Multiple commercially available and popular programmes are available to practising engineers for assessment of masonry arch bridges. They are based on experimental formulae, 2D-models and finite-element models and discrete-element models (2D as well as 3D), referred in Section 1.3.2. Basic understanding starts with a two-hinge arch. Minimum load applied to a fixed position, that causes the arch to turn into a mechanism, i.e. four hinges. This approach was further extended by Heyman (*1982*) introducing thrust lines. The arch become mechanism when thrust lines become tangential at four locations. Arch geometry, backfill and compressive strength of masonry prism are principal parameters required for accurate estimation of the collapse load.

Archie-M applies the traditional thrust line analysis combined with a zone of thrust for modelling finite crushing strength. Collapse load is estimated by varying the load factor until the thrust line touches an external border of the arch and making a fourth hinge.

RING uses a rigid-plastic block formulation where the collapse load is found by maximizing the load factor with linear programming. The constraints are equilibrium, no-tension, no-sliding and crushing of masonry. The software allows to analyse the ultimate limit state, determining the amount of live load that can be applied before structural collapse; and permit investigation of the mode of response when supports undergo small movements.

Further elasto-plastic models have started to evolve, not yet a preferred practising tool this is not discussed in detail here. Instead, cohesive zone based ANSYS numerical

model discussed in previous section is now implemented for the ARCH 02. Following sections discuss the load capacities calculated based on all three methods.

5.2.1 ARCH02 Archie-M & RING Analysis

In this section both Archie M and RING analysis is performed for ARCH02 to assess theoretical load capacities. Both software's are customised for practical arches with backfill and loaded with regulated vehicles. Following modifications are applied to represent the bare, or skeletal. arch model in absence of regular backfill in laboratory.

To perform ARCHI-M analysis, road profile is modelled as three-point segment to avoid backfill.

Loads modelled as multiple axle loads.

Double axles to represent 2 x 11 kN constant load and 4 single axle loads required to reach mechanism, see next image.

Summary of results, refer Appendix A1 for details,

Effective width = 3140 mm

Total single axle loads = 4 x 112.82 kN = 451.28 kN

Capacity of 657 mm arch = 451.28 x (657/3140) = **94.4 kN**

Figure - 5.1 Archie-M Analysis Results for Arch 02.

For RING analysis backfill are modelled nominally. In this model favourable effects of backfill are avoided by ignoring dispersion of live load and contributions from horizontal pressures.

Loads modelled as sing axle load.

The default single 100 kN axle is run for analysis.

Effective Bridge Width

CALCULATION	WIDTH (MM)
Auto computed	2490.91

ANALYSIS RESULT	ANALYSIS TYPE	SOLVER
Adequacy factor = 3.38869; Scenario 1 @ 2869mm (this is the critical case)	ULS	CLP

Mode of response at current load case

Summary of results, refer Appendix A1 for details,

Effective width = 2490 mm

Total single axle loads = 3.38869 x 100 kN = 338.869 kN

Capacity of 657 mm arch = 338.869 x (657/2490.91) = **89.4 kN**
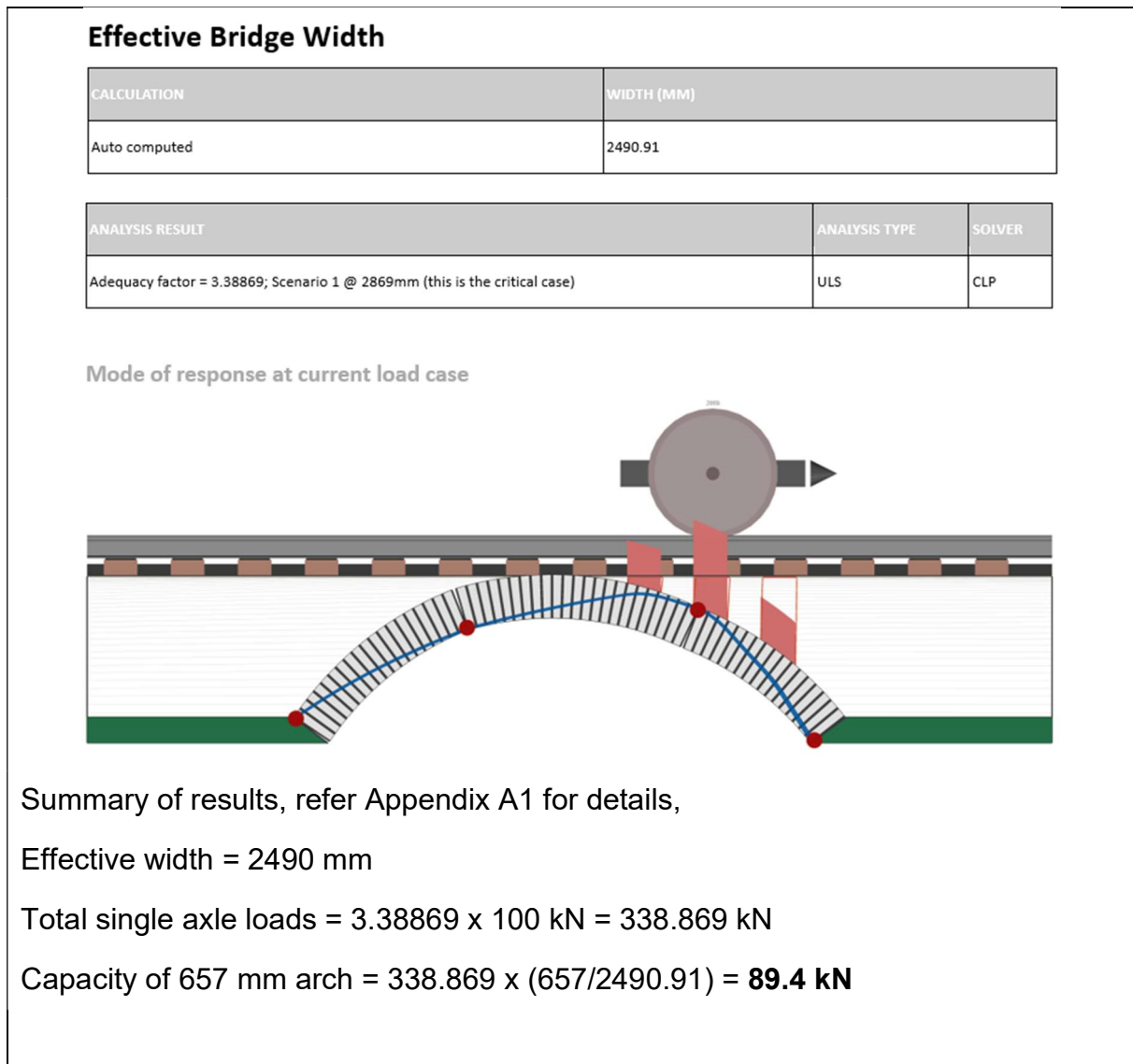
Figure - 5.2 RING Analysis Results for Arch 02.

5.2.2 ARCH02 CZM ANSYS Numerical Analysis

Numerical model discussed in previous section is now extended to Arch 02 and analysed for the load deflection behaviour. Initial tested material properties are used for this analysis. 80 kN load, Figure - 5.3, is predicted by numerical analysis. The collapse load differences (*Audenaert and Beke, 2010*) by multiple methods are studies and reported as follows: collapse load elasto-plastic ≤ collapse load Ring ≤ collapse load Archie-M. All three models produce almost similar collapse mode. Comparing multiple load capacities, the collapse load CZM 80 kN ≤ collapse load Ring 89.4 kN ≤ collapse load Archie-M 94.4 kN. This comparison agree with similar observations by Audenart (*Audenaert and Beke, 2010*).

Arch 02 was tested to six stages of increased cyclic loading repeated every time by 10^5 cycles. As the loads were increased in steps, resulting deflections also increased rapidly, finally entering the non-linear (inelastic) range. First visible signs of cracks

noted in laboratory at alternate load of 25 kN, this is considered 30% of the numerical load capacity of 80 kN. Beyond this point, further increase in loads caused rapid growth in deflection with noticeable propagation of cracks. At 40 kN deflection increased significantly, see Figure - 3.15, this is around 50% of the minimum load capacity. Finally, four hinges were observed at 50 kN load after 10^4 cycles and loading paused immediately. Further increase of load to 60 kN led to complete collapse of the arch.

Applying a C_{min} abnormal load factor of = 1.8 (*CS 454, 7.2.1*) to analysed capacity, [(80/1.8) =] 44.4 kN is predicted reasonably well.

Ring, Archie-M, elasto-plastic (*Audenaert and Beke, 2010*) and this CZM ANSYS model are all able to determine the four-hinge collapse mode. Commonly all present load capacity assessments only provide stability conditions or overall estimates of the collapse load. Figure - 5.3 is plotted to present a comparison between multiple limit state approaches. RING and Archie-M only provide a safe load without any information of arch deformation. ANSYS CZM numerical model provide load-deflection relationships, this is based on virgin material properties. Two further horizontal lines are plotted after applying appropriate factor of safety. For Archie-M loads, γ_{fL} = 3.4 is applied, this is same as NR/CIV025 and previous BD21/01, resulting safe load capacity of 27.8 kN. For the CZM ANSYS model a C_{min} = 1.8 applied for abnormal single load as per CS 454, with capacity of 44.4 kN.

Interestingly the Arch 02 only survived 10^3 cycles at 50 kN. If only 50 kN were meant to be applied in a similar cyclic pattern, same arch is predicted to survive 7.7×10^4 load cycles, see Table 3.9. The safe capacity though proved to meet calculated ultimate limit state prediction, life of arch failed to survive reasonable duration. This is due to its history of cumulative cyclic loading, and hence induced damages, applied in stages of 10^5 cycles starting from as low as 17% loads, less than 1/5 of ultimate capacity. Therefore, even though all limit state load capacity methods offer credible safe load predictions, there is no credible indication or prediction of safe life of an arch.

Also plotted in Figure - 5.3, deformation recorded by LDVT at 10^3 cycles of loads during the test at laboratory. A complete inclusion of data over 10^5 cycles at every load step is not included for clarity.

The fundamental observation from Figure - 5.3 is none of the analysis methods and load capacities represent actual arch behaviour, noted during the test, refer *ARCH 02 ¼ point – cyclic load test* line plotted in the graph. Notably the guidance on (*CS 454*) assessment of masonry arches aims to avoid further distress and reduction in life of the arch.

The difference in load-deflection curves between the CZM ANSYS numerical output at ¼ point and the laboratory tests prove that arches undergo increased deformation

under repeated cyclic loadings during their life span. Increased magnitude of cyclic load further makes the condition worse, arch deformation tend to increase with recurring increased magnitude of loading.
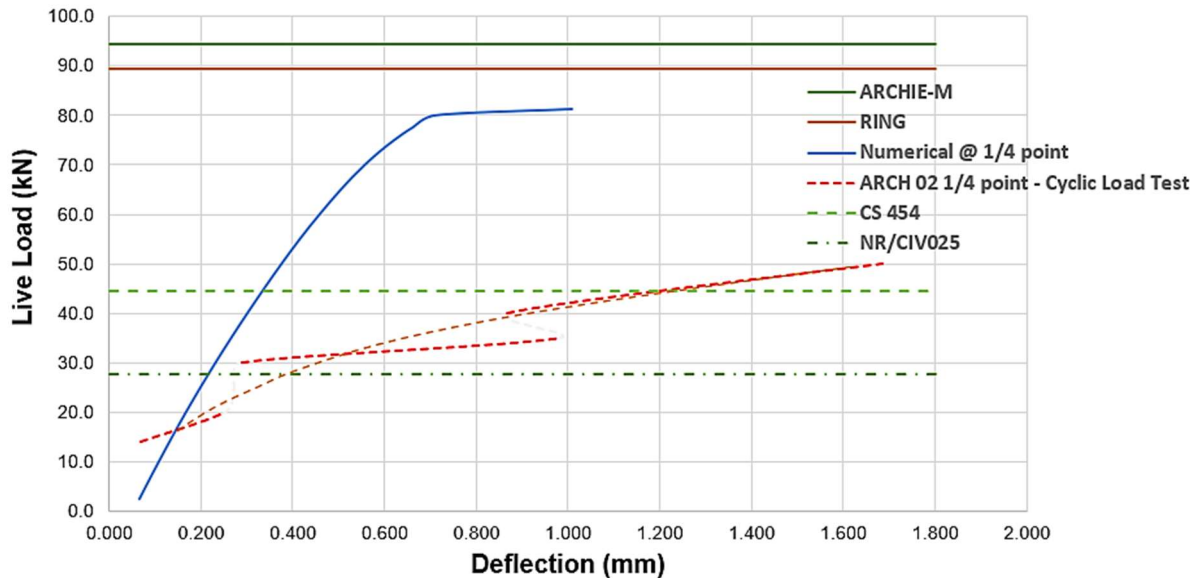
Figure - 5.3 Load-deflection Analysis Results Plotted with Cyclic Coad Test Data for Arch 02.

Therefore Figure - 5.3 can be summarised as, cumulative and increased cyclic load, even at lower intensities than numerical safe capacity, applied in stages over the life of an arch increases deformation and continuously introduce damages. This resulting continuous damage to arch geometrical and material properties reduce life of an arch therefore adversely affected by fatigue.

5.2.3 Limitation of Numerical Analyses

Clearly current methods of analysis based on parent material properties do not correspond or represent the damaged deformation of arches and therefore any derived load capacities become unreliable. Because there is no indication of how long an arch can withstand when same load is applied repeatedly.

None of the current guides or the existing assessment methods refer explicitly to progressive damages due to fatigue behaviour or any associated fatigue-induced serviceability failures. Arch 02 test carried out for this thesis and the arches tested at University of Salford have clearly proved that the cumulative effect of cyclic loadings leads to arch failure and reduces safe load carrying capacity significantly.

Apart from damages due to applied loading, arches undergo further deterioration due to environmental causes, poor quality backfill, freeze-thaw damages and external modifications. It is conclusive that load capacity assessment based on parent material

properties clearly fail to assess safe load capacity. Therefore, a real time damaged based model is necessary and proposed for a reliable assessment of capacity.

5.3 Proposed Damage Based Approach

Any proposed model to account for fatigue damage under repeated loading need to include highly sophisticated constitutive law. Derivation of such a law require complex material properties and their behaviour studies. Fatigue is by now well established for materials like steel, aluminium and carbon fibres used in precision equipment's and aero industries. These materials are either isotropic in their behaviour or produced under strict quality control. On the contrary masonry, more so for existing over century old, structures have widely variable material properties. Environmental exposure makes their behaviour further complicated. Therefore, a simplified procedure is proposed for existing masonry structures, this is considered suiTable for practising engineers and readily determined with an accepTable reliability.

It is possible to measure arch response under passing trains, live load, as reported in Marsh Lane underbridge study (*Acikgoz et al. 2018*). Deformation response of a bridge under live loads is an outcome of collective response from all contributory effects such as damages due to loss of bricks and mortars, cracks, freeze-thaw, backfill properties, spandrels and supports. Following measurement of deflection under live loads always compare them with analysis results, like one in Figure - 5.3. Then re-analyse the model with calibrated secant modulus and normal stiffness as described below.

As the arches deform, the initiation, growth and coalescence of micro defects decrease the stiffness (i.e., degradation of material properties), which is represented by the growth of the damage variable D ($0 \leq D \leq 1$). For undamaged material. D is 0. While D = 1 corresponds to a completely damaged with zero stiffness. The Secant modulus and the normal stiffness of the damaged arch is considered a function of its initial value.

Following approach is proposed to incorporate real time damaged properties in the damage based numerical analysis of arches.

<u>Methodology</u>

1. Calculate Material Properties by Test

2. Numerically Analyse Arch, similar to Figure - 5.3, with Test Properties, E_0, Kn_0

   - Calculate Deflection, δ_q at ¼ point under numerically applied live load, P_{LL}

3. For same Applied live load, P_{LL}

   - Measure Deflection in-situ, $\delta_{q\,S}$ at ¼ point.
   - Record data for at least 10^3 repetitions, preferably monitor for 10^5 cycles,

4. Reanalyse the Arch with following modified properties

- $E_{DS} = E_0 (\delta_q / \delta_{q\,s})^m$
- $Kn_0 = Kn_0 (\delta_q / \delta_{q\,s})^n$
- Calculate deflection at Quarter Point, **u** at crown for future LL

  Where,

  m = between 0.9 to 1.0

  $m^2 + n^2 = 1$

5. Calculate Parametric Strain, eq 5.2,

6. Use Figure - 3.26 to derive Residual Life of Arch

As a case study in Table - 5.1, Arch 02 damage analysis is performed based on above methodology. Live load value of 30 kN is chosen. This is loading stage, immediately one following the appearance of first visible crack at 25 kN.

Table 5.1 Damage Property Derivation for Arch 02 @ 30 kN Cyclic Load

Arch condition	Deflection @ ¼ intrados (mm)		Remarks	
Undamaged	$\delta_q = 0.232$		Refer Figure - 5.3	
Damaged (test)	$\delta_{q\,s} = 0.288$		25% of undamaged	
Damage model	$\delta_{q\,c} = 0.291$		Within 1% of calculated, for	
	$\delta_{q\,c}/Rq = 0.11 \times 10^{-3}$	eq 3.7	m = 0.97 n = 0.24	
	$N = 1.6 \times 10^6$	Figure - 3.26		

Following Table – 5.2, this approach is further extended when arch has been subjected to higher cyclic loading resulting further damage. Consider post 35 kN.

Table 5.2 Damage Life Prediction for Arch 02 @ 30 kN Cyclic Load Following Application of 35 kN of Cyclic Load for 10^5 cycles.

Damage model	$\delta_q = 0.815$		Within 5% of calculated, for	
	$\delta q/Rq = 0.36 \times 10^{-3}$	eq 3.7	m = 0.98 n = 0.2	
	$N = 3.98 \times 10^5$	Figure - 3.26		
i.e., life reduction = $[3.98 \times 10^5/1.6 \times 10^6] = 1/4$, to 25%				

See Figure - 5.4 for representation above damage modelling approach.
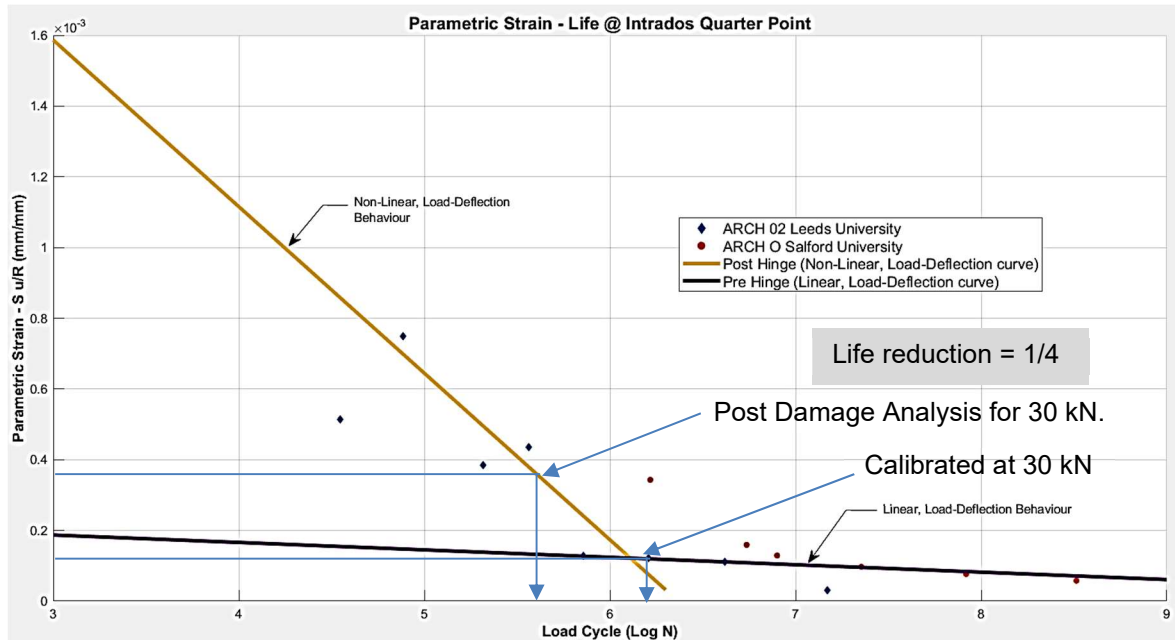
Figure - 5.4 Damaged Life Prediction.

This is now evident that parent material properties fail to represent present state of an arch and their overall condition. These include all cumulative damages due to increased traffic, environmental damages, material deterioration, contribution from stiffnesses from backfill and spandrels. Therefore, calculated load capacities are unreliable and their application to probabilistic models, based on low cycle fatigue (LCF), lead to unreliable outcome. Figure - 5.4 above focus on ascertaining the fatigue effects due to high cycle fatigue (HCF) life so that the assessed capacity do not cause additional distress and reduce service life.

In Figure - 5.5 below, further observations made regarding safe life of a masonry arch. Initially predicted deflection at quarter point of Arch 02 based on virgin material properties corresponding to ultimate limit state (ULS) capacity of Arch 02 is shown as point **A**. If same load is applied cyclically over a longer duration of time, this will cause continued distress therefore damaged deformation will increase to point **B**. Depending on the degree of damage the arch has undergone safe load capacity will now reduce between 20-14 kN, corresponding deformations of damaged arch are shown as points **C** and **D**. Now applying the parametric stain-life prediction analogy as per Figure - 5.4, predicted life of the arch are listed in Table - 5.3.
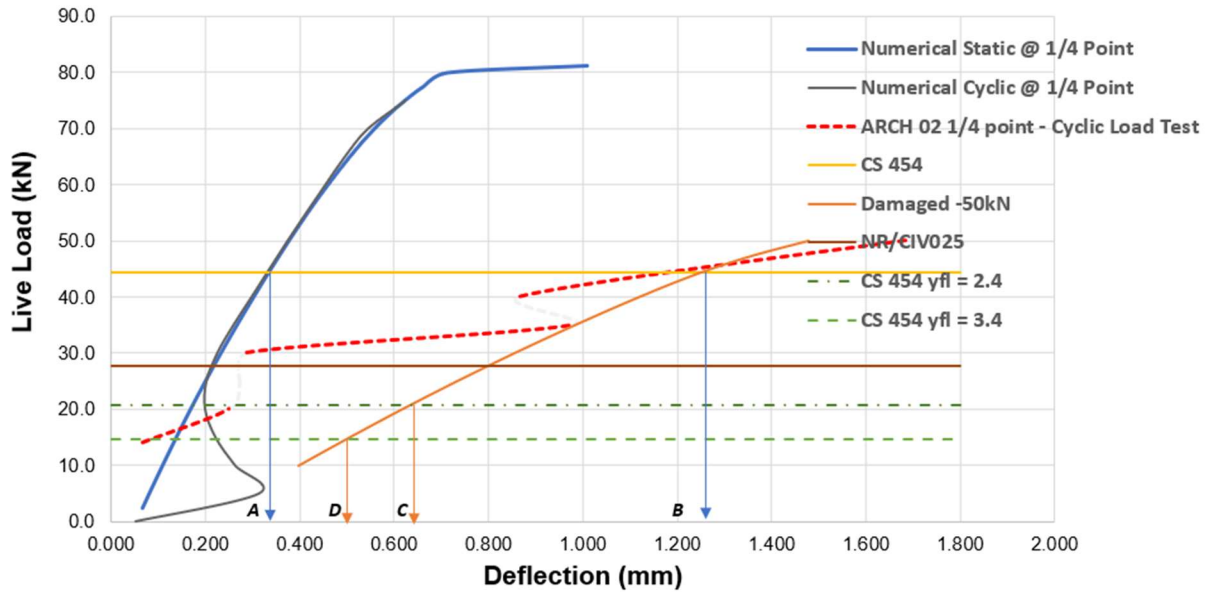
Figure - 5.5 Post Damage Life Corresponding to ULS.

Table 5.3 Post-Damage Safe-Life Prediction for Arch 02.

ULS (kN)	Condition	δ_q deflection @quarter point (mm)	δ_q/Rq	Predicted life, refer Figure - 5.4
44.4	**A** - Before damages	0.268	0.097×10^{-3}	$> 10 \times 10^6$
	B - Post damage	1.272	0.463×10^{-3}	3.1×10^5 , **1/30 of A**
20.8	**C** – low damage factor	0.616	0.224×10^{-3}	6.3×10^5 **plan maintenance**
14.7	**D** – conservative factor	0.451	0.164×10^{-3}	1.5×10^6 **reasonable**

Table - 5.3 suggest that the ULS factor of safety based on the life of an arch shall be chosen based on acceptable life, point **D**. Alternatively reduced life, point **C**, prediction provide credible early warning for future maintenance or replacement of the asset.

The above fatigue damage model proposed in this section provide means of measuring parametric strains from arch deformations under service loads then predict life of the arch. The damaged material modelling reliably takes care of present state of the structure subjected to fatigue effects demonstrated by Table 5.1. Thereby predict the residual life of existing arches as shown Table 5.3, through a reliable and affordable approach.

5.4 Parametric Study

Test programme for this thesis limited to multi-ring arch and one geometry. To overcome this limitation reference is made to similar arches tested at University of Salford, see Section 3.8.2. Bricks and mortar properties used for both tests are same. Geometries of both tests varied. The Salford arch is 5 m span compared to Leeds arch, which is 3.6 m span, see Table - 5.4 for details. Deflection of any structure not only depend on loads and span, in addition cross section dimensions and material parameter like modulus of elasticity also contribute to their outcome.

It is therefore important to harmonise bridge properties both geometric and material before comparing and validating any generic methodology.

Table 5.4 Arch Dimensions for Parametric Study.

	Leeds Arch	Salford Arch
Arch Name	Arch 02	Arch "O"
Span (mm)	3600	5000
Rise (mm)	900	1250
Span: Rise	4:1	
Ring Thickness (mm)	320	330
Arch Width (mm)	657	675
Number of rings	3	3
Dead Load (kN)	2x 11	2x 22.5
Shape	Semi-Circular	

5.4.1 Effect of Geometrical Section Properties

Classical analysis of arch show that the critical load of arch is always found to be proportional to $Ps = EI/L^3$. For masonry arches these are,

      E   : Secant modulus of leasticity

      I   : $Bdt^3/12$, B = effective width of arch

      dt   : ring thickness

      L   : Arch span

For same material properties harmonised relationship is $B.dt^3/L^2$. For validation of equation 3.8, 3.9 and Figure - 3.26 same stiffness correction is applied.

For Arch 02:

      B   = 0.657 m

      dt   = 320 mm

      L   = 3600 mm

      Ps   = $\{B \times dt^3/L^3\}$ = 4.61x10^{-4}

             = 1/2170

Therefore, while calculating parametric stain at quarter point of arches with different geometries following relationship is applied.

$$\varepsilon_p = \frac{2170 \, Ps \, \delta q}{Rq} \qquad \text{(eq 5.1)}$$

Where,

      Ps   : $B . dt^3/L^3$

      δq : deflection at quarter point

      Rq : radius at quarter point

For example, the Salford Arch O strains in Table 3.14 are multiplied by,

      For Arch O:

           B   = 0.675 m

           dt   = 330 mm

           L   = 5000 mm

           Ps   = $\{B \times dt^3/L^3\}$ = 1.9x10^{-4}

           εp = 2170 x 1.9x10^{-4} x $\delta q/Rq$

               = 0.42 $\delta q/Rq$

5.4.2 Effect of Brick Bond

This thesis work is based on three-ring segmental arches chosen with three-ring stretcher brick bond. Though this is most commonly occurring bond type for masonry arches, two additional types of bonds are also seen. Cohesive modelling of Salford Arch – G in 4.5.2 is further investigated for following three bond types, Figure - 5.5. Tests have shown that static loading resulted radial cracks only, while cyclic loading developed ring separation just before failure of all arches. In following analysis two load cases are considered.

1. Static loading applied at one ¼ span,
2. Cyclic alternate loading applied ¼ and ¾ span to differentiate the arch behaviours due to brick bond under cyclic loading.

a)   b)   c)
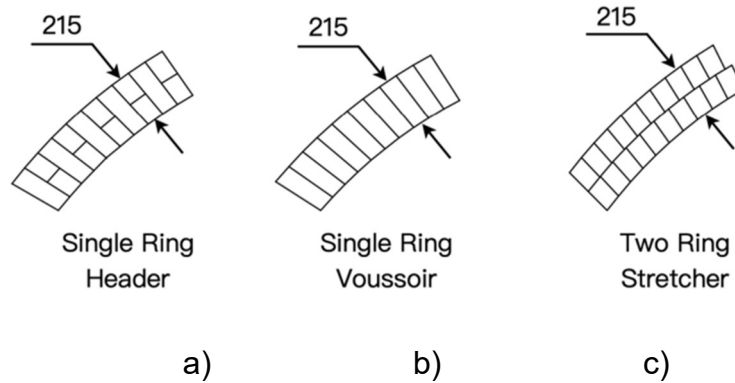
Figure - 5.5 Varying brick bonds in masonry arches, Thickness in mm.
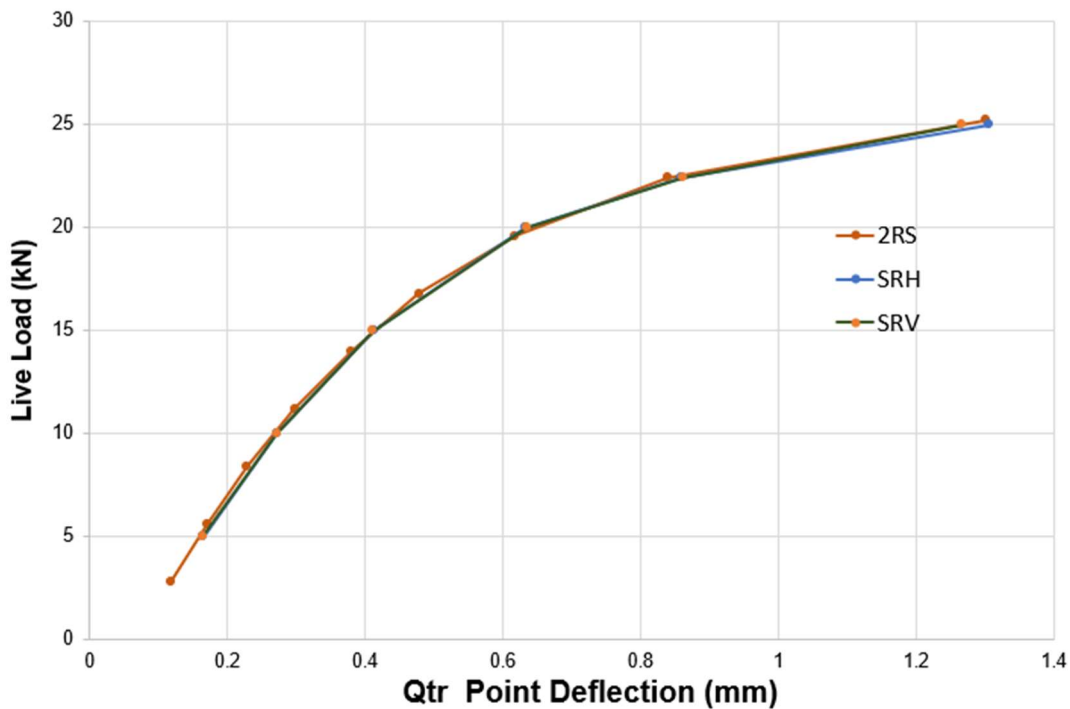
Figure - 5.6 Static Load-deflection Response for All Three Brick Bonds at Quarter Point.

Figure - 5.6 static shows load-deflection curves for all three brick bonds are predominantly overlapping for a static loading applied at ¼ span. Therefore, load displacement behaviour is similar across there bond types. Ring analysis for these three brick bonds for Arch G also confirmed same load capacity. This is due to presence of full depth radial interface for all three bond types.
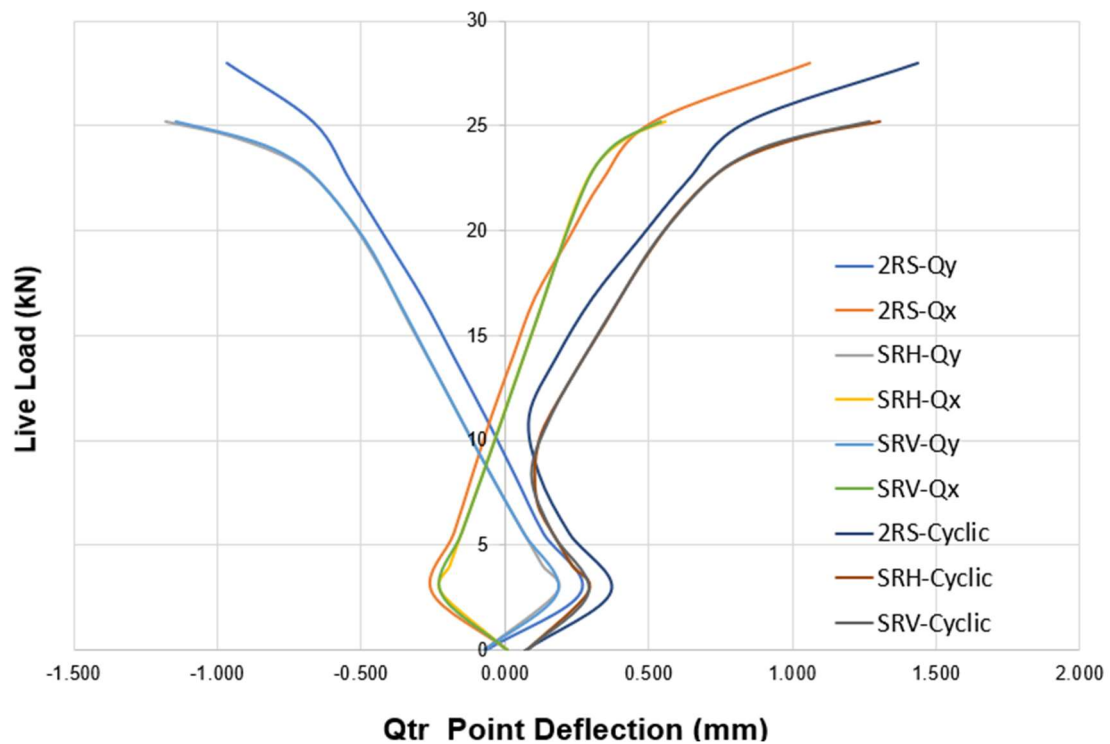
Figure - 5.7 Cyclic Load-deflection Response for Three Brick Bonds at Quarter Points.

Figure - 5.7 cyclic load-deflection curves for three brick bonds are interesting. Single ring header (SRH) and single ring voussoir (SRV), predominantly overlapping for a cyclic loading applied at ¼ and ¾ span. However, two ring stretcher (2RS) arch type deflections at quarter points differ from remaining two brick bonds. Vertical deflection due to two rings are less. But horizontal deflections tend to increase beyond a load of 18 kN this is when interface slip start to effect different behaviour for multi ring arches. This is attributed to interface shear between two rings. However total deflections for 2RS bonds always remained approximately 10% less than other two types. SRH and SRV failed during cyclic analysis at 25.2 kN, while 2RS converged to 28 kN like the test.

Comparing resultant displacements between three different bond types, two (multi) ring stretcher type arches are found to be 10% stiffer and hence offer similar increased load capacity.

Therefore, for brick bonds other than multi-ring arches capacity and corresponding displacements need to be reduced by a multiplier of 1.1. Note this multiplier is only for referring to graph in Figure - 3.26.

Hence equation 5.1, is further modified to,

$$\varepsilon_p = \frac{F_b \ (2170 \ x \ Ps) \delta q}{Rq} \qquad\qquad \text{(eq 5.2)}$$

Where

F_b :1.0 for multi ring arches

         :1.1 for other brick bonds

5.5 Flow Chart for Fatigue Analysis

This section summarises appropriate steps to derive fatigue life of an existing masonry arch bridge. Any bridge assessment start with inspection for assessment process. This include carrying out geometrical survey of the complete bridge. This can be accomplished using a LiDAR based survey. Apart from carrying out dimensional survey, LiDAR also capture spots of local deterioration. Then it is necessary to understand condition of the structure, a tactile approach is best suited. Samples of masonry cores are collected to determine the makeup and strength of constituent brick and mortars. These data provide information for basic understanding of arch.

Survey information collected typically provide good understanding and information about static response of arch bridge. All inspections are carried out in absence of live vehicles, called wheels free condition. Only visible information is collected. Masonry arches have significant hidden elements due to their inherent construction. Only way to understand their condition is to measure the response of the bridge under live loads. This is the most important parameter as repeated in this thesis work. Therefore, record bridge displacements at bridge crown, ¼ and ¾ spans under known passing train for duration between $10^3 - 10^5$ cycles. For an hourly service of typical four coach's train this account between 1 week to a year of monitoring. For more frequent service, this duration will reduce.

Based on the material properties and bridge survey, prepare appropriate numerical model. A complete 3D model is cumbersome. To capture masonry behaviour an interface model is recommended. For all practical purposes a 2D model is suitable for an arch. Based on the test properties calculate arch capacity and importantly deflections and crown, ¼ and ¾ spans. Analyse the numerical model under same railway loading as measured at site.

Compare analysis results with measured responses. Accordingly calibrate secant modulus and contact normal stiffness. Rerun the numerical analysis then determine

revised load capacity. Also determine corresponding deflections at ¼ span. Referring to the parametric strain-life equation and curve in Figure - 3.26 determine the arch life for the calibrated load capacity. If this life is unacceptable, derive reduced capacity based on acceptable life alternatively plan for future maintenance of the arch.

Above steps are represented as a flow-chart in Figure - 5.8.
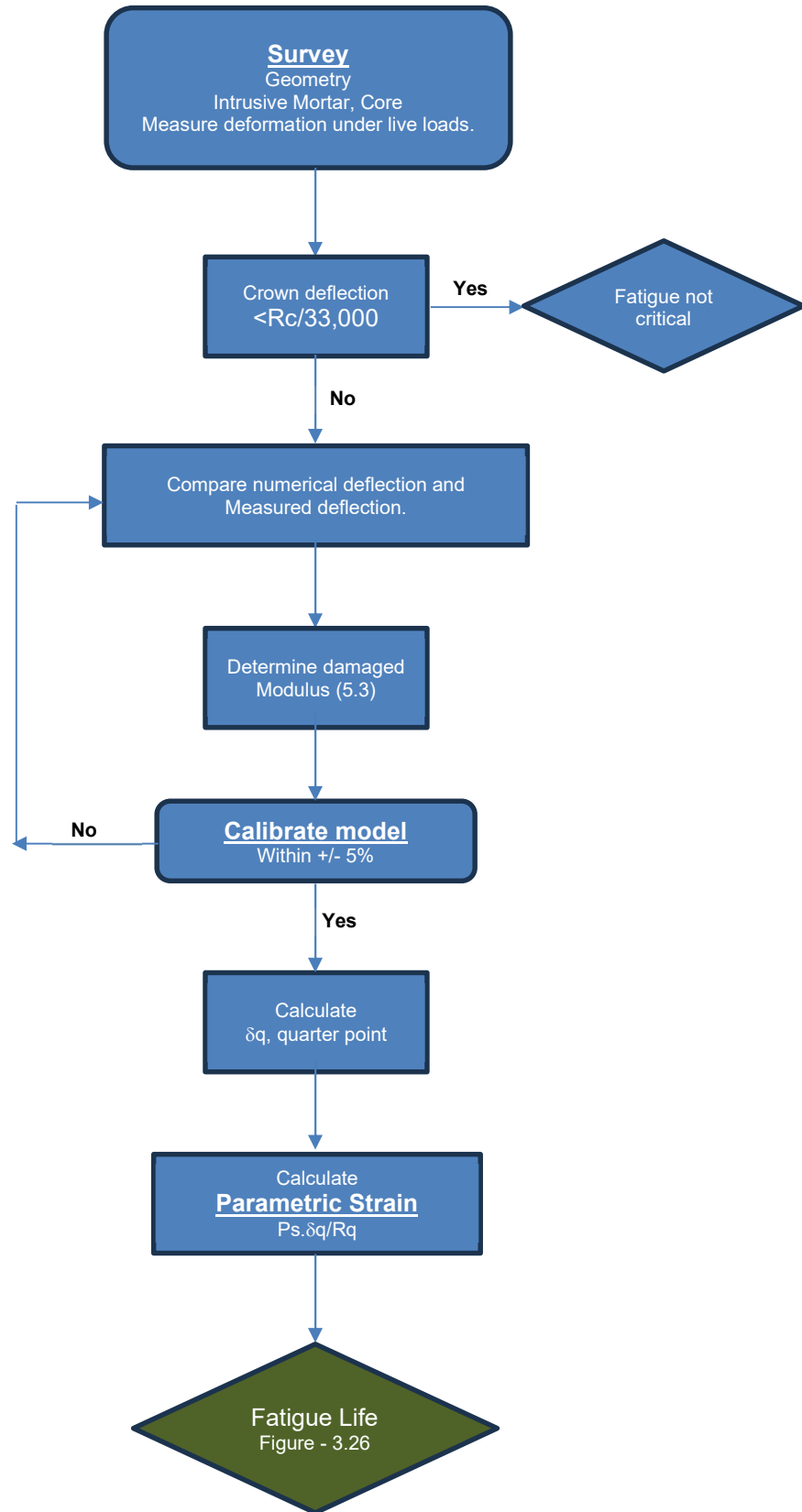
Figure - 5.8 Flow-chart for Determining Arch Life.

5.6 Summary

Finally, a deformation-based damaged model fatigue assessment methodology has been proposed in this chapter. For real scale arches subjected to daily loads and exposed to environments, damages and stiffnesses are a combination of various contributory factors discussed in previous sections in detail.

Proposed damage model is based on the in-situ measurements under actual live loads. Any measured deformations on real arches therefore will be combined response of contributory effects of cumulative damages. Hence this approach is considered more reliable than assessments based on loads and stresses.

Limitations and further opportunities are discussed in the next section.

Chapter 6
Conclusion and Recommendation for Future Works

Fatigue assessment of masonry is an area of recent interests to researchers as well practicing engineers. So far, all works were based on tests carried out on masonry prisms and later handful of tests on arches subjected to near capacity loading. This research for the first time tried to establish fatigue in masonry arches based on deformations measured directly under the applied loads and subsequent damages. Stages of loading started from very low intensity to start with so that high cycle fatigue (HCF) can be explored.

6.1 Conclusion

Before predicting fatigue life, it is necessary to witness the behaviour of a real scale arch subjected to alternate cyclic loading. All previous works have focussed on arch load capacity and their failure rather than recording progressive damage. Hence those previous works never considered or recorded arch responses under high cycle fatigue, (HCF).

Planned laboratory tests on arch subjected to cyclic loading followed expected sequence of cracking. Stage I cracking initiated after 10^4 cycles for both arches. Stage II cracks propagated up to 10^5 cycles even for low amplitude stresses applied to Arch 01. Arches therefore reach the crack propagation phase even at a considerably low stress levels of cyclic loading, therefore making fatigue assessment more so important for determining the arch capacity to withstand safe load for an expected life. Limiting numerical analysis to compressive strengths is clearly not enough. Cross section of arch reduces continuously with increasing crack lengths.

Subjecting arches to very low alternating stresses of loading it was possible to observe the linear load-deflection (elastic nature) relationship of the arch under initial loading. LVDT and laser measurements have recorded increasing deflection therefore, progressive damages even at low loads. Confirming that arches do not have infinite life. More so when existing arches, when undergone history of damages, subjected to increased and more frequent loading.

Arches not only accumulate damages under loads during course of their life. There are multiple contributory factors like environmental damages, water seepage, loss of mortars, quality of backfill and contributions from substructures. These variety of contributors collectively make any realistic modelling very complex and practically impossible. Therefore, it is necessary to monitor arches continuously to derive an equivalent single damage factor at any time of assessment for all practical purposes.

Present design and assessment guidance are based on limiting compressive strengths on masonry and application of suitable factor of safety. Strengths are determined from recovered core samples.

Presently there is no guidance on determining damaged material properties and considering them in the analysis. Recording arch deformations over multiple loading stages helped to understand progressive behaviour changes. Therefore, leading to damage modelling by stiffness degradation in this thesis. Unless this is acknowledged, any present method of assessment will fall short of any reliability. All future assessments need to be based on measurements carried out directly under live loads and calibrating models to reflect these measurements. Then predicting arch capacities based on their modified stiffness will become meaningful, rather than only controlling compressive strengths.

For the loading and laboratory measurements on tested arches fatigue damages initiate after total deformation at the crown of the arch reaching R/33,000. This has been noted in the research.

6.2 Fatigue is Obvious

Masonry arches do follow fundamental fatigue principles. Predicted life of arches carrying same magnitude of load pre and post damages differ significantly.

Material properties calculated in accordance with IRS 70778-3:2020, recommendations for the inspection, assessment and maintenance of masonry arch bridges offer better correlation for material properties. Stiffnesses calculation based on the IRS recommendations do not have any provisions for calibration with existing responses. They need to be calibrated with real time measurements of deflection under passing loads to capture global damages. This is done by measuring live load deflection and comparing them with analysis results. Then safe capacity assessment is progressed reliably. Therefore, further guidance on damage modelling is necessary for practicing engineers.

It is possible to establish a reliable fatigue life assessment criterion based on the elementary fatigue principles. More tests are necessary to propose a universally acceptable fatigue assessment procedure. Tests carried out for this thesis suggest that at least 10^5 cycles of loading leads to stage II cracks.

Clearly calculating safe capacity loads (ULS principle) based on fixed material properties, like compressive strengths, significantly overestimate the capacity for arch life. This approach is clearly the reason that asset owners worldwide regularly spend resources including time and money for unplanned repetitive maintenance works resulting continuous loss of revenue and reliability.

For analytical purposes magnitude of alternating stresses are more important and they contribute to crack initiation. This suggests that the analytical criteria for fatigue life shall be limited by maximum allowable alternating stress under love loads. Tensile strength of masonry should also become part of material tests from recovered samples. Presently there are no guidance or practices where the serviceability criteria are defined by the allowable tensile stress, crack widths and deflections due to live loads.

Furthermore, stress-based assessments are unreliable due to contributions from multiple parameters. With the initiation of cracks, masonry section properties also change rapidly. Their effects are not considered in the present analysis methods. Focussing on stress-based assessments and modelling individual damages for real scale arches are cumbersome and uneconomical.

Deformation, damages, and modified stiffness-based approach capture contributions to damages from all contributory sources resulting outcome of the assessment become more practical. realistic and credible. There are few critical issues need to be considered when assessments are carried out by damaged stiffness-based approach.

- Deformation needs to me measured and calibrated under known live, variable loads.
- Follow two stage process, calibrate model and calculate deformations due to in-situ test parameters. Further repeat the numerical analysis following model calibration comparing deflection at ¼ spans due to variable load.
- Predict residual life based on the total parametric strains calculated on arches considering present state of damages, subjected to change in load regime. Analysis based on virgin properties of the arches overestimate future capacities.
- Overall, a factor of safety between 4 and 3 needed to limit future fatigue damages to acceptable limit.

6.3 Limitations

This research is based on only two arch tests. Arch 01 was continued at constant amplitude cyclic loading. This arch was demolished and removed from further tests due to unforeseen overlapping programme issues with other research works. Arch 02 was accelerated with cumulative/increasing amplitude loading.

Fatigue in masonry arch is an ongoing area of research, therefore lacks prescribed guidance on minimum number of test or specimens required for a conclusive outcome. Though two tests have proved that fatigue does occur in masonry arches subject to cyclic loading, major limitation of these research is number of tests performed. Outcome of this research could have further improved with additional number of tests. Additional at least three tests on bare arches, two arches between 20-30% of fatigue

capacities and one at 50% of fatigue capacity certainly help. These tests continued at constant amplitude cyclic loading continued till failure could prove the recommendations of Figure 3.26. These tests could certainly prove that parametric-strain life approach presented is in this research is a reliable way forward in predicting residual life of masonry arches.

Due to limited number of tests, Miner's rule has been used to predict life of the arch. Primarily this is based on calculated elastic stresses. Concept of this research is based on the deformation measurements and damaged analysis therefore significantly improves reliability. Depending on elastic stresses for estimating life under various stages of loading is considered a limitation. Further recommendations have been proposed in the next section to overcome this problem.

Measuring deflection of masonry arches under live load is very challenging for many reasons. Arches are inherently very stiff and deflect very little compared to beams and slabs. Any measurements need to be precise and implement high resolution technologies. In the laboratory laser LDVTs located at fixed datums were used to avoid secondary effects. Measuring in-situ deflection and strains of real scale arch is difficult, and results need to be used with caution. Running locomotives vibrate the surroundings. Therefore, measuring instruments and target also vibrate during passing of trains. This parametric strain-life proposal is directly dependent on the accuracy of measured deflections, any in-situ measurements are susceptible to imperfections. Though laboratory tests are comparatively reliable in defining the methodologies, measuring deflections require improved technologies and analytical skills before deriving a reliable result.

Construction and testing of arches are expensive and time consuming. Restricted loading frequency of 0.5 Hz have increased the overall duration of tests. For fatigue tests with reasonable duration, tests should be carried out with frequency, 2 Hz is considered achievable in similar tests carried out at other UK Universities. As discussed in previous paragraphs, testing at higher frequencies will significantly reduce time of prolonged loading continued to failure. One million (1×10^6) cycles of loading can be achieved in six days at this rate of loading.

Parametric guidance considering brick bond type and arch geometries are based on limited assessments. Only one additional size of arch is considered in the derivation. Therefore equation 5.2 could become debatable for generic application. Lack of tests on various sizes of arches are a significant limitation of this research. Such tests are cost prohibitive for a research project. Both arches considered in this research are made of similar bricks and mortar. They are selected being representative of majority of bridge stocks recorded in United Kingdom. Lack of combination of bricks and mortar and their effects are also considered a limitation in this research. An elasto-plastic

numerical modelling suggest that weaker material will lead to increased deflection, hence reduce fatigue. Without carrying out tests on real arch, it is not immediately obvious for verification.

Fatigue and Strain-life in masonry is not yet an established practice. Therefore, there are no prescribed guidance on minimum number of specimen and tests that should be considered representative. Infrastructure bodies and asset owners need to prescribe methods and minimum number of tests for a reliable outcome.

6.4 Recommendation for Future Works

The approach to fatigue or residual life assessment of masonry arches, presented in this thesis based on actual measured deformations are a step change. Limitations discussed in the previous section impose doubts on reliability of the proposal. more so because the proposed methodology is novel in implementation. To establish a credible damage model and strain life relations following additional works are recommended:

A. Carry out similar tests on a range of arch spans. To start with follow
1) Test between 6-10 m single span arches. They constitute 85% of the overall assets.
2) For single step loadings continue tests up to 2×10^6 million cycles.
3) For multi-stage loadings or while deciding steps, set from 20%-50% of theoretical load capacity with tests carried out at every 5% load increments.
4) This will allow developing clear guidance on serviceability criteria for limiting deflection for arches and their lifelong capacities in fatigue.
B. Establish a guidance on minimum number of tests and variability of material properties to ascertain a reliable result. Based on A.3), above seven stages of loading times three, i.e., twenty-one tests per span will be required.
C. Instead of using Miner's rule for damage assessment, carry out bespoke tests continued to failure at constant amplitude of loading. As suggested above.
D. This laboratory test was maintained at 0.5 Hz frequency due to the limitations in the hydraulic system. Tests at 2 Hz can significantly reduce time duration.

Overall if progressed as recommended, the damaged model parametric strain-based life prediction clearly offer the most reliable method for assessment of existing masonry arches.

List of References

Abrams, D.P., Noland, J.L., Atkinson, R.H., and Waugh, P., (1985). Response of Clay-Unit Masonry to Repeated Compressive Forces. 17. 1-17. 14. Proceedings of 7th international brick masonry conference. Melbourne; 1985. p. 565-576.

Acikgoz, S., Kechavarzi, C., Soga, K., DeJong, M.J., (2018) Dynamic response of a damaged masonry rail viaduct: Measurement and interpretation. Engineering Structures 168, 544- 558.

Addess, D., Sacco, E., and Di Re, P., (2017), A micro-macro homogenization for modelling the masonry out-of-plane response, AIMETA 2017 XXIII Conference, The Italian Association of Theoretical and Applied Mechanics.

Al Hancq, Raymond Browell, Calculating and Displaying Fatigue Results, ANSYS, Inc. March 29, 2006

Alexakis, H., Liu, H. & DeJong, M. (2020). Damage identification of brick masonry under cyclic loading based on acoustic emissions. Engineering Structures. 221. 110945. 10.1016/j.engstruct.2020.110945.

Alfano, G., Sacco, E., (2006), Combining Interface Damage and Fiction in a Cohesive-zone Model, International Journal for Numerical Methods in Engineering, vol. 68, pp. 542–582.

Alfano, G., Marfia, S., Sacco, E., (2006), A cohesive damage-friction interface model accounting for water pressure on crack propagation, Computer Methods in Applied Mechanics and Engineering Volume 196, Issues 1–3, 1 December 2006, Pages 192-209

ANSYS Theory, Version 18.2 Fracture delamination along composites and laminated composite structure. *Release 18.2 - © ANSYS, Inc.*

ASTM. Standard test method for compressive strength of masonry prisms. In: Annual Book of ASTM Standards, vol. 4.05, ASTM, Ed., West Conhohocken, ASTM International; 2014. p. 889–95.

Alfano, G. and Crisfield, M. A., (2001), Finite Element Interface Models for the delamination analysis of laminated composites, International Journal for Numerical Methods in Engineering, Volume 50, Issue 7, 10 March 2001, Pages 1710-1736

Alshebani, M.M, Sinha, S.N., (2001). Stiffness Degradation of Brick Masonry Under Cyclic Compressive Loading, Vol. 15. Masonry International. 13–16.

Audenaert, A., Beke, J., (2010), Applicability analysis of 2D-models for masonry arch bridge assessment: Ring, Archie-M and the elasto-plastic model. Issue 4, Volume 5, October 2010 ISSN: 1991-8747,

Nelson, L.A, Swift, G.M., Smith, C.C., Gilbert, M., Melbourne, C., (2018) Influence of railway loading on the performance of soil-filled masonry arch bridges. Proceedings of the Institution of Civil Engineers - Bridge Engineering. pp. 1-36. ISSN 1478-4637

Nelson, L. A. and Swift, G., (2020), Experimental investigation of the residual behaviour of damaged masonry arch structures, Structures, Volume 27, Pages 2500-2512, ISSN 2352-0124,

BD16/97; Unreinforced Masonry Arch Bridges, The Assessment of Highway Bridges and Structures, DMRB Volume 3, Section 4

Bannantine, J.A.,Comer, J.J, Handrock, J., (1990), "Fundamentals of Metal Fatigue Analysis", New Jersey, Prentice Hall .

Barla, M., Beer, G., (2012), Special issue on advances in modelling rock engineering problems. International Journal of Geomechanics; 12:617.

Bayraktar, A.,Turkar, T.,Altunisik, A.C., (2014), Experimental frequencies and damping ratios for historical masonry arch bridges. November 2014 Construction and Building Materials 75 DOI: 10.1016/j.conbuildmat.2014.10.044

Bicanic, N., (2003), Fragmentation and discrete element methods. Comprehensive Structural Integrity. Oxford: Pergamon; 2003. pp. 427-57.

Binda, L., Learning from failure – long-term behaviour of heavy masonry structures. Advances in architecture, vol. 23. Southampton: WIT Press; 2008

Bleck, W., Dahl, W., Nonn, A., Amlung, L., Feldmann, M., Schäfer, D., Eichler, B., (2009), Numerical and experimental analyses of damage behaviour of steel moment connection, Engineering Fracture Mechanics, Volume 76, Issue 10, 2009, Pages 1531-1547, ISSN 0013-7944,

Bolzon, G., Maier, G. & Tin-Loi, F., (1995), Holonomic and nonholonomic simulations of quasi–brittle fracture: A comparative study of mathematical programming approaches. In: Proceedings of fracture mechanics of concrete structures. p. 885–98.

Bolzon, G., Maier, G. & Tin-Loi, F. (1997), On multiplicity of solutions in quasi-brittle fracture computations. Computational Mechanics 19, 511–516 (1997). https://doi.org/10.1007/s004660050201

Boothby, T.E., Domalik, D. E., Dalal. V. A. (1998), Service Load Response of Masonry Arch Bridges, Journal of Structural Engineering, Volume 124, Issue 1 TECHNICAL PAPERS

Boothby, T.E. (1995), Collapse modes of masonry arch bridges. J Brit Mason Soc 1995;9(2):62–9.

Bosch, M.J and Schreurs, P.G, (2006), An improved description of the exponential Xu and Needleman cohesive zone lar for mixed mode decohesion, Engineering Fracture Mechanics, Volume 73, Issue 9, June 2006, Pages 1220-1234

Brencich, Antonio., Corradi, A & Gambarotta, L. (2006). Strength of eccentrically compressed brickwork pillars: a theoretical and experimental analysis. 7th International Masonry Conference. October. 30.

British Standard, BS EN 771-1 :2011+A1:2015 - Specification for masonry units

British Standard, BS EN 1052-3 Methods of Test for Masonry-Part 3: Determination of Initial Shear Strength, British Standard, 2002.

British Standard, BS1377 PART 7 1990 - Shear strength tests (total stress)

Brookes, C.L. and Mullett, P.J., (2004), Service load testing, numerical simulation and strengthening of masonry arch bridges. Arch Bridges ARCH´04 CIMNE, Barcelona.

Campbell, J A, Numerical Model for Nonlinear Analysis of Masonry Walls, PhD Thesis July 2012.

Carraraa, P., Ambatia, M., Alessib, R., De Lorenzisa. L, (2020), A framework to model the fatigue behavior of brittle materials based on a variational phase-field approach; Computational Methods Appl. Mech. Engrg 361 (2020) 112731.

Carpinteri, A., Lacidogna, G., Paggi, M., (2007), Acoustic emission monitoring and numerical modeling of FRP delamination in RC beams with non-rectangular cross-section. Mater Struct;40(6):553–66.

Carpinteri, A., Grazzini, A., Lacidogna, G., Manuello, A., (2014) Durability evaluation of reinforced masonry by fatigue tests and acoustic emission technique. Struct Control Health Monit 21:950–961

Casamassima, V.M., and D'Amato, M., (2019) Fatigue Assessment and Deterioration Effects on Masonry Elements: A Review of Numerical Models and Their Application to a Case Study. Front. Built Environ. 5:65. DOI: 10.3389/fbuil.2019.00065

Casas, J.R., (2009), A probabilistic fatigue strength model for brick masonry under compression. Constr Build Mater;23(8):2964–72.

Casas, J.R., (2011), Reliability-based assessment of masonry arch bridges. Constr Build Mater ;25(4):1621–31.

Cavicchi, A. and Gambarotta, L., (2005), Collapse analysis of masonry bridges taking into account arch–fill interaction. Eng Struct ;27(4):605–15.

Cavicchi, A.and Gambarotta, L., (2006), Two-dimensional finite element upper bound limit analysis of masonry bridges. Comput Struct;84(31–32):2316–28.

CD 376; Unreinforced Masonry Arch Bridges, Highways Structures Design, DMRB Volume 2, Section 2 March 2020

Cervenka, J. and Papanikolaou, V. K., (2008), Three-Dimensional Combined Fracture – Plastic Material Model for Concrete. Int. Journal of Plasticity, Volume 24, Issue 12, ISSN 0749-6419.

Cecchi, A.and Milani, G., (2008), A kinematic FE limit analysis model for thick English bond masonry walls. Int J Solids Struct ;45(5):1302–31.

Česnik, M. and Slavič, J., (2013) Vibrational Fatigue and Structural Dynamics for Harmonic and Random Loads. Journal of Mechanical Engineering 60(2014)5, 339-348

Chaimoon, K. and Attard, M. M., (2007), Modelling of unreinforced masonry walls under shear and compression, Engineering Structures 29, 2056–2068.

Cancelliere, I., Imbimbo, M. and Sacco, E., (2010), Experimental tests and numerical modeling of reinforced masonry arches, Engineering Structures 32 p776–792

Chaboche, J.L., Girard, R. and Levasseur, P., (1997), On the interface debonding models, International Journal of Damage Mechanics, Volume 6, Issue 3, Pages 220-257.

Clark, G. W., (1994), Bridge analysis testing and cost causation: serviceability of brick masonry. British Rail Research Report LR-CE5-151.

Coffin, L. F., (1954) A Study of the Effects of Cyclic Thermal Stresses on a Ductile Metal, *Trans. ASME*. Aug 1954, 76(6): 931-949 (19 pages)

Cross-Rudkin, P.M.S., Chrimes, M.M, Bailey. M.R. (2008), Biographical Dictionary of Civil Engineers in Great Britain and Ireland. Volume 2: 1830–1890. Thomas Telford, London.

Crumley, J., and Kennedy, W. (1977). Fatigue and Repeated-load Elastic Characteristics of Inservice Portland Cement Concrete. Texas, USA: Center of Highway Research, The University of Texas.

CS 454 Assessment of highway bridges and structures version 1.1.0 October 2022

Cundall, P. A., (1971), A computer model for simulating progressive large-scale movements in blocky rock systems. In Proceedings of the Symposium on Rock Fracture (ISRM), vol. 1, paper II II 8. Nancy, France.

Cundall, P. A. (1988), Formulation of a three-dimensional distinct element model - Part I: A scheme to detect and represent contacts in a system composed of many polyhedral blocks. International Journal of Rock Mechanics and Mining Sciences 25(3): 107–116.

Cundall, P. A. and Strack, O.D.L., (1979), A discrete numerical model for granular assemblies. Geotechnique 29(1): 47–65.

Cundall, P. A. and Hart, R.D., (1989), Numerical modeling of discontinua. In Proceedings of the First US Conference on Discrete Element Methods. CSM Press, Colorado.

Cundall P. A. and Strack O.D.L., (1979), A discrete numerical model for granular assemblies. Geotechnique 1979a;29(1): 47e65.

Cundall P. A. and Strack O.D.L., (1979), The distinct element method as a tool for research in granular media e part II. Rep. NSF Grant ENG76-20771. Minneapolis, USA: Department of Civil & Mineral Engineering, University of Minnesota; 1979b.

Cundall P.A.and Hart R.D., (1992), Numerical modelling of discontinua. Engineering Computations 1992; 9:101e13.

Davidson, D., Chan, K., McClung, R., and Hudak, S., (2003), Cyclic Loading and Fatigue in Comprehensive Structural Integrity.

Decarbonising Transport – Setting the Challenge, Rail Delivery group 2020.

Dobromil, P., Jan, C., Radomir, P., (2010), Material model for finite element modelling of fatigue crack growth in concrete; Procedia Engineering 2, 203–212.

Elber, W., Fatigue crack closure under cyclic tension, Engineering Fracture Mechanics. 2 (1) (1970) 37–45, arXiv:1011.1669v3.

EN 1991-2:2003. Eurocode 1. Actions on structures – Part 2: Traffic loads on bridges.

EN 1993-1-9:2003. Eurocode 3. Design of steel structures – Part1-9: Fatigue.

Fatemi, A. and Yang, L., (1998), Cumulative fatigue damage and life prediction theories: a survey of the state of the art for homogeneous materials, Int. 1. Fatigue Vol. 20, No. I, pp. 9-34, 1998 © Elsevier Science Ltd.

Freight Rail Usage 2018-19 Q4 Statistical Release Publication, ORR date: 6 June 2019

Forced and Ambient vibration testing on full scale bridges, October 2013; The LRF Centre for Safety and Reliability Engineering, University of Aberdeen & Department of Civil and Environmental Engineering, University of Auckland

Fox, F. (1885-6), Viaduct over the River Esk at Whitby, and the Embankments and Culverts in the Ravines. Paper No. 2117. Minutes of the Proceedings of the Institution of Civil Engineers, 86 (4): 301-311.

Garrity, S.W. (2015). The complex engineering design challenges of masonry arch rehabilitation. In: Amoêda, R. Lira, S. & Pinheiro, C. eds. Proc. 2nd Int. Conf. on Preservation, Maintenance and Rehabilitation of Historical Buildings and Structures, 22nd – 24th July, Porto. Barcelos: Green Lines Institute for Sustainable Development, 139-150. ISBN: 978-989-8734-10-5

Gentile, A. and Saisi, A., (1889), Ambient vibration testing and condition assessment of the Paderno iron Arch bridge. Construction and Building Materials Volume 25, Issue 9, September 2011, Pages 3709-3720

Geubelle, P.H. and Baylor, J.S., (1998), Impact-induced delamination of composites: a 2D simulation, Composited Part B: Engineering, Volume 29, Issue 5, September 1998, Pages 589-602Geubelle. P.H and Baylor. J.S, Impact-induced delamination of composites: a 2D simulation, Composited Part B: Engineering, Volume 29, Issue 5, September 1998, Pages 589-602

Gao, X., Koval. G. & Chazallon, C., (2019), A Discrete Element Model for Damage and Fatigue Crack Growth of Quasi-Brittle Materials. Advances in Materials Science and Engineering. 2019. 1-15. 10.1155/2019/6962394.

Gilbert, M., Casapulla, C., & Ahmed, H.. (2006). Limit analysis of masonry block structures with non-associative frictional joints using linear programming. Computers & Structures. 84. 873-887. 10.1016/j.compstruc.2006.02.005.

Gilbert, M. and Melbourne, C., (1994), Rigid-block analysis to masonry arches. Struct Eng ; 72:356–61.

Grasselli, G. and A. Lisjak, A., (2014), A review of discrete modelling techniques for fracturing processes in discontinuous rock masses Journal of Rock Mechanics and Geotechnical Engineering 6 p301-314.

Grgic, D. and Amitrano, D., (2009), Creep of a porous rock and associated acoustic emission under different hydrous conditions. J Geophys Res-Solid, Earth;114(B10201).

Harvey, W.J., (1991), Stability strength elasticity and thrust lines in masonry arches. Struct Eng ;69(9):181–4.

Hendry, A.W., Davies, S.R., Royles, R., Ponniah, D.A., Forde, M.C.and Komeyli-birjandi, F., (1986), TRRL Contractor Report 26; Load test to collapse on a masonry bridge at Bergower, Starthclyde.

Heyman Jacques (1982): The Masonry Arch; Ellis Horwood series in engineering science, Ellis Horwood, Chichester, 117 pp

Hayward, A. (2011), Train loads on bridges 1825 to 2010. International Journal for the History of Engineering & Technology. 81 (2), pp. 159–191

Hart, R.D., Cundall, P.A. and Lemos, J.V., (1988), Formulation of a three-dimensional distinct element model — part II: mechanical calculations. International Journal of Rock Mechanics and Mining Sciences 25(3): 117–125.

Hilerborg, A., Modeer, M. and Petersson, P.E., (1976), Analysis of crack formation and crack growth in concrete by means of fracture mechanics and finite elements, Cement and Concrete Research, Volume 6, Issue 6, Pages 773-781

Holmen, J.O. (1982), Fatigue of Concrete by Constant and Variable Amplitude Loading. ACI Special Publication, 75, 71-110

Hughes, T.G. and Blackler, M.J., (1997), A review of the UK masonry arch assessment methods. Proceedings of the Institute of Civil Engineers ; 122:305–15.

ICE Manual for Bridge Engineering; Institution of Civil Engineers, 2nd Edition 2008

IRS 70778-3:2020 Recommendations for the inspection, assessment and maintenance of masonry arch bridges.

Page, J., (1987), TRRL Digest of Research Report 110; Load test to collapse on two arch bridges at Preston, Shropshire and Prestwood, Staffordshire. ISSN: 0266-5247

Pippard, A.J.S., (1948), The approximate estimation of safe loads on masonry bridges, Civil engineer in war: Institution of Civil Engineers, 1, 365

Pippard, A.J.S. and Ashby, R.J., 1939, An experimental study of the voussoir arch, Journal of the Institution of Civil Engineering, 10, 383-403

Kaechele, L., (1963), Review and Analysis of Cumulative Fatigue Damage Theories, research sponsored by the US Air Force under Project RAND – Contract No AF49(638)-700.

Kazerani, T., Yang, Z,Y. and Zhao, J., (2012), A discrete element model for predicting shear strength and degradation of rock joint by using compressive and tensile test data. Rock Mechanics and Rock Engineering ;45(5):695-709.

Kazerani, T.and Zhao, J., (2010), Micromechanical parameters in bonded particle method for modelling of brittle material failure. International Journal for Numerical and Analytical Methods in Geomechanics ;34(18):1877-95

Kim,Y. and Hwang, W.I., (2019), High-Cycle, Low-Cycle, Extremely Low-Cycle Fatigue and Monotonic Fracture Behaviors of Low-Carbon Steel and Its Welded Joint; Materials , 12, 4111; doi:10.3390/ma12244111

Klerck, P.A., Sellers, E.J. and Owen, D.R.J., (2004), Discrete fracture in quasi-brittle materials under compressive and tensile stress states. Computer Methods in Applied Mechanics and Engineering;193(27-29):3035-56.

Klerck, P.A., The finite element modelling of discrete fracture in quasi-brittle materials. PhD Thesis. Swansea, UK: University of Wales; 2000.

Koltsida, I.S., Tomor, A.K. and Booth, C.A., (2013), The use of digital image correlation technique for monitoring masonry arch bridges; University of the West of England, Faculty of Technology and Environment, Bristol, UK

Koltsida, I.S., Tomor, A.K. and Booth, C.A., (2018), Probability of fatigue failure in brick masonry under compressive loading, International Journal of Fatigue 112, 233–239.

Koltsida, I. S, Tomor, A. K. and Booth, C. A., (2018), Experimental evaluation of changes in strain under compressive fatigue loading of brick masonry. Constr Build Mater; 162:104–12.

Koltsida, I. S, Tomor, A. K. and Booth, C. A., (2019), Strain evolution of brick masonry under cyclic compressive loading. Materials and Structures p 52:76

Kuczma, M., Wybranowska, K., (2005) ―Numerical homogenization of elastic brick masonry,‖ Civil and Environmental engineering reports of University of Zielona Góra, Poland, pp. 135 - 152.

Kwooi-Hock Ng, 1999, Analysis of masonry arch bridges; PhD thesis.

Lay, M. G. (1992), Ways of the World: a history of the World's roads and the vehicles that used them. New Brunswick: Rutgers University Press.

Lee, Y. L, Barkey, M.E., Kang, H.Y., (2011), Metal Fatigue Analysis Handbook: Practical Problem-solving Techniques for Computer-aided Engineering, Publisher Elsevier, 2011, ISBN 0123852056, 9780123852052

Lemos, J.V., (1995), Assessment of the ultimate load of a masonry arch using discrete elements. In Computer Methods in Structural Masonry—3, eds., J. Middleton and G. N. Pande. Swansea: Books & Journals International. 294–302.

Lemos, J.V., (1997), Discrete element modelling of the seismic behaviour of stone masonry arches. In Computer Methods in Structural Masonry — 4, eds., G.N. Pande, J. Middleton, and B. Kralj. London: E & FN Spon, 220–227.

Lemos, J.V., (2001), Modelling the behaviour of a stone masonry arch structure under cyclic loads. In Computer Methods in Structural Masonry — 5, eds. T.G. Hughes and G.N. Pande. Swansea: Computers & Geotechnics Ltd., 101–108.

Lemos, J.V., (2006), Modeling of historical masonry with discrete elements. In Computational Mechanics — Solids, Structures and Coupled Problems, eds. C.A. Mota Soares, J.A.C. Martins, H.C. Rodrigues and J.A.C. Ambro´ sio. Dordrecht: Springer, 375–392.

Lemos J.V., (2007), Discrete element modelling of masonry structures; International Journal of Architectural Heritage, 1: 190–213.

Liu, B., Drougkas, A., Sarhosis, V., (2023)., A material characterisation framework for assessing brickwork masonry arch bridges: From material level to component level testing, Construction and Building Materials,
Volume 397, 132347, ISSN 0950-0618,

Llu, J., Xiang, C. and Yuan, H., (2009), Prediction of 3D small fatigue crack propagation in shot-peened specimens, Computational Materials Science, Volume 46, Issue 3, Pages 566-571

Lockner, D. and Byerlee, J., (1977), Acoustic emission and creep in rock at high confining pressure and differential stress. Bull Seismol Soc Am ;67(2):247–58.

Lorig, L.J., Cundall, P.A. (1989), Modeling of Reinforced Concrete Using the Distinct Element Method. In: Shah, S.P., Swartz, S.E. (eds) Fracture of Concrete and Rock. Springer, New York, NY. https://doi.org/10.1007/978-1-4612-3578-1_28

Lourenco, P. B. (1996), Computational strategies for Masonry structures, PhD thesis, Delft University of Technology.

Lourenço, P. B., Milani, G., Tralli. A.and Zucchini, A., (2007), Analysis of masonry structures: review of and recent trends in homogenisation techniques. Can J Civ Eng;34(11):1443–57.

Lourenco, P. B. and Rots, J. G., (1997), `Multisurface interface model for analysis of masonry structures', Journal of Engineering Mechanics (ASCE) 123(7), 660-668.

Lourenco, P. B., Rots, J. G. and Blaauwendraad, J., (1995), `Two approaches for the analysis of masonry structures: micro and macro-modeling', Heron 40(4), 313340.

Lourenco, P. B., Rots, J. G. and VanderPluijm, R., (1999), `Understanding the tensile behaviour of masonry parallel to the bed joints: a numerical approach.', Masonry Int; the British Masonry Society winter 12(3), 96-103.

Lourenco, P. B., Rots, J. and Blaauwendraad, J., (1998), `Continuum model for masonry: parameter estimation and validation', Journal of Structural Engineering 124(6), 642-652.

Lourenco, P.B., (2002) Computations of historical masonry constructions. Progress in Structural Engineering and Materials, 4(3):301–319.

Lourenco, P.B., (2013), Computational strategies for masonry structures; multi-scale modelling, dynamics, engineering applications and other challenges; Congreso de Métodos Numéricos en Ingeniería 25-28 junio 2013.

Manual for the design of plain masonry in building structures to Eurocode 6 - The Institution of Structural Engineers, February 2008

Macorini, L. & Izzuddin, B. (2011). A non-linear interface element for 3D mesoscale analysis of brick-masonry structures. International Journal for Numerical Methods in Engineering. 85. 1584 - 1608. 10.1002/nme.3046.

Manson, S. (1953) Behaviour of Materials under Conditions of Thermal Stress. NACA Technical Note, Tech. Rep. 2933.

McEwen, C. (2010), Jaggermen's Bridges on Packhorse Trails. Keighley: Sledgehammer Engineering
Press Limited.

McKibbins, L. D., Melbourne, C., Sawar, N., Gaillard C. S., (2006), CIRIA C656: Masonry arch bridges: condition appraisal and remedial treatment, CIRIA, London.

Laterza, M., D'Amato, M. and Casamassima, V.M., (2016), Fatigue behavior of old masonry arch bridges; Proceedings of the 7th International Conference on Safety and Durability of Structures ICOSADOS 2016 May 10 - 12, UTAD, Portugal.

McCall, J., (1958), Probability of fatigue failure of plain concrete. J Am Concr Inst 1958;55(8):233–44.

Baker, M.G., (1996), Finite Element analysis of masonry with application to arch bridges; PhD thesis.

Medeiros, A., Zhang, X., Ruiz, G., Yu, R., De Souza. M. and Lima, V., (2015), Effect of the loading frequency on the compressive fatigue behavior. Int J Fatigue; 70:342–50.

Melbourne, C. and Hodgson, J.A., (1996), The behaviour of skewed brickwork arch bridges. In: Arch bridges (Ed. Melbourne); p. 309–20.

Melbourne, C. and Walker, P.J., TRRL Contractor Report 189; Load test to collapse on a full-scale model six metre span brick arch bridge.

Melbourne, C. and Tomor, A.K. (2006) Application of Acoustic Emission for Masonry Arches, Strain - International Journal for Strain Measurement, 42, p. 165-172

Melbourne, C., Wang, J. and Tomor, A. K., (2007) A new masonry arch bridge assessment strategy (SMART); ARCH'07 – 5th International Conference on Arch Bridges,

Miller, K. J., (1987), The behaviour of short fatigue cracks and their initiation. II. A general summary
Fatigue Fract. Eng. Mater. Struct., 10 (1987), pp. 93-113

Miller, O., Freund, L.B. and Needleman, A., (1999) Energy dissipation in dynamic fracture of brittle materials Modelling and Simulation in Materials Science and Engineering, Volume 7, Issue 4, 573 doi:10.1088/0965-0393/7/4/307

Miller, R.K., Hill, E.v.K., and Moore, P.O., (2005), Nondestructive Testing Handbook, 3rd Ed., Vol. 6. Acoustic Emission Testing. Columbus, OH: American Society for   nondestructive Testing,, p. 32.

Milani, G., Tralli, A. (2011), Simple SQP approach for out-of-plane loaded homogenized brickwork panels accounting for softening. Computer Struct ;89(1–2):201–15.

Milani, G., Lourenço, P.B., (2012), 3D non-linear behaviour of masonry arch bridges, Computers and Structures 110–111, 133–150.

Mynarz M. and Mynarzova, L., (2018), Non-linear approaches to the response of brick masonry wall to lateral loading, International Journal of GEOMATE, Vol.14, Issue 42, pp.76-82

Miner, M.A. (1945) Cumulative damage in fatigue. J.Appl.Mech., Vol.12, pp. A159-A164.

Munjiza, A., Andrews, K.R.F. and White, J.K. (1999), Combined single and smeared crack model in combined finite-discrete element analysis. Int. J. Numer. Meth. Engng., 44: 41-57.

Munjiza, A. and Andrews, K.R.F. (1998), NBS contact detection algorithm for bodies of similar size. Int. J. Numer. Meth. Engng., 43: 131-149

Munjiza, A. and Andrews, K.R.F. (2000), Penalty function method for combined finite-discrete element systems comprising large number of separate bodies. International Journal for Numerical Methods in Engineering 49(11):1377-1396

Munjiza, A., John, N.W.M., (2002) Mesh size sensitivity of the combined FEM/DEM fracture and fragmentation algorithms, Engineering Fracture Mechanics, Volume 69, Issue 2, Pages 281-295, ISSN 0013-7944,

Munjiza, A., Owen, D.R.J. and Bicanic, N. (1995), "A combined finite-discrete element method in transient dynamics of fracturing solids", Engineering Computations, Vol. 12 No. 2, pp. 145-174.

Munjiza, A. The combined finite-discrete element method. Chichester, UK: John Wiley & Sons Ltd.; 2004.

Nationalencyklopedin: (2010). Bd 35, ISBN 918636538X, 9789186365387

Needleman, A., An analysis of decohesion along in imperfect interface, International Journal of Fracture, Volume 42, Issue 1, January 1990, Pages 21-4

NR/GN/CIV/025 The Structural Assessment of Underbridges, Network Rail Publication assessment of Railway Bridges, June 2006

Onoue, K. and Matsushita, H., (2012) Reduction mechanisms of fatigue strength of concrete under compression due to permeation of liquids, Construction and Building Materials, Volume 37, Pages 82-92, ISSN 0950-0618

Orduna, A. Seismic assessment of ancient masonry structures by rigid blocks limit analysis. PhD thesis, University of Minho, PT; 2005.

Owen, D.R.J. & Feng, Y.. (2001). Parallelised finite/discrete element simulation of multi-fracture solids and discrete systems. Engineering Computations. 18. 557-576. 10.1108/02644400110387154.

Ozen Engineering, ANSYS R16 Course notes, Session 04 Fracture Mechanics using Cohesive Zone Material (CZM) Model

Page, A. (1978). Finite element model for masonry. ASCE J Struct Div. 104. 1267-1285. 10.1061/JSDEAG.0005406.

Page, A.W., Kleeman, P.W., & Dhanasekar, M. (1985). An In-Plane Finite Element Model for Brick Masonry. New analysis techniques for structural masonry (p. 18). Chicago, Illinois, USA: American Society of Civil Engineers.

Page, J. (1993),. State of the art review. Masonry arch bridges. Transport Research Laboratory. London:
HMSO.

Pålmgren, A. (1924) The endurance of ball bearings (in German). Z. Ver.Deut. Ing., Vol.68, pp.339-341.

Pan, B., Tian, L., Song, X., (2016), Real-time, non-contact and targetless measurement of vertical deflection of bridges using off-axis digital image correlation, NDT & E International. Volume 79, Pages 73-80, ISSN 0963-8695,

Paris, P.C., & Erdogan, F. (1963). A Critical Analysis of Crack Propagation Laws. Journal of Basic Engineering, 85, 528-533.

Paris, P.C., Gomez, P.M. and Anderson, W. E., (1961), A rational analytic theory of fatigue. The trend inf Engineering, 13:9–14,

Pelà, L., Aprile, A. & Benedetti, A. (2009). Seismic assessment of masonry arch bridges. Engineering Structures. 31. 1777-1788. 10.1016/j.engstruct.2009.02.012.

Pippard, A.J.S. (1948) The approximate estimation of safe loads on masonry bridges. The civil engineer in war: Institue of Civil Engineers; 1:365-372. Thomas Telford Ltd

Pippard, A. J. S. and Ashby, R. J., (1939), An experimental study of the voissour arch. J Institute of Civil Engineers; 10:383–403.

Pluijm, R. (1997). Non-Linear Behaviour of Masonry under Tension. HERON, 42 (1), 1997. 42. ISSN 0046-7316

Radnić, J., Harapin, A., Smilović, M., Grgić, N. & Glibić, M. (2012). Static and dynamic analysis of the old stone bridge in Mostar. Gradjevinar. 64. 655-665. 10.14256/JCE.715.2012.

Ribeiro, D., Calçada, R., Ferreira, J. and Martins, T.,(2014), Non-contact measurement of the dynamic displacement of railway bridges using an advanced video-based system, Engineering Structures, Volume 75, 2014, Pages 164-180, ISSN 0141-0296,

Ritchie, R. (2002). Fatigue of brittle materials. Elsevier Science Ltd.. Comprehensive Structural Integrity. Vol. 4: Cyclic Loading and Fatigue, 4. LBNL Report #: LBNL-51149

Roberts, T.M., Hughes, T.G., Dandamudi, V.R. & Bell, B., (2006). Quasi-static and high cycle fatigue strength of brick masonry. Construction and Building Materials. 20. 603-614. 10.1016/j.conbuildmat.2005.02.013.

Robert D. C., David S., Markus M. E., Plesha, R., Witt, j., Concepts and Application of Finite Element Analysis, Fourth Edition, John Wiley & Sons, 2002, ISBN 978-0-471-35605-9

Roca, P., Cervera, M., Gariup, G., Pela', L., (2010). Structural analysis of masonry historical constructions. Classical and advanced approaches. Arch. Comput. Methods Eng. 17, 299–325. https://doi.org/10.1007/s11831-010-9046-1

Ronca, P., Franchi, A. and Crespi, P., (2004) Structural failure of historic buildings: masonry fatigue tests for an interpretation model. In:Structural analysis of historical constructions – possibilities of numerical and experimental techniques. Pg 273-9 ISBN 04 1536 379 9

Ruddock, T., (1979), Arch bridges and their builders, 1735 – 1835. Cambridge: Cambridge University
Press.

Sacco, E. & Toti, J. (2010). Interface Elements for the Analysis of Masonry Structures. International Journal for Computational Methods in Engineering Science and Mechanics. 11. 354-373. 10.1080/15502287.2010.516793.

Safe management of railway structures (Phase 2) - Compendium Report, September 2005 RSSB, Mott McDonald

Samuelsson A. Wiberg N-E. (1995): Byggnadsmekanik - Strukturmekanik (Building mechanic – structural mechanic. In Swedish), Chalmers, Göteborg,

Schijve, J., (2003), Fatigue of structures and materials in the 20th century and the state of the art, International Journal of Fatigue, Volume 25, Issue 8, Pages 679-702, ISSN 0142-1123,

Shi. G, Goodman, R. (1988), Discontinuous deformation analysis e a new method for computing stress, strain and sliding of block systems. In: Proceedings of the 29th US Symposium on Rock Mechanics. Rotterdam: A.A. Balkema.

Ravi, S., Viswanathan, S., Nagarajan, T., Srinivas, V., & Narayanan, P. (2014), Experimental and Numerical Investigations on Material Behaviour of Brick Masonry. 2nd International Conference on Research in Science, Engineering and Technology (ICRSET'2014), March 21-22.

Smoljanović, H., Nikolić, Ž. & Zivaljic, N., (2015). A combined finite–discrete numerical model for analysis of masonry structures. Engineering Fracture Mechanics. 136. 1-14. 10.1016/j.engfracmech.2015.02.006.

Sparks, P.R., & Menzies, J.B. (1973). The effect of rate of loading upon the static and fatigue strengths of plain concrete in compression. Magazine of Concrete Research, 25, 73-80.

Suresh, S., Fatigue of Materials, Cambridge University Press, Cambridge, 1998.

Sustainable Bridges; Methods of Analysis of Damaged Masonry Arch Bridges, Background Document D4.7.3

TRRL – Contractor's report 244 Masonry properties for assessing Arch Bridges, A. W. Hendry, 1990

Tateishi, K. & Hanji, T. (2004). Low cycle fatigue strength of butt-welded steel joint by means of new testing system with image technique. International Journal of Fatigue. 26. 1349-1356. 10.1016/j.ijfatigue.2004.03.016.

Lin, T.J. & LaFave, J. (2012). Experimental structural behavior of wall-diaphragm connections for older masonry buildings. Construction and Building Materials. 26. 180–189. 10.1016/j.conbuildmat.2011.06.008.

Tomor, A.K. (2016) *Acoustic emission monitoring of masonry arch bridges.* Technical Report. international Union of Railways (UIC), France.

Tomor, A. K., De Santis, S. & Wang, J. (2014). Fatigue deterioration process of brick masonry. Masonry International. 26. 41-48.

Tomor, A.K, Verstrynge, E. (2013), A joint fatigue-creep deterioration model for masonry with acoustic emission-based damage assessment. Construction and Building Materials Volume 43, June 2013, Pages 575-588

Tvergaard, V. and Hutchinson, J. W., (1992),The relation between crack growth resistance and fracture process parameters in elastic-plastic solids, Journal of the Mechanics and Physics of Solids, Volume 40, Issue 6, Pages 1377-1397

UIC Report. (2004): Assessment, Reliability and Maintenance of Masonry Arch Bridges (ed. Orbán, Z., UIC Masonry Arch Bridges Study Group). State-of-the-Art Research Report of the International Union of Railways, Paris.

Sarhosis. V., Garrity, S.W. and Sheng, Y., (2015), Influence of brick–mortar interface on the mechanical behaviour of low bond strength masonry brickwork lintels, Engineering Structures, Volume 88, 2015, Pages 1-11, ISSN 0141-0296,

Van Beek, G. W. 1987. Arches and vaults in the ancient Near East. Scientific American, 257(1): 96-103.

Verstrynge, E. Long-term behaviour of monumental masonry constructions: modelling and probabilistic evaluation. PhD thesis. civil engineering department, K.U. Leuven: Leuven; 2010.

Vicente, M., Gonzalez, D., Minguez, J. and Martinez J. (2014). Residual modulus of elasticity and maximum compressive strain in HSC and FRHSC after high-stress-level cyclic loading. Struct. Concrete. 15, 210–218. doi: 10.1016/j.conbuildmat.2013.02.045

Wang, J., Heath, A. and Walker, P., (2013), Experimental investigation of brickwork behaviour under shear, compression and flexure, Construction and Building Materials, 48: 448-456.

Wang, J., Heath, A. and Walker, P., (2013), Transverse behaviour of masonry arch bridges: Investigation of spandrel wall failure. 7th International Conference on Arch Bridges, Oct 2013, Split, Croatia.

Wang, J., Heath, A. and Walker, P., (2014). Numerical analysis of triplet Shear test on brickwork masonry. Advanced Materials Research, 831: 437-441.

Wang, J., Tomor, A. K., Melbourne, C. and Yousif, S., (2013), Critical review of research on high-cycle fatigue behaviour of brick masonry, Construction and Building Materials 38 (2013) 602–609 Elsevier Ltd

Walter, S., A History of Fatigue, Engineering and Fracture Mechanics Vol 54, No 2. Pp 263-300, 1996

Wöhler, A., Über die festigkeits-versuche mit eisen und stahl, Z. Bauwes. (XX) (1870) 73–106.

Yifei, C.,Dave, C. & Alireza, N. (2017). Discontinuum Modeling of Solid Deformation Pore-Water Diffusion Coupling. International Journal of Geomechanics. 17. 04017033. 10.1061/(ASCE)GM.1943-5622.0000903.

Yuan, H., Lln, G. and Cornec, A. (1996), Verification of a cohesive zone model for ductile fracture, Journal of Engineering Materials and Technology, Volume 118, Issue 2, 01 Pages 192-200

Zanuy, C., Albajar, L. and De la Fuente, P. (2011). The fatigue process of concrete and its structural influence. Mater. de Constr. 61, 385–399. doi: 10.3989/mc.2010.54609

Background Information

Appendix A
Supporting Analyses and Test Data

Appendix A1 – Analytical Capacities of 3.6 m Arch

Bridge Name: LEEDS ARCH   Bridge Location: GEL
Bridge Number: 01
Number of spans: 1

SAFETY FACTORS
Factor for deadload: 1.00   Factor for superimposed deadload: 1.00   Factor for surfacing: 1.00
Factor for live load: 1.23   Factor for load effect: 1.00   Factor for material strength: 1.00

Applied distribution mode: Archie-M, BD21/97
Applied live load pressure: Active pressure

STRUCTURE PROPERTIES
Road shape: Curved (3-point method)
Road points: (-256, 195) (1800, 1222)   (3856, 200)
Depth of surfacing: 1   [mm]   Depth of overlay: 0   [mm]
Surface unit weight: 15.00   [kN/m3]   Overlay unit weight: 1.00   [kN/m3]
Available width: 3140   [mm]
Min. effective width: 3140   [mm]

Fill unit weight: 18.00   [kN/m3]   Fill phi: 30   degree

Left abutment   Base level: 0   [mm]   Height: 0   [mm]   Width: 600   [mm]
Right abutment   Base level: 0   [mm]   Height: 0   [mm]   Width: 600   [mm]

SPAN 1
Shape: Circular
Span: 3600   [mm]   Rise: 900   [mm]   Q-rise: 712   [mm]
Ring thickness at crown: 320   [mm]   Ring thickness at springing: 320   [mm]   Mortar loss: 0   [mm]
Masonry unit weight: 20.00   [kN/m3]   Masonry strength: 5.00   [MPa]

Backing:

Span	Position	Type	Height [mm]		Width [mm]	Unit weight [kN/m3]	Strength [MPa]
1	left	NONE	0	0	0.00	0.00	
1	right	NONE	0	0	0.00	0.00	

Segment	Intrados.x	Intrados.z	Extrados.x	Extrados.z	Road.z	Fx dead	Fz dead	My dead	Fx live	Fz live	My live	Fx passive	Fx total	Fz total	My total	Thrust in	Thrust out	Extra-Thrust	
0	0	0	-256	192	195	0.00	0.00	0.00	0.00	0.00	0.00	0.00	-180.63	-176.96	-13.31	28	78	242	
1	65	82	-182	286	288	0.00	-0.72	-0.07	0.00	-0.00	0.00	0.00	-180.63	-176.24	-9.81	14	64	256	
2	133	161	-104	376	378	0.00	-0.72	-0.06	0.00	-0.00	0.00	0.00	-180.63	-175.52	-7.47	5	55	265	
3	205	237	-22	462	464	0.00	-0.72	-0.06	0.00	-0.00	0.00	0.00	-180.63	-174.80	-6.30	-0	50	270	
4	280	309	64	545	547	0.00	-0.72	-0.05	0.00	-0.00	0.00	0.00	-180.64	-174.09	-6.29	0	50	270	
5	358	377	153	623	625	0.00	-0.72	-0.05	0.00	-0.00	0.00	0.00	-180.64	-173.37	-7.45	5	55	265	
6	440	442	246	697	699	0.00	-0.72	-0.04	0.00	-0.00	0.00	0.00	-180.64	-172.65	-9.76	14	64	256	
7	524	504	343	767	769	0.00	-0.72	-0.04	0.00	-0.00	0.00	0.00	-180.64	-171.93	-13.22	29	78	242	
8	612	561	443	832	834	0.00	-0.72	-0.03	0.00	-0.00	0.00	0.00	-180.64	-171.21	-17.81	49	97	223	
9	702	614	545	893	895	0.00	-0.72	-0.03	0.00	-0.00	0.00	0.00	-180.64	-170.50	-23.52	74	122	198	
10	794	662	651	949	950	0.00	-0.72	-0.02	0.00	-0.00	0.00	0.00	-180.64	-169.78	-30.34	104	151	169	
11	888	707	758	999	1001	0.00	-0.72	-0.02	0.00	-0.00	0.00	0.00	-180.64	-169.06	-38.24	140	187	133	
12	984	747	868	1045	1047	0.00	-0.72	-0.01	0.00	-0.00	0.00	0.00	-180.64	-168.34	-47.21	183	229	91	
13	1083	783	980	1086	1087	0.00	-0.72	-0.00	0.73	-6.05	0.08	0.00	-181.37	-161.58	-56.68	231	276	44	
14	1182	813	1094	1121	1123	0.00	-0.72	0.00	5.44	-52.50	-0.05	0.00	-186.81	-108.36	-61.65	273	315	5	
15	1283	840	1210	1151	1153	0.00	-0.72	0.01	7.75	-89.19	-0.17	0.00	-194.57	-18.45	-58.22	281	320	-0	***
16	1385	861	1326	1176	1178	0.00	-0.72	0.01	3.96	-56.06	-0.18	0.00	-198.52	38.33	-49.86	246	284	36	
17	1488	878	1444	1195	1197	0.00	-0.72	0.02	0.37	-6.69	-0.12	0.00	-198.89	45.74	-41.69	200	238	82	
18	1592	890	1562	1209	1211	0.00	-0.72	0.02	-0.00	0.00	0.00	0.00	-198.89	46.46	-34.50	159	197	123	
19	1696	898	1681	1217	1219	0.00	-0.72	0.03	-0.00	0.00	0.00	0.00	-198.89	47.18	-28.18	124	163	157	
20	1800	900	1800	1220	1222	0.00	-0.72	0.03	-0.00	0.00	0.00	0.00	-198.89	47.90	-22.74	94	134	186	

21	1904	898	1919	1217	1219	-0.00	-0.72	0.04	0.00	0.00	0.00	0.00	-198.89	48.61	-18.19	70	111	209
22	2008	890	2038	1209	1211	-0.00	-0.72	0.05	0.00	0.00	0.00	0.00	-198.89	49.33	-14.54	52	92	228
23	2112	878	2156	1195	1197	-0.00	-0.72	0.05	0.00	0.00	0.00	0.00	-198.89	50.05	-11.81	38	78	242
24	2215	861	2274	1176	1178	-0.00	-0.72	0.06	-0.05	-0.83	0.10	0.00	-198.84	51.61	-10.01	28	69	251
25	2317	840	2390	1151	1154	-0.00	-0.72	0.06	-0.60	-8.44	0.91	0.00	-198.25	60.77	-9.06	23	64	256
26	2418	813	2506	1121	1124	-0.00	-0.72	0.07	-1.26	-14.53	1.54	0.00	-196.98	76.01	-8.17	18	60	260
27	2517	783	2620	1086	1089	-0.00	-0.72	0.07	-0.96	-9.31	0.98	0.00	-196.02	86.04	-6.72	10	53	267
28	2616	747	2732	1045	1048	-0.00	-0.72	0.08	-0.16	-1.33	0.12	0.00	-195.85	88.10	-5.24	3	46	274
29	2712	707	2842	999	1003	-0.00	-0.72	0.08	0.00	0.00	0.00	0.00	-195.85	88.82	-4.61	-0	43	277
30	2806	662	2949	949	952	-0.00	-0.72	0.08	0.00	0.00	0.00	0.00	-195.85	89.54	-4.95	2	45	275
31	2898	614	3055	893	897	-0.00	-0.72	0.09	0.00	0.00	0.00	0.00	-195.85	90.26	-6.28	8	51	269
32	2988	561	3157	832	836	-0.00	-0.72	0.09	0.00	0.00	0.00	0.00	-195.85	90.98	-8.58	19	61	259
33	3076	504	3257	767	772	-0.00	-0.72	0.10	0.00	0.00	0.00	0.00	-195.85	91.71	-11.86	34	77	243
34	3160	442	3354	697	702	-0.00	-0.72	0.10	0.00	0.00	0.00	0.00	-195.84	92.43	-16.12	55	97	223
35	3242	377	3447	623	628	-0.00	-0.72	0.10	0.00	0.00	0.00	0.00	-195.84	93.15	-21.34	81	123	197
36	3320	309	3536	545	550	-0.00	-0.72	0.11	0.00	0.00	0.00	0.00	-195.84	93.87	-27.53	112	153	167
37	3395	237	3622	462	468	-0.00	-0.72	0.11	0.00	0.00	0.00	0.00	-195.83	94.60	-34.66	148	189	131
38	3467	161	3704	376	382	-0.00	-0.72	0.11	0.00	0.00	0.00	0.00	-195.83	95.32	-42.74	191	232	88
39	3535	82	3782	286	293	-0.01	-0.72	0.11	0.00	0.00	0.00	0.00	-195.82	96.05	-51.76	241	280	40
40	3600	0	3856	192	200	-0.01	-0.72	0.12	0.00	0.00	0.00	0.00	-195.82	96.77	-61.68	297	336	-16	***

APPLIED LOAD CASES

1. Double Axle (1.3   m) Total weight: 176.58   [kN]   Position: 2454   [mm]
18.00   2   1.00   9.00   1.30   9.00   1.00   1.80   2.50
Effective width: 3140   [mm]   Distribution length: 311   [mm]
2. Single Axle Total weight: 112.82   [kN]   Position: 1155   [mm]
11.50   1   1.00   11.50   1.00   1.80   2.50
Effective width: 3140   [mm]   Distribution length: 311   [mm]
3. Single Axle Total weight: 112.82   [kN]   Position: 1155   [mm]
11.50   1   1.00   11.50   1.00   1.80   2.50
Effective width: 3140   [mm]   Distribution length: 311   [mm]
4. Single Axle Total weight: 112.82   [kN]   Position: 1155   [mm]
11.50   1   1.00   11.50   1.00   1.80   2.50
Effective width: 3140   [mm]   Distribution length: 311   [mm]
5. Single Axle Total weight: 112.82   [kN]   Position: 1155   [mm]
11.50   1   1.00   11.50   1.00   1.80   2.50
Effective width: 3140   [mm]   Distribution length: 311   [mm]

This report was generated by LimitState:RING 4.0.5.30070 - limitstate.com

LimitState:RING idealizes a masonry arch bridge as an assemblage of rigid blocks and uses computational limit analysis methods to directly model the mode of response. The factor that would, when applied to the specified live loads, lead to the ULS (collapse) or PLS (service load limit) states being reached is reported, unless in support movement mode. This factor is termed the Adequacy Factor. When appropriate partial factors are included in the model, the Adequacy Factor should be greater than 1.0 for a safe and serviceable structure, considering the ULS and PLS respectively.

For more information, refer to the LimitState:RING User Manual.

Summary

BRIDGE NAME	LOCATION	REFERENCE NO.	MAP REFERENCE
ARCH02	GEL		

BRIDGE TYPE	NAME OF ASSESSOR	ASSESSING ORGANIZATION	DATE OF ASSESSMENT
Railway	AC	LEEDS	Sun Feb 4 2024

COMMENTS

ANALYSIS RESULT	ANALYSIS TYPE	SOLVER
Adequacy factor = 3.38869; Scenario 1 @ 2869mm (this is the critical case)	ULS	CLP

Mode of response at current load case
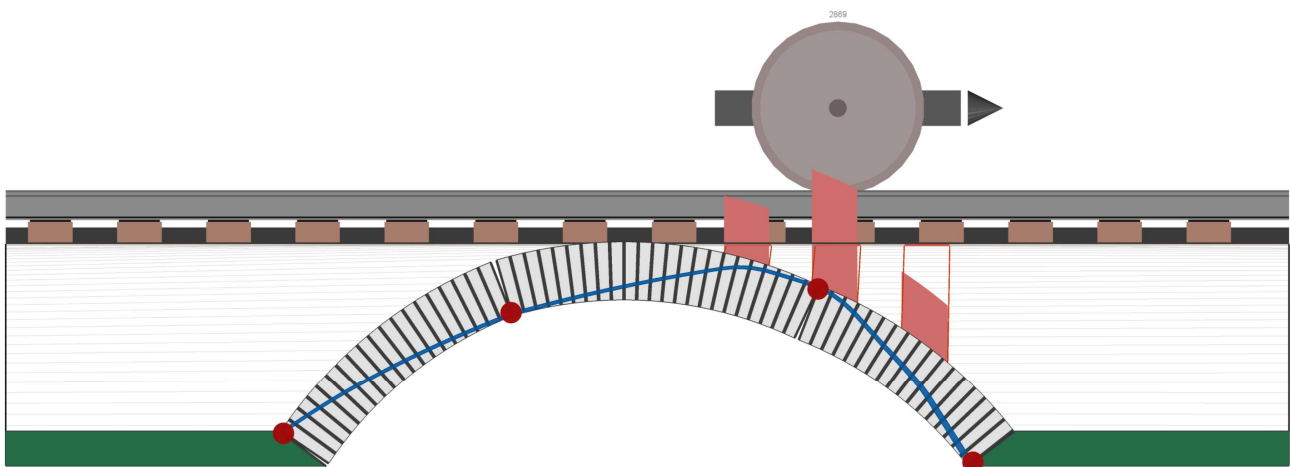
Adequacy Factor vs Load Position
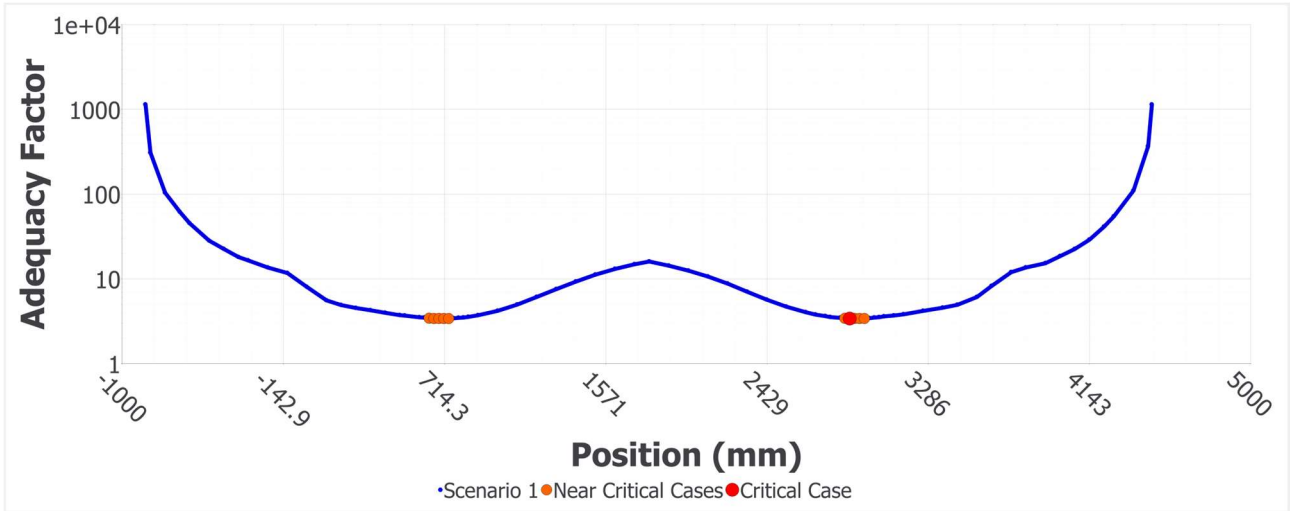
Units

Unless specified otherwise, the following units are used throughout this report:

DISTANCE	FORCE (PER M WIDTH)	MOMENT (PER M WIDTH)	ANGLE	UNIT WEIGHT	MATERIAL STRENGTH
mm	kN	kNm	Degrees	kN/m^3	N/mm^2

* = per metre width

Effective Bridge Width

CALCULATION	WIDTH (MM)
Auto computed	2490.91

Auto Bridge Width Inputs

DIMENSION	FRONT	BACK
Load dispersion angle: Surface (deg.)	15	15
Load dispersion angle: Backfill (deg.)	30	30
Additional width of arch (mm)	0	0

DIMENSION	FRONT	BACK
Maximum spread (mm)	5000	5000

Maximum effective bridge width (mm) = 5000

Geometry

Global

NO. SPANS	EFFECTIVE BRIDGE WIDTH
1	2490.91

Span 1

SPAN 1:	TYPE	SHAPE	NO. RINGS	SPAN	RISE	AUTO ANGLE	LHS ANGLE	RHS ANGLE
	Multi-ring	Segmental	1	3600	900	Yes	0	0
	59	320						

Fill Profile Properties

X	Y	SURFACE FILL DEPTH
1800	1230	10

Coordinates relative to left intrados springing of Span 1

Partial Factors

NAME	APPLICATION	TYPE	VALUE
Load effects factor	Load effects factor	Multiplier	1
Vehicle loads	Track load	Multiplier	1
	Axle load	Multiplier	1

NAME	APPLICATION	TYPE	VALUE
	Dynamic / impact	Multiplier	1
Material loads	Ballast unit weight	Multiplier	1
	Masonry unit weight	Multiplier	1
	Fill unit weight	Multiplier	1
Material strength	Masonry compressive strength	Divisor	1
	Masonry shear bond strength	Divisor	1
	Masonry friction	Divisor	1

Material Properties

Masonry

PROPERTY	VALUE
Unit weight	20
Model crushing	Yes
Compressive strength	5
Model radial sliding	Yes
Radial friction	0.6
Radial shear	0
Model inter-ring sliding	No
Inter-ring friction	Varies
Inter-ring shear	Varies

Backfill Basic Properties

UNIT WEIGHT	ANGLE OF FRICTION	COHESION	MODEL LIVE LOAD DISPERSION	MODEL HORIZONTAL PRESSURES	BACKING COMPRESSIVE STRENGTH
18	37.5	0	No	No	5

Backfill Advanced Properties

PROPERTY	VALUE
Live load dispersion type	Uniform
Cutoff angle	0
Soil arch interface: Friction multiplier	0.66
Soil arch interface: Adhesion multiplier	0.5

Backfill spandrel zone parameters

PARAMETER	ULS / PLS	ACTIVE / PASSIVE	VALUE
Factor ma	ULS	Active	0
maKa	ULS	Active	0
Factor mp	ULS	Passive	0
mpKp	ULS	Passive	0
Factor mpc	ULS	Passive	0
mpcKpc c	ULS	Passive	0
mpKp >= 1	ULS	Passive	No

Auto apply horizontal pressures = Yes

Horizontal pressures

POSITION	HORIZONTAL PRESSURES
Abutment 0	Auto
Abutment 1	Auto

Track/Ballast

UNIT WEIGHT	ANGLE OF DISPERSION OF LIVE LOADS
18	15

Track properties(railway underline bridge only)

TRACK LOAD PER UNIT AREA	SPACING BETWEEN SLEEPERS	
2	500	
SLEEPER LENGTH	SLEEPER BREADTH	SLEEPER HEIGHT
2400	250	125

Vehicles

NAME	AXLE #	FORCE	LOCAL POSITION	WIDTH	CONTACT
Default 100kN Single Axle	1	100	0	2400	250

Load Cases

SCENARIO	TYPE	VEHICLE	POSITION	DIRECTION	EFFECTIVE WIDTH	DYNAMIC AXLES	ADEQUACY FACTOR
Scenario 1	Auto	Default 100kN Single Axle	-875	Left to right	3603.94		1140
Scenario 1	Auto	Default 100kN Single Axle	-849	Left to right	3603.94		308.6
Scenario 1	Auto	Default 100kN Single Axle	-771	Left to right	3603.94		103.9
Scenario 1	Auto	Default 100kN Single Axle	-693	Left to right	3511.31		61.84
Scenario 1	Auto	Default 100kN Single Axle	-641	Left to right	3439.87		45.4
Scenario 1	Auto	Default 100kN Single Axle	-537	Left to right	3309.42		28.24
Scenario 1	Auto	Default 100kN Single Axle	-459	Left to right	3221.41		22.53

Appendix A2 – Arch 01 Test Data

Schedule of Tests

Prism Test		01/11/2019	DIC Trial	Nikon
		06/11/2019	DIC	Nikon

Hydraulic pressure	=	5000	psi
Turn down	=	**80**	bar
1 bar	=	14.507	psi
	=	1161	psi

Arch Test — 25/11/2019 10:00:00

No of Blows	Time (Sec)	Day	Time Lapsed		Clock Time		Log Scale
1	2.0E+00	2	00:00:02		10:00:02		0.3
10×10^0	1.0E+01	20.0	00:00:20		10:00:20		1
10×10^1	1.0E+02	200.0	00:03:20		10:03:20		2
10×10^2	1.0E+03	2000.0	00:33:20		10:33:20		3
10×10^3	1.0E+04	20000.0	Day 1	05:00:00	25/11/2019	15:00:00	4
10×10^4	1.0E+05	200000.0	Day 3	02:00:00	28/11/2019	12:00:00	5
40×10^4	4.0E+05	800000.0	Day 10	22:40:00	05/12/2019	08:40:00	5.6
70×10^4	7.0E+05	1400000.0	Day 17	22:40:00	12/12/2019	08:40:00	5.8
90×10^4	9.0E+05	1800000.0	Day 21	15:06:40	16/12/2019	01:06:40	6.0

	Timestamp	TZ	Load Cell 1 (kN)	Load Cell 2 (kN)
Free Standing	21/11/2019 13:29:00	n	0.17	0.24
11 kN	21/11/2019 13:31:00	n	10.65	10.82
21 - 11 kN	21/11/2019 13:35:45	n	10.77	21.01
11 - 21 kN	21/11/2019 13:46:10	n	20.38	10.94
11 kN	22/11/2019 12:25:15	n	10.75	10.86
21 - 11 kN	22/11/2019 12:26:19	n	10.73	20.38
11 - 21 kN	22/11/2019 12:31:11	n	20.28	10.91
11 kN	22/11/2019 12:41:45	n	10.74	10.93
21 - 11 kN	22/11/2019 12:42:14	n	10.76	20.43
11 - 21 kN	22/11/2019 12:46:49	n	20.25	10.93
11 kN	22/11/2019 13:38:45	n	10.76	10.94
21 - 11 kN	22/11/2019 13:39:55	n	10.76	20.41
11 - 21 kN	22/11/2019 13:44:05	n	20.32	10.93
11 kN	25/11/2019 09:36:34	n	11.04	10.95
21 - 11 kN	25/11/2019 10:32:02	n	11.30	20.23
11 - 21 kN	25/11/2019 10:34:13	n	20.35	10.96
11 kN	28/11/2019 11:40:00	n	10.88	10.88
21 - 11 kN	28/11/2019 09:43:00	n	10.77	20.19
11 - 21 kN	28/11/2019 09:45:30	n	20.12	10.98
11 kN	05/12/2019 11:23:30	n	11.12	11.15
21 - 11 kN	05/12/2019 11:25:40	n	11.09	20.55
11 - 21 kN	05/12/2019 11:30:40	n	20.39	11.08
11 kN	12/12/2019 12:03:40	n	10.94	11.13
21 - 11 kN	12/12/2019 12:05:50	n	10.92	20.58
11 - 21 kN	12/12/2019 12:09:50	n	20.42	11.07
11 kN	17/12/2019 13:57:40	n	11.05	11.03
21 - 11 kN	17/12/2019 13:58:50	n	11.01	20.49

Arch Test	No of Blows	Time (Sec)		Day	Time Lapsed	25/11/2019	10:00:00		Log Scale
	.						Clock Time		
	$10x10^5$	1.0E+06	2000000.0	Day 24	03:33:20	19/12/2019	13:33:20		6
		2.0E+06	4000000.0	Day 47	07:06:40	11/01/2020	17:06:40		6.3
		2.5E+06	5000000.0	Day 58	20:53:20	22/01/2020	06:53:20		6.4
		3.0E+06	6000000.0	Day 70	10:40:00	03/02/2020	20:40:00		6.5
		4.0E+06	8000000.0	Day 93	14:13:20	26/02/2020	00:13:20		6.6
		5.0E+06	10000000.0	Day 116	17:46:40	20/03/2020	03:46:40		6.7
	$10x10^6$	1.0E+07	20000000.0	Day 232	11:33:20	14/07/2020	21:33:20		7
	$10x10^7$	1.0E+08	##########	Day 2315	19:33:20	28/03/2026	05:33:20		8

	Timestamp	TZ	Load Cell 1 (kN)	Load Cell 2 (kN)
Free Standing	21/11/2019 13:29:00	n	0.17	0.24
11 - 21 kN	17/12/2019 14:01:50	n	20.44	10.99

0.049

-0.023   -0.044   -0.083   0.114

-0.153

Control LVDT 1 (mm)	Control LVDT 2 (mm)	LVDT 1 (50) (mm)	LVDT 2 (50) (mm)		LVDT 3 (25) (mm)	Laser (200) (mm)	SG 1 (µStrain)	SG 2 (µStrain)	SG 3 (µStrain)	SG 4 (µStrain)	SG 5 (µStrain)
83.046	70.596	38.451	24.180		8.943	151.597	-4073.43	-3643.36	-3898.21	-3864.24	-4209.34
80.505	67.023	38.428	24.136		8.861	151.542	-4058.01	-3638.34	-3900.87	-3860.99	-4205.19
		-0.023	-0.044	0.0494	-0.0827	-0.0552					
80.311	62.953	38.461	24.014		8.806	151.694	-4072.55	-3636.27	-3898.21	-3863.05	-4202.52
		0.011	-0.166	0.1660	-0.1372						
77.168	65.451	38.545	24.173		8.790	151.483	-4038.10	-3610.96	-3872.03	-3834.21	-4176.99
					-0.153						
82.740	100.513	38.587	24.099		8.808	151.637	-5031.47	-4600.28	-4857.59	-4816.14	-5156.71
82.736	97.858	38.605	24.018		8.789	151.698	-5023.76	-4594.06	-4854.93	-4812.88	-5147.78
81.135	100.041	38.583	24.161		8.785	151.489	-5015.68	-4583.62	-4844.49	-4795.93	-5136.73
82.270	100.042	38.588	24.092		8.798	151.637	-5039.93	-4605.45	-4868.72	-4824.88	-5158.92
82.274	97.750	38.607	24.010		8.777	151.717	-5036.67	-4603.38	-4864.57	-4821.61	-5154.75
		0.157	-0.169	0.231	-0.166	0.120					
80.891	99.918	38.585	24.173		8.778	151.483	-5038.45	-4609.01	-4867.81	-4821.32	-5163.38
		0.135	-0.007	0.135	-0.165	-0.114					
82.234	99.776	38.616	24.084		8.788	151.652	-4998.78	-4570.98	-4827.89	-4793.83	-5137.10
82.289	97.594	38.616	24.001		8.758	151.721	-4998.49	-4569.79	-4828.18	-4793.23	-5132.94
81.080	99.796	38.601	24.167		8.757	151.486	-4999.38	-4572.45	-4828.49	-4794.12	-5137.71
87.615	99.602	38.562	24.066		8.730	151.563	-4124.36	-3697.80	-3951.48	-3923.11	-4260.58
87.599	98.230	38.571	24.021		8.664	151.526	-5019.19	-4590.42	-4844.70	-4813.89	-5153.39
87.603	97.633	38.538	23.985		8.663	151.428	-5020.98	-4593.37	-4845.59	-4815.96	-5156.96
87.623	99.104	38.566	24.042		8.660	151.584	-5048.96	-4617.11	-4871.15	-4842.11	-5177.53
87.612	97.743	38.471	23.991		8.633	151.423	-5028.97	-4598.38	-4851.19	-4824.52	-5159.00
					-0.311						
87.592	98.546	38.500	23.988		8.627	151.427	-5028.08	-4601.04	-4852.66	-4823.93	-5163.90
87.651	98.694	38.623	24.043		8.617	151.449	-4995.85	-4568.69	-4821.72	-4793.29	-5132.67
87.698	96.651	38.472	23.945		8.573	151.584	-4997.17	-4569.97	-4821.84	-4794.00	-5127.74
87.564	98.494	38.505	24.143		8.571	151.261	-5002.54	-4577.11	-4828.98	-4798.48	-5139.94
87.599	98.469	38.567	24.039		8.585	151.275	-4951.12	-4527.06	-4776.19	-4749.27	-5089.63
87.647	96.448	38.436	23.945		8.540	151.407	-4950.76	-4526.41	-4777.62	-4750.40	-5086.01
87.583	98.296	38.537	24.134		8.540	151.259	-4943.99	-4518.14	-4767.90	-4742.73	-5083.38
87.629	98.434	38.600	24.019		8.544	151.323	-4568.10	-4141.67	-4391.82	-4368.75	-4703.24
87.653	96.517	38.409	23.937		8.518	151.427	-4570.16	-4143.46	-4395.06	-4371.71	-4701.75
		-0.041	-0.243	0.24633	-0.4259						

Control LVDT 1 (mm)	Control LVDT 2 (mm)	LVDT 1 (50) (mm)	LVDT 2 (50) (mm)		LVDT 3 (25) (mm)	Laser (200) (mm)	SG 1 (ÂµStrain)	SG 2 (ÂµStrain)	SG 3 (ÂµStrain)	SG 4 (ÂµStrain)	SG 5 (ÂµStrain)
83.046	70.596	38.451	24.180		8.943	151.597	-4073.43	-3643.36	-3898.21	-3864.24	-4209.34
87.545	98.382	38.471	24.123		8.517	151.173	-4568.69	-4141.67	-4389.75	-4366.09	-4702.94
					-0.264	-0.4241					

| | | | | -2.08E-06 | -2.62E-05 | 3.01E-06 | -8.16E-05 | | | 1.02E-05 | 6.62E-06 |
| | | | | -9.25E-04 | 7.26E-05 | | | | | | |
SG 6 (µStrain)	SG 7 (µStrain)	SG 8 (µStrain)	SG 9 (µStrain)	SG 10 (µStrain)	SG 11 (µStrain)	SG 12 (µStrain)	SG 13 (µStrain)	SG 14 (µStrain)	SG 15 (µStrain)	SG 16 (µStrain)	SG 17 (µStrain)
-4607.46	-4384.72	-4345.85	-4643.52	-4118.51	-4630.40	-5572.49	-9120.77	-4898.27	-5080.77	-5458.44	-5844.59
-4601.79	-4376.11	-4333.98	-4634.87	-4115.83	-4625.33	-5566.48	-9104.10	-4892.60	-5075.98	-5449.74	-5837.97
-4594.05	-4368.39	-4330.73	-4615.80	-4117.91	-4651.57	-5569.49	-9202.38	-4889.03	-5076.89	-5448.23	-5837.97
-4572.42	-4347.02	-4302.82	-4596.26	-4078.43	-4552.77	-5538.70	-9112.16	-4869.82	-5051.44	-5428.24	-5815.62
-5543.90	-5323.37	-5273.41	-5569.88	-5064.18	-5582.72	-6551.92	-9764.25	-5872.83	-6057.04	-6434.83	-6821.13
-5531.35	-5310.87	-5264.20	-5555.84	-5059.41	-5601.55	-6547.09	-9757.44	-5861.48	-6057.33	-6429.41	-6812.99
-5528.37	-5310.26	-5263.58	-5556.44	-5040.65	-5523.29	-6528.81	-9728.75	-5853.43	-6034.27	-6417.46	-6802.25
-5542.81	-5321.42	-5277.72	-5573.57	-5070.83	-5584.63	-6560.44	-9738.28	-5881.63	-6064.63	-6439.73	-6829.98
-5539.84	-5316.96	-5269.70	-5563.42	-5068.47	-5604.34	-6555.01	-9732.41	-5866.68	-6049.03	-6429.82	-6816.40
-5550.57	-5328.86	-5278.03	-5575.06	-5065.49	-5542.81	-6558.03	-9717.58	-5884.92	-6064.63	-6442.74	-6828.76
-5526.59	-5305.14	-5257.86	-5549.88	-5046.65	-5532.27	-6509.18	-9606.40	-5831.83	-6016.58	-6393.33	-6778.28
-5518.53	-5296.81	-5253.39	-5542.12	-5047.53	-5563.04	-6510.08	-9607.31	-5825.84	-6012.08	-6388.23	-6776.17
-5527.49	-5308.71	-5259.33	-5554.37	-5042.19	-5453.48	-6509.47	-9600.53	-5835.41	-6018.07	-6394.83	-6780.09
-4643.52	-4428.23	-4379.87	-4667.35	-4171.81		-5640.95	-9667.10	-4957.60	-5142.84	-5516.66	-5905.85
-5536.96	-5321.73	-5269.38	-5559.96	-5062.31		-6533.80	-10307.95	-5855.37	-6040.48	-6413.40	-6795.70
-5539.65	-5324.40	-5272.66	-5562.94	-5063.20		-6534.69	-10310.11	-5856.56	-6041.08	-6415.50	-6800.83
-5556.71	-5343.83	-5293.85	-5579.72	-5089.41		-6570.91	-10245.33	-5891.05	-6074.44	-6449.26	-6834.10
-5537.50	-5325.27	-5277.07	-5564.67	-5074.17		-6543.98	-10227.69	-5869.97	-6052.73	-6425.37	-6810.73
-5544.96	-5332.99	-5277.97	-5566.77	-5072.98		-6544.29	-10228.93	-5869.39	-6050.32	-6425.07	-6808.91
-5518.82	-5296.82	-5255.19	-5535.54	-5046.39		-6511.78	-10067.03	-5835.96	-6016.82	-6391.73	-6773.63
-5513.90	-5288.04	-5251.47	-5524.94	-5046.50		-6515.30	-19278.81	-5834.64	-6012.79	-6389.82	-6775.06
-5524.92	-5305.31	-5254.17	-5538.96	-5043.55		-6517.35	-19401.38	-5846.88	-6025.06	-6399.69	-6784.95
-5475.97	-5252.59	-5211.00	-5490.58	-5002.21		-6471.28	-12935.30	-5787.34	-5960.30	-6341.07	-6725.54
-5469.33	-5243.04	-5207.97	-5482.75	-5003.03		-6475.43	-12938.68	-5786.70	-5965.91	-6344.61	-6722.77
-5468.23	-5246.07	-5202.11	-5481.97	-4989.13		-6462.04	-12930.10	-5786.21	-5957.65	-6340.55	-6718.43
-5091.35	-4869.94	-4829.55	-5107.16	-4620.33		-6095.54	-12430.10	-5415.04	-5595.37	-5969.02	-6347.20
-5085.69	-4861.62	-4824.51	-5098.81	-4622.71		-6097.94	-12435.48	-5415.64	-5596.88	-5970.81	-6351.11

SG 6 (ÂµStrain)	SG 7 (ÂµStrain)	SG 8 (ÂµStrain)	SG 9 (ÂµStrain)	SG 10 (ÂµStrain)	SG 11 (ÂµStrain)	SG 12 (ÂµStrain)	SG 13 (ÂµStrain)	SG 14 (ÂµStrain)	SG 15 (ÂµStrain)	SG 16 (ÂµStrain)	SG 17 (ÂµStrain)
-4607.46	-4384.72	-4345.85	-4643.52	-4118.51	-4630.40	-5572.49	-9120.77	-4898.27	-5080.77	-5458.44	-5844.59
-5091.05	-4865.48	-4825.98	-5102.39	-4614.10		-6091.92	-12400.36	-5418.92	-5593.87	-5974.12	-6355.04
						-5.25E-04				-5.12E-04	-5.07E-04

SG 18 (µStrain)	SG 19 (µStrain)			
-5494.73	-4903.34			
-5493.83	-4892.91			
-5486.33	-4894.40			
-5461.54	-4865.34			
-6467.31	-5875.83			
-6464.61	-5872.83			
-6446.34	-5853.73			
-6479.44	-5882.23			
-6467.11	-5872.36			
-6477.03	-5882.82			
-6436.03	-5833.91			
-6429.72	-5830.91			
-6435.42	-5833.01			
-5550.86	-4960.90			
-6449.19	-5857.16			
-6450.40	-5860.75			
-6489.29	-5894.04			
-6479.83	-5866.69			
-6481.94	-5870.58			
-6439.85	-5835.66			
-6437.94	-5835.24			
-6452.63	-5843.59			
-6376.53	-5778.68			
-6371.66	-5781.32			
-6362.48	-5773.67			
-5996.04	-5408.17			
-5998.45	-5411.46			

SG 18 (µStrain)	SG 19 (µStrain)			
-5494.73	-4903.34			
-6004.45	-5408.17			

Appendix A3 – Arch 02 Test Data

Cycle	Time	Timestamp	TZ	Load Cell 1 (kN)	Load Cell 2 (kN)	Control LVDT 1 (mm)	Control LVDT 1_MN (mm)	Control LVDT 1_MX (mm)	Control LVDT 2 (mm)	Control LVDT 2_MN (mm)	Control LVDT 2_MX (mm)	LVDT 1 (HORIZONTAL) (mm)	LVDT 1 (HORIZONTAL)_MN (mm)	LVDT 1 (HORIZONTAL)_MX (mm)	LVDT 2 (VERTICAL) (mm)	LVDT 2 (VERTICAL)_MN (mm)	LVDT 2 (VERTICAL)_MX (mm)
1	00:00:02	04/11/2020 11:06:10	n	0.0399	0.8863	89.5813	89.5813	89.9777	90.7872	90.7590	90.7911	36.6181	36.6149	36.6186	18.5520	18.5520	18.5624
		04/11/2020 11:13:00	n	11.5229	11.2863	87.3466	87.3346	87.3544	82.2486	82.2208	82.2486	36.6186	36.6181	36.6224	18.5092	18.5069	18.5104
												0.0005	0.0032	0.0037	-0.0428	-0.0451	-0.0521
												0.0428	0.0452	0.0522			
		04/11/2020 11:17:20	n	25.6223	11.2424	87.2830	87.2712	87.2951	79.8781	79.8781	79.9220	36.6145	36.6130	36.6172	18.5995	18.5978	18.6013
		04/11/2020 11:34:40	n	10.9614	25.2302	85.4811	85.4651	85.4811	81.7594	81.7118	81.7594	36.6130	36.6108	36.6156	18.4335	18.4324	18.4358
												-0.0057	-0.0073	-0.0068	-0.0757	-0.0745	-0.0745
												0.0759	0.0749	0.0749			
		04/11/2020 11:42:30	n	10.9780	11.1477	86.7736	86.7576	86.7736	81.7397	81.7237	81.7397	36.6119	36.6119	36.6145	18.5481	18.5481	18.5510
		04/11/2020 11:44:20	n	26.0556	11.2061	86.4733	85.6452	86.6574	79.9180	79.8184	80.9123	36.6124	36.6119	36.6140	18.6065	18.4225	18.6094
100	00:03:20	04/11/2020 11:43:20	n	10.9327	26.1545	85.7811	85.6650	86.7176	80.8964	79.9020	81.0196	36.6130	36.6108	36.6151	18.4324	18.4266	18.6071
												-0.0073	0.0806		-0.0803		
1000	00:33:20	04/11/2020 12:11:40	n	25.9598	11.1356	86.2312	85.5391	86.3913	79.8874	79.6882	80.7010	36.6126	36.6115	36.6174	18.5617	18.3765	18.5819
		04/11/2020 12:12:40	n	11.3043	26.1121	85.7791	85.5472	86.3873	80.3539	79.6005	80.6131	36.6163	36.6136	36.6168	18.3956	18.3782	18.5796
												-0.0023	-0.0045	-0.0055	-0.1137	-0.1287	0.0692
												0.1137	0.1288	0.0694		-0.1287	
10000	05:33:20	04/11/2020 19:12:20	n	26.0133	11.3630	86.2775	85.2856	86.4256	79.4316	79.3281	80.4520	36.6053	36.6053	36.6096	18.5513	18.3262	18.5571
		04/11/2020 19:13:30	n	11.4303	25.9167	85.7573	85.4655	86.3535	79.9416	79.3241	80.2128	36.6069	36.6064	36.6096	18.3719	18.3343	18.5456
													-0.0117	0.1730		-0.1726	
100000	07:33:20	06/11/2020 09:38:50	n	25.8673	10.9747	85.5562	85.1287	86.1162	79.4173	78.9712	79.6602	36.6091	36.6086	36.6129	18.4714	18.2971	18.4922
		06/11/2020 09:38:41	n	11.4288	26.3848	85.3445	84.9568	86.0163	79.5009	78.9872	80.0507	36.6129	36.6081	36.6129	18.3284	18.2837	18.5258
												-0.0052	-0.0068	-0.0058	-0.2237	-0.2683	-0.0367
												0.2237	0.2684	0.0371		-0.2232	
		09/11/2020 11:20:30	n	11.6074	10.9601	86.9157	86.8875	86.9157	80.7870	80.7492	80.8187	36.6056	36.6056	36.6077	18.4480	18.4463	18.4503
100001		09/11/2020 11:26:30	n	30.9866	11.1423	86.7018	86.6818	86.7018	77.9599	77.9400	77.9838	36.6041	36.6036	36.6068	18.5526	18.5491	18.5537
		09/11/2020 11:35:40	n	10.8362	31.1716	84.4130	84.3969	84.4170	80.6409	80.5931	80.6529	36.6070	36.6070	36.6086	18.1928	18.1920	18.1963
												-0.0126	-0.0093	-0.0110	-0.1040	-0.1057	-0.1121
												0.1048	0.1061	0.1126			
												-0.0111	-0.0079	-0.0101	-0.3592	-0.3601	-0.3662
												0.3594	0.3601	0.3663			
194100		11/11/2020 16:05:00		31.1442	11.3396	85.3034	84.0173	85.7551	78.0334	77.6993	79.6891	36.4358	36.4347	36.4502	18.4410	18.1142	18.4717
		11/11/2020 16:06:00		11.3934	30.8902	84.4843	84.0173	85.7271	79.0000	77.6993	79.6850	36.4459	36.4331	36.4486	18.1460	18.1130	18.4729

	Cycle	Time	Timestamp	TZ	Load Cell 1 (kN)	Load Cell 2 (kN)	Control LVDT 1 (mm)	Control LVDT 1 _MN (mm)	Control LVDT 1 _MX (mm)	Control LVDT 2 (mm)	Control LVDT 2_MN (mm)	Control LVDT 2_MX (mm)	LVDT 1 (HORIZONTAL) (mm)	LVDT 1 (HORIZONTAL)_MN (mm)	LVDT 1 (HORIZONTAL)_MX (mm)	LVDT 2 (VERTICAL) (mm)	LVDT 2 (VERTICAL)_MN (mm)	LVDT 2 (VERTICAL)_MX (mm)
													-0.1722	-0.1818	-0.1701	-0.4061	-0.4390	-0.0896
													0.4411	0.4752	0.1922			
			12/11/2020 13:48:00	n	11.0917	10.5986	86.4914	86.4914	88.4965	80.4179	80.4179	82.6186	36.7146	36.7114	36.7167	18.4201	18.3923	18.5151
	200000		12/11/2020 13:56:00	n	36.0361	11.2334	84.9494	83.3523	85.5972	77.3227	76.9335	79.5714	36.5594	36.5583	36.6377	18.5452	18.0918	18.5926
			12/11/2020 13:57:00	n	11.0307	35.8545	83.8949	83.3364	85.6012	78.7429	76.9295	79.5594	36.5663	36.5562	36.5706	18.1271	18.0918	18.5943
													0.0964	0.0965	0.0980	-0.1319	-0.1597	-0.0474
													0.1634	0.1866	0.1089			
													-0.0518	-0.0587	-0.0480	-0.4249	-0.4602	0.0319
													0.4281	0.4639	0.0577			
	299999		14/11/2020 22:06:00	n	35.8783	10.6513	83.9608	82.7644	84.9873	77.1106	76.4197	78.9081	36.4744	36.4707	36.4850	18.3727	17.9610	18.4573
			14/11/2020 22:07:00	n	11.6456	36.2011	83.3425	82.7565	84.9913	77.9611	76.4078	78.9001	36.4840	36.4723	36.4872	18.0166	17.9610	18.4596
													-0.1341	-0.1426	-0.1315	-0.5354	-0.5910	-0.1029
													0.5520	0.6080	0.1669			
			16/11/2020 10:37:00	n	10.9023	11.4735	85.4954	85.4875	87.6593	80.0043	79.9365	81.3785	36.8166	36.8150	36.8187	18.2951	18.2922	18.4070
	300000		16/11/2020 10:55:00	n	40.8120	13.0473	84.5241	82.4296	85.0235	76.3125	76.0506	78.9921	36.6529	36.6502	36.6833	18.5106	17.9710	18.5430
			16/11/2020 10:56:00	n	10.7929	41.1769	82.7923	82.4137	85.0076	78.2796	76.0467	78.9842	36.6555	36.6496	36.6630	17.9965	17.9722	18.5447
													0.1985	0.2001	0.2001	-0.2569	-0.2598	-0.1555
													0.3247	0.3279	0.2534			
													0.0374	0.0347	0.0443	-0.5555	-0.5799	-0.0177
													0.5568	0.5809	0.0478			
	399999		19/11/2020 10:21:00	n	40.9552	11.6362	83.1000	81.6822	84.4923	76.4759	75.3735	78.4268	36.5539	36.5469	36.5614	18.2315	17.8163	18.4157
			19/11/2020 10:22:00	n	11.6345	41.3537	82.9924	81.6822	84.5123	76.6228	75.3695	78.4070	36.5560	36.5464	36.5624	17.9565	17.8175	18.4169
													-0.0642	-0.0680	-0.0573	-0.3206	-0.7357	-0.1467
													0.3269	0.7388	0.1575			
			19/11/2020 11:59:00	n	10.9592	11.1979	84.6833	84.6753	84.7073	78.9509	78.9389	78.9828	36.5639	36.5601	36.5649	18.1306	18.1272	18.1318
	400000		19/11/2020 13:22:00	n	46.0226	12.8240	82.9349	81.2991	84.5105	75.8720	74.9170	78.3855	36.5511	36.5479	36.5655	18.2935	17.7577	18.4337
			19/11/2020 13:23:00	n	10.7770	45.5505	82.3814	81.3030	84.5064	76.7724	74.9249	78.3975	36.5586	36.5468	36.5650	17.8528	17.7583	18.4319
													-0.0543	-0.0548	-0.0537	-0.4214	-0.4249	-0.4307
													0.4249	0.4284	0.4340			
													-0.0596	-0.0681	-0.0537	-0.6992	-0.7937	-0.1305
													0.7018	0.7966	0.1411			
	501000		23/11/2020 09:56:00	n	46.1883	11.6150	81.6140	80.2119	83.6583	75.8568	74.5411	78.0334	36.5523	36.5459	36.5682	18.1382	17.6865	18.4192
			23/11/2020 09:57:00	n	11.4938	45.8350	81.8011	80.2159	83.6702	75.7934	74.5570	78.0572	36.5629	36.5448	36.5666	17.8692	17.6860	18.4204
														-0.0153	0.4415		-0.4412	
													-0.0552	-0.0701	-0.0521	-0.6828	-0.8660	-0.1421
													0.6851	0.8689	0.1513			
			00/01/1900 00:21:00	n	11.0575	11.0058	83.8298	83.8179	83.8458	78.2920	78.2522	78.3396	36.5475	36.5438	36.5485	18.0654	18.0608	18.0665
	501001		23/11/2020 11:58:00	n	51.0750	11.5946	81.4848	79.5642	83.5047	75.1256	73.9825	77.9758	37.6251	37.6203	37.7245	18.2878	17.6176	18.4645
			23/11/2020 11:59:00	n	11.1242	50.6519	80.9877	79.5602	83.5088	75.8313	73.9706	77.9719	37.7064	37.6209	37.7250	17.7812	17.6182	18.4640

	Cycle	Time	Timestamp	TZ	Load Cell 1 (kN)	Load Cell 2 (kN)	Control LVDT 1 (mm)	Control LVDT 1 _MN (mm)	Control LVDT 1 _MX (mm)	Control LVDT 2 (mm)	Control LVDT 2_MN (mm)	Control LVDT 2_MX (mm)	LVDT 1 (HORIZONTAL) (mm)	LVDT 1 (HORIZONTAL)_MN (mm)	LVDT 1 (HORIZONTAL)_MX (mm)	LVDT 2 (VERTICAL) (mm)	LVDT 2 (VERTICAL)_MN (mm)	LVDT 2 (VERTICAL)_MX (mm)
													-0.0706	-0.0711	-0.0701	-0.4866	-0.4913	-0.4959
													0.4917	0.4964	0.5008			
													1.0883	1.0060	1.1063	-0.7708	-0.9338	-0.0985
													1.3336	1.3726	1.1107			
	600001		25/11/2020 18:57:00	n	50.8357	11.3234	80.0731	78.3570	82.8025	75.8307	75.8148	75.8505	38.3665	38.3634	38.4909	18.0844	17.3776	18.4506
			25/11/2020 18:58:00	n	11.7404	51.1903	80.3402	78.3451	82.8066	75.8425	75.8188	75.8465	38.4293	38.3623	38.4920	17.6947	17.3782	18.4500
														1.7442	2.0775		-1.1287	
													1.8112	1.7474	1.8733	-0.8573	-1.1738	-0.1124
													2.0038	2.1051	1.8767			
			26/11/2020 09:14:00	n	11.0061	11.1828	82.8389	82.8190	82.8469	75.7597	75.7239	75.7597	38.3823	38.3812	38.3844	18.0041	18.0023	18.0064
	600002		26/11/2020 10:44:50	n	61.1626	11.1066	85.7766	85.7645	85.7925	72.1687	72.1687	72.1964	38.8400	38.8363	38.8400	18.5962	18.5927	18.5962
			26/11/2020 10:53:00	n	10.9353	60.8681	80.3070	80.2911	80.3111	78.4272	78.3756	78.4591	38.8272	38.8272	38.8293	17.3660	17.3660	17.3713
													1.7642	1.7663	1.7657	-0.5480	-0.5497	-0.5561
													1.8473	1.8499	1.8512			
													2.2091	2.2123	2.2106	-1.1860	-1.1860	-1.1912
													2.5073	2.5101	2.5112			
	601000		26/11/2020 11:23:50	n	60.4102	10.9560	79.4823	77.6522	80.6940	73.8412	72.9127	76.3142	39.9380	39.9380	40.0471	18.3545	17.4027	18.5969
			26/11/2020 11:24:50	n	11.5620	60.5740	79.1279	78.2128	81.1538	74.7526	72.7699	75.9848	40.0523	39.9417	40.1718	17.6193	17.4137	18.5478
														1.7905	1.8713		0.5437	
													3.4342	3.3268	3.5531	-0.9327	-1.1383	-0.0147
													3.5586	3.5161	3.5532			
			26/11/2020 11:29:50	n	10.4685	10.9629	82.4471	82.4230	82.4550	77.8032	77.7834	77.8191	40.0508	40.0508	40.0539	18.0422	18.0422	18.0445
	601001		26/11/2020 11:51:40	n	71.1521	10.9805	85.8860	85.8662	85.8901	70.2518	70.2319	70.2518	40.8269	40.8269	40.8284	18.9850	18.9833	18.9861
			26/11/2020 11:57:50	n	11.0034	71.1280	78.9395	78.9395	78.9794	78.1279	78.1279	78.1954	40.6429	40.6413	40.6471	17.2401	17.2401	17.2483
													3.4327	3.4359	3.4353	-0.5098	-0.5098	-0.5179
													3.4703	3.4735	3.4741			
													4.0248	4.0264	4.0284	-1.3119	-1.3119	-1.3142
													4.2332	4.2348	4.2374			

	Cycle	Time	Timestamp	TZ	Load Cell 1 (kN)	Load Cell 2 (kN)	Control LVDT 1 (mm)	Control LVDT 1 _MN (mm)	Control LVDT 1 _MX (mm)	Control LVDT 2 (mm)	Control LVDT 2_MN (mm)	Control LVDT 2_MX (mm)	LVDT 1 (HORIZONTAL) (mm)	LVDT 1 (HORIZONTAL)_MN (mm)	LVDT 1 (HORIZONTAL)_MX (mm)	LVDT 2 (VERTICAL) (mm)	LVDT 2 (VERTICAL)_MN (mm)	LVDT 2 (VERTICAL)_MX (mm)

LVDT 3 (MIDDLE) (mm)	LVDT 3 (MIDDLE)_MN (mm)	LVDT 3 (MIDDLE)_MX (mm)	Laser (200) (mm)	Laser (200)_MN (mm)	Laser (200)_MX (mm)	SG 1 (µStrain)	SG 2 (µStrain)	SG 3 (µStrain)	SG 4 (µStrain)	SG 5 (µStrain)	SG 6 (µStrain)	SG 7 (µStrain)	SG 8 (µStrain)	SG 9 (µStrain)	SG 10 (µStrain)	SG 11 (µStrain)	SG 12 (µStrain)	SG 13 (µStrain)	SG 14 (µStrain)
		0.0888	0.0489		0.0451														
31.3099	31.3088	31.3129	115.4126	115.3976	115.4182	-3723.442	-2491.012	-2807.077	-2432.265	-1842.505	-1200.625	-2354.794	-3043.895	-1788.336	-2761.424	-1551.728	-2405.841	-2560.411	-2845.930
31.3995	31.3990	31.4017	115.4615	115.4559	115.4634	-3723.442	-2569.236	-2951.169	-2429.611	-1911.237	-1229.431	-2355.683	-3080.550	-1778.968	-2803.079	-1535.412	-2402.027	-2023.524	-2847.695
0.0896	0.0901	0.0888	0.0489	0.0583	0.0451														
31.4840	31.4834	31.4872	115.5685	115.5646	115.5779	-3806.888	-2626.893	-3006.199	-2483.425	-1970.562	-1268.317	-2415.937	-3144.175	-1833.611	-2845.699	-1275.586	-2477.562	-2099.268	-2905.078
31.4916	31.4900	31.4938	115.3823	115.3710	115.3823	-3777.969	-2622.475	-3004.731	-2483.141	-1961.799	-1259.874	-2402.731	-3133.524	-1829.797	-2867.397	-1632.886	-2474.032	-2086.975	-2879.752
0.0845	0.0845	0.0856			0.1145														
0.1741	0.1746	0.1743			0.1145	0.000	0.000	0.000	0.000	0.000	0.000				0.000	0.000	0.000		
0.1817	0.1811	0.1809				0.000	0.000	0.000	0.000	0.000	0.000				0.000	0.000	0.000		
		0.1776																	
31.4454	31.4454	31.4492	115.4161	115.4105	115.4180	-3778.253	-2621.598	-3010.038	-2487.831	-1967.637	-1304.122	-2402.731	-3135.597	-1831.278	-2864.447	-1488.986	-2460.246	-2089.320	-2878.567
31.5427	31.5411	31.5432	115.5685	115.3202	115.5685	-3778.858	-2618.648	-2999.424	-2487.251	-1964.131	-1263.947	-2414.764	-3134.104	-1831.858	-2851.599	-1320.130	-2465.825	-2089.320	-2880.048
31.5329	31.5302	31.5329	115.3315	115.3258	115.5741	-3795.607	-2623.943	-3009.162	-2509.863	-1967.637	-1261.911	-2403.619	-3149.495	-1834.783	-2859.436	-1432.384	-2458.481	-2087.852	-2893.007
					0.1051	0.000	0.000	0.000	0.000	0.000	0.000				0.000	0.000	0.000		
0.2328	0.2322	0.2303	0.1559		0.1070	0.000	0.000	0.000	0.000	0.000	0.000				0.000	0.000	0.000		
31.6042	31.6042	31.6074	115.5702	115.3407	115.5702	-3694.203	-2538.679	-2933.582	-2408.155	-1882.407	-1182.291	-2326.561	-3055.307	-1799.653	-2770.603	OverRange	-2392.878	-1991.792	-2811.524
31.6096	31.6074	31.6096	115.3633	115.3521	115.5683	-3696.573	-2539.851	-2920.304	-2400.813	-1885.332	-1176.466	-2326.561	-3056.492	-1749.884	-2770.011	OverRange	-2388.176	-1996.185	-2805.045
		0.2945			0.1520	0.000	0.000	0.000	0.000	0.000	0.000				0.000		0.000		
		0.2057				0.000	0.000	0.000	0.000	0.000	0.000				0.000		0.000		
		0.2079																	
31.6577	31.6572	31.6610	115.5932	115.3488	115.5932	-3665.228	-2505.320	-2885.161	-2371.270	-1846.162	-1147.841	-2294.682	-3023.394	-1717.159	-2736.354	OverRange	-2338.399	-1931.535	-2765.202
31.6566	31.6566	31.6604	115.3920	115.3808	115.5914	-3668.201	-2501.211	-2884.272	-2364.520	-1859.883	-1142.880	-2290.289	-3022.814	-1715.986	-2781.391	OverRange	-2344.556	-1933.287	-2770.199
						0.000	0.000	0.000	0.000	0.000	0.000				0.000		0.000		
		0.3516			0.1318	0.000	0.000	0.000	0.000	0.000	0.000				0.000		0.000		
31.7730	31.7681	31.7763	115.5614	115.3208	115.5765	-3819.083	-2602.950	-2985.107	-2459.877	-1934.634	-1244.546	-2401.583	-3129.489	-1809.025	-2814.511	OverRange	-2467.517	-2039.840	-2854.673
31.7774	31.7660	31.7774	115.3659	115.3113	115.6047	-3820.564	-2605.011	-2985.983	-2459.877	-1949.543	-1242.805	-2395.091	-3128.896	-1813.123	-2826.323	OverRange	-2472.207	-2041.593	-2859.992
		0.3746			0.1583														
		0.4633				0.000	0.000	0.000	0.000	0.000	0.000				0.000		0.000		
		0.4644				0.000	0.000	0.000	0.000	0.000	0.000				0.000		0.000		
		0.4639																	
31.6912	31.6912	31.6934	115.4204	115.4054	115.4261	-3958.817	-2622.010	-3035.166	-2495.970	-1907.049	-1298.142	-2404.705	-3173.403	-1871.323	-2894.102	OverRange	-2526.511	-2056.841	-2932.297
31.7771	31.7771	31.7798	115.5834	115.5816	115.5872	-4105.285	-2796.562	-3193.119	-2642.527	-2138.625	-1440.222	-2597.035	-3319.604	-1999.248	-3023.970		-2698.330	-2288.436	-3072.216
31.8224	31.8218	31.8245	115.1010	115.0934	115.1010	-3806.951	-2310.230	-2963.655	-2463.267	-1982.506	-1356.299	-2390.464	-3095.510	-1831.740	-2811.272		-2520.789	-2067.257	-2928.896
		0.3805			0.0079	0.000	0.000	0.000	0.000	0.000	0.000				0.000	0.002	0.000		
		0.4669			0.1689	0.000	0.000	0.000	0.000	0.000	0.000				0.000	0.002	0.000		
		0.5116																	
		0.4892																	
32.0011	31.9968	32.0374	115.9754	115.4699	115.9923	-5844.694	-4501.394	-4881.248	-4329.245	-3839.104	-3100.360	-4295.053	-5025.789	-3713.904	-4681.155	OverRange	-4356.668	-3979.306	-4774.334
32.0347	31.9957	32.0374	115.5168	115.4717	115.9829	-5838.124	-4445.830	-4759.829	-4287.987	-3705.970	-2994.686	-4196.867	-5028.764	-3709.503	-4679.383	OverRange	-4353.730	-3981.066	-4781.425

LVDT 3 (MIDDLE) (mm)	LVDT 3 (MIDDLE)_MN (mm)	LVDT 3 (MIDDLE)_MX (mm)	Laser (200) (mm)	Laser (200)_MN (mm)	Laser (200)_MX (mm)	SG 1 (µStrain)	SG 2 (µStrain)	SG 3 (µStrain)	SG 4 (µStrain)	SG 5 (µStrain)	SG 6 (µStrain)	SG 7 (µStrain)	SG 8 (µStrain)	SG 9 (µStrain)	SG 10 (µStrain)	SG 11 (µStrain)	SG 12 (µStrain)	SG 13 (µStrain)	SG 14 (µStrain)
		0.6357			0.5741														
		0.7245				-0.002	-0.002	-0.002	-0.002	-0.002	-0.002				-0.002		-0.002		
		0.7245			0.5308	-0.002	-0.002	-0.002	-0.002	-0.002	-0.002				-0.002		-0.002		
		0.7245																	
31.8142	31.7328	31.8142	115.7381	115.5839	115.8397	-5737.115	-4390.573	-4772.786	-4192.194	-3732.495	-3023.847	-4183.615	-4919.489	-3605.206	-4636.434	OverRange	-4282.315	-3876.062	-4684.637
32.0017	31.9865	32.0358	115.9920	115.3585	115.9958	-5745.471	-4398.842	-4779.294	-4201.642	-3735.446	-3032.017	-4192.777	-4927.498	-3613.141	-4627.248	OverRange	-4287.026	-3876.348	-4667.863
32.0352	31.9881	32.0374	115.3566	115.3416	115.9939	-5741.888	-4394.998	-4776.641	-4193.657	-3739.860	-3027.058	-4181.855	-4928.688	-3609.025	-4634.649	OverRange	-4288.798	-3889.278	-4684.637
		0.5012			0.4214	-0.002	-0.002	-0.002	-0.002	-0.002	-0.002				-0.002		-0.002		
		0.7228			0.5775	-0.002	-0.002	-0.002	-0.002	-0.002	-0.002				-0.002		-0.002		
		0.7245																	
		0.7236																	
32.3717	32.3509	32.3868	115.5595	114.9918	115.6160	-4141.292	-2749.354	-3070.286	-2581.845	-2086.627	-1396.048	-2543.413	-3270.450	-1962.810	-2969.013	OverRange	-2630.575	-2239.618	-2994.285
32.3841	32.3509	32.3868	115.0445	114.9918	115.6103	-4006.536	-2406.806	-3077.064	-2465.288	-2087.504	-1324.800	-2457.646	-3270.758	-1913.945	-2880.172	OverRange	-2690.810	-2244.309	-3007.532
		1.0739			0.1977	0.000	0.000	0.000	0.000	0.000	0.000				0.000		0.000		
		1.0739			-0.1221	0.000	0.000	0.000	0.000	0.000	0.000				0.000		0.000		
		1.0739																	
32.0761	31.9684	32.0783	115.6465	115.6032	115.7743	-5761.655	-4393.859	-4774.597	-4180.425	-3731.365	-3020.360	-4193.418	-4920.130	-3606.722	-4636.489	OverRange	-4272.624	-3877.556	-4659.325
32.2615	32.2610	32.3080	116.0639	115.2820	116.0678	-5765.535	-4395.929	-4774.906	-4181.007	-3729.307	-3021.823	-4192.538	-4921.022	-3611.705	-4627.885	OverRange	-4286.770	-3888.143	-4657.255
32.3037	32.2621	32.3101	115.3082	115.2801	116.0639	-5763.750	-4393.264	-4775.489	-4173.929	-3734.601	-3016.852	-4186.921	-4922.510	-3610.527	-4637.679	OverRange	-4287.067	-3897.540	-4670.892
		0.7654			0.3561	-0.002	-0.002	-0.002	-0.002	-0.002	-0.002				-0.002		-0.002		
		0.9951			0.6495	-0.002	-0.002	-0.002	-0.002	-0.002	-0.002				-0.002		-0.002		
		0.9972																	
		0.9961																	
32.6879	32.6501	32.6917	115.5906	114.9140	115.7072	-4005.510	-2615.927	-3001.445	-2526.821	-1976.840	-1363.650	-2423.162	-3149.478	-1841.940	-2845.055	OverRange	-2675.989	-2138.994	-2897.662
32.6906	32.6517	32.6917	115.0887	114.9083	115.7204	-3928.142	-2530.918	-3162.784	-2516.526	-1858.048	-1213.124	-2330.093	-3154.206	-1846.631	-2863.200	OverRange	-2655.672	-2224.336	-2915.930
						0.000	0.000	0.000	0.000	0.000	0.000				0.000		0.000		
		1.3788			0.2890	0.000	0.000	0.000	0.000	0.000	0.000				0.000		0.000		
		1.3788																	
		1.3788																	
32.5608	32.5565	32.5614	115.2766	115.2560	115.2992	-4018.027	-2629.870	-3012.968	-2529.331	-1970.779	-1258.710	-2428.767	-3155.328	-1834.344	-2853.303	OverRange	-2682.849	-2116.114	-2899.517
32.7145	32.6686	32.7631	116.2804	115.3913	116.3162	-5962.397	-4501.586	-4885.579	-4398.489	-3839.644	-3125.757	-4302.943	-5037.248	-3717.357	-4729.088	OverRange	-4517.268	-4014.545	-4776.607
32.7615	32.6697	32.7631	115.5434	115.3876	116.3162	-5963.314	-4501.288	-4884.104	-4392.290	-3841.999	-3121.071	-4297.935	-5038.141	-3716.774	-4733.241	OverRange	-4520.801	-4026.024	-4806.199
		1.2484			-0.1190	-0.002	-0.002	-0.002	-0.002	-0.002	-0.002				-0.002		-0.002		
		1.4502			0.8980	-0.002	-0.002	-0.002	-0.002	-0.002	-0.002				-0.002		-0.002		
		1.4502																	
		1.4502																	
33.0377	32.9622	33.0495	115.9721	115.0927	116.0794	-5872.476	-4373.356	-4756.446	-4265.720	-3707.351	-2981.948	-4179.370	-4895.090	-3584.527	-4595.747	OverRange	-4406.719	-3885.928	-4646.428
33.0463	32.9617	33.0495	115.3556	115.0946	116.0832	-5868.880	-4370.108	-4757.921	-4262.186	-3710.290	-2974.373	-4174.943	-4896.875	-3585.692	-4627.448	OverRange	-4406.421	-3897.978	-4660.363
					0.6611	-0.002	-0.002	-0.002	-0.002	-0.002	-0.002				-0.002		-0.002		
		1.7366			0.8027	-0.002	-0.002	-0.002	-0.002	-0.002	-0.002				-0.002		-0.002		
		1.7366																	
		1.7366																	
32.8495	32.8452	32.8511	115.2318	115.5266	115.5510	-5862.310	-4368.336	-4753.483	-4265.720	-3704.115	-2977.287	-4179.370	-4894.507	-3578.650	-4590.701	OverRange	-4351.821	-3849.801	-4607.884
33.1177	33.0450	33.1613	116.0384	115.0444	116.1965	-5891.666	-4393.254	-4776.359	-4287.352	-3728.954	-3003.124	-4203.121	-4920.396	-3611.088	-4625.180	OverRange	-4411.255	-3923.686	-4689.537
33.1516	33.0450	33.1613	115.2528	115.0426	116.1927	-5890.166	-4390.005	-4774.599	-4278.214	-3731.012	-2995.833	-4198.980	-4921.290	-3611.683	-4651.265	OverRange	-4415.694	-3942.518	-4707.440

LVDT 3 (MIDDLE) (mm)	LVDT 3 (MIDDLE)_MN (mm)	LVDT 3 (MIDDLE)_MX (mm)	Laser (200) (mm)	Laser (200)_MN (mm)	Laser (200)_MX (mm)	SG 1 (µStrain)	SG 2 (µStrain)	SG 3 (µStrain)	SG 4 (µStrain)	SG 5 (µStrain)	SG 6 (µStrain)	SG 7 (µStrain)	SG 8 (µStrain)	SG 9 (µStrain)	SG 10 (µStrain)	SG 11 (µStrain)	SG 12 (µStrain)	SG 13 (µStrain)	SG 14 (µStrain)
		1.5382			0.1327	-0.002	-0.002	-0.002	-0.002	-0.002	-0.002				-0.002		-0.002		
		1.8484			0.7782	-0.002	-0.002	-0.002	-0.002	-0.002	-0.002				-0.002		-0.002		
		1.8484																	
		1.8484																	
33.4482	33.3366	33.4773	115.8310	114.4801	116.0531	-4053.238	-2552.984	-2932.764	-2450.691	-1826.999	-1153.000	-2358.245	-3087.228	-1780.443	-2807.841	OverRange	-2597.430	-2093.220	-2840.515
33.4536	33.3371	33.4800	114.9060	114.4801	116.0569	-3935.829	-2531.514	-2704.696	-2309.591	-1769.917	-1022.931	-2314.292	-3024.569	-1400.885	-2818.736	OverRange	-2660.472	-2114.617	-2844.649
					0.6348	0.000	0.000	0.000	0.000	0.000	0.000				0.000		0.000		
		2.1644			0.8212	0.000	0.000	0.000	0.000	0.000	0.000				0.000		0.000		
		2.1671																	
		2.1657																	
33.2036	33.2026	33.2063	115.1870	115.1739	115.1890	-4014.340	-2515.418	-2901.304	-2413.461	-1852.279	-1105.360	-2319.896	-3043.886	-1719.964	-2795.250	OverRange	-2574.270	-2052.552	-2855.620
33.3220	33.3203	33.3230	116.5042	116.4910	116.5079	-5965.980	-4451.599	-4835.748	-4352.692	-3783.832	-3051.213	-4258.979	-4983.155	-3661.766	-4663.510	OverRange	-4562.197	-4087.856	-4794.291
33.3106	33.3101	33.3128	114.6940	114.6865	114.6940	-5971.815	-4451.713	-4840.321	-4338.658	-3793.615	-3040.799	-4248.551	-4981.494	-3651.004	-4799.755	OverRange	-4603.176	-4007.836	-4757.430
		1.8934			-0.2293	-0.002	-0.002	-0.002	-0.002	-0.002	-0.002				-0.002		-0.002		
		2.0101			1.0897	-0.002	-0.002	-0.002	-0.002	-0.002	-0.002				-0.002		-0.002		
		1.9998																	
		2.0050																	
33.5025	33.3780	33.5128	116.4742	114.6634	116.5741	-5980.082	-4462.525	-4847.319	-4363.333	-3798.204	-3059.956	-4265.467	-5000.392	-3685.275	-4698.214	OverRange	-4619.057	-4029.505	-4772.712
33.5068	33.3796	33.5144	115.0553	114.6559	116.5760	-5975.581	-4455.136	-4845.534	-4346.522	-3797.621	-3048.290	-4258.475	-4989.990	-3667.348	-4793.130	OverRange	-4622.912	-4036.286	-4780.695
					1.1559	-0.002	-0.002	-0.002	-0.002	-0.002	-0.002				-0.002		-0.002		
		2.1998			1.3871	-0.002	-0.002	-0.002	-0.002	-0.002	-0.002				-0.002		-0.002		
		2.2014																	
		2.2006																	
33.2681	33.2681	33.2719	115.6504	115.6316	115.6504	-5965.403	-4451.603	-4842.286	-4349.175	-3787.641	-3036.314	-4257.012	-4991.775	-3662.637	-4726.853	OverRange	-4535.261	-4004.189	-4772.996
33.4719	33.4708	33.4729	116.8247	116.8191	116.8285	-5976.588	-4458.104	-4845.266	-4363.313	-3796.400	-3060.757	-4261.628	-4993.887	-3671.718	-4620.251	OverRange	-4614.920	-4115.847	-4818.896
33.4110	33.4105	33.4170	113.9676	113.9545	113.9676	-3931.098	-2279.519	-2698.824	-2233.663	-1803.659	-1064.843	-2322.648	-2943.147	-1685.453	-2872.068	OverRange	-2707.092	-2049.388	-2787.242
		1.9589			0.2322	-0.002	-0.002	-0.002	-0.002	-0.002	-0.002				-0.002		-0.002		
		2.1600			1.4102	0.000	0.000	0.000	0.000	0.000	0.000				0.000		0.000		
		2.1040																	
		2.1320																	

SG 15 (µStrain)	SG 16 (µStrain)	SG 17 (µStrain)	SG 18 (µStrain)	SG 19 (µStrain)	SG 20 (µStrain)	SG 21 (µStrain)					
-2550.414	-3527.255	-2463.095	-2374.739	-3366.612	-2205.889	-3478.899					
-3127.882	-3522.207	-2498.356	-2398.793	-3361.292	-2206.172	-3564.355					
-3190.323	-3587.094	-2551.888	-2443.226	-3423.471	-2255.276	-3636.377					
-3131.746	-3524.494	-2403.323	-2452.322	-3419.904	-2277.604	-3652.719					
	0.000			0.000	0.000	0.000					
	0.000			0.000	0.000	0.000					
-3157.480	-3559.188	-2528.956	-2498.409	-3412.227	-2264.088	-3646.486					
-3116.960	-3518.853	-2379.897	-2441.165	-3414.881	-2284.059	-3678.589					
-3156.888	-3573.135	-2471.984	-2427.971	-3408.660	-2258.794	-3658.964					
	0.000			0.000	0.000	0.000					
	0.000			0.000	0.000	0.000					
-2971.380	-3460.798	-2070.881	-2360.595	-3326.276	-2203.515	-3606.007					
-3044.065	-3469.387	-2185.893	-2361.768	-3328.942	-2175.614	-3586.386					
	0.000			0.000	0.000	0.000					
	0.000			0.000	0.000	0.000					
-2833.251	-3412.268	OverRange	-2325.480	-3296.738	-2166.369	-3585.395					
-2876.314	-3422.940	OverRange	-2321.075	-3298.502	-2144.924	-3575.277					
	0.000			0.000	0.000	0.000					
	0.000			0.000	0.000	0.000					
-2983.342	-3502.908	OverRange	-2416.468	-3378.879	-2266.953	-3686.032					
-3039.389	-3519.805	OverRange	-2413.840	-3379.175	-2239.355	-3681.268					
	0.000			0.000	0.000	0.000					
	0.000			0.000	0.000	0.000					
-3184.341	-3592.584	OverRange	-2491.859	-3451.544	-2333.253	-3750.313					
-3284.707	-3741.303	49496.504	-2625.795	-3621.511	-2460.968	-3915.774					
-3036.470	-3569.248	OverRange	-2174.697	-3424.432	-2363.123	-3723.939					
	0.000			0.000	0.000	0.000					
	0.000			0.000	0.000	0.000					
-4906.452	-5410.838	OverRange	-4307.736	-5294.761	-4177.366	-5646.077					
-4978.865	-5427.226	97530.224	-4305.963	-5237.697	-4142.839	-5631.721					

SG 15 (µStrain)	SG 16 (µStrain)	SG 17 (µStrain)	SG 18 (µStrain)	SG 19 (µStrain)	SG 20 (µStrain)	SG 21 (µStrain)					
	-0.002	#VALUE!		-0.002	-0.002	-0.002					
	-0.002	0.100		-0.002	-0.002	-0.002					
-4868.472	-5324.763	OverRange	-4229.289	-5193.965	-4044.660	-5508.362					
-4811.566	-5302.162	OverRange	-4221.937	-5189.502	-4074.440	-5546.895					
-4874.696	-5328.928	31075.272	-4228.124	-5192.180	-4033.762	-5531.658					
	-0.002			-0.002	-0.002	-0.002					
	-0.002			-0.002	-0.002	-0.002					
-3189.473	-3622.628	OverRange	-2577.438	-3547.997	-2437.374	-3897.991					
-3216.066	-3660.580	OverRange	-2575.981	-3531.726	-2394.768	-3925.177					
	0.000			0.000	0.000	0.000					
	0.000			0.000	0.000	0.000					
-4865.246	-5309.632	OverRange	-4228.738	-5180.650	-4041.760	-5546.349					
-4832.356	-5287.626	OverRange	-4219.898	-5181.245	-4079.782	-5575.644					
-4870.589	-5314.108	OverRange	-4219.898	-5180.650	-4028.506	-5564.883					
	-0.002			-0.002	-0.002	-0.002					
	-0.002			-0.002	-0.002	-0.002					
-3059.606	-3491.893	OverRange	-2421.396	-3395.048	-2359.803	-3835.407	19.607	19.604	19.692		
-3103.042	-3537.255	OverRange	-2461.314	-3463.442	-2276.610	-3826.211	19.682	19.606	19.693		
	0.000			0.000	0.000	0.000					
	0.000			0.000	0.000	0.000					
-3088.820	-3523.182	OverRange	-2455.664	-3415.990	-2288.530	-3808.962	19.643	19.640	19.644		
-4954.099	-5385.674	OverRange	-4348.640	-5303.554	-4213.881	-5723.600	19.600	19.600	19.692		
-4990.609	-5429.462	#########	-4338.610	-5302.364	-4143.328	-5714.649	19.688	19.599	19.694		
	-0.002			-0.002	-0.002	-0.002					
	-0.002			-0.002	-0.002	-0.002					
-4804.995	-5273.852	OverRange	-4213.946	-5168.100	-4106.173	-5590.775	19.590	19.584	19.674		
-4847.060	-5307.165	#########	-4224.187	-5167.504	-4027.758	-5594.965	19.665	19.582	19.676		
	-0.002			-0.002	-0.002	-0.002					
	-0.002			-0.002	-0.002	-0.002					
-4774.200	-5265.830	OverRange	-4171.993	-5133.746	-4021.274	-5571.360	19.617	19.610	19.617		
-4836.773	-5308.126	OverRange	-4256.406	-5204.988	-4146.711	-5615.939	19.583	19.578	19.677		
-4895.477	-5346.819	#########	-4246.699	-5204.393	-4057.050	-5619.956	19.673	19.577	19.678		

SG 15 (µStrain)	SG 16 (µStrain)	SG 17 (µStrain)	SG 18 (µStrain)	SG 19 (µStrain)	SG 20 (µStrain)	SG 21 (µStrain)					
	-0.002			-0.002	-0.002	-0.002					
	-0.002			-0.002	-0.002	-0.002					
-2989.130	-3464.504	OverRange	-2396.373	-3332.731	-2333.628	-3666.436	19.531	19.525	19.618		
-3037.858	-3492.970	#########	-2395.793	-3351.068	-2231.409	-3781.254	19.595	19.525	19.618		
	0.000			0.000	0.000	0.000					
	0.000			0.000	0.000	0.000					
-2978.901	-3446.839	OverRange	-2374.725	-3320.115	-2222.690	-3730.621	19.590	19.589	19.593		
-4996.817	-5424.668	#########	-4309.350	-5258.317	-4125.892	-5689.838	19.525	19.524	19.526		
-4927.774	-5384.582	#########	-4323.334	-5263.494	-4255.047	-5554.568	19.639	19.639	19.643		
	-0.002			-0.002	-0.002	-0.002					
	-0.002			-0.002	-0.002	-0.002					
-4907.794	-5396.084	OverRange	-4308.486	-5272.307	-4270.475	-5526.084	19.516	19.511	19.630		
-4951.694	-5413.961	OverRange	-4306.998	-5269.034	-4143.884	-5692.558	19.618	19.511	19.630		
	-0.002			-0.002	-0.002	-0.002					
	-0.002			-0.002	-0.002	-0.002					
-4929.143	-5407.998	OverRange	-4309.081	-5261.608	-4176.056	-5659.469	19.586	19.586	19.587		
-5028.055	-5443.817	#########	-4309.062	-5261.648	-4131.182	-5689.338	19.479	19.479	19.483		
-3048.309	-3426.769	14740.574	-2233.367	-3235.152	-2224.840	-3559.401	19.631	19.631	19.636		
	-0.002			-0.002	-0.002	-0.002					
	0.000			0.000	0.000	0.000					

Papers for Publishing

Arnab Chakraborty, Parametric Strain-Life Assessment Based on In-situ Measurement and Damage Model Numerical Analysis for Segmental Multi-Ring Masonry Arches, 2024 Draft, under review.